

“ACTIVE FLUX” BASED WIDE SPEED RANGE MOTION SENSORLESS CONTROL OF PERMANENT MAGNET SYNCHRONOUS MACHINES

Teză destinată obținerii
titlului științific de doctor inginer
la
Universitatea “Politehnica” din Timișoara
în domeniul INGINERIE ELECTRICĂ
de către

Ing. Mihaela Codruța Paicu

Conducător științific:	prof.dr.ing. Ion Boldea
Referenți științifici:	prof.dr.ing. Ioan Adrian Viorel
	prof.dr.ing. Mircea Rădulescu
	prof.dr.ing. Dorin Popovici

Ziua susținerii tezei: 26.06.2009

Seriile Teze de doctorat ale UPT sunt:

- | | |
|------------------------|---|
| 1. Automatică | 7. Inginerie Electronică și Telecomunicații |
| 2. Chimie | 8. Inginerie Industrială |
| 3. Energetică | 9. Inginerie Mecanică |
| 4. Ingineria Chimică | 10. Știința Calculatoarelor |
| 5. Inginerie Civilă | 11. Știința și Ingineria Materialelor |
| 6. Inginerie Electrică | |

Universitatea „Politehnica” din Timișoara a inițiat seriile de mai sus în scopul diseminării expertizei, cunoștințelor și rezultatelor cercetărilor întreprinse în cadrul școlii doctorale a universității. Seriile conțin, potrivit H.B.Ex.S Nr. 14 / 14.07.2006, tezele de doctorat susținute în universitate începând cu 1 octombrie 2006.

Copyright © Editura Politehnica – Timișoara, 2009

Această publicație este supusă prevederilor legii dreptului de autor. Multiplicarea acestei publicații, în mod integral sau în parte, traducerea, tipărirea, reutilizarea ilustrațiilor, expunerea, radiodifuzarea, reproducerea pe microfilme sau în orice altă formă este permisă numai cu respectarea prevederilor Legii române a dreptului de autor în vigoare și permisiunea pentru utilizare obținută în scris din partea Universității „Politehnica” din Timișoara. Toate încălcările acestor drepturi vor fi penalizate potrivit Legii române a drepturilor de autor.

România, 300159 Timișoara, Bd. Republicii 9,
tel. 0256 403823, fax. 0256 403221
e-mail: editura@edipol.upt.ro

PREFACE

This thesis represents an approach and a contribution to the sensorless control methods for the permanent magnet synchronous machines by introducing a novel concept called "active flux". Based on this concept, the rotor position and speed estimation becomes simpler and with a less computation effort than using signal injection method. Beside the implementation of the sensorless vector control and DTFC systems, the thesis proposes two control strategies for the motion sensorless control of the permanent magnet synchronous machines in wide speed range.

Motivation

The target of this thesis is to offer a advanced and robust control alternative to sensorless control methods for synchronous machines with permanent magnets.

A very important part of the thesis was the development of two simulation control models and their implementation on a dSpace system of a sensorless vector control and direct torque and flux control for interior permanent magnet synchronous machine (Chapter 3 and Chapter 4). This was done within the Institute of Energy Technology, Aalborg University, Aalborg, Denmark.

The other part of the thesis was the development of two control strategies for the motion-sensorless control of a permanent magnet assisted reluctance synchronous machine (PM-RSM) (Chapter 5). Their implementation on dSpace system was carried out in the Intelligent Motion Control Laboratory of the Faculty of Electrical Engineering, University "Politehnica" of Timisoara, Timisoara, Romania.

The motion sensorless control of the IPMSM, respectively PM-RSM is obtained via model-based stator flux estimation using the "active flux" concept. Most of the considered solutions existent in literature are either too complicated or require a lot of computation effort. The scope of this thesis is to bring new contributions in the sensorless control methods research area for the permanent magnet synchronous machines and the "active flux" concept is indeed a real contribution.

Acknowledgements

I wish to thank and to express my gratitude to my supervisor Prof. Ion Boldea for his fruitful and constructive ideas, his guidance and support which made this work possible.

Many thanks to Prof. Gheorghe Daniel Andreescu from Faculty of Automation and Computers, Timisoara, for the technical discussions and for his numerous and invaluable inputs during the experimental work.

Assoc. Prof. Lucian Tutelea deserves my special gratitude.

I want to thank to all of those who contributed to my engineering education and also to my colleagues from Intelligent Motion Control Laboratory at Faculty of Electrical Engineering, Timisoara.

Finally, and most of all, I want to thank and express my love to my family and to my boyfriend. Their love and support was priceless during all this period.

Timisoara, April 15th , 2009

Mihaela Codruta Paicu

Paicu, Mihaela Codruta

"Active Flux" Based Wide Speed Range Motion Sensorless Control Of Permanent Magnet Synchronous Machines

Teze de doctorat ale UPT, Seria 6, Nr. 16, Editura Politehnica, 2009, 270 pagini, 111 figuri, 9 tabele.

ISSN: 1842-7022

ISBN: 978-973-625-911-1

Keywords: active flux observer, flux-weakening, maximum torque per ampere, sensorless control, synchronous motor drives, variable speed drives

Abstract

The main goal of the thesis is to offer new solutions for the sensorless control system of the permanent magnet synchronous machines in a wide speed range.

A novel concept called "active flux" is introduced for unified motion sensorless AC drives and particularity, in this thesis for the IPMSM and PM-RSM.

The key element of a sensorless controlled drive is the estimation of the rotor position and speed. Different estimation methods exist in the literature, but achieving low speed operation was possible by now only with the signal injection method. Based on the "active flux", this estimation is now achieved much simpler and with less computation effort than using signal injection method.

To show the versatility of the novel active flux concept, experimental results from two different experimental platforms, containing two PMSMs prototypes (the IPMSM and PM-RSM) and with four proposed control methods (vector control, direct torque control and two equivalent proposed strategies for wide speed range) are presented and discussed.

Consequently, once the performance of the position sensorless control drive is presented, the position sensed one is not included in the thesis.

Objectives of the thesis

The main objectives of the thesis are:

- to present a state of the art of the sensorless control methods existent in literature
- to find a robust and accurate method for rotor position and speed estimation, especially for low speed operation
- to develop different simulation models for all the control systems proposed in the thesis
- to implement a vector control strategy for the IPMSM
- to implement a direct torque and flux control for the IPMSM
- to develop and implement two novel sensorless control systems for a wide speed range for the PM-RSM, which are capable to give maximum available torque using an optimum current pair over the entire speed range

Outline of the thesis

The thesis is organized in 7 chapters following the above-presented objectives.

First chapter introduces the reader to the state-of the art of the sensorless control techniques for the synchronous machines with permanent magnets existent in the literature. Detailed information is given for the thirteen of the most used sensorless control methods.

In **the second chapter**, the novel concept of active flux for unified ac motion sensorless is introduced. The purpose is to familiarize the reader with the active flux concept, which is used throughout the thesis. Then, the simulation results on a IPMSM weak permanent magnets and large magnetic saliency are shown in order to validate the proposed control strategy based on the active flux estimation. The key element of a motion sensorless drive is the flux linkage observer, which was analyzed, by digital simulations, in its both forms parallel and series.

The third chapter presents a comprehensive implementation of the motion-sensorless control of IPMSM drives via vector control. It is based on the active flux concept and it does not use the signal injection method. The importance of dead time and voltage drops in inverter compensation and also of the stator resistance variation as well as the fact that the magnetic saturation is mandatory to be included, especially at startup and low speed, were analyzed and some of them were proven by digital simulations. The stability of the active flux observer is also analyzed. First the main aspects control are discussed, the new issues (active flux observer and rotor position-speed estimator) are then detailed. Being entirely an experimental work, a lot of experimental results are presented and discussed.

In **the fourth chapter** direct torque and flux control (DTFC) with space vector modulation (SVM) is implemented for a motion-sensorless control of IPMSM. Here as well, a lot of experimental results are presented validating the active flux concept. The control strategy and the observers were developed in Matlab-Simulink and implemented using a dSpace 1103 single-board control and acquisition interface. Different tests were performed, and sample results are presented and discussed. The **fifth chapter** introduces two control strategies for the sensorless control of permanent magnet reluctance synchronous motor (PM-RSM) in a wide speed range. Ample digital simulations and experimental results at various speeds for motoring and generating seem very encouraging. By these experimental results the proposed strategies provide stable and reliable operation up to a speed equal eight times the machine base speed.

The **sixth chapter** describes in detail the two experimental platforms.

The **seventh chapter** summarizes the conclusion and the contributions of the thesis. Some suggestions on future work are also presented.

Table of Contents

PREFACE	3
MOTIVATION.....	3
ACKNOWLEDGEMENTS.....	4
OBJECTIVES OF THE THESIS.....	5
OUTLINE OF THE THESIS.....	5
NOMENCLATURE	11
CHAPTER 1 SENSORLESS TECHNIQUES FOR PMSMS – STATE OF THE ART	13
1.1. INTRODUCTION.....	13
1.2. CONTROL BACKGROUND.....	14
1.2.1. Scalar Control	14
1.2.2. Vector Control	16
1.2.3. Direct Torque and Flux Control	17
1.2.4. Sensorless Control Methods.....	18
1.2.4.1. General overview	18
1.2.4.2. The classical back emf model.....	20
1.2.4.3. The extended back emf model	22
1.2.4.4. MRAS.....	23
1.2.4.5. Extended Kalman Filter	25
1.2.4.6. Sliding mode observer.....	26
1.2.4.7. Adaptive and/or robust observers based on fundamental excitation and advanced models	30
1.2.4.8. Fundamental model scheme problems	31
1.2.5. Sensorless Control through Signal Injection.....	32
1.2.5.1. High frequency signal injection	33
1.2.5.2. INFORM-method	36
1.2.5.3. Low frequency signal injection.....	38
1.2.6. Sensorless Control without Additional Test Signal Injection.....	40
1.2.7. Emerging Techniques.....	41
1.3. PROPOSED SOLUTION.....	42

1.4. CONCLUSION.....	43
REFERENCES	44
CHAPTER 2 ACTIVE FLUX CONCEPT FOR UNIFIED AC DRIVES	54
2.1. INTRODUCTION.....	54
2.2. ACTIVE FLUX CONCEPT.....	55
2.3. AC UNIDRIVE BASED ON ACTIVE FLUX CONCEPT.....	61
2.4. CASE STUDY: IPMSM SENSORLESS CONTROL IN WIDE-SPEED RANGE.....	64
2.4.1. The Active Flux Observer	64
2.4.2. The Speed and Position Estimators.....	67
2.4.3. Flux and Torque Referencers.....	69
2.4.4. Digital Simulation Results.....	70
2.5. CONCLUSION.....	80
REFERENCES	81
CHAPTER 3 “ACTIVE FLUX” SENSORLESS VECTOR CONTROL OF IPMSM.....	85
3.1. INTRODUCTION.....	85
3.2. MATHEMATICAL MODEL OF THE SATURATED IPMSM.....	87
3.3. ACTIVE FLUX CONCEPT FOR IPMSM	88
3.4. VECTOR CONTROL SYSTEM.....	90
3.5. STATE OBSERVERS.....	93
3.5.1. The Active Flux Observer	93
3.5.1.1. Stability	96
3.5.1.2. Inverter Nonlinearities	100
3.5.1.3. The inductance variation due to magnetic saturation	103
3.5.1.4. The resistance variation.....	105
3.5.2. Position-Speed Estimator and Torque Estimator.....	108
3.6. DIGITAL SIMULATION RESULTS.....	110
3.6.1. Overall simulated control system description.....	110
3.7. EXPERIMENTAL RESULTS.....	122
3.8. CONCLUSION.....	135
REFERENCES	136
CHAPTER 4 “ACTIVE FLUX” DTFC-SVM SENSORLESS CONTROL OF IPMSM	139
4.1. INTRODUCTION.....	139

4.2. ACTIVE FLUX CONCEPT FOR THE IPMSM	142
4.3. DTFC-SVM SENSORLESS CONTROL SYSTEM.....	143
4.4. STATE OBSERVERS.....	146
4.4.1. Active Flux Observer.....	146
4.4.2. Position-Speed Estimator and Torque Estimator.....	148
4.5. DIGITAL SIMULATION RESULTS.....	149
4.6. EXPERIMENTAL RESULTS.....	157
4.7. CONCLUSION.....	170
REFERENCES	171
CHAPTER 5 WIDE SPEED RANGE SENSORLESS CONTROL OF PM-RSM VIA “ACTIVE FLUX MODEL”	174
5.1. INTRODUCTION.....	175
5.2. MATHEMATICAL MODEL OF PM-RSM INCLUDING MAGNETIC SATURATION EFFECTS.....	177
5.3. SENSORLESS VECTOR CONTROL SYSTEM.....	178
5.4. WIDE SPEED RANGE SENSORLESS CONTROL SYSTEM (STRATEGY 1).....	179
5.5. WIDE SPEED RANGE SENSORLESS CONTROL SYSTEM (STRATEGY 2).....	184
5.6. ACTIVE FLUX OBSERVER FOR THE PM-RSM.....	186
5.7. DIGITAL SIMULATIONS.....	187
5.7.1. Digital Simulations Results Using the Proposed Wide Speed Range Control Strategy 1	187
5.7.2. Digital Simulations Results Using the Proposed Control Strategy 2	194
5.8. EXPERIMENTAL WORK.....	200
5.8.1. Experimental Results with PM-RSM Using the Vector Control System	200
5.8.1.1. Stator observers performance at low speed	200
5.8.1.2. Experimental Results with PM-RSM Using the Sensorless Vector Control System	204
5.8.2. Experimental Results with PM-RSM Using the Proposed Control Strategy 2.....	213
5.8.2.1. Experimental Results with PM-RSM as Motor Using the Proposed Control Strategy 2.....	213
5.8.2.2. Experimental Results with PM-RSM as Generator Using the Proposed Control Strategy 2	222
5.9. COMPARISON BETWEEN THE VECTOR CONTROL AND THE PROPOSED CONTROL STRATEGY 2	223
5.10. FINAL CONCLUSION.....	229
5.11. APPENDIX.....	230
REFERENCES	233
CHAPTER 6 EXPERIMENTAL PLATFORMS AND SOFTWARE IMPLEMENTATION	236
6.1. EXPERIMENTAL SETUP 1.....	236

6.1.1. Test machine (IPMSM).....	238
6.1.2. Three phase inverter.....	239
6.1.3. Load control system: SIMOVERT MASTER DRIVE.....	241
6.1.4. Acquisition system.....	246
6.1.4.1. Voltage and current sensors.....	246
6.1.4.2. Encoder.....	247
6.1.5. dSpace DS1103 platform.....	249
6.2. EXPERIMENTAL SETUP 2.....	251
6.2.1. Three phase inverter.....	253
6.2.2. Dc-Link Power supply.....	253
6.2.3. Test machine (PM-RSM).....	253
6.2.4. Load control system.....	254
6.2.5. Acquisition system.....	255
6.2.5.1. Current sensors.....	255
6.2.5.2. Encoder.....	256
6.2.6. dSpace DS1103 platform.....	256
6.3. MATLAB/SIMULINK SOFTWARE.....	257
6.3.1. Acquisition blocks.....	258
6.3.2. Software protection block to prevent any damage upon the inverters.....	259
6.3.3. Machine control and estimation algorithms.....	261
6.4. CONCLUSION.....	262
REFERENCES.....	263
CHAPTER 7 CONCLUSION AND CONTRIBUTIONS.....	264
7.1. SENSORLESS TECHNIQUES FOR PMSMs – STATE OF THE ART.....	264
7.2. ACTIVE FLUX CONCEPT FOR UNIFIED AC DRIVES.....	264
7.3. “ACTIVE FLUX” SENSORLESS VECTOR CONTROL OF IPMSM.....	265
7.4. “ACTIVE FLUX” DTFC-SVM SENSORLESS CONTROL OF IPMSM.....	265
7.5. WIDE SPEED RANGE SENSORLESS CONTROL OF PM-RSM VIA “ACTIVE FLUX MODEL”.....	266
7.6. ORIGINAL CONTRIBUTIONS.....	266
7.7. FUTURE WORK.....	268
AUTHOR’S PAPERS RELATED TO THE PH. D. THESIS.....	269
AUTHOR’S CV.....	270

Nomenclature

Abbreviations

ac	Alternating current;
dc	Direct current;
DTFC	Direct torque and flux control;
EKF	Extended Kalman filter;
EMF	Electromotive force;
IM	Induction machine;
INFORM	Indirect flux detection by online reactance measurement;
IPMSM	Interior permanent magnet synchronous machine;
LPF	Low pass filter;
MRAS	Model-reference adaptive systems;
PI	Proportional integral controller;
PID	Proportional integral derivative controller;
PM	Permanent magnet;
PLL	Phase-locked loop;
PWM	Pulse width modulation;
PM-RSM	Permanent magnet reluctance synchronous motor;
SMO	Sliding mode observer;
SVM	Space vector modulation;
VC	Vector control;

Symbols

B	Viscous friction coefficient;
i_a, i_b, i_c	Instantaneous stator a, b, c phase currents;
I_d, I_q	Stator currents in d, q rotor reference frame;
I_α, I_β	Stator currents in α, β stator reference frame;

I_S	Magnitude of the stator current vector;
J	Inertia of the motor shaft and the load system;
L_d, L_q	Rotor d- and q- axis inductances;
$L_{dm}i_F$	Field current stator-flux linkage;
L_S	Stator total inductance;
L_{SC}	Short-circuit inductance of the IMs;
p_1	Number of pole pairs of the motor;
R_S	Stator resistance per phase;
T_e	Electromagnetic torque;
V_α, V_β	stator voltage in α, β stator reference frame;
V_{dc}	DC-link voltage;
V_S	Magnitude of the stator voltage vector;
V_{comp}	Compensation voltage;
ω_b	Base speed;
ω_r	Electrical rotor speed;
θ_{er}	Electrical rotor position;
$\theta_{\psi_d^a}$	Active flux angle;
ψ_d^a	Active flux;
ψ_{PM}	Rotor permanent magnet flux;
ψ_S	Stator flux linkage;

Subscripts

$a;b;c$	Stator a,b,c phases;
s	Stator quantity;
r	Rotor quantity;

Superscripts

*	Reference quantity;
^	Estimated quantity;

Chapter 1

Sensorless Techniques for PMSMs – State of the Art

Abstract

The main focus of this chapter is on control techniques which are being applied to make ac drives a rapidly growing area. A particular feature is the increasing importance of speed or position sensorless techniques. The generic term “sensorless” could be considered misleading: the techniques are position sensorless, but usually require sensing of current and sometimes voltage.

Sensorless techniques for estimating rotor position from measurements of voltage and current have been the subject of intensive research. This chapter reviews the state of the art in these sensorless techniques.

1.1. Introduction

For some years, permanent magnet synchronous machines (PMSMs) have got a wide application range in the field of speed-variable ac drives because they offer a lot of advantages compared to other motor types like induction motors. They offer:

- higher efficiency due to low rotor losses
- compact construction and higher torque per volume ratio
- inherent positioning capability due to synchronous operation
- simple sensorless flux detection using either back EMF or saliency effects.

A disadvantage of PMSMs (without damper windings) compared to induction motors is that they cannot be controlled feed-forward with high quality. Hence, PMSMs are usually operated in a closed control loop.

The position sensor reduces the robustness of the drive, increases the costs and needs some extra space. Hence, for low-cost applications, substituting the

sensor by mathematical models yields an economic solution with an additional benefit of better efficiency than induction motor solutions.

Sensorless techniques are discussed next with the methods broadly divided into two classes; those using the fundamental properties or model of the machine, and those exploiting subsidiary features, often by using signal injection.

Fundamental model methods are widely applicable to the main classes of ac machines used in drives, but are inherently incapable of prolonged working at zero speed. Signal injection methods are capable of zero speed operation, but the properties used are usually machine-specific, limiting the generality of their industrial application.

1.2. Control background

Scalar control uses magnitude and frequency control. Vector control uses orientation in addition. Variants include direct flux and torque control (DTC).

1.2.1. Scalar Control

Scalar control is based on steady state relationships; usually only magnitude and frequency are controlled, not space vector orientation. Making terminal voltage magnitude proportional to frequency results in an approximately constant stator flux; this is desirable to maximize capability of the motor.

The classical variable frequency V/f scheme is a scalar control based on this principle, with voltage boost at low frequency usually introduced to counteract the larger effect of stator resistance at low speeds.

Scalar control, often open-loop apart from stator current monitoring for fault detection, gives an economical drive with good behavior, but transients may not be well controlled. More sophisticated variants can improve behavior, perhaps with better handling of parameter variations, particularly of stator resistance. Buja and Kazmierkowski [3] describe the evolution of the still widely used scalar control methods and their progression to VC.

Several authors have shown that synchronous motor drives can be stabilized by appropriate modulation of the inverter frequency [8] and [9].

In these papers the frequency modulation signal is derived in order to implement the stabilizing loop using the input power perturbations in the system ($u_s i_s \cos \varphi$) and two phase currents are needed. The functional block diagram is shown in Fig. 1.1.

This method keeps constant the product of the proportional gain of the applied frequency (modulated by input power perturbations) and the rotor speed, i.e. changing the k_p inversely proportional to the rotor speed in order to obtain almost a constant damping factor in the system.

With the open loop V/f control methods described above the drive can operate from 5% to 100% of rated speed with the required low performance (low dynamic systems) for pumps, fans and compressors.

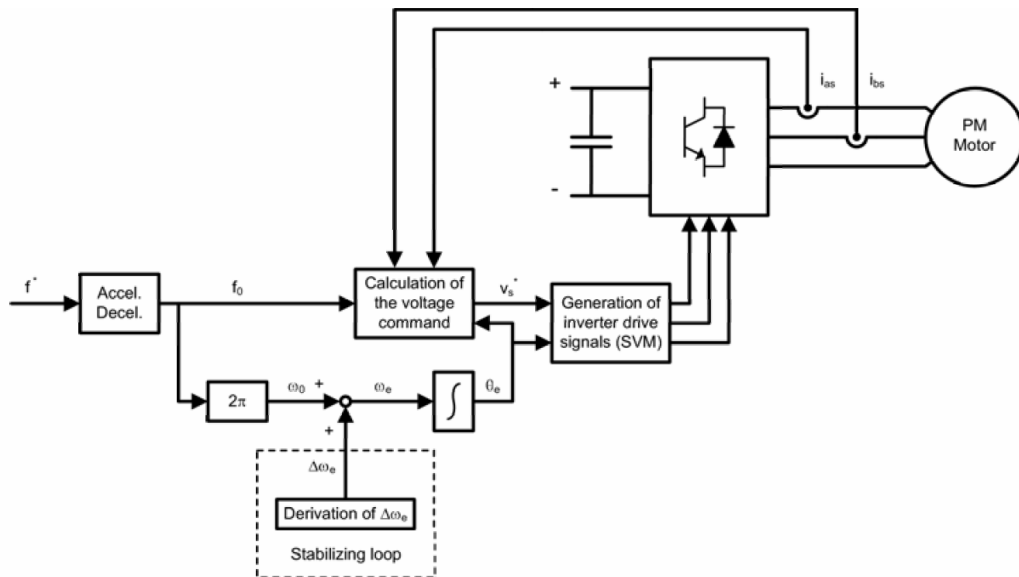


Fig. 1.1. Stabilizing of open-loop controlled PMSM

1.2.2. Vector Control

First, we are concentrating on the basics of VC. This control method and its variants, combined with advances in both power electronics and electronic processing power, are mainly responsible for the increased modern use of ac machines in higher performance dynamic applications.

In VC the instantaneous position of voltage, current, and flux space vectors are controlled, ideally giving correct orientation both in steady state and during transients. Coordinate transformations (three phase to two or $d - q$ axes) to new field coordinates are a key component of standard VC, giving a linear relationship between control variables and torque. It is ideally suited to current control via PWM voltage switching.

The VC usually separates current into field and torque producing components. The perpendicular field system makes the relationships between the machine variables simple, in principle. The flux is a function of the field (producing component) or d -axis current, the torque is proportional to the product of this flux and the torque (producing component) or q -axis current. If the flux is established and can be held constant, the torque response is governed by the current and can be fast and well-controlled.

Full advantages of VC are given only if the instantaneous position of the rotor flux vector can be established.

Two variants of VC are used, direct and indirect. In the direct method the instantaneous rotor position for this flux is found either by sensors, or more usually by estimators, or a combination; Blaschke [10] was a pioneer of the approach. Fig. 1.2 shows a basic scheme.

This need for rotor position or velocity is most obviously required in an SM such as a brushless PM machine since stator excitation must be synchronous to the rotor. It also applies to an IM drive, although the basic symmetry of the rotor implies only relative velocity is originally needed. A straightforward method is to attach a rotor sensor, e.g., an encoder to measure rotor position or speed, and this is still preferred in many cases, but sensorless schemes are gaining ground.

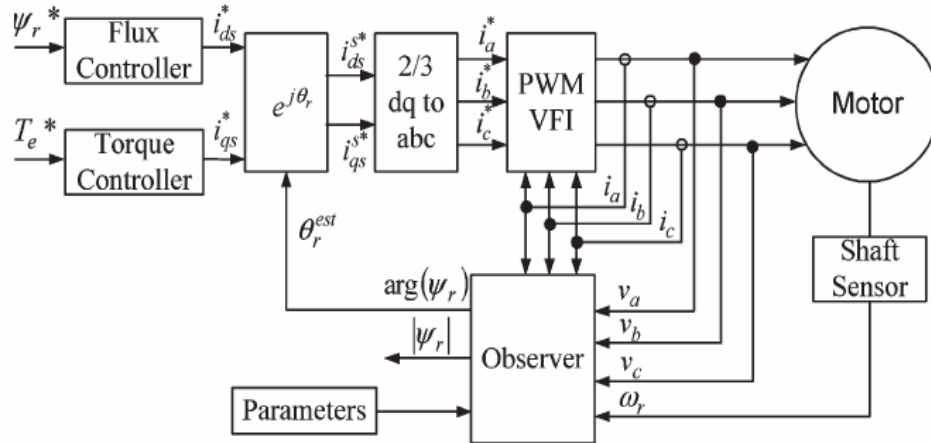


Fig. 1.2. Basic direct VC scheme with an observer used for rotor flux estimation

1.2.3. Direct Torque and Flux Control

DTC also exploits vector relationships, but replaces the coordinate transformation concept of standard VC with a form of bang-bang action, dispensing with PWM current control [3].

In standard VC the q -axis current component is used as the torque control quantity. With constant rotor flux it directly controls the torque. In a standard three-phase converter, simple action of the six switches can produce a voltage vector with eight states, six active and two zero. The voltage vector and stator flux then move around a hexagonal trajectory; with sinusoidal PWM this becomes a circle. With either, the motor acts as a filter, so rotor flux rotates continuously at synchronous speed along a near-circular track.

In DTC the bang-bang or hysteresis controllers impose the time duration of the active voltage vectors, moving stator flux along the reference trajectory, and determining duration of the zero voltage vectors to control motor torque. At every sampling time the voltage vector selection block chooses the inverter switching state to reduce the flux and torque error. Depending on the DTC switching sectors, circular or hexagonal stator flux vector path schemes are possible. Types of DTC

include: switching table based, direct self control, space vector modulation, and constant switching frequency [3].

DTC has these features compared to standard VC:

- no current control loops so current not directly regulated
- coordinate transformation not required
- no separate voltage PWM
- stator flux vector and torque estimation required

However, two of the major drawbacks are the high torque and flux ripples.

A high-performance torque control of the synchronous reluctance machine (SynRM) can be obtained by using a conventional Direct Torque Control (DTC) scheme. However, the digital implementation of the conventional DTC needs very short sampling time in order to maintain low torque ripple and its switching frequency is variable, which are the commonly mentioned drawbacks. To overcome these shortcomings a Predictive DTC (PDTC) scheme for the SynRM has been proposed in [4]-[7], based on the idea of Direct Mean Torque Control (DMTC), first proposed for the induction machine (IM).

Although there are several industrial applications that require a fast torque control, the majority of applications require a speed or position control and therefore the direct torque control scheme should be modified in order to get for example a speed control. This means that an outer speed loop can be added to the DTC and to maintain the main feature of the DTC, that is sensorless, an estimator of the rotor speed have to be implemented.

1.2.4. Sensorless Control Methods

1.2.4.1. General overview

There is intensive research worldwide devoted to sensorless methods. Such techniques typically measure stator quantities, usually current, directly via transducers, and voltage, although not often with a direct measurement. Signal injection methods are also used. Fig. 1.3 shows a typical schematic of a sensorless scheme.

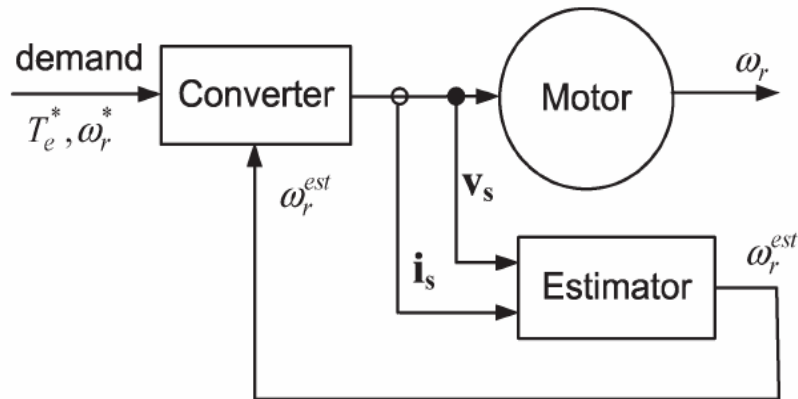


Fig. 1.3. Schematic of a speed sensorless scheme

Advantages of such “sensorless” schemes include [1], [2]:

- more compact drive with less maintenance
- no cable to machine transducers, easier application particularly to existing machines, reduced electrical noise
- transducer cost avoided
- suitable for hostile environments, including temperature.

Despite much effort and progress, operation at very low speed is still problematic.

Sensorless control of both IM and PM machines can use fundamental model-based estimation methods, which in their simpler forms typically work well above about 2% of base speed. These fundamental model-based methods usually describe the machine by dq axis equations, where sinusoidal distribution around the airgap is assumed. As this neglects space harmonics, slotting effects, etc., it is often termed a fundamental model. Fundamental models have an inherent limit. As the stator frequency approaches zero the rotor-induced voltage goes to zero.

Methods are either implemented in open-loop form or as closed-loop observers (estimators), making use of the error between measured and estimated quantities to improve their behavior.

Fundamental model-based schemes will have difficulty maintaining or properly controlling speed in this very low speed region, but cope quite well with fairly rapid transient reversals of speed through zero. The time constant of the LPF-

based integrator determines how rapid the transition has to be for good behavior. Inaccurate reference model parameters, mainly stator resistance, also limit low speed results.

Combined flux and speed estimation is by no means straightforward. Challenges include gaining good damping at all speeds, low parameter sensitivity, low noise gain, and —most importantly— stability for all operating conditions. During recent years, works comparing and building bridges between the schemes have appeared.

1.2.4.2. The classical back emf model

This method [14], [15] is a sensorless estimation for permanent magnet synchronous motors (PMSM) based on the integration of back EMF. It is only used on surface-mounted permanent magnet synchronous motors (SMPMSM), not on salient-pole permanent magnet motors such as interior PM motors.

The stator flux linkage $\bar{\psi}_s$ is derived from the stator voltage equation:

$$\bar{u}_s = R_s \bar{i}_s + \frac{d\bar{\psi}_s}{dt} + j\omega_k \bar{\psi}_s \quad (1.1)$$

by integration:

$$\bar{\psi}_s(t) = \int [\bar{u}_s(t) - R_s \bar{i}_s(t)] dt \quad (1.2)$$

Furthermore flux linkage $\bar{\psi}_m$ due to permanent magnets is calculated from stator flux linkage $\bar{\psi}_s$:

$$\bar{\psi}_s = L_s \bar{i}_s + \bar{\psi}_m \quad (1.3)$$

and yields in the $\alpha\beta$ stator-oriented reference frame to equations:

$$\psi_{ma}(t) = \int [u_{sa}(t) - R_S i_{sa}(t)] dt - L_S \bar{i}_{sa}(t) \quad (1.4)$$

$$\psi_{m\beta}(t) = \int [u_{s\beta}(t) - R_S i_{s\beta}(t)] dt - L_S \bar{i}_{s\beta}(t)$$

Normally, the integration is stabilized by a certain feedback. The argument of flux linkage vector $\bar{\psi}_m$ is the searched rotor position θ (Fig. 1.4):

$$\theta = \arg[\bar{\psi}_m] = \text{atan} \left[\frac{\psi_{m\beta}}{\psi_{ma}} \right] = \text{atan} \left\{ \frac{\int [u_{sa}(t) - R_S i_{sa}(t)] dt - L_S \bar{i}_{sa}(t)}{\int [u_{s\beta}(t) - R_S i_{s\beta}(t)] dt - L_S \bar{i}_{s\beta}(t)} \right\} \quad (1.5)$$

The performance of this method depends on the quality and accuracy of the estimated flux and measured values of the voltage and currents. Integration drift is a problem when using (1.4), but can be avoided by using a proper integration technique [16].

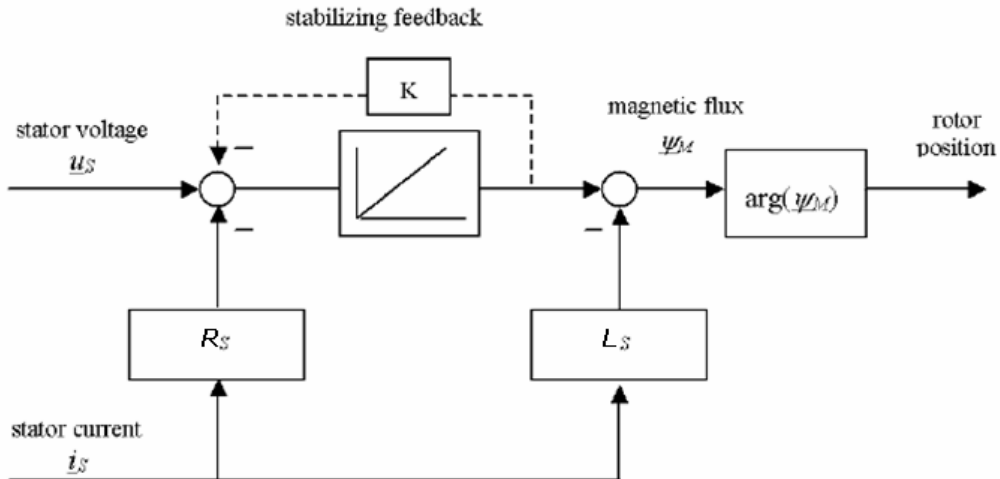


Fig. 1.4. EMF model for position detection at higher speed

Moreover, in this method, machine parameters are used, and therefore, it is sensitive to parameter variations. Furthermore, the initial rotor position is detectable with this technique; consequently, a different starting strategy should be used.

1.2.4.3. The extended back emf model

Using well known two-axis theory the flux linkage $\bar{\psi}_s$ in the dq rotor-oriented reference frame is given by:

$$\begin{aligned}\bar{\psi}_{s,dq} &= \bar{\psi}_{m,dq} + L_d i_d + j L_q i_q \quad \Big| \cdot e^{j\theta} \\ \bar{\psi}_{s,\alpha\beta} &= \bar{\psi}_{m,\alpha\beta} + (L_d i_d + j L_q i_q) \cdot (\cos\theta + j \sin\theta) \\ \bar{\psi}_{s,\alpha\beta} &= \bar{\psi}_{m,\alpha\beta} + L_d i_d \cos\theta - L_q i_q \sin\theta + j(L_q i_q \cos\theta + L_d i_d \sin\theta)\end{aligned}\quad (1.6)$$

which yields to:

$$\begin{aligned}\psi_{m\alpha} &= \psi_{s\alpha} - L_d i_d \cos\theta + L_q i_q \sin\theta \\ \psi_{m\beta} &= \psi_{s\beta} - L_q i_q \cos\theta - L_d i_d \sin\theta\end{aligned}\quad (1.7)$$

The rotor position θ follows with simplified notation to:

$$\text{atan} \left\{ \frac{\int [u_\alpha - R_s i_\alpha] dt - L_d i_d \cos\theta + L_q i_q \sin\theta}{\int [u_\beta - R_s i_\beta] dt - L_q i_q \cos\theta - L_d i_d \sin\theta} \right\} \quad (1.8)$$

The BEMF method is based on the motor equations to determine the induced electromotive-force, from current and voltage measurements. In the related literature we find several approaches, that include deterministic observers [19]-[20], stochastic filtering [21]-[22], and other techniques [23]-[24].

Some techniques are quite simple to implement but rely on the machine parameter's and exhibit poor performance at low speed since the amplitude of the back-emf is proportional to the speed. Hence, [25] describes an extended EMF- and parameter observer to achieve high dynamical operation in the whole speed range.

1.2.4.4. MRAS

In model-reference adaptive systems (MRASs), the outputs of two flux estimators - often the "current model" (CM) and the "voltage model" (VM) - are compared, and the difference is used to adjust the rotor-speed estimate to its correct value.

The usual MRAS estimates speed using two different machine models, one being speed dependant. Differences between the models can be used to reduce the error in the speed estimate (or to adjust the rotor-speed estimate to its correct value), often with an internal proportional-integral controller. The basic MRAS block diagram is drawn as Fig. 1.5.

How well the ideal integrator in the reference model is approximated is one defining factor for performance. Good behavior with an IM above 2 Hz stator frequency was reported by Schauder [27] in pioneering industrial based developments. Ohtani *et al.* [28] in early work described a torque MRAS with better behavior. Better independence to motor parameters, particularly stator resistance, is claimed by matching a lag circuit to rotor time constant. Application to a printing press is described, needing 0.1% rated speed stability. Tests at about 18 rpm or 1/100 of rated speed were shown.

Such schemes are popular as they are not as complex as other model-based approaches and can be implemented more economically [2]. In an early comparison Armstrong *et al.* [29] compared a basic rotor flux MRAS and EKF estimator behavior.

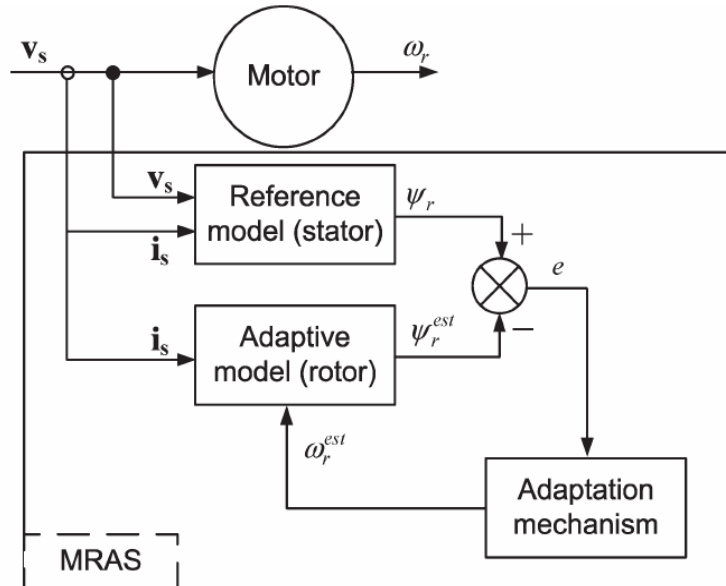


Fig. 1.5. MRAS speed sensorless scheme, * = demand, est = estimated

The EKF was more resilient to parameter changes, but MRAS is simpler (with a computing complexity ratio of almost 20:1) and can even be better at low speed. Performance was said to already rival an encoded indirect VC drive. A step of 96 to 19 r/min was used in tests.

Later developments include parameter adaptation, which is important for low speed behavior. Recently Rashed *et al.* [30] report an indirect VC MRAS for rotor flux and stator resistance estimation in a PMM. Operation at 2 rad/s is shown. Cirrincione *et al.* [31] use a NN predictive adaptive model in a MRAS based IM drive, comparing with an older MRAS scheme. A ± 50 rad/s reversal is used in the tests, then ± 10 rad/s. Low speed behavior is limited by the LP integrator, with 5 rad/s used in their test. Some zero speed tests are also shown, being viable because of the adaptive model used, and are better than before.

1.2.4.5. Extended Kalman Filter

Another method to extract the rotor position and speed information is to use the state observers which are based on the dynamic model of the machines. These dynamic models are driven with the input as the one for the real machine. The accuracy of the model ensures that the states of the modeled machine follow the states of the real machine. The error between the output of the real machine, which is measurable and the output of the modeled machine is used in the observer to correct any error in the estimated state.

A particular case of parameter estimation is using the Kalman Filter (Fig. 1.6). A Kalman Filter [35] provides an optimum observation of noisy sensed signals and parameter variations, but is computationally intensive. The critical step in Kalman filter design is to select the coefficient values to yield the best possible position estimation performance.

Kalman Filter and Extended Kalman filter have been widely advocated for drives despite the considerable added complexity over MRAS [29] and lower sensitivity to parameters.

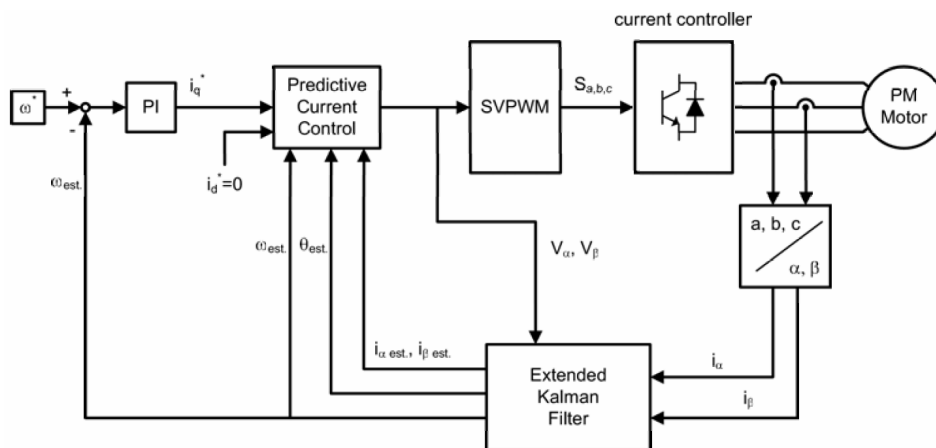


Fig. 1.6. Parameter estimation using the Kalman Filter for PM-motors

Extended Kalman filter can solve nonlinear equation directly by numeric iteration. Kalman filter also considers the errors of the parameters and the noises in the measurement, so it is very robust with the parameters' errors and measurement

noises. Also the initial rotor position is not necessary for the start-up. By a proper compensation in the observer equation, the other unexpected equilibrium points of the observer are moved off. The motor can start up successfully from any unknown initial position [37], [38].

Their performance depends on choices for the filter matrices, so this has attracted continuing research attention, see for example Bolognani *et al.* [39], Akin *et al.* [40] although trial and error methods are widely used.

Compared to the traditional observer, using EKF, the orders of model and the matrixes are reduced; the complexity and the computational time are also decreased. In [43] the load torque is also observed by EKF and compensated in order to reduce the ripple caused by a sudden change of the load torque.

Although the EKF is straightforward and simple to apply, it has three important drawbacks:

1. Costly and sometimes complex derivation of the Jacobian/Hessian matrices.
2. Only first-order accuracy.
3. The linearization can lead to filter instability.

To overcome the above drawbacks, Julier and Uhlmann [43] introduced a novel estimation tool, known as the Unscented Kalman filter (UKF) for replacing the EKF in nonlinear filtering problems. The main advantage of the UKF is that linearization of the state and covariances is no longer necessary. Instead of linearizing using Jacobian matrices, the UKF uses a deterministic sampling approach to capture the mean and covariance estimates with a minimal set of sample points. Although the UKF has been applied to a wide range of estimation problems, little research work has been done on its application to position and speed estimation in sensorless PMSM drives [44], [45].

1.2.4.6. Sliding mode observer

Among different observation methods used, the sliding mode observer (SMO) is a promising approach and an effective technique due to its outstanding robustness properties against system parameter uncertainties and external disturbances [32]-[34].

The dynamic equations of a PMSM without saliency in the stationary reference frame ($\alpha - \beta$) can be expressed in matrix form as:

$$\dot{\bar{i}}_S = A \cdot \bar{i}_S + B \cdot (\bar{V}_S - \bar{e}_S) \quad (1.9)$$

$$A = \begin{bmatrix} -R_S/L_S & 0 \\ 0 & -R_S/L_S \end{bmatrix} \quad B = \begin{bmatrix} 1/L_S & 0 \\ 0 & 1/L_S \end{bmatrix} \quad (1.10)$$

where

$$\bar{i}_S = \begin{bmatrix} i_{\alpha S} \\ i_{\beta S} \end{bmatrix} \quad \bar{V}_S = \begin{bmatrix} V_{\alpha S} \\ V_{\beta S} \end{bmatrix} \quad \bar{e}_S = \begin{bmatrix} e_{\alpha S} \\ e_{\beta S} \end{bmatrix} = \omega_r \cdot \psi_{PM} \begin{bmatrix} -\sin(\theta_r) \\ \cos(\theta_r) \end{bmatrix}$$

L_S , R_S and ψ_{PM} represent stator inductance, stator resistance and magnitude of permanent magnet flux respectively. ω_r is the rotor velocity and θ_r the rotor position angle.

In principle, a sliding mode observer consists of a stator current estimator with discontinuous control. Due to the fact that stator currents of motor can be measured through current sensors in PMSM drive systems, the sliding mode manifold $s(x) = 0$ is selected on stator current trajectory. In this way, when the state (i.e., the estimated stator current) reaches the manifold, the sliding mode happens and then is enforced. Finally, the current estimation error keeps zero and the estimated currents track the real ones regardless of certain disturbances and uncertainties of the drive system.

Considering (1), the proposed sliding mode observer is defined as:

$$\dot{\bar{i}}_S = A \cdot \bar{i}_S + B \cdot (\bar{V}_S^* + \bar{Z}) \quad (1.11)$$

$$\text{where} \quad \bar{i}_S = \begin{bmatrix} \hat{i}_{\alpha S} \\ \hat{i}_{\beta S} \end{bmatrix} \quad \bar{V}_S^* = \begin{bmatrix} V_{\alpha S}^* \\ V_{\beta S}^* \end{bmatrix} \quad (1.12)$$

In (2), the superscript '*' denotes a command variable and '^' denotes estimated variables.

The control \bar{z} has a form of discontinuous function. Normally, it can be expressed in:

$$\bar{z} = -k \cdot \text{sign}(\hat{i}_s - \bar{i}_s) \quad (1.13)$$

where k , normally positive ($k > 0$), is the switching gain of the discontinuous control \bar{z} .

Define the dynamic sliding-mode motion equation as:

$$\dot{S} = A \cdot S + B \cdot (\bar{z} + \bar{e}_s) \quad (1.14)$$

where $S = (\hat{i}_s - \bar{i}_s)$ (1.15)

If the switching gain, i.e., k , is large enough to guarantee:

$$S^T \cdot \dot{S} < 0 \quad (1.16)$$

then, sliding mode will occur and we get

$$\bar{e}_s = \begin{bmatrix} e_{as} \\ e_{\beta s} \end{bmatrix} = -\bar{z}_{eq} \quad (1.17)$$

Furthermore, based on (6), the rotor position angle can be calculated as:

$$\theta_r = -\tan^{-1} \left(\frac{e_{as}}{e_{\beta s}} \right) = -\tan^{-1} \left(\frac{z_{eq\alpha}}{z_{eq\beta}} \right) \quad (1.18)$$

The equivalent control \bar{z}_{eq} can be obtained by using a first order low-pass filter (LPF) in the form of:

$$\bar{z}_{eq} = \begin{bmatrix} Z_{eq\alpha} \\ Z_{eq\beta} \end{bmatrix} = \frac{\omega_c}{s + \omega_c} \bar{z} \quad (1.19)$$

The cutoff frequency ω_c of the LPF should be properly designed to preserve the slow component (i.e., the equivalent control) of the discontinuous control as well as effectively filter out its high-frequency component.

In general, the Δ -vicinity of sliding mode manifold, within which the state oscillates, should be as small as possible to make the real motion close to ideal sliding mode. The maximum of width Δ will be determined by the switching frequency of the discontinuous control and its switching gain. Normally only one switching gain is designed and applied for full speed range, which must meet the necessary stability condition of SMO. However, the range of state oscillation (corresponding to the ripples on the estimated currents) would vary with operating conditions. In practice, at low motor speeds, the estimation error of stator currents might be large due to the comparatively high gain and the limited or fixed switching frequency. As a boundary solution to chattering problem, the sign function is normally replaced by a saturation function as shown in Fig. 1.7. When the magnitude of current error is less than E_0 , the control \bar{z} changes to:

$$\bar{z} = -k_s \cdot (\bar{i}_s - \hat{i}_s) \quad (1.20)$$

where $k_s = k/E_0$.

For SMO-based sensorless controls of PMSM, two challenges have to be dealt with properly: first, the very small magnitude of the back-EMF at low speeds and second, the sufficient high switching gain that satisfies the necessary conditions for the convergence of SMO over full speed range. As known, the minimum operating frequency or speed and the accuracy of the estimated rotor position angle depend on the quantization error of discrete-time observers. On the other hand, the required high switching gain will normally cause large ripples (or chattering) on the estimated signals, and eventually big estimation error of rotor position.

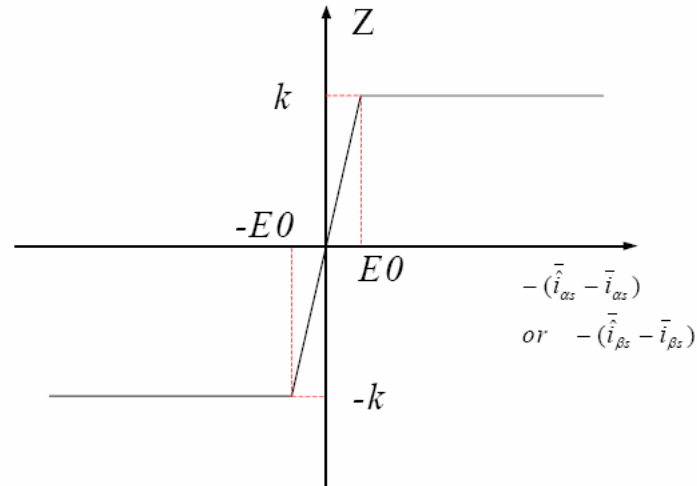


Fig. 1.7. Diagram of the saturation function

1.2.4.7. Adaptive and/or robust observers based on fundamental excitation and advanced models

As it was shown before, for the control of the speed or position of the PMSM, many studies were carried out in the last decade. However, the performance of the PMSM control is very sensitive to external load disturbances and parameter variations in the plant. To overcome these problems, several control strategies such as adaptive control were developed [47].

By using an adaptive (closed-loop) observer, the noise in the estimated angle can be reduced without degrading the dynamic performance. The adaptive observer (as it is shown in) consists of a state observer augmented with a speed adaptation loop. The state observer mimics the electrical dynamics of the PMSM. An observer gain can be used to modify the properties of the observer. An error term is calculated from the measured and estimated quantities, and the rotor speed is usually adjusted by a PI mechanism. The current or the stator flux can be used as a state variable of the observer [48]–[51]. An observer design using the stator flux error as a state variable has also been proposed [52].

In [53] the rotor speed and position can be estimated in a wide speed range, including zero speed, by means of an adaptive observer that is augmented with an HF signal injection technique at low speeds.

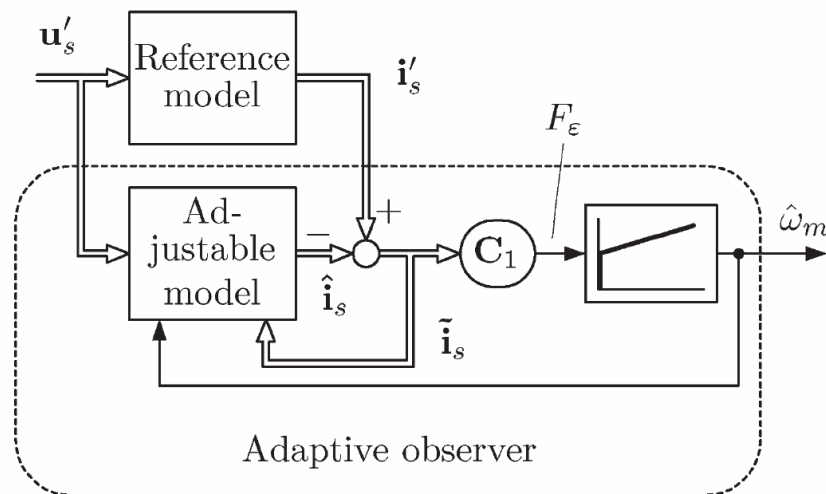


Fig. 1.8. Block diagram of the adaptive observer. In addition, the reference model (the actual motor) is shown.

1.2.4.8. Fundamental model scheme problems

Low speed operation is the main area where difficulties arise [1]. The problems can include the following:

- Signal acquisition errors: These are a basic limitation for very low speed operation; minor dc components in the measured signals can produce substantial offsets in the estimated flux linkage even if a pure integrator could be used.
- Inverter: The inverter introduces nonlinear dead-time effects; very good performance at low speed will require compensation. Further nonlinearities come from power device forward voltage drops and may also require modeling.

Additional effects include the sensitivity of voltage drop and dead time compensation to the exact point of current reversal. Estimating the stator voltage vector from the PWM index can then become inaccurate.

- Model parameters: Parameters can be determined in a commissioning phase, either offline or using the inverter to self test, aiding accuracy of estimation. This might include finding a good initial value of the stator resistance using a dc test.

1.2.5. Sensorless Control through Signal Injection

Operation at very low speed and continuously at zero may need signal injection techniques for position estimation, particularly in PMSMs, and inductance may vary with position. These methods utilize asymmetric properties, either the saliency of the rotor, arising naturally in at least some PM types, or magnetic saturation.

The underlying principle behind almost all low and zero speed sensorless techniques is the use of additional excitation to extract the saliency information. A high frequency voltage or current is injected into the motor and the resulting signal is processed to determine the rotor position.

As the magnetic saliencies have a periodicity two times the periodicity of one electrical turn, these methods have a 180° ambiguity (they cannot distinguish north from south pole).

The high frequency injected signal (carrier) can be rotating [49], [54],, or pulsating signal along a specific axis [55], [56], or a pulse-based excitation [46]. The important feature is that the injected signal must be persistent exciting and have sufficiently high frequency components to provide the position estimation with high bandwidth.

The method based on the alternating carrier proved being able to track even very low saliencies.

1.2.5.1. High frequency signal injection

When the high-frequency stator voltage is added to the fundamental voltage, the corresponding high-frequency stator current is affected by the rotor saliency [57], [58], [59]. Therefore, information of the rotor position is extracted from current measurement [60], [61]. The two techniques used to detect the PM rotor position by means of high-frequency signal injection, are briefly summarized hereafter.

$$\begin{aligned} L_{avg} &= \frac{L_q + L_d}{2} \\ \text{Let} \quad L_{diff} &= \frac{L_q - L_d}{2} \end{aligned} \tag{1.21}$$

be the average and difference inductances of the high-frequency motor model. Taking into account the saturation, the inductances vary according to the actual operating point. Referring to the high-frequency motor model, the d - and q -axis inductances in (1.21) are the incremental inductances (also called dynamic or differential inductances), corresponding to the actual operating point.

Pulsating Voltage Vector Technique

A pulsating voltage vector is superimposed along the estimated d -axis at a constant carrier frequency ω_c . In the estimated synchronous reference frame, such a voltage vector is given by:

$$\begin{aligned} \hat{v}_{dc} &= V_c \cos(\omega_c t) \\ \hat{v}_{qc} &= 0 \end{aligned} \tag{1.22}$$

The corresponding high-frequency current components can be expressed as:

$$\begin{aligned}\hat{i}_{dc} &= \frac{V_c}{\omega_c L_{dc} L_{qc}} [L_{avg} + L_{diff} \cos(2\theta_{err})] \sin(\omega_c t) \\ \hat{i}_{qc} &= \frac{V_c}{\omega_c L_{dc} L_{qc}} [L_{diff} \sin(2\theta_{err})] \sin(\omega_c t)\end{aligned}\tag{1.23}$$

where a rotor speed $\omega_r = 0$ is fixed for the sake of simplicity.

In (1.23), θ_{err} is the electrical angle error between the estimated and the actual dq synchronous reference frame.

Equation (1.23) shows that high-frequency component of q -axis current in the estimated rotor reference frame becomes zero when the rotor position angle error is zero. Thus only q -axis component could be processed as follows, obtaining the rotor position estimation error signal $\varepsilon(\theta_{err})$ as:

$$\varepsilon(\theta_{err}) = LPF[\hat{i}_{qc} \sin(\omega_c t)]\tag{1.24}$$

where LPF means low-pass filter. It becomes:

$$\varepsilon(\theta_{err}) = \frac{V_c}{\omega_c} \frac{L_{diff}}{2L_{dc}L_{qc}} L_{diff} \sin(2\theta_{err})\tag{1.25}$$

It can be noted that the error signal is proportional to the sine function of twice the rotor position estimation error. However, it is important to observe that the information of the rotor position strongly depends on the difference inductance L_{diff} . The error signal disappears when $L_{dc} = L_{qc}$.

Rotating Voltage Vector Technique

Alternatively, a voltage vector rotating at a constant carrier frequency ω_c is superimposed to the fundamental voltage. In the stationary reference frame $\alpha\beta$, such a voltage vector is given by:

$$\bar{v}_{a\beta c} = V_c e^{j\omega_c t} \quad (1.26)$$

Neglecting the stator resistance, the corresponding high-frequency current vector is given by:

$$\bar{i}_{a\beta c} = \frac{L_{avg} \bar{v}_{a\beta c} - L_{diff} e^{j2\theta_r} \bar{v}_{a\beta c}^*}{j\omega_c L_{dc} L_{qc}} \quad (1.27)$$

where superscript "*" means the complex conjugate, and θ_r is the rotor position angle in electrical radians.

In order to achieve a signal related to the rotor position angle, the current vector (1.27) is firstly multiplied by $e^{-j\omega_c t}$ and the result is processed by means of a high pass filter (heterodyning scheme) [9], yielding:

$$HPF[\bar{i}_{a\beta c} e^{-j\omega_c t}] = j \frac{V_c}{\omega_c} \frac{L_{diff}}{L_{dc} L_{qc}} e^{j2(\theta_r - \omega_c t)} \quad (1.28)$$

Let $\hat{\theta}_r$ be the estimated rotor position angle, the signal (1.28) is multiplied by $e^{j2(\omega_c t - \hat{\theta}_r)}$. Then, the rotor position estimation error ε signal corresponds to the real part of such a product, which is:

$$\varepsilon = -\frac{V_c}{\omega_c} \frac{L_{diff}}{L_{dc} L_{qc}} \sin[2(\theta_r - \hat{\theta}_r)] \quad (1.29)$$

Also in this case the information of the rotor position depend on the difference inductance L_{diff} .

As far as the high-frequency voltage injection techniques, it has been observed that there is not a substantial difference between the two techniques.

The actual position tracking is performed by a PLL-like speed and position observer.

However, the HF signal forces the phase current to have multiple zero-crossings when the fundamental phase current is close to zero. The zero-current

clamping (ZCC) effect relevant to multiple zero-crossings causes the disturbances that significantly affect the quality of the position estimate [62], [63]. With the presence of the ZCC effect, HF signal injection-based sensorless controllers are prone to position error ripples. This side effect significantly limits the current/velocity control bandwidth and the dynamic response of the motor torque that can be achieved, and eventually results in a loss of field orientation.

An interesting correction method based on a ZCC modeling in the *abc* reference frame is proposed in [64].

In the case of small saliencies normally they need either additional voltage sensors [65], [68] or an additional design of artificial saliencies [67], the main problem in case of small saliencies is the reduced estimation quality due to the nonlinear behavior of the inverter. However, there are also approaches to eliminate these disadvantages, a modified kind of excitation based on frequency amplitude modulation methods has been presented [66], and another attempt uses certain signal decoupling methods, such as [69]. These high frequency injection methods generally need any kind of tracking observer.

1.2.5.2. INFORM-method

Rotor position detection techniques based on phase inductance evaluation, such as the INFORM method allow for reliable low- and zero-speed operation in machines showing self or induced anisotropy. However, such techniques give discrete position detection and need to be complemented by a state observer or a Kalman filter, also requiring a shift to other sensorless methods as the speed increases.

The INFORM-method (“Indirect Flux Detection by Online Reactance Measurement”) [70], [71] consists in applying to the machine special voltage test phasors and then measuring the current response.

The principle was first introduced in 1988 [72]. It utilizes the saliency based on saturation in the stator teeth and in rotor and stator yokes as well as geometric saliencies. It should be noted that the stator current can have a considerable influence on the saturation situation. The resulting position varying inductances cause a dependence of the current changes due to terminal voltage phasors. The

space phasors can either be a special measurement sequence interrupting the current control algorithm or can be integrated into the pulse pattern [73]. The tests do practically not disturb the torque production because the current change necessary for testing is in the range of only a few percents of rated current and can almost be neglected in the phase currents. The relation of the change of current space phasor per time ($d\bar{i}_s/dt$) over the test voltage space phasor (\bar{u}_s) corresponds to the rotor angle. However, for eliminating the back-EMF and the stator resistance typically two opposite space phasors are applied to the PMSM (It should be mentioned that there are several other possibilities):

$$\bar{u}_{s,1} = \bar{i}_{s,1} \cdot R_s + X_s \cdot \frac{d}{dt} \bar{i}_{s,1} + j \cdot \omega_{m,1} \cdot \bar{\psi}_M \quad (1.30)$$

$$\bar{u}_{s,2} = \bar{i}_{s,2} \cdot R_s + X_s \cdot \frac{d}{dt} \bar{i}_{s,2} + j \cdot \omega_{m,2} \cdot \bar{\psi}_M \quad (1.31)$$

$$\bar{u}_{s,2} = -\bar{u}_{s,1} \quad (1.32)$$

Assuming constant speed and a constant current during the measurement sequence the back-EMF and stator resistance terms can be eliminated, subtraction of the equation yields the complex INFORM reactance:

$$\bar{x}_s(2\gamma) = \frac{2\bar{u}_{s,1}}{\frac{d}{dt}(\bar{i}_{s,1} - \bar{i}_{s,2})} \quad (1.33)$$

This complex quantity represents a curve in the Gaussian plane and could be used to calculate the rotor angular position. However, in practice the inverted value \bar{Y}_{INFORM} is used since divisions can be avoided. As a result of certain calculations, the mentioned dependence can be modeled as follows (Y_{INFORM} : INFORM-based estimated rotor position):

$$\bar{Y}_{INFORM} = Y_0 + \Delta Y e^{j(2Y_{INFORM} - 2Y_U)} \quad (1.34)$$

Fig. 1.9 describes this function in more detail. The voltage test space phasor \bar{y}_{INFORM} is assumed in the horizontal direction ($\gamma_U = 0$). Turning the rotor (d-axis) from POS1 to POS3, the quantity y_{INFORM} describes a half circle in the complex plane. Repeating the test of Fig. 1.9 with different voltage test space phasors ($\gamma_U = 2\pi/3$, $\gamma_U = 4\pi/3$), the measurements yield one complex equation per independent test direction. Hence, the parameters γ_0 and $\Delta\gamma$ can be eliminated and the rotor position can be calculated. A detailed explanation is given in [71].

Combining this low speed model with an “EMF model” for higher speed enables covering the whole speed range. In recent years the direct INFORM-measurement sequence was persistently optimized especially with respect to the duration and the repetition rate of the measurement [74], even strategies for minimizing the current distortions have been presented [75].

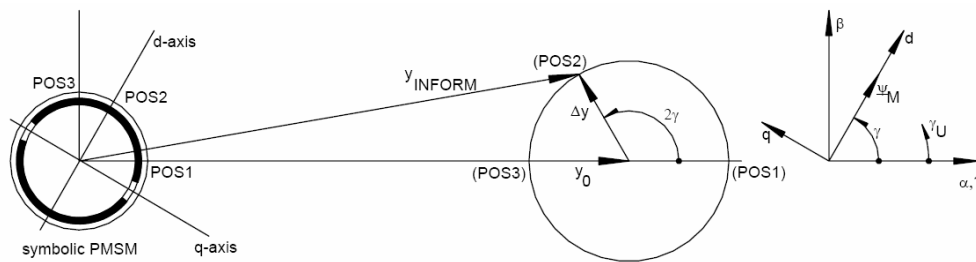


Fig. 1.9. Complex curve at horizontal ($\gamma_U = 0$) test voltage space phasor when turning the rotor

1.2.5.3. Low frequency signal injection

In most of these methods of high frequency voltage signal presented above, the magnetic saliency ($L_d < L_q$) of the PMSM is exploited. It was first introduced in the case of induction machines [76], but it can be applied also in the case of PMSM.

An LF current signal $i_c(t) = \sqrt{2}I_c \cos(\omega_c t)$ is superimposed on the estimated d-axis Fig. 1.10.

If there is an error $\tilde{\theta}$ between the estimated and ideal d-axis, the injected signal will induce back-EMF ripples, which could be used to estimate rotor speed.

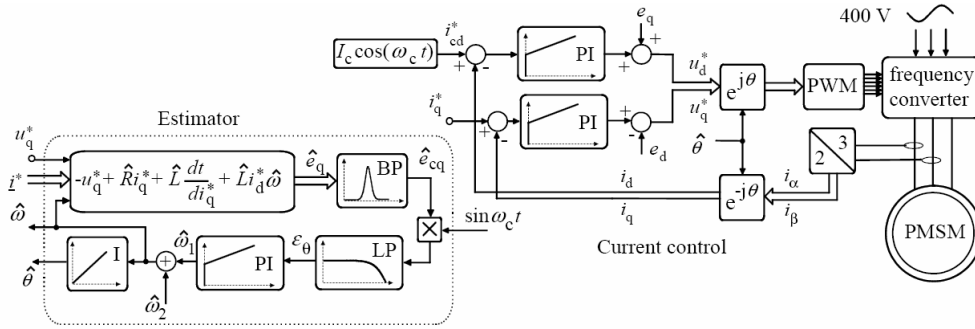


Fig. 1.10. Basic structure of the current control and low frequency estimator

The back-EMF ripples on the estimated q-axis can be expressed as:

$$\hat{e}_{cq} = \cos \tilde{\theta} \sin \tilde{\theta} \frac{3p^2 \psi_m^2 I_c}{J \omega_c} (\sin \omega_c t) \approx \tilde{\theta} \frac{3p^2 \psi_m^2 I_c}{J \omega_c} (\sin \omega_c t) \quad (1.35)$$

where p is the number of pole pairs, J is the total moment of inertia and ψ_m is the permanent magnet flux. In order to adjust $\tilde{\theta}$ to zero, some deduction is made as following and finally an error signal F_ϵ is obtained:

$$F_\epsilon = LPF \{e_{cq}(t) \sin(\omega_c t)\} = LPF \left\{ -\tilde{\theta} \frac{3p^2 \psi_m^2 I_c}{J \omega_c} \cdot \frac{1 - 2 \cos(2\omega_c t)}{2} \right\} = -\tilde{\theta} \frac{3p^2 \psi_m^2 I_c}{2J \omega_c} \quad (1.36)$$

where LPF means low-pass filter.

It can be seen that, if F_ϵ is adjusted to zero, ϵ will be zero and the exact rotor position can be obtained.

The low frequency estimator uses the motor model but it is somewhat insensitive to parameter errors.

In [77] the low frequency method is analyzed in the case of symmetric PMSM ($L_d = L_q$) and tested only by simulations. The saliency of the motor is a

distortion for the low-frequency estimator method. Thus the basic idea is quite different compared to the high frequency methods, where the saliency is a necessary condition for the estimator. In [78] the effect of saliency in the case of low-frequency injection is analyzed theoretically and verified by measurements.

While, the LF signal injection method needs to be combined with advanced observers to improve its dynamic response, the HF signal injection method has better dynamic performances but larger noise.

1.2.6. Sensorless Control without Additional Test Signal Injection

As it was said before, to overcome the low and zero speed problems of model-based observers for the sensorless control of AC drives, the research on the tracking of the inherent saliencies of AC machines increased. In these methods the machine is usually excited by a high frequency or transient test signal to produce a response that contains rotor/flux position information.

Other approaches to identify the machine saliency use the machine response during some defined voltage test vectors [81], [82]. Recent approaches [83]-[84] modify the fundamental switching pattern to obtain the position information without the cost of additional test signal injection. Also, the measurements are taken at the inverter terminals hence overcoming the need of additional wires or separate terminal boxes [82].

The position information in [83], [84] is sensed by measuring the current derivatives during the active switching states of the inverter. Various approaches were reported for the measurement of the current derivative [83], [85]-[89]. The task is made more complex as the current derivative is to be measured over a very short time.

In [90] a new method for the rotor-position estimation of the IPMSM which uses the slope of the stator phase current to estimate the rotor position is proposed. No extra circuit, injecting signal, or modifying PWM switching states is required. The proposed estimation technique is unrelated to the parameters of the motor, the back EMF, and the input dc bus voltage. As a result, it is very robust. The proposed estimation method can be applied at standstill, low-speed, and high-speed operation conditions. Moreover, the proposed method can be applied for both adjustable speed control and precise position control.

1.2.7. Emerging Techniques

The following are unique sensorless methods. They do not fall into the previous categories because of their peculiarities. These methods range from artificial intelligence to variations in the machine structure. In [91] a neural network is trained to obtain a non-linear relation between measured voltage and currents and rotor position. In the training phase, the rotor position is used to estimate the stator flux linkage vector. This flux linkage vector is compared with estimated flux as:

$$\psi_s = \int (u_s - R_s i) dt \quad (1.37)$$

The difference is used to modify the neural network weights. This method needs a known initial position.

Fuzzy logic can also be used to estimate the rotor position. Knowing the relationship between the measured voltage and currents and rotor position, it is possible to develop a fuzzy system to produce estimates of the rotor position.

It has been shown that a properly designed direct fuzzy controller can outperform conventional proportional integral derivative (PID) controllers [92].

All these methods using the artificial intelligence can achieve high performance, but they are relatively complicated and require large computational time.

Some methods use a modified machine structure to estimate the rotor position.

In [93], a small sensing coil is placed inside the stator windings. The rotor position may be determined by injecting high frequency voltage or current into one coil and detecting the induced voltage or current in another coil. The second harmonic of the measured signal is used to estimate the rotor position.

It is possible to create machine saliency attaching small pieces of aluminum to the surface of the magnets. This saliency can be used to determine the rotor position, as in methods that use inductance variation.

Other methods are based on irregularities or deviations from measurable voltage or currents. Since some parameters are not ideal, as supposed in a

theoretical machine analysis, the voltage and current waveforms are not equal to those ideally obtained. The irregularities can be used to estimate rotor position.

In [94], the methods detect irregularities in the phase current when the back emf and current are misaligned. These irregularities are used to correct the rotor position that yields the commutation instants.

1.3. Proposed solution

The underlying principle behind almost all low and zero speed sensorless techniques presented so far is the use of additional excitation to extract the saliency information. In this case, the saliency is a necessary condition for the estimator. Furthermore, these kinds of techniques are not so easy to implement and require a lot of computation effort.

In contrast, at low speeds, the emf model based observers fail.

For the salient-pole rotor machines and even for PMSMs machines with a nonsalient structure provided that a suitable induced saliency is generated by saturation effects, the magnetic saturation plays a key role causing changes in motor parameters. Thus, the magnetic saturation poses notable problems in flux, rotor position and speed estimations for motion-sensorless control, especially in the low-speed range (below 30 rpm in general), leading to numerous dedicated state observers.

Consequently, for the rotor position and speed estimation, it is necessary to find a solution for which the magnetic saturation will not be any more a problem and for which its computation effort to be less than for the other techniques.

This thesis introduces a novel concept, called *active flux or torque-producing flux* and its utilization in all ac drives by render all salient-pole traveling field machines into nonsalient-pole ones, so the magnetic saliency will be no longer a key factor.

It will be demonstrated in the next chapter that the active-flux vector is aligned to the rotor d axis for all synchronous machines and to the rotor-flux vector axis for induction machines. This way, the rotor position is equal to the active-flux

angle and consequently it can be estimated without requiring a large computation effort.

1.4. Conclusion

Control techniques, which are being applied to make ac drives a rapidly growing area, have been reviewed, starting with scalar control.

Direct torque control has an increasing interest because of its properties, but still few people are working on this subject. In the other hand, sensorless vector control with different algorithm to estimate the rotor position is far the most popular area based on the published papers. In contrast with this, it is shown that the performance achieved by means of V/f control is the same that the one achieved with sensorless vector control except for low speed operation and starting torque.

Speed or position sensorless techniques are of increasing importance. Their features were discussed, splitting techniques into fundamental model-based and signal injection techniques.

Model-based methods have long been available, offering behavior said 20 years ago to rival schemes with sensors. This behavior has been extended at very low speed, and is now truly impressive.

Exact comparison between schemes is difficult, because of a lack of standardization in tests.

The best performance requires parameter adaptation and correction of inverter nonlinearities.

Signal injection can offer extended zero speed, but is machine property-dependent.

The performances achievable from both classes of methods are now such that increasingly they will be applied to more demanding practical applications in industry with very good static and dynamic behavior.

Revising all these sensorless techniques with their advantages and disadvantages, a solution is proposed.

References

- [1] J. Holtz, "Sensorless control of induction machines—with or without signal injection?" *IEEE Trans. Ind. Electron.*, vol. 53, no. 1, pp. 7–30, Feb. 2006.
- [2] J. Holtz, "Sensorless control of induction motor drives," *Proc. IEEE*, vol. 90, no. 8, pp. 1359–1394, Aug. 2002.
- [3] G. S. Buja, and M. P. Kazmierkowski, "Direct torque control of PWM inverter-fed AC motors—A survey," *IEEE Trans. Ind. Electron.*, vol. 51, no. 4, pp. 744–757, Aug. 2004.
- [4] I. Boldea, L. Janosi and F. Blaabjerg, "A modified direct torque control (DTC) of reluctance synchronous motor sensorless drive" *Electric Machines & Power Systems*, vol.28, no.2, pp.115-128, 2000.
- [5] M. Pacas and R. Morales Caporal, "Predictive torque and flux control for the Synchronous reluctance machine" in *Proc. Power Electronics and Intelligent Control for Energy Conservation, (PELINCEC'05)*, Warsaw, Poland, 2005, on CD-ROM.
- [6] R. Morales Caporal and M Pacas, "A predictive torque control for the synchronous reluctance machine taking into account the magnetic cross saturation", *IEEE Trans. Industrial Electronics*, vol. 54, no. 2, 2007.
- [7] R. Morales Caporal, M, Pacas and J. J. Rodríguez Rivas, "Predictive direct torque control for a synchronous reluctance machine with predetermined stator flux compensation down to zero speed," in *Proc. IEEE International Electric Machines and Drives Conference (IEMDC'07)*, Antalya, Turkey, 2007, on CD-ROM.
- [8] P. C. Perera, F. Blaabjerg, J. K. Pedersen, and P. Thogersen, "A sensorless, stable v/f control method for permanent-magnet synchronous motor drives," *IEEE Trans. Ind. Applicat.*, vol. 39, no. 3, pp. 783-791, May/June 2003.
- [9] R. Ancuti and I. Boldea, "V/f control of PM-SM super high speed drives with flux and power angle stabilizing loops," in *Proc. OPTIM 2006*, Brasov, May 2006.

- [10] F. Blaschke, "The principle of field orientation as applied to the new transvector closed loop control system in a PWM inverter induction motor drive," *Siemens Rev.*, vol. 39, no. 5, pp. 217–220, 1972.
- [11] L. Harnefors, and H. P. Nee, "A general algorithm for speed and position estimation of AC motors," *IEEE Trans. Ind. Electron.*, vol. 47, no. 1, pp. 77–83, Feb. 2000.
- [12] B. Terzic, and M. Jadric, "Design and implementation of the extended Kalman filter for the speed and rotor position estimation of brushless DC motor," *IEEE Trans. Ind. Electron.*, vol. 48, no. 6, pp. 1065–1073, Dec. 2001.
- [13] B. Nahid-Mobarakeh, F. Meibody-Tabar, and F.-M. Sargos, "Back EMF estimation-based sensorless control of PMSM: Robustness with respect to measurement errors and inverter irregularities," *IEEE Trans. Ind. Appl.*, vol. 43, no. 2, pp. 485–494, Mar./Apr. 2007
- [14] S. Chi, J. Sun, "A novel sliding mode observer with multilevel discontinuous control for position sensorless PMSM drives," in *Conf. Rec. IEEE-APEC*, June, 2008, pp. 127–131.
- [15] T. Senjyu, "Vector control of permanent magnet synchronous motors without position and speed sensors," *Power Electronics Specialists Conference, PESC Record.*, 26th Annual IEEE Volume 2, 18-22 June 1995 pp.759-765.
- [16] J. X. Shen, Z. Q. Zhu, and D. Howe, "Improved speed estimation in sensorless pm brushless ac drives," *IEEE Trans. Ind. Appl.*, vol. 38, no. 4, pp. 1072–1080, Jul./Aug. 2002
- [17] A. Nasiri, "Full digital current control of permanent magnet synchronous motors for vehicular applications," *IEEE Trans. Veh. Technol.*, vol. 56, no. 4, pp. 1531–1537, Jul. 2007
- [18] Y. Liu, Z. Q. Zhu, and D. Howe, "Instantaneous torque estimation in sensorless direct-torque-controlled brushless DC motors," *IEEE Trans. Ind. Appl.*, vol. 42, no. 5, pp. 1275–1283, Sep./Oct. 2006.
- [19] H. Kim, M. C. Harke, and R. Lorenz, "Sensorless control of interior permanent-magnet machine drive with zero-phase lag position estimation," *IEEE Trans. Ind. Applicat.*, vol. 39, pp. 784–789, Nov./Dec. 2003.

- [20] S. Ichikawa, C. Zhiqian, M. Tomita, S. Doki, and S. Okuma, "Sensorless control of an interior permanent magnet synchronous motor on the rotating coordinate using an extended electromotive force," *Proc. IECON'01*, vol. 3, pp. 1667–1672, Dec. 2001.
- [21] S. Morimoto, K. Kawamoto, M. Sanada, and Y. Takeda, "Sensorless control strategy for salient-pole pmsm based on extended emf in rotating reference frame," *IEEE Trans. Ind. Applicat.*, vol. 38, pp. 1054–1061, July/Aug. 2002.
- [22] S. Bolognani, R. Oboe, and M. Zigliotto, "Sensorless full-digital PMSM drive with emf estimation of speed and rotor position," *IEEE Trans. Ind. Electron.*, vol. 46, pp. 184–191, 1999.
- [23] N. Ertugrul and P. Acarnely, "A new algorithm for sensorless operation of permanent magnet motors," *IEEE Trans. Ind. Applicat.*, vol. 30, pp. 126–133, Jan./Feb. 1994.
- [24] H. Rasmussen, V. Vadstrup, and H. Borsting, "Sensorless field oriented control of pm motor including zero speed.," *Proc. IEMDC'03*, 2003.
- [25] J.-L. Shi, T.-H. Liu, and Y.-C. Chang, "Position Control of an Interior Permanent-Magnet Synchronous Motor Without Using a Shaft Position Sensor," *IEEE Trans. on Ind. Electron.*, vol. 54, no. 4, Aug. 2007.
- [26] L. Shi, T.-H. Liu, and Y.-C. Chang, "Adaptive controller design for a sensorless IPMSM drive system with a maximum torque control," *Proc. Inst. Electr. Eng.—Electric Power Appl.*, vol. 153, no. 6, pp. 823–833, Nov. 2006.
- [27] Schauder, "Adaptive speed identification for vector control of induction motors without rotational transducers," *IEEE Trans. Ind. Appl.*, vol. 28, no. 5, pp. 1054–1061, Sep./Oct. 1992.
- [28] Ohtani, N. Takada, and K. Tanaka, "Vector control of induction motor without shaft encoder," *IEEE Trans. Ind. Appl.*, vol. 28, no. 1, pp. 157–164, Jan./Feb. 1992.
- [29] J. Armstrong, D. J. Atkinson, and P. P. Acarnley, "A comparison of estimation techniques for sensorless vector controlled induction motor drives," in *Proc. IEEE Int. Conf. Power Electron. Drive Syst.*, May 26–29, 1997, vol. 1, pp. 110–116.

- [30] Rashed, P. F. A. MacConnell, A. F. Stronach, and P. P. Acarnley, "Sensorless indirect-rotor-field-orientation speed control of a permanent magnet synchronous motor with stator-resistance estimation," *IEEE Trans. Ind. Electron.*, vol. 54, no. 3, pp. 1664–1675, Jun. 2007.
- [31] Cirrincione and M. Pucci, "An MRAS-based sensorless high performance induction motor drive with a predictive adaptive model," *IEEE Trans. Ind. Electron.*, vol. 52, no. 2, pp. 532–551, Apr. 2005.
- [32] Z. Yan, C. Jin, and V. I. Utkin, "Sensorless Sliding-Mode Control of Induction Motors," *IEEE Trans. Ind. Electron.*, vol 47, no. 6, pp. 1286-1297, Dec. 2000.
- [33] Zhang Yan, and Utkin V., "Sliding Mode Observers for Electric Machines – An Overview", *IECON0_28th Annual Conference of the IEEE Industrial Electronics Society*, vol 3, pp. 1842-1847, 5-8 Nov. 2002.
- [34] Z. Xu, and M. F. Rahman, "An Adaptive Sliding Stator Flux Observer for a Direct-Torque-Controlled IPM Synchronous Motor Drive", *IEEE Trans. Ind. Electron.*, vol 54, no. 5, pp. 2398-2405, Oct. 2007.
- [35] A. Bado, S. Bolognani, and M. Zigliotto, "Effective estimation of speed and rotor position of a pm synchronous motor drive by a kalman filtering technique," in *Proc. PESC'92*, vol. 2, 29June-3July 1992, pp. 951-957.
- [36] J. Atkinson, P. P. Acarnley, and J. W. Finch, "Observers for induction motor state and parameter estimation," *IEEE Trans. Ind. Appl.*, vol. 27, no. 6, pp. 1119–1127, Nov./Dec. 1991.
- [37] L. Gasc, M.Fadel, S. Astier, and L. Calegari, "Sensorless control for PMSM with reduced order torque observer associated to Kalman filter", *EPE 2005*, 11-14 Sept. 2005
- [38] B. Nahid Mobarakeh, F. Meibody-Tabar, and F.M. Sargos, "A globally converging observer of mechanical variables for sensorless PMSM," *Proc. PESC*, Vol. 2, pp. 885-890, June 2000.
- [39] S. Bolognani, L. Tubiana, and M. Zigliotto, "Extended Kalman filter tuning in sensorless PMSM drives," *IEEE Trans. Ind. Applicat.*, vol. 39, no. 6, pp. 1741–1747, Nov./Dec. 2003.

- [40] B. Akin, U. Orguner, A. Ersak, and M. Ehsani, "Simple derivative-free nonlinear state observer for sensorless AC drives," *IEEE/ASME Trans. Mechatronics*, vol. 11, no. 5, pp. 634–643, Oct. 2006.
- [41] M. Barut, S. Bogosyan, and M. Gokasan, "Speed-sensorless estimation for induction motors using extended Kalman filters," *IEEE Trans. on Ind. Electron.*, vol. 54, no. 1, pp. 272–280, Feb. 2007.
- [42] W. Chenchen, LI. Yongdong, "A Novel Speed Sensorless Field-Oriented Control Scheme of IM Using Extended Kalman Filter with Load Torque Observer," in *Conf. Rec. IEEE-APEC' 08*, June, 2008, pp. 1796-1802.
- [43] Julier, S.J., Uhlmann, J.K., Durrant-Whyte, H.F. "A new approach for filtering nonlinear systems", in *Proceedings of the American Control Conference*, vol.3, 21-23 June 1995, pp.1628–1632.
- [44] Akin, B., Orguner, U., Ersak, A. "State estimation of induction motor using unscented Kalman filter", in *Proceedings of 2003 IEEE Conference on Control Applications, 2003 (CCA 2003)*, vol.2, 23-25 June 2003, pp.915 – 919.
- [45] S. Bolognani, M. Zigliotto and M. Zordan, "Sensorless full-digital PMSM drive with EKF estimation of speed and rotor position", *IEEE Trans. on Industrial Electronics*, vol.46, Issue 1, Feb.1999, pp.184–191.
- [46] T. Aihara, A. Toba, T. Yanase, A. Mashimo, and K. Endo, "Sensorless torque control of salient-pole synchronous motor at zero speed operation," *Proc. APEC'97*, vol. 2, pp. 715–720, Feb. 1997.
- [47] Rasmussen H, Vadstrup R, Borsting H. "Adaptive observer for speed sensorless PM motor control," *Conference Record of the 38th IAS Annual Meeting*. Vol.1, 12-16 Oct. 2003, pp. 599-603.
- [48] A. Consoli, G. Scarcella, and A. Testa, "Industry application of zerospeed sensorless control techniques for pm synchronous motors," *IEEE Trans. on Ind. Applicat.*, vol. 37, pp. 806–812, March/April 2001.
- [49] M. Rashed, P. MacConnell, A. Stronach, and P. Acarnley, "Sensorless indirect rotor field orientation speed control of permanent magnet synchronous motor using adaptive rotor flux estimator," in *Proc. IEEE CDC-ECC*, Seville, Spain, Dec. 2005, pp. 647–652.

- [50] A. Piippo and J. Luomi, "Adaptive observer combined with HF signal injection for sensorless control of PMSM drives," in Proc. IEEE IEMDC, San Antonio, TX, May 2005, pp. 674–681.
- [51] S. Koonlaboon, and S. Sangwongwanich, "Sensorless control of interior permanent-magnet synchronous motors based on a fictitious permanent magnet flux model," in Conf. Rec. IEEE IAS Annual Meeting, Hong Kong, Oct. 2005, vol. 1, pp. 311–318.
- [52] S. Shinnaka, "New 'D-State-Observer'-based vector control for sensorless drive of permanent-magnet synchronous motors," IEEE Trans. Ind. Appl., vol. 41, no. 3, pp. 825–833, May/Jun. 2005.
- [53] A. Piippo, M. Hinkkanen, and J. Luomi, "Analysis of an Adaptive Observer for Sensorless Control of Interior Permanent Magnet Synchronous Motors," IEEE Trans. Ind. Electron., vol. 55, no. 2, pp. 570–576, Febr., 2007.
- [54] M. J. Corley, and R. D. Lorenz, "Rotor position and velocity estimation for a salient-pole permanent magnet synchronous machine at standstill and high speed," IEEE Trans. Ind. Appl., vol. 34, pp. 784–789, July/Aug. 1998.
- [55] M. Linke, R. Kennel, and J. Holtz, "Sensorless position control of permanent magnet synchronous machines without limitation at zero speed," Proc. IECON'02, vol. 34, pp. 784–789, Nov. 2002.
- [56] J.-H. Jang, J.-I. Ha, M. Ohto, K. Ide, and S.-K. Sul, "Analysis of permanent-magnet machine for sensorless control based on high frequency signal injection," IEEE Trans. Ind. Appl., vol. 39, pp. 1595–2004, May/June 2003.
- [57] S. Morimoto, K. Kawamoto, M. Sanada, and Y. Takeda, "Sensorless control strategy for salient-pole PMSM based on extended EMF in rotating reference frame," IEEE Trans. Ind. Appl., vol. 38, no. 4, pp. 1054–1061, Jul./Aug. 2002.
- [58] M. Harke, H. Kim, and R. D. Lorenz, "Sensorless control of interior permanent magnet machine drives for zero-phase-lag position estimation," IEEE Trans. Ind. Appl., vol. IA-39, no. 12, pp. 1661–1667, Nov./Dec. 2003.
- [59] M. Linke, R. Kennel, and J. Holtz, "Sensorless speed and position control of synchronous machines using alternating carrier injection," in Proc. Int. Elect. Mach. Drives Conf. (IEMDC'03), Madison, WI, 2–4 Jun. 2003, pp. 1211–1217.

- [60] A. Consoli, G. Scarcella, G. Tutino, and A. Testa, "Sensorless field oriented control using common mode currents," in Proc. Ind. App. Conf., Rome, Italy, Oct. 8–12, 2000, vol. 3, pp. 1866–1873.
- [61] H. Kim, and R. D. Lorenz, "Carrier signal injection based sensorless control methods for IPM synchronous machine drives," Conf. Rec. IEEE IAS Annual Meeting, vol. 2, pp. 977–984, 2003.
- [62] N. Teske, G. M. Asher, M. Sumner, and K. J. Bradley, "Analysis and suppression of high-frequency inverter modulation in sensorless position-controlled induction machine drives," IEEE Trans. Ind. Applicat., vol. 39, pp. 10-18, Jan./Feb. 2003.
- [63] J. M. Guerrero, M. Leetmaa, F. Briz, A. Zamarron, and R. D. Lorenz, "Inverter nonlinearity effects in high-frequency signal-injection-based sensorless control methods," IEEE Trans. Ind. Applicat., vol. 41, pp. 618-626, Mar./Apr. 2005.
- [64] C. H. Choi, and J. K. Seok, "Compensation of zero current clamping effects based on high frequency signal injection," in Conf. Rec. IEEE IAS Annual Meeting, Tampa, FL, Oct. 2006, CD-ROM.
- [65] J. Holtz, "Sensorless position control of induction motors – an emerging technology," Proc. IECON, 31 Aug.-4 Sept. 1998, vol.1, pp. I1 - I12.
- [66] M. Linke, R. Kennel, J. Holtz, "Sensorless position control of permanent magnet synchronous machines without limitation at zero speed," IECON 02, IEEE 2002 28th Annual Conference of the Industrial Electronics Society , 5-8 Nov. 2002, vol.1, pp. 674 – 679.
- [67] R. Lorenz, "Sensorless drive control methods for stable, high performance, zero speed operation," Int. Conference on Power Electronics and Motion Control, EPE-PEMC, Kosice 2000, on CD-ROM.
- [68] A. Consoli, G. Scarcella, A. Testa, "A new zero frequency flux detection approach for field oriented control drives," IEEE Trans. Ind. Appl., Vol. 36, No. 3, May/June 2002, pp. 797-804.
- [69] C.A. Silva, G.M. Asher, M. Sumner, K.J. Bradley, "Sensorless rotor position control in a surface mounted PM machine using HF voltage injection," EPE-PEMC, 2002 Dubrovnik & Cavtat, Croatia, on CD-ROM.

- [70] M. Schroedl, "Sensorless control of AC Machines at low speed and standstill based on the 'INFORM'-method," IEEE Ind. Appl. Society Meeting, San Diego, 1996, vol.1, pp. 270-277.
- [71] M. Schroedl, "Sensorless control of AC machines," VDI-Fortschrittsberichte, VDI Verlag Duesseldorf, 1992, vol 21, no. 117.
- [72] M. Schroedl, "Detection of the rotor position of a permanent magnet synchronous machine at standstill," International Conference on El. Drives and Machines, ICEM 1988, Pisa, pp. 195-197.
- [73] T. Wolbank, P. Weinmeier, "The impact of different methods to generate INFORM test pulses for sensorless control of AC-machines on power electronics and the performance of the drive," Int. Conf. on Power Conversion and Intelligent Motion, PCIM, Nuremburg, 1998, pp. 517-523.
- [74] E. Robeischl, M. Schroedl, K. Salutt, "Improved INFORM-measurement sequence and evaluation for sensorless permanent magnet synchronous motor drives," 10th International Power Electronics and Motion Control Conference, EPE-PEMC, 2002, Cavtat & Dubrovnik, Croatia, on CD-ROM.
- [75] E. Robeischl, M. Schroedl, "Optimized INFORM-measurement sequence for sensorless PM synchronous motor drives with respect to minimum current distortion, Trans. Ind. Applicat., IEEE, Vol. 40, No. 2, March-April 2004, pp. 591-598.
- [76] V.-M. Leppänen, "A Low-Frequency signal-injection method for speed sensorless vector control of induction motors," Thesis for the degree of doctor of science in technology, Helsinki University of technology, Institute of intelligent power electronics, Espoo, 2003.
- [77] T. Kereszty, V.-M. Leppänen, and J Luomi, "Sensorless control of surface magnet synchronous motors at low speeds using low-frequency signal injection," Conference record of the 29th annual conference of the IEEE industrial electronics society, IECON'03, Roanoke, VA, 2-6, November 2003, pp. 1239-1243.
- [78] M. Eskola, and H. Tuusa, "Sensorless control of salient pole PMSM using a low-frequency signal injection," EPE'05, pp. P.1-P.10.

- [79] R. Leidhold, and P. Mutschler, "Sensorless position-control method based on magnetic saliencies for a long-stator linear synchronous-motor," in Proc. IECON, Paris, France, 7-10 November 2006. pp. 781-786.
- [80] J.-H. Jang, S.-K. Sul, J.-I. Ha, K. Ide, and M. Sawamura, "Sensorless drive of surface-mounted permanent-magnet motor by high-frequency signal injection based on magnetic saliency," IEEE Trans. Ind. Appl., vol. 39 no. 4, pp. 1031-1038, 2003.
- [81] J. Holtz, and H. Pan, "Elimination of saturation effects in sensorless position-controlled induction motors," IEEE Trans. on Ind. Appl., vol. 40, no. 2, pp. 623-631, 2004.
- [82] C. Caruana, G. M. Asher, and J. C. Clare, "Sensorless flux position estimation at low and zero frequency by measuring zero sequence currents in delta connected cage induction machines," in Conf. Rec. IEEE-IAS Annual Meeting, 2003.
- [83] J. Juliet, and J. Holtz, "Sensorless acquisition of the rotor position angle for induction motors with arbitrary stator windings, in Conf. Rec. IEEE-IAS Annual Meeting, Seattle, USA, 2004.
- [84] G. Qiang, G. M. Asher, M. Sumner, and M. P., "Position estimation of AC machines at all frequencies using only space vector PWM based excitation, PEMD, 2006.
- [85] T. Wolbank, J. Machl, and H. Hauser, "Closed-loop compensating sensors versus new current derivative sensors for shaft-sensorless control of inverter fed induction machines, IEEE Trans. on Instrumentation and Measurement, Vol. 55, No. 4, pp. 1311-1315, 2004.
- [86] M. Jansson, L. Harnfors, O. Wallmark, and M. Leksell, "Synchronization at startup and stable rotation reversal of sensorless nonsalient PMSM drives," IEEE Trans. Ind. Electron., vol. 53, no. 2, pp. 379-387, Apr. 2006.
- [87] J. K. Seok, J. K. Lee, and D. C. Lee, "Sensorless speed control of nonsalient permanent-magnet synchronous motor using rotor-position tracking PI controller," IEEE Trans. Ind. Electron., vol. 53, no. 2, pp. 399-405, Apr. 2006.
- [88] Y. H. Chang, T. H. Liu, and C. C. Wu, "Novel adjustable micro permanent magnet synchronous-motor system without using a rotor-position/speed

- sensor," *Proc. Inst. Electr. Eng.—Electr. Power Appl.*, vol. 153, no. 3, pp. 429–438, May 2006.
- [89] S. Ichikawa, M. Tomita, S. Doki, and S. Okuma, "Sensorless control of permanent-magnet synchronous motors using online parameter identification based on system identification theory," *IEEE Trans. Ind. Electron.*, vol. 53, no. 2, pp. 363–372, Apr. 2006.
- [90] J.-L. Shi, T.-H. Liu, and Y.-C. Chang, "Position control of an interior permanent-magnet synchronous motor without using a shaft position sensor," *IEEE Trans. on Instrumentation and Measurement*, vol. 55, no. 4, pp. 1311–1315, 2004.
- [91] F. Huang, and D. Tien, "A neural network approach to position sensorless control of brushless dc motors," *Proc. IECON*, vol. 2, Aug. 1996, pp. 1167–1170.
- [92] A. G. Aissaoui, M. Abid, H. Abid, A. Tahour, A. K. Zeblah, F. Huang, and D. Tien, "A Fuzzy logic controller for synchronous machine," *Journal of Electrical Engineering*, vol. 58, no. 5, pp. 285–290, 2007.
- [93] K. J. Binns, K. M. Al-Aubidy, and D. W. Shimmin, "Implicit rotor position sensing using search coils for a self-commutating permanent magnets drive system," *IEE Proceedings*, vol. 137, no. 4, pp. 253–258, July 1990.
- [94] J. I. Itoh, N. Nomura, and H. Oshawa, "A comparison between V/f control and position sensorless vector control of permanent magnet synchronous motor," *Proc. Power Conversion Conf.*, vol. 3, Osaka, Japan, Apr. 2002, pp. 1310–1315.

Chapter 2

Active Flux Concept for Unified AC Drives

Abstract

This chapter introduces a rather novel (or generalization) concept, called *active flux or torque-producing flux* and its utilization in all ac drives by employing a unified state observer for motion-sensorless control in a wide speed range. The active-flux concept turns all salient-pole traveling field machines into nonsalient-pole ones. The active-flux vector is aligned to the rotor d axis for all synchronous machines and to the rotor-flux vector axis for induction machines. This way, the rotor position and speed observer seems more amenable to a wide speed range, with fewer dynamic errors. This observer, based on the active-flux concept, is pretty much the same for all ac drives. An example of implementation for an interior permanent-magnet synchronous motor with weak permanent magnets and large magnetic saliency that compares very favorably with respect to most signal injection method, down to 1 rpm and up to 4000 rpm, is provided through digital simulations [33].

2.1. Introduction

Ac motor variable-speed drives are now applied to all industries for motion control to increase industrial productivity and save electric energy. Field orientation control [1], direct torque control [2]-[7], feedback linearization control, or scalar control (V/f and I/f with stabilizing loops) are typical for modern high-performance ac drives. Rotor and stator flux, or rotor position orientation-control are standard. For motion-sensorless control, the flux, rotor position and speed all have to be estimated on-line by adequate state observers for a wide speed range, with reasonable steady-state and dynamic errors [8]-[32]. For salient-pole ac machines (such as strong permanent-magnet (PM) interior permanent-magnet synchronous motor (IPMSM), weak-PM IPMSM, or PM-assisted reluctance synchronous motors), reluctance synchronous machines, or dc-excited salient-pole synchronous machines,

magnetic saturation plays a key role in heavy load applications. Thus, fundamental model state observers for flux, rotor position and speed become less reliable and more complicated. They differ in structure from the ac machine type. The initial rotor position estimation is essential for sensorless control of synchronous machines; a few solutions are presented in [13].

For low speeds, signal injection was introduced [8]-[10], [12]-[21] down to 1 rpm in the speed-control mode, but with notable speed deviation during torque perturbation transients. One way around this problem is to build a machine with reliable saliency in saturated conditions in order to secure accurate rotor position estimation [23]. All existing state observers with signal injection for salient-pole rotor ac machines exploit the main dq magnetic anisotropy.

In contrast, this chapter introduces a novel concept which turns all salient-pole rotor ac machines into fictitious nonsalient-pole machines such that the rotor position and speed estimations become simpler. The *active flux* concept introduced here refers to the torque-producing flux in the electromagnetic torque formulae of ac machines. Note that the *extended emf* concept [29]-[31] may be considered similar, but it was derived differently and differs from active flux in concept and during current (torque) transients. Also, the *fictitious PM flux model* in [32] is derived solely for IPMSM and is equivalent to the active flux model. Reference [32] makes no attempt to generalize the concept to IM and to all SMs (with or without PMs), and consequently discusses an interesting, but involved, IPMSM-dedicated state observer with sensorless performance down to 100 rpm in experiments.

So, in a way, the active flux introduced here may be considered a generalization of both extended emf [29]-[31] and fictitious PM flux [32] models for all ac drives, with a unified state observer for active flux, rotor position and speed.

2.2. Active Flux Concept

Let us now start directly by defining the active flux (ψ_d^a) as the flux that multiplies the i_q current in the dq -model torque expression of all ac machines [25]:

$$T_e = 1.5p_1\psi_d^a i_q \quad (2.1)$$

with $\psi_d^a = \psi_{PMd}$ for surface permanent-magnet synchronous motor (SPMSM); (2.2)

$$\psi_d^a = \psi_{PMd} + (L_d - L_q)i_d \text{ for IPMSM } (L_d < L_q); \quad (2.3)$$

$$\psi_d^a = L_{dm}i_f + (L_d - L_q)i_d \text{ for dc-excited synchronous machines } (L_d \geq L_q); \quad (2.4)$$

$$\psi_d^a = (L_d - L_q)i_d \text{ for reluctance synchronous machines (Relsyn) } (L_d \gg L_q); \quad (2.5)$$

$$\psi_d^a = (L_s - L_{sc})i_d \text{ for induction machines (IMs) in the } dq \text{ rotor flux axis} \\ (L_s \gg L_{sc}); \quad (2.6)$$

The d axis corresponds to the rotor pole axis in all synchronous machines (SMs) in (2.2)-(2.5), and to the rotor flux axis in IMs.

L_d , L_q are the dq inductances, ψ_{PMd} is the PM flux linkage: weak (0.1-0.3 per unit (p.u.)), or strong (0.7-0.9 p.u.), with no, small ($L_d / L_q = 0.6 - 0.7$), or large ($L_d / L_q = 1 / 3$) magnetic saliency rotors; $L_{dm}i_f$ is the field current stator-flux linkage, and L_s , L_{sc} are, respectively, the no-load, and the short-circuit inductance of the IMs.

Eq. (1) leads intuitively to a nonsalient-pole rotor ac machine whose inductance would go against i_q , that is L_q , which for some cases is dependent mainly on i_q current, i.e., $L_q(i_q)$, as cross-coupling for q axis is rather small [25], [26].

Let us now simply demonstrate how the new concept leads to a fictitious nonsalient-pole rotor general ac machine by starting with the space-phasor stator-voltage equation in stator coordinates:

$$\vec{V}_s^S = R_s \vec{i}_s^S + d\vec{\psi}_s^S / dt \quad (2.7)$$

By definition, the active flux vector $\vec{\psi}_d^{as}$ observer is:

$$\bar{\psi}_d^{as} = \int (\bar{V}_s^s - R_s \bar{i}_s^s + \bar{V}_{comp}) dt - L_q \bar{i}_s^s \quad (2.8)$$

The $\bar{\psi}_d^{as}$ axis falls along the d axis and thus (as in (2.1)-(2.6))

$$\bar{\psi}_d^{as} = \psi_d^a \cos \theta_{\psi_d^a} + j \psi_d^a \sin \theta_{\psi_d^a} \quad (2.9)$$

\bar{V}_{comp} compensates various errors in the $\bar{\psi}_d^{as}$ estimation, such as inverter nonlinearity, dead time, integration dc-offset, and stator resistance variation, which are crucial at low speeds [22].

The equivalent inductance L_q in (2.8) and the active flux angle $\theta_{\psi_d^a}$ are given in TABLE 2.1, where s is the slip of the IMs, and ω_1 is the stator flux frequency. Note that for all SMs, the electrical rotor position is equal to the active flux angle, $\theta_{er} = \theta_{\psi_d^a}$.

TABLE 2.1

Equivalent inductance L_q and active flux angle $\theta_{\psi_d^a}$ of ac machines

	SPMSM	IPMSM	Relsyn	DC-excited SM	IM
L_q	$L = const$	$L_q(i_q) > L_d$	$L_q = const < L_d$	$L_q(i_q) < L_d$	$L_s = const \ll L_{sc}$
$\theta_{\psi_d^a}$	θ_{er}	θ_{er}	θ_{er}	θ_{er}	$\theta_{er} + \int s \omega_1 dt$

Now, transforming equations (2.7), (2.8) into active flux dq coordinates, it is a formality to obtain:

$$\bar{V}_s = R_s \bar{i}_s + (s + j\omega_r) L_q \bar{i}_s + (s + j\omega_r) \bar{\psi}_d^a \quad (2.10)$$

Again, it is evident that (2.10) refers to a nonsalient-pole equivalent machine. The actual saliency is hidden rather simply in $\bar{\psi}_d^a$ (2.2)-(2.6).

The derivation of (2.10) from the dq model of IPMSM (for example) is straightforward. Starting with the dq model of IPMSM,:

$$V_d = R_s i_d + sL_d i_d - \omega_r L_q i_q + (sL_q i_d - sL_q i_d) \quad (2.11)$$

$$V_q = R_s i_q + sL_q i_q + \omega_r (\psi_{PM_d} + L_d i_d) + (\omega_r L_q i_d - \omega_r L_q i_d) \quad (2.12)$$

two equations are added to prepare them for the space-phasor form:

$$\begin{aligned} V_d + jV_q = R_s (i_d + ji_q) + sL_q (i_d + ji_q) + j\omega_r L_q (i_d + ji_q) \\ + s(\psi_{PM_d} + (L_d - L_q)i_d) + j\omega_r (\psi_{PM_d} + (L_d - L_q)i_d) \end{aligned} \quad (2.13)$$

with $\psi_d^a = \psi_{PM_d} + (L_d - L_q)i_d$. Finally, (2.10) is obtained

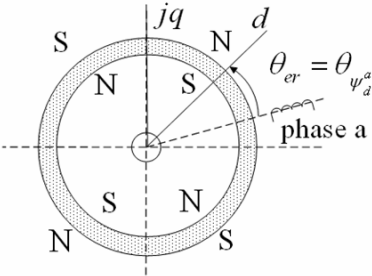
The transformer and motion-induced voltages related to L_q in the dq model (2.13) are clearly seen. This is a definitive sign that the virtual IPMSM, or any other salient pole rotor machine, is now a nonsalient-pole rotor machine. Note that in [29]-[31], the extended emf:

$$E_{ex} = \omega_r (\psi_{PM} + (L_d - L_q)i_d) + s(L_d - L_q)i_q \quad (2.14)$$

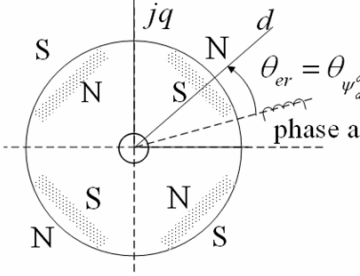
which leads to (2.13) only in steady state, does not correspond to a complete nonsalient machine, because only the transformer voltages reveal L_q along both axes, while the motion emfs both contain L_d .

It means that when observing extended emf, the machine saliency returns (under steady state also), complicating the position and speed estimation, at least in the dq model. This is only to say that active flux leads, by phenomenological changes, to a completely nonsalient machine model which may simplify rotor position and speed estimation over a wide speed range, for both the stator and active-flux coordinates.

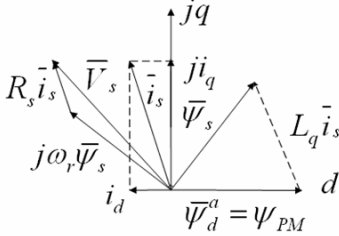
To explain the concept quickly, the steady-state vector diagram with $\overline{\psi}_d^a$ in the foreground is drawn in Fig. 2.1 for all six main ac machine types in (2.2)-(2.6). For the dc-excited SM, the unity power factor conditions are shown in Fig. 2.1e.



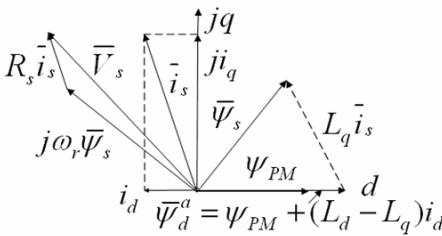
$L_d = L_q = L_s$ (no saliency)



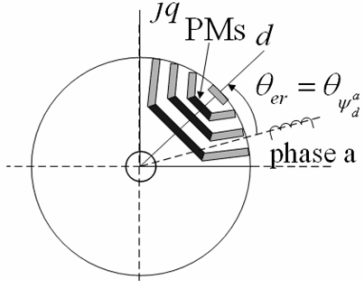
$L_d < L_q$ (small saliency)



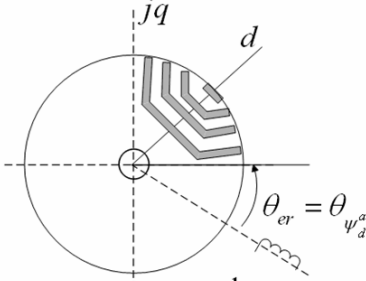
(a)



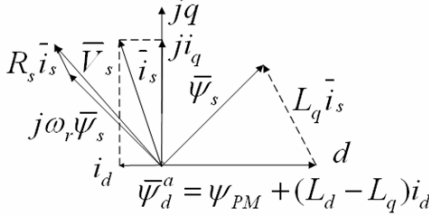
(b)



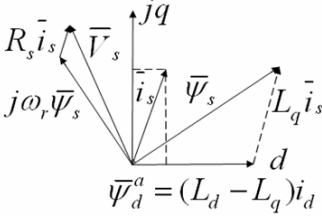
$L_d \ll L_q$ (high saliency)



$L_d \gg L_q$



(c)



(d)

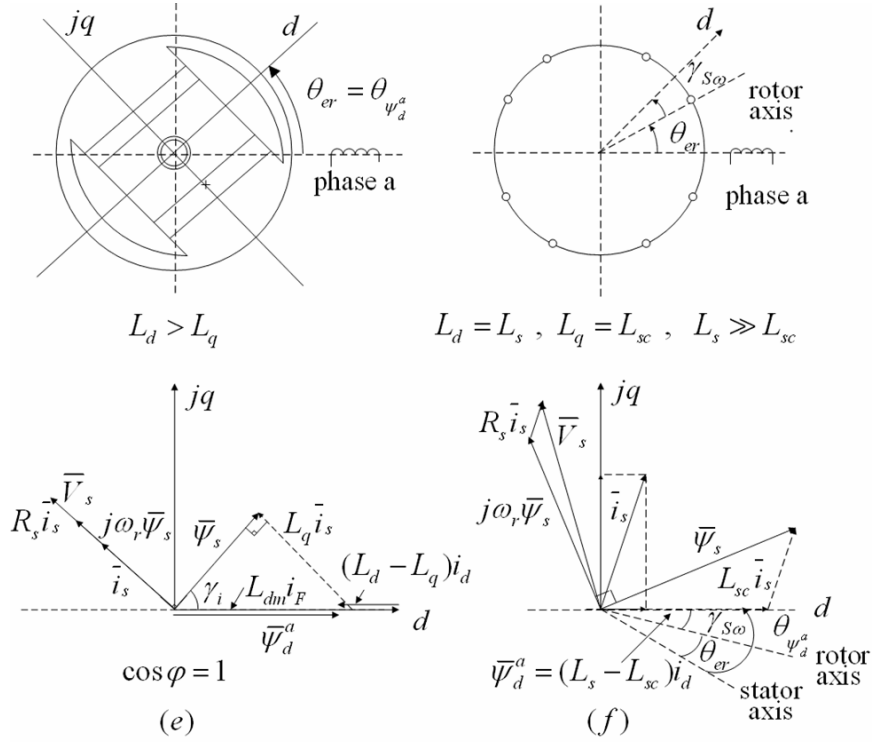


Fig. 2.1. Vector diagrams with active flux $\bar{\psi}_d^a$ for: a) SPMSM, b), c) IPMSMs, d) Relsyn, e) dc-excited SM, and f) IM

Only for the IM, which in rotor flux orientation behaves as a large saliency Relsyn with $L_d \rightarrow L_s$ and $L_q \rightarrow L_{sc} (L_s \gg L_{sc})$ [25], the active flux angle, $\theta_{\psi_d^a}$, falls along the rotor-flux axis (and not the rotor axis) and thus:

$$(\theta_{\psi_d^a})_{IM} = \theta_{er} + \theta_{s\omega_1}; \quad \theta_{s\omega_1} = \int s\omega_1 dt; \quad s\omega_1 = \frac{i_q R_r}{i_d L_r}, \quad (2.15)$$

$\theta_{s\omega_1}$ is the known slip-speed angle, dependent on i_d, i_q , and L_r/R_r is the rotor time constant.

A few remarks may be in order:

- The active flux $\bar{\psi}_d^a$ is the torque-producing virtual flux on the d axis that multiplies i_q in the torque expression of ac machines in the dq modeling.
- The active-flux axis is the rotor axis for all SMs (PM axis for PMSM, excitation axis for dc-excited SM, or the maximum inductance axis for Relsyn), and the rotor flux axis for the IM.
- In active-flux orientation control, all ac machines behave as if they have nonsalient rotor poles with torque current i_q and inductance L_q . Only for IPMSM and dc-excited SMs, L_q is notably dependent on i_q and thus $L_q(i_q)$ has to be known if precision control is required [25], [28].
- The active flux observer in the stator coordinates is basically a voltage model, where the integrator offset, stator resistance and inverter nonlinearities have to be compensated, at least for low speeds.

The main advantage is that this observer is practically the same in structure for all ac machines. It leads to the estimations of both ψ_d^a amplitude and $\theta_{\psi_d^a}$ angle with respect to stator phase a ($\theta_{\psi_d^a} = \theta_{er}$ for all SMs).

2.3. AC Unidrive Based on Active Flux Concept

The PMSMs, Relsyns and IMs are systems with two electric inputs (i_d and i_q), while the dc-excited SMs have three input (i_F , i_d and i_q). One input reference i_q^* (or reference torque) is served by the speed loop, while the other one (i_d^*) or two (i_F^* , i_d^*) are calculated from energy conversion optimization criteria: max torque per current, or per stator flux versus speed for limited voltage, and, respectively, unity power factor for dc-excited SMs.

To provide decoupled torque control, ψ_d^a should be kept rather constant up to the base speed.

The relationship between $\bar{\psi}_d^a$ and $\bar{\psi}_s$ in any reference frame is obtained from (2.8) and the vector diagrams in Fig. 2.1:

$$\bar{\psi}_d^a = \bar{\psi}_s - L_q \bar{i}_s \quad (2.16)$$

This way, vector current control in active flux coordinates becomes straightforward (see Fig. 2.2).

Note that only $\psi_d^{a*}(\hat{\omega}_r)$ or $\psi_d^{a*}(T_e^*)$ differ from one ac machine to another. The active-flux vector control makes the emf compensation optional. Some differences between various ac machine controls may also occur in the state observer, in order to achieve reliable low-speed performance.

The scheme in Fig. 2.2 holds for all PMSMs, Relsyns and for the IMs.

For the dc-excited SM operating at unity power factor, a slightly different first part of the scheme in Fig. 2.2 is required, as seen in Fig. 2.3. In this case, the field-current channel handles the active-flux closed-loop control to secure unity power factor. This time ψ_d^{a*} is not constant with regard to load and rotor speed.

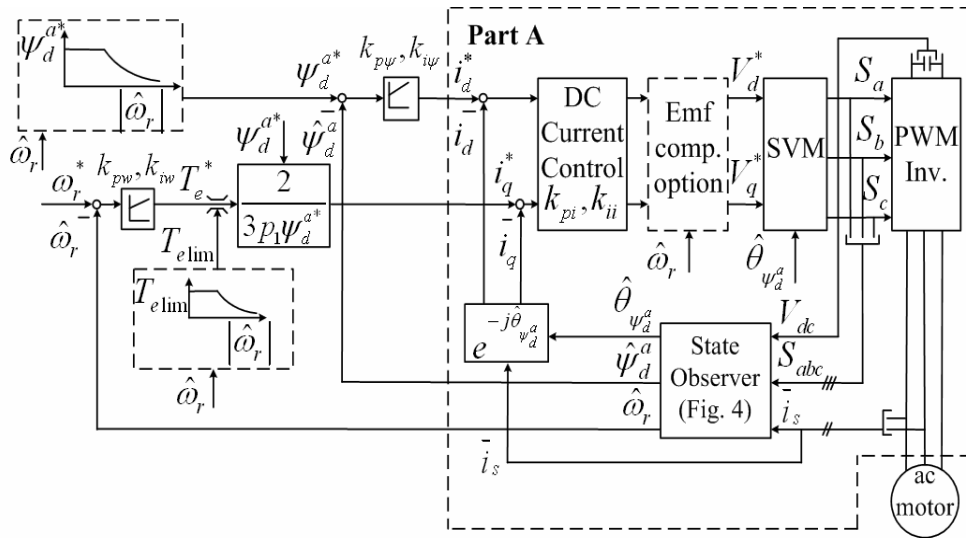


Fig. 2.2. Sensorless vector control in active-flux $\hat{\psi}_d^a$ dq model for PMSM, Relsyn and IM

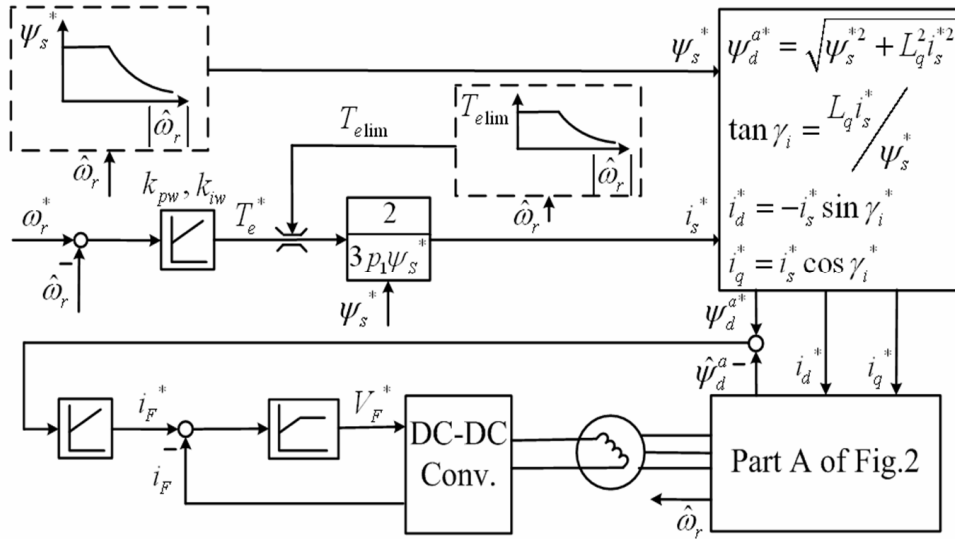


Fig. 2.3. Sensorless active-flux vector control for unity power factor dc-excited SM.

The active flux, rotor position and speed state observer are the key issues here. In principle, the voltage model in the stator or even in the active-flux dq coordinates is used with proper \bar{V}_{comp} compensation for reliable performance at very low speed (Fig. 2.4).

The \bar{V}_{comp} compensation voltage should take care of inverter nonlinearities (power switch voltage drops, dead-time), integrator offset [22], stator resistance variation and magnetic saturation through an eventual current model [16]. So, it is the voltage compensation block that individualizes the machine type, with influence mainly at very low speeds. To be more specific, an implementation of active-flux sensorless vector control for the IPMSM with large saliency and weak PMs is presented.

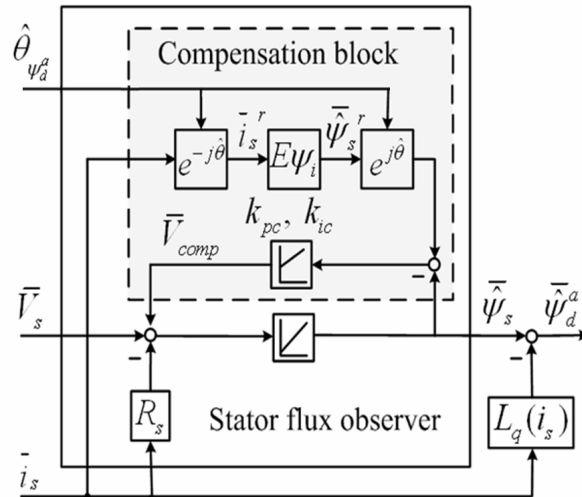


Fig. 2.4. Active flux observer in stator coordinates for PMSM, employing parallel stator flux observer

2.4. Case Study: IPMSM Sensorless Control in Wide-Speed Range

2.4.1. The Active Flux Observer

Since the relationship between $\bar{\psi}_d^a$ and $\bar{\psi}_s$ is obtained from (2.16), the important role is played in fact by the stator flux observer.

The stator flux observer combines voltage-current models: the current model, including magnetic saturation, prevails at low speed, while the voltage model prevails at medium and high-speed with a smooth transition between them depending on speed.

Two combined flux observers were developed, investigated and compared (Fig. 2.4, respectively Fig. 2.5). Both are based on the voltage and on the current models, but one is using them in parallel and one in series. The topologies and the results are also illustrated and discussed.

The parallel observer (Fig. 2.4) contains the same models operated in parallel, but using the flux estimation error. This time, the PI correction loop encloses only the voltage model, while the current model is open loop operated.

In Fig. 2.4, the expression of the current model flux estimator in rotor reference $E\psi_{si}$ consists in:

$$\bar{\psi}_{si}^s = [L_d i_d + \psi_{PM} + jL_q(\hat{T}_e) i_q] e^{j\hat{\theta}_r}; \quad i_d + j i_q = \bar{i}_s^s e^{-j\hat{\theta}_r} \quad (2.17)$$

The serial observer (Fig. 2.5) contains the voltage model in stator reference serially connected with the current model in rotor reference, using a PI compensator driven by the current estimation error. Both models are enclosed within the correction loop.

The rotor position estimation $\hat{\theta}_{\psi_d^a}$ is required by both observers for the coordinate transformations in the current model within the flux observer – but only at low speed, because at medium and high-speed the voltage model becomes dominant.

The parameters of the active flux observer in Fig. 2.4, respectively in Fig. 2.5 are: for the compensator block $k_{pc} = 4$; $k_{ic} = 4$, respectively $k_{pc} = 3$; $k_{ic} = 9$ for PI controller type $(k_p + k_i / s)$.

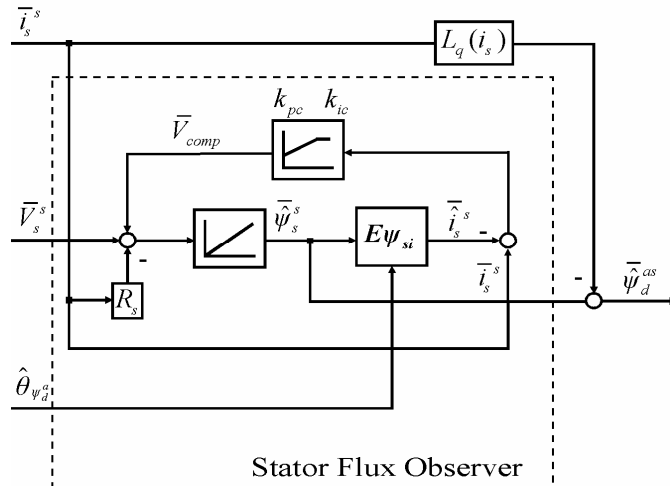


Fig. 2.5. Active flux observer employing serial stator flux observer

In order to compare the two observer typologies, a digital simulation for the IPMSM drive with encoder was performed. As it was expected, both observers display almost similar behavior. In Fig. 2.6, the errors between the stator flux estimations provided by both parallel and serial observers and the measured stator flux are illustrated and, as it can be seen, they are very small.

The main difference with respect to series observers is the fact that correction loop encloses the voltage model only, while the current model may affect the system's overall behavior to a larger or smaller degree, depending on the PI controller gains.

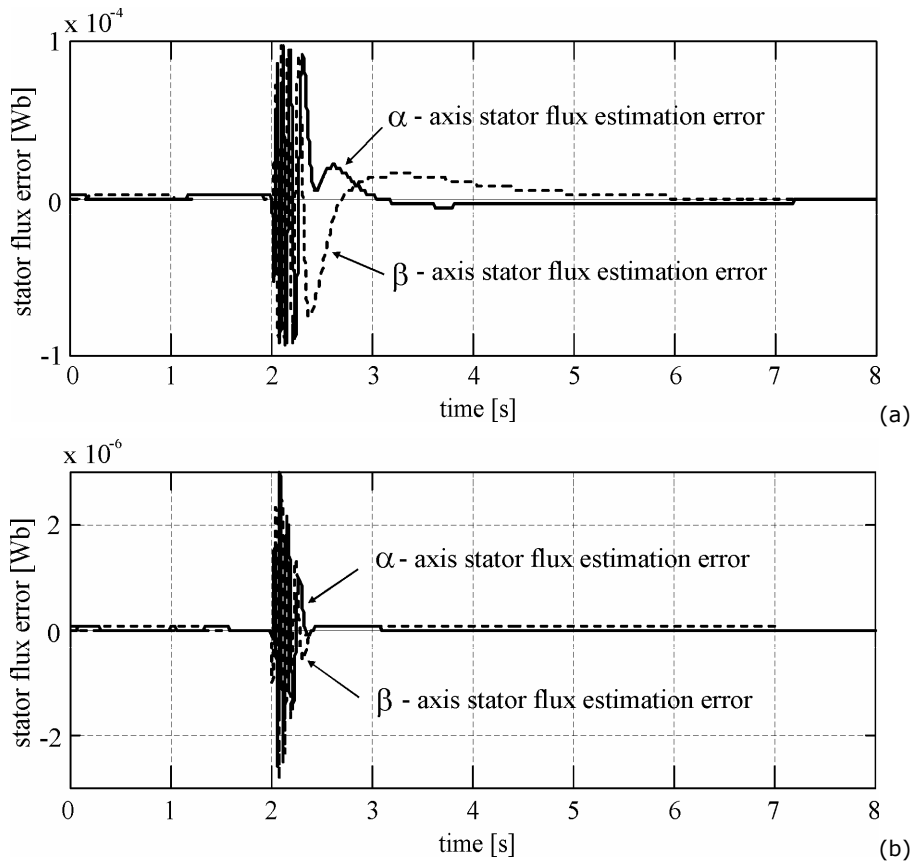


Fig. 2.6. IPMSM speed reversal of ∓ 1 rpm with full-step load at 2 s: a). $\alpha\beta$ -axes stator flux estimation errors for the **parallel** model; (b). $\alpha\beta$ -axes stator flux estimation errors for the **serial** model

2.4.2. The Speed and Position Estimators

For low speed operation a speed observer with signal injection was used in [16] as shown in Fig. 2.7. A rotating carrier-voltage $V_c = V_c \exp(j\omega_c t)$ with $V_c = 1V$ and $\omega_c = 500$ Hz was injected in the stator superimposing on top of driving fundamental stator-voltage \bar{V}_s (Fig. 2.7a). The resulting stator current \bar{I}_s , modulated by the position dependent inductances with magnetic saliency, contains carrier-current harmonics with rotor position information θ_r .

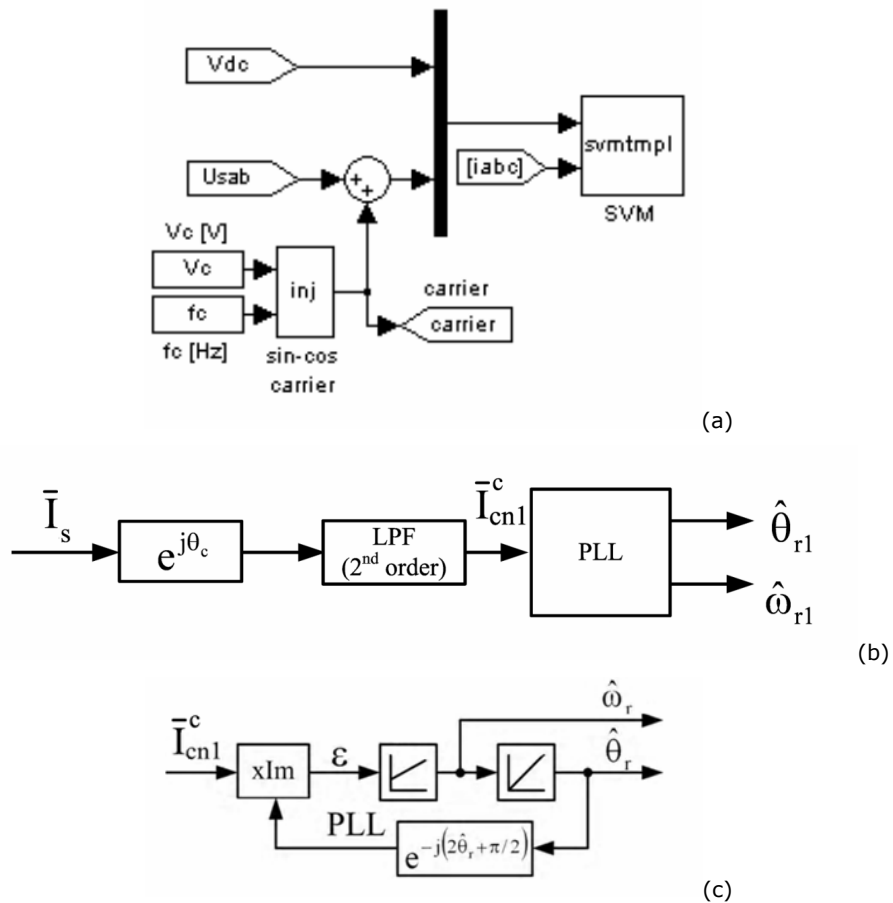


Fig. 2.7. Speed and position observers with signal injection: (a). rotating carrier-voltage, (b). observer with synchronous low-pass filter and (c). PLL used in (b)

Usually, the negative 1st order sequence harmonic $\bar{I}_{cn1}^c = I_{cn1} \exp\{j(-\theta_c + 2\theta_r + \frac{\pi}{2})\}$ with $\theta_c = \omega_c t$ is selected from the measured stator current.

An observer with synchronous low-pass filter (LPF) in carrier reference (Fig. 2.7b) was used to select the \bar{I}_{cn1}^c harmonic. A phase-locked loop (PLL) tracking observer shown in Fig. 2.7c extracts the estimation of rotor speed $\hat{\omega}_r$ and position $\hat{\theta}_r$ from the phase of \bar{I}_{cn1}^c harmonic in carrier reference, with PLL error $\varepsilon \approx 2I_{cn1}(\theta_r - \hat{\theta}_r)$.

For medium and high-speed operation above 50 rpm, the signal injection is disabled to reduce losses, and thus the associated speed and position observer from is also inhibited. Now, new speed estimation is required with a smooth transition between the two of them. A solution is to estimate the rotor speed $\hat{\omega}_r$ from the estimated stator flux vector $\hat{\psi}_s$:

$$\hat{\omega}_r = \hat{\omega}_{\psi_s} + \frac{d\hat{\theta}_{\psi_{dq}}}{dt}; \quad \hat{\omega}_{\psi_s} = \frac{d\hat{\theta}_{\psi_s}}{dt} \quad (2.18)$$

where $\hat{\omega}_{\psi_s}$ and $\hat{\theta}_{\psi_s}$ are the estimated speed and position of $\hat{\psi}_s$ in $\alpha\beta$ - stator reference, which is given by any of the two models of stator flux observer in Fig. 2.4-Fig. 2.5 (parallel or serial); $\hat{\theta}_{\psi_{dq}}$ is the estimated position of $\hat{\psi}_s$ in dq -rotor reference.

The first main component of the rotor speed in (2.18), i.e., $\hat{\omega}_{\psi_s}$ is extracted together with $\hat{\theta}_{\psi_s}$ from the $\hat{\psi}_s$ phase using a phase-locked loop (PLL) similarly as in Fig. 2.8.

The second component, living only in transient regimes, is obtained from the electric torque expression that can be derived as:

$$\hat{T}_e = \frac{3}{2} p_1 \frac{\hat{\psi}_s \psi_{PMq}}{L_q} \cos \hat{\theta}_{\psi_{dq}} + \frac{3}{2} p_1 \frac{\hat{\psi}_s^2}{2} \left(\frac{1}{L_q} - \frac{1}{L_d} \right) \sin 2\hat{\theta}_{\psi_{dq}} \quad (2.19)$$

The solution for the position/speed estimation proposed in this chapter is based on the active flux observer presented in the above paragraph, from which the active flux vector in *stator reference* is provided. As this vector has the d -axis

orientation, the electrical rotor position and speed simply yields by using the PLL illustrated in Fig. 2.8.

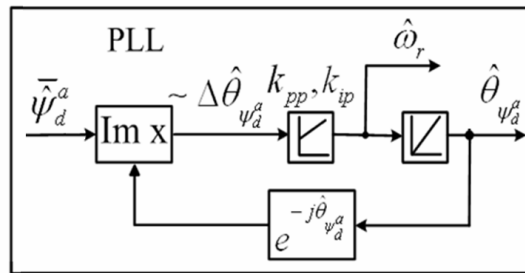


Fig. 2.8. Position/speed PLL estimator based on the active flux vector for PMSM

The parameters of the position/ speed PLL estimator in Fig. 2.8 are:
 $k_{p_PLL} = 50$; $k_{i_PLL} = 100$.

The above presented solutions (the one which employs the signal injection at low speeds and the stator flux speed at medium-high speeds and the proposed one based on active flux concept) were both tested in Matlab/Simulink in order to compare them. The digital simulation results will be presented in paragraph 2.4.4.

2.4.3. Flux and Torque Referencers

To ensure the flux weakening operation above base speed, the $\psi_{s\max}^*(\omega_r)$ envelope is employed:

$$\begin{aligned} \psi_{s\max}^*(\omega_r) &= K_{MG} \frac{V_{sb}}{\omega_b} = V_{s0}; & \text{for } \omega_r < \omega_b \\ \psi_{s\max}^*(\omega_r) &= V_{s0} \frac{\omega_r}{\omega_b}; & \text{for } \omega_r \geq \omega_b \end{aligned} \quad (2.20)$$

Thus, taking account of (2.15), for the active flux referencer, the bellow relation is used:

$$\psi_{d\max}^{\theta*}(\omega_r) = \sqrt{(\psi_{s\max}^*(\omega_r))^2 + (L_q i_s)^2} \quad (2.21)$$

Finally, making use of (2.1), the torque referencer yields as:

$$T_{e\max}^*(\omega_r) = \frac{3}{2} p_1 \psi_{d\max}^{\theta*}(\omega_r) i_{q\max} \quad (2.22)$$

2.4.4. Digital Simulation Results

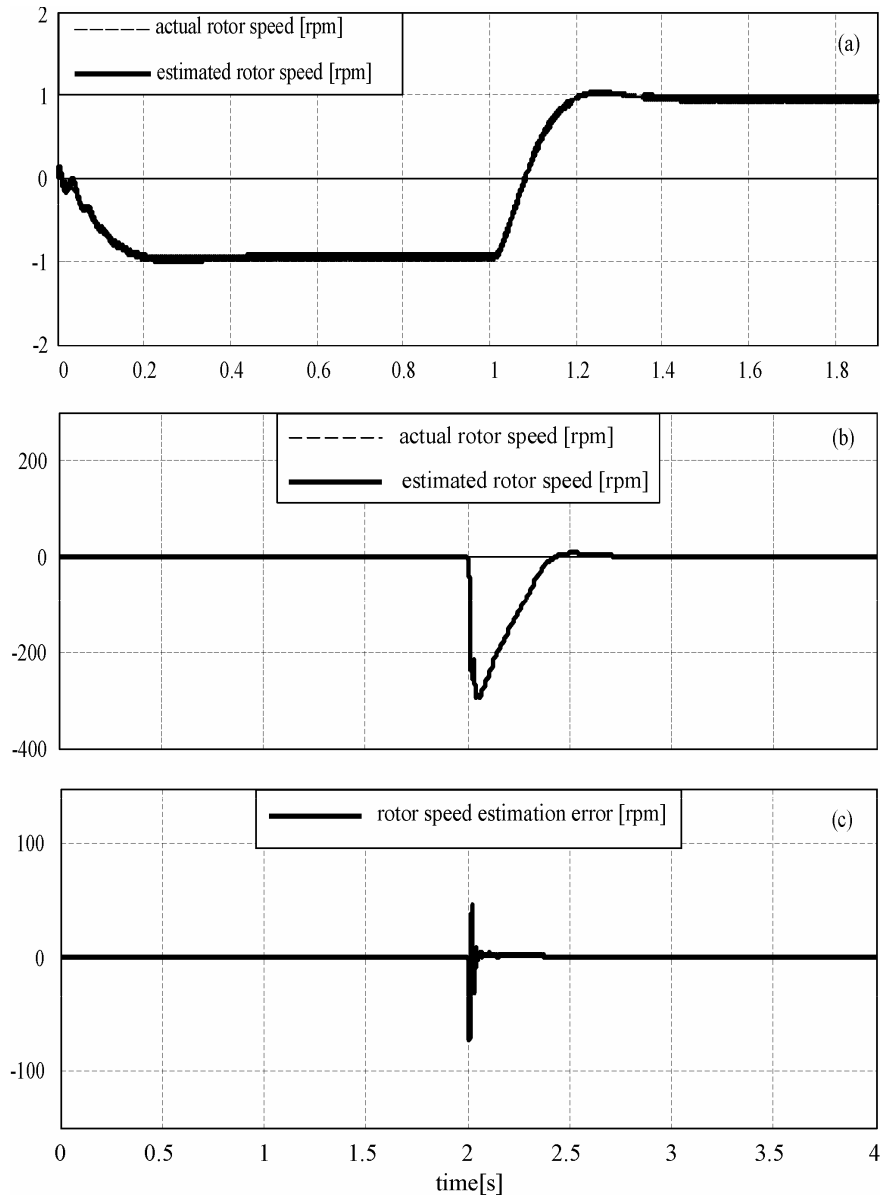
Comprehensive digital simulations have been run to compare the speed response to severe torque perturbations in a wide speed range: from 1 rpm to 4000 rpm. For comparison, rotor position and speed estimations from signal injection at very low speeds are also implemented.

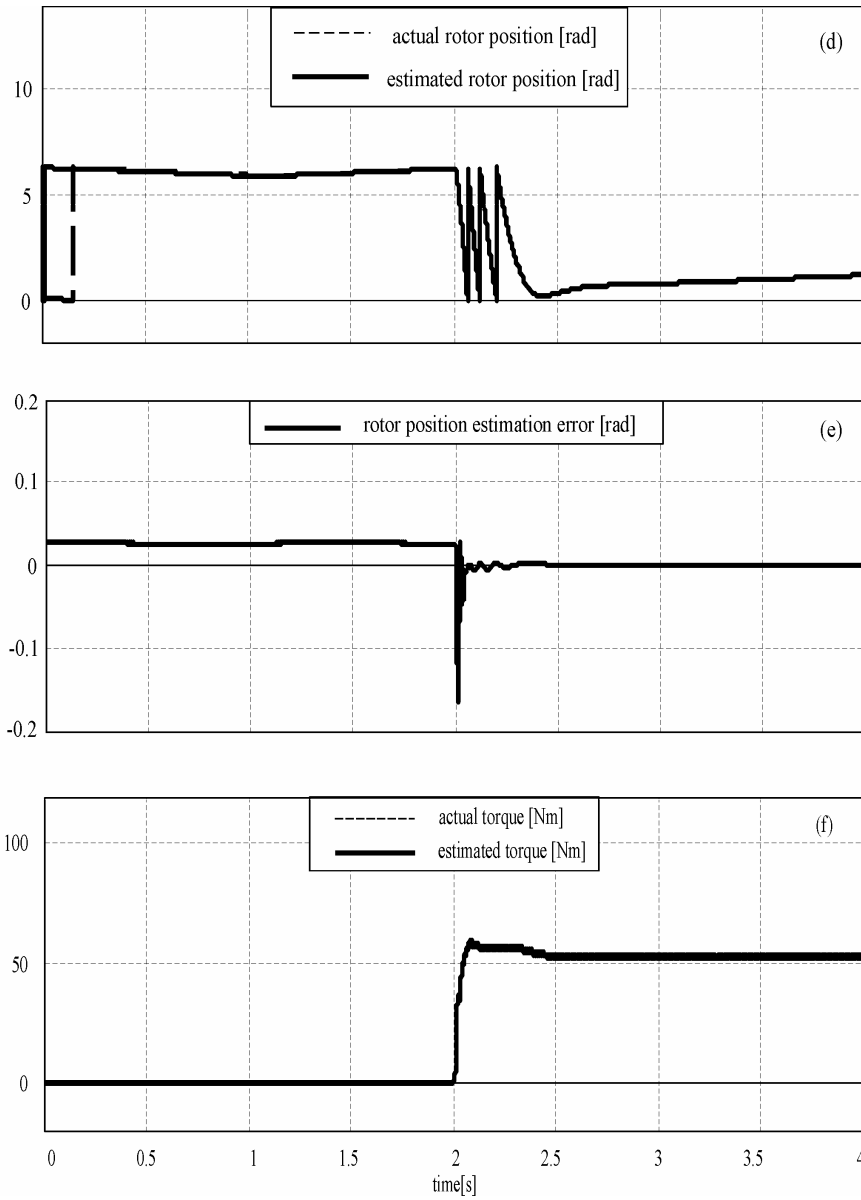
Fig. 2.9 shows speed reversal at very low speeds from -1 rpm to +1 rpm, followed by full-step load transients. It is evident that the speed response, speed, and rotor position estimations at 1 rpm are very good with the active flux observer. For the same heavy 100% torque-step transient, by using the stator-flux speed ($\hat{\omega}_{\psi_s}$) only, or the rotor speed ($\hat{\omega}_r$) from the signal injection method, (instead of rotor speed estimation) the responses (not shown) have been unstable.

Fig. 2.9a shows the actual and estimated rotor speed given by the active-flux observer during a ± 1 rpm speed reversal. It is very clear that the active-flux observer provides good estimation even at this very low speed, using the rotor-position estimation feedback to the current model in the stator flux observer.

The apparent curves overlapping in Fig. 2.9 is partly due to the large scale, but also due to the very good estimation with the same machine parameters as in the dq model.

At $t = 2$ s, the 100% step-torque transient at 1 rpm reveals the actual rotor speed and position, and their errors are very small, indeed (Fig. 2.9b-e). The estimated torque and stator flux from the active-flux observer and their actual values around 1 rpm in Fig. 2.9f-g show very good agreement.





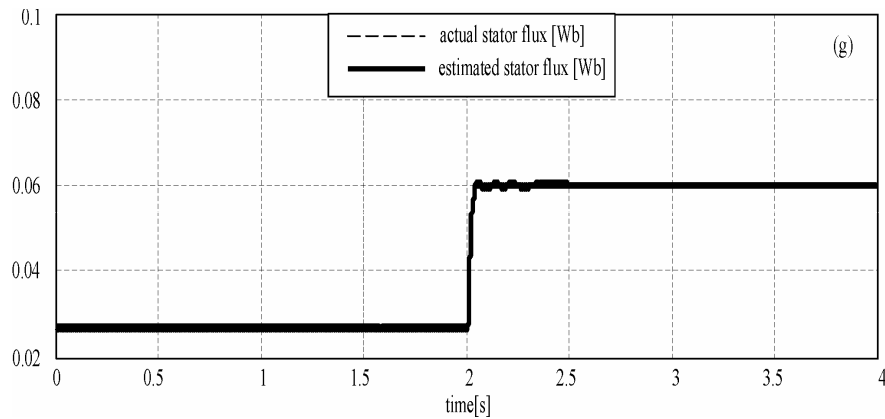


Fig. 2.9. IPMSM speed reversal of ∓ 1 rpm with full-step load at 2 s in sensorless active-flux control: a) zoom of the actual rotor speed and estimated rotor speed (overlapped) to accentuate the start-up and speed reversal, b) actual rotor speed and estimated rotor speed (overlapped), c) rotor speed estimation error, d) actual rotor position and estimated rotor position (overlapped), e) rotor position estimation error, f) actual torque and estimated torque (overlapped), and g) actual stator flux and estimated stator flux (overlapped)

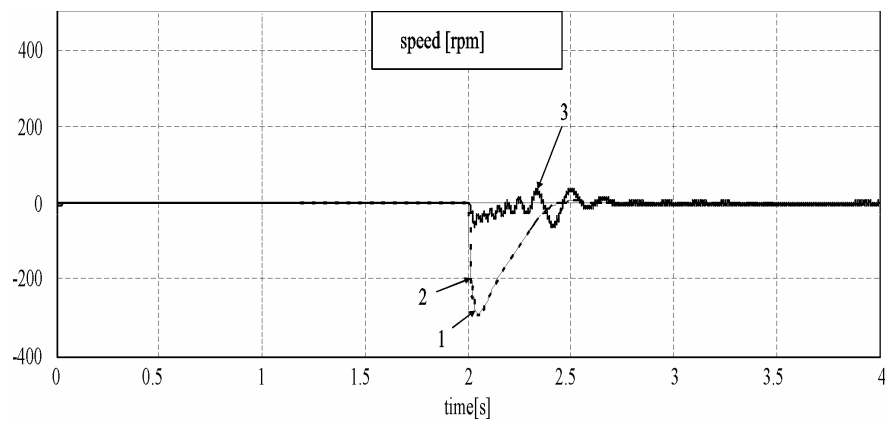


Fig. 2.10. IPMSM speed reversal of ∓ 1 rpm with full-step load in sensorless control: (1) actual rotor speed, (2) estimated rotor speed from active flux (overlapped), and (3) estimated rotor speed from signal injection.

Fig. 2.10 contains all the rotor speed values: actual, estimated from active-flux observer, and from signal injection. Again, the rotor-speed transient from the active-flux observer (curve 2) is notably superior to the speed from the signal injection (curve 3).

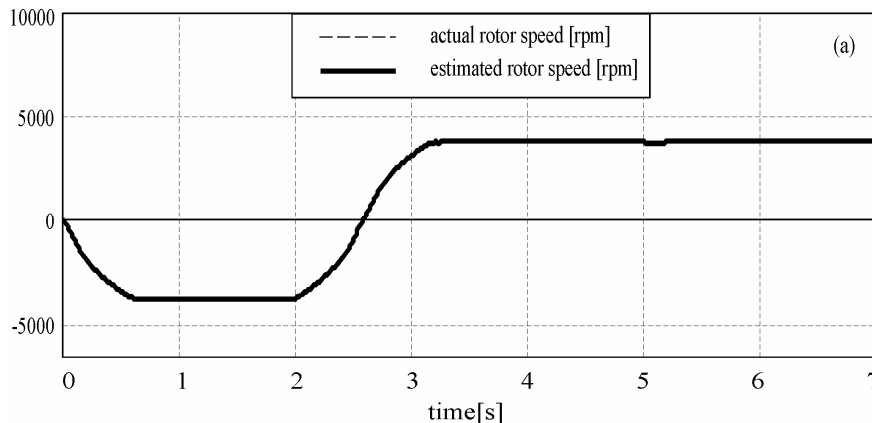
Fig. 2.11 shows high-speed transients: start-up to -4000 and speed reversal from -4000 rpm to +4000 rpm, followed by a 33% step torque perturbation.

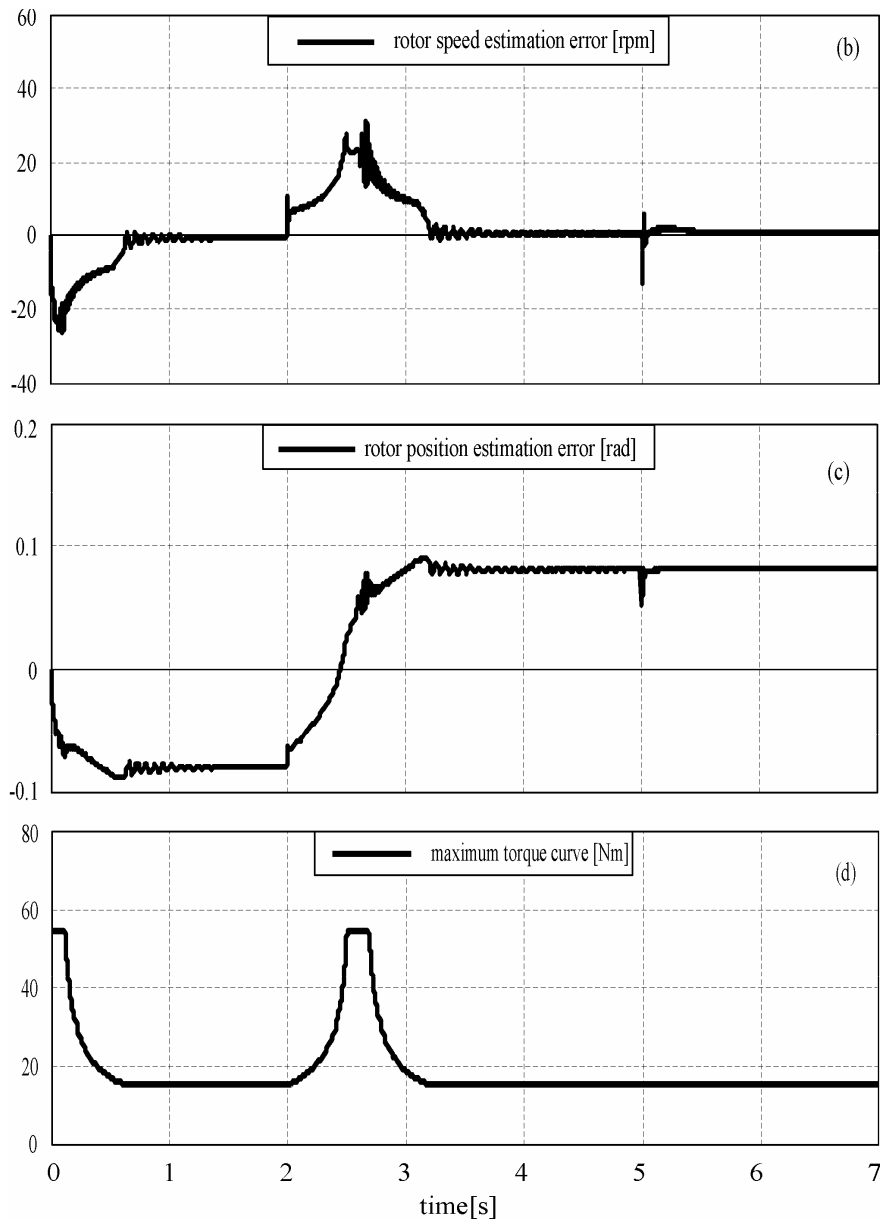
Fig. 2.11a-c illustrate the transients of the actual and estimated rotor speed and position and their estimation errors that are reasonably low. The ∓ 4000 rpm speed reversal with the 33% step-torque applied at $t = 5$ s shows the maximum speed dynamic error to be below 30 rpm, while for steady state, the speed error is less than 1 rpm.

Fig. 2.11d shows the maximum torque available versus speed (time) to illustrate that the ∓ 4000 rpm transient was torque-limited by speed, and due to voltage limitations.

Fig. 2.11e shows that the active-flux observer provides for very good torque estimation (curves are overlapped), from 0 to 4000 rpm.

Fig. 2.11f-g show the maximum reference, and the actual and estimated stator flux illustrating good performance with torque disturbance from -4000 rpm to 4000 rpm. Flux weakening is evident in Fig. 2.11g, where the stator flux achieves the permanent magnet flux value when voltage limitation occurs.





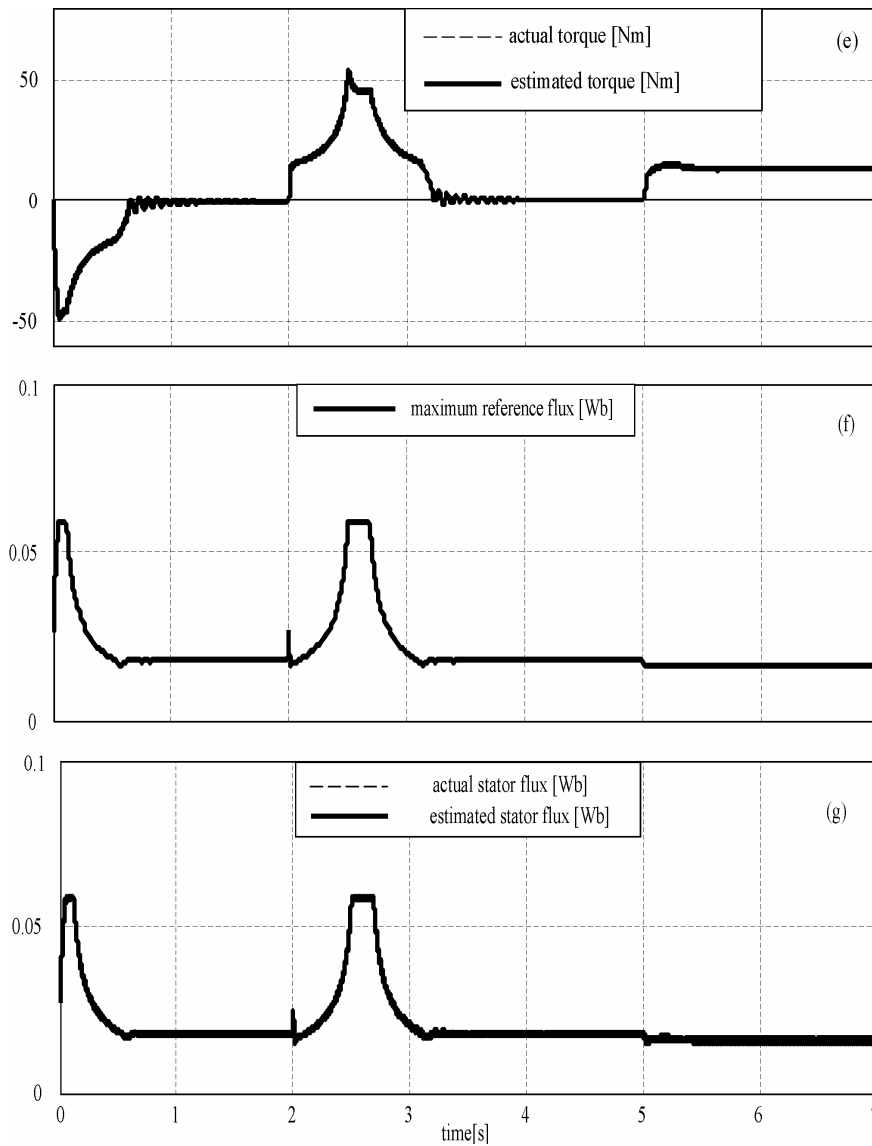
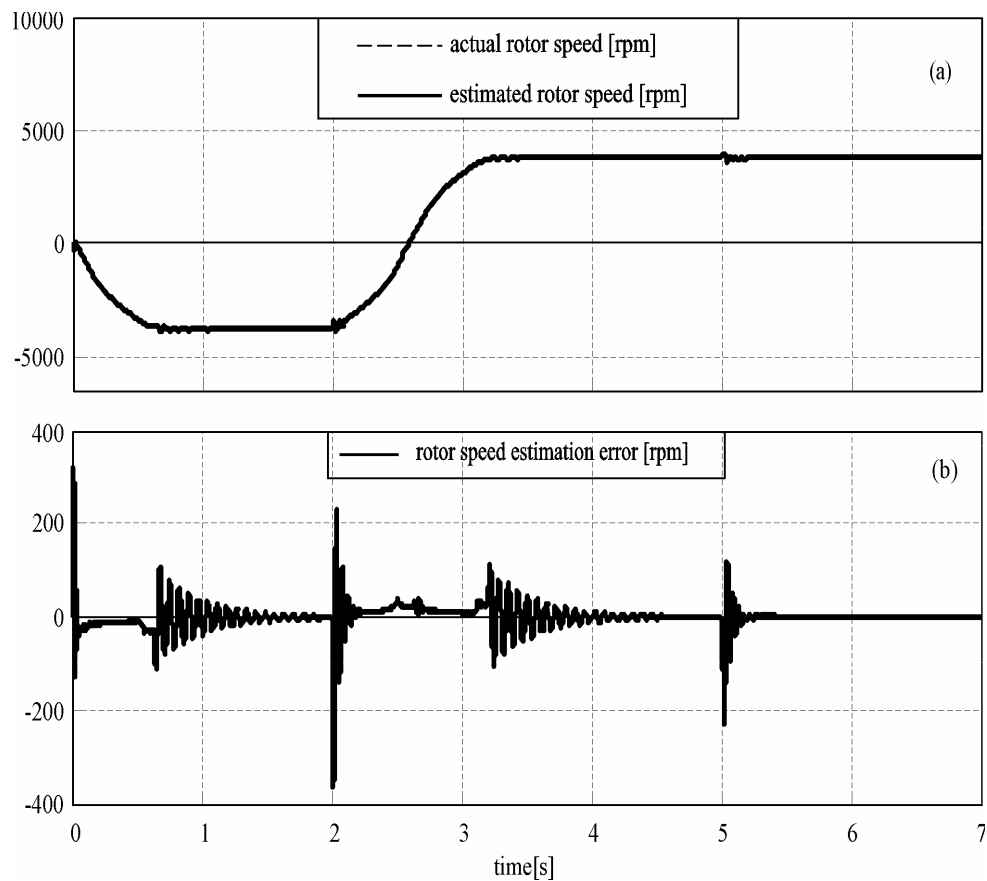


Fig. 2.11. IPMSM speed reversal of ∓ 4000 rpm with a 33 % step load in sensorless active-flux control: a) actual rotor speed and estimated rotor speed (overlapped), b) rotor speed estimation error, c) rotor position estimation error, d) maximum torque reference, e) actual torque and estimated torque (overlapped), f) maximum flux reference, and g) actual stator flux and estimated stator flux (overlapped)

Fig. 2.11a-b show actual rotor speed and its estimation using the stator-flux speed estimation in the IPMSM speed reversal of ∓ 4000 rpm. As it was expected, due to the fact that the second component in (2.17) was very precisely computed, during transients, notably larger errors are visible higher than 300 rpm.

In Fig. 2.11c-d the actual rotor position and its estimation using the stator-flux speed estimation in the IPMSM speed reversal of ∓ 4000 rpm were illustrated. In this case the rotor position estimation error is comparable with the rotor position estimation error when using the active flux speed estimation in the IPMSM control system.



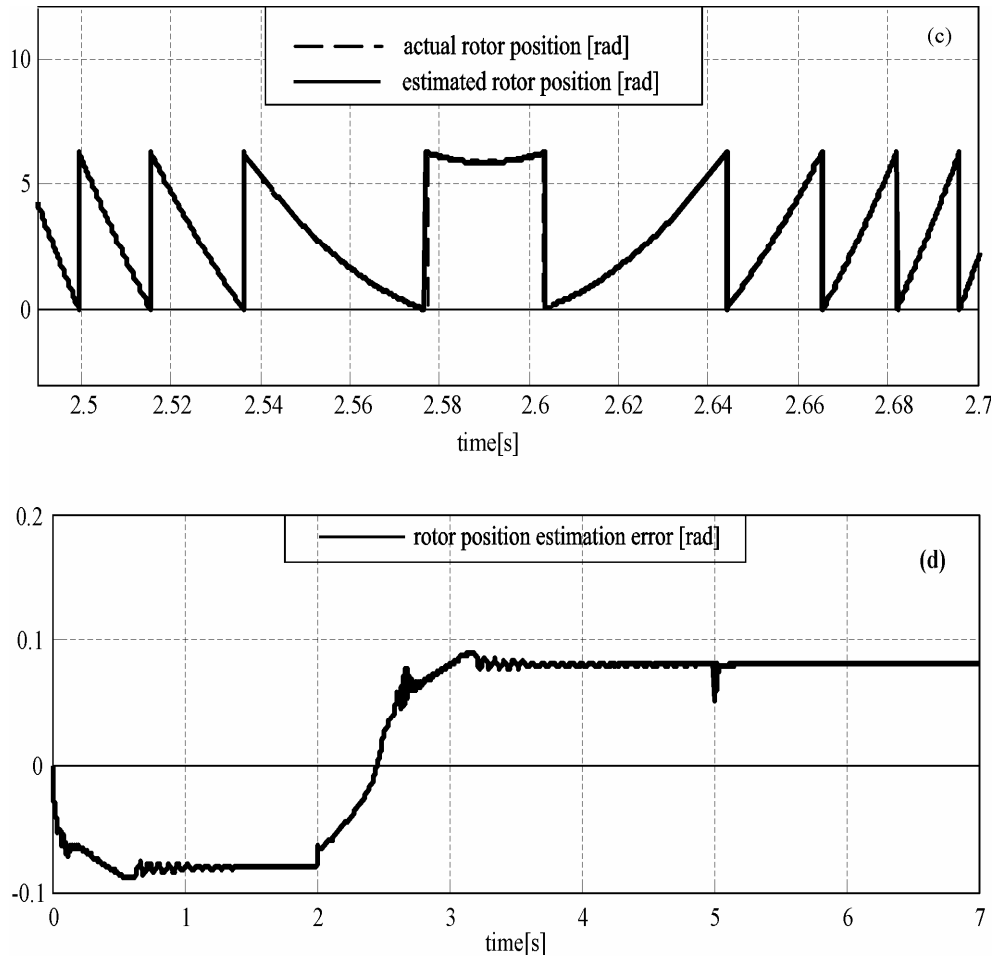


Fig. 2.12. IPMSM speed reversal of ± 4000 rpm using stator-flux speed estimation: a). actual rotor speed and estimated rotor speed from stator flux (overlapped), b). rotor speed estimation error, c). actual rotor position and estimated rotor position from stator flux (almost overlapped), and d). rotor position estimation error

In conclusion, for the IPMSM, an elaborated motion-sensorless vector control with space vector modulation (SVM) system was previously put in place and shown to operate experimentally down to 1 rpm [16]. It is based on a hybrid stator-flux observer with combined voltage and current models using a PI flux-error compensator and employs signal injection for rotor position estimation needed only in the current model at very low speed. However, it failed to respond properly at fast torque transients at very low speeds, and the speed observer, based mainly on the stator flux speed, was considered the main cause of this unfavorable behavior.

So, the actual solution presented in Fig. 2.4 starts from a proper stator flux observer section with verified results close to 1 rpm [16], but without signal injection, using the active flux observer for rotor position and speed estimation.

Note that in practice, the initial rotor position should be set to zero by using a specific voltage vector sequence to align the rotor with *a*-phase.

This initial position is mandatory in the integrator in Fig. 2.4; otherwise stator flux estimation errors may occur, which, for the very low speed performance, are critical.

The control system parameters in Fig. 2.2 with PI controller type $k_p(1 + k_i/s)$ are given in TABLE 2.2

TABLE 2.2

PI speed controller	$k_{pw}=1.1$
	$k_{iw}=12$
PI active flux controller	$k_{p\psi}=200$
	$k_{i\psi}=50$
PI current controller	$k_{pi}=1$
	$k_{ii}=200$

For this case study the IPMSM data are given in TABLE 2.3.

TABLE 2.3

Parameters of the prototype IPMSM

Rated power	6 kW
Based speed	1000 rpm
Max. speed	4000 rpm
Rated torque	51 Nm
Rated phase to phase voltage	4
Rated phase current	0.01 Ω
Stator resistance per phase (R_s)	0.01 Ω
q-axis inductance (L_q)	0.625 mH
d-axis inductance (L_d)	0.181 mH
Rotor permanent - magnet (ψ_{PM})	0.027 Vsrad ⁻¹
Inertia of the rotating system (J)	10 ⁻³ kgm ²
Viscous friction coefficient (B_m)	10 ⁻⁴ Nms/rad

2.5. Conclusion

- A rather novel (or generalization) concept - *active flux* - along the d axis was introduced. It represents the *torque-producing flux*, which renders all salient-pole traveling-field (induction and synchronous) machines into nonsalient-pole machines with $L_q(i_s)$ inductance along the q axis.
- Active-flux orientation control is shown to be applicable to all ac machines by two generic schemes with a sizable common part. For SMs, the rotor position is equal to the active-flux angle.

- Rotor position and speed estimations based on the active-flux observer are shown to be simpler than existing solutions and very similar for all ac machines, as magnetic saliency is no longer a key factor.
- The active-flux concept allows for easy self-commissioning sequences.
- The active-flux concept applies both to vector control and to DTC with active flux and torque-closed loops.
- The active-flux orientation was applied in digital simulations to a high-saliency IPMSM with very promising results — from 1 rpm to 4000 rpm — without signal injection.
- The results of the digital simulations were illustrated and discussed.
- Two stator flux observers were developed and compared. Both are based on the voltage and on the current models, but one is using them in parallel and one in series. The topologies and the results are also illustrated and discussed.

References

- [1] P. Vas, *Sensorless vector and direct torque control*, Oxford University Press, 1998.
- [2] I. Takahashi and T. Noguchi, "A new quick-response and high-efficiency control strategy of an induction motor," in *Conf. Record IEEE-IAS 1985 Annual Meeting*, pp. 496–502.
- [3] M. Depenbrock, "Direct self-control (DSC) of inverter-fed induction machine," *IEEE Trans. Power Electronics*, vol. 3, no. 4, pp. 420–429, 1988.
- [4] I. Boldea and S. A. Nasar, "Torque vector control (TVC) – a class of fast and robust torque-speed and position digital controllers for electric drives," *Electric Machines and Power Systems*, vol. 15, no. 3, pp. 135–148, 1988.

- [5] Z. Xu, and M. F. Rahman, "Direct torque and flux regulation of an IPM synchronous motor drive using variable structure control approach," *IEEE Trans. Power Electronics*, vol. 22, no. 6, pp. 2487–2498, November 2007.
- [6] G. S. Buja, and M. P. Kazmierkowski, "Direct torque control of PWM inverter-fed ac motors—a survey," *IEEE Trans. Industrial Electronics*, vol. 51, no. 4, pp. 744–757, August 2004.
- [7] M. F. Rahman, M. E. Haque, L. Tang, R. Zhang, "Problems associated with direct torque control of IPM synchronous motor drive and their remedies " , *IEEE Trans*, vol.IE-51, no.4,2004, pp. 799-809.
- [8] Holtz and H. Pan, "Elimination of saturation effects in sensorless position-controlled induction motors," *IEEE Trans. Industry Application*, vol. 40, no. 2, pp. 623–631, 2004.
- [9] S. Shinnaka, "New 'mirror-phase vector control' for sensorless drive of permanent-magnet synchronous motor with pole saliency," *IEEE Trans. Industry Applications*, vol. 40, no. 2, pp. 599–606, March-April 2004.
- [10] P. Guglielmi, M. Pastorelli, G. Pellegrino, and A. Vagati, "Position-sensorless control of permanent-magnet-assisted synchronous reluctance motor," *IEEE Trans. Industry Applications*, vol. 40, no. 2, pp. 615–622, March-April 2004.
- [11] C. Lascu, I. Boldea, and F. Blaabjerg, "Direct torque control of sensorless induction motor drives: a sliding-mode approach," *IEEE Trans. Industry Applications*, vol. 40, no. 2, pp. 582–590, March-April 2004.
- [12] G.-D. Andreescu and I. Boldea, "Integrated sensors of rotor position and speed based on signal injection for IPM-synchronous motor drives," in *Proc. International Conf. on Intelligent Engineering Systems IEEE-INES 2004*, Cluj-Napoca, Romania, pp. 317–375.
- [13] H. Kim, K. K. Huh, M. Harke, J. Wai, R. D. Lorenz, and T. A. Jahns, "Initial rotor position estimation for an integrated starter alternator IPM synchronous machine," in *Proc. 10th European Conf. on Power Electronics and Applications EPE-2003*, Toulouse, France, pp. 1875–1881.
- [14] M. Linke, R. Kennel, and J. Holtz, "Sensorless speed and position control of synchronous machines using alternating carrier injection," in *Proc. IEEE*

- International Electric Machines and Drives Conf. IEMDC'03, Madison, WI, USA, vol. 2, pp. 1211–1217.
- [15] M. W. Degner and R. D. Lorenz, "Using multiple saliencies for the estimation of flux, position, and velocity in AC machines," *IEEE Trans. Industry Applications*, vol. 34, no. 5, pp. 1097–1104, Sept./Oct. 1998.
- [16] C. I. Pitic, G.-D. Andreescu, F. Blaabjerg, and I. Boldea, "IPMSM motion-sensorless direct torque and flux control," in *Proc. 31st Annual Conf. of IEEE Industrial Electronics Society IECON 2005*, Raleigh, NC, USA, pp. 1756–1761.
- [17] Andreescu, G.-D., Pitic, C.I., Blaabjerg, F., and Boldea, I.: "Combined flux observer with signal injection enhancement for wide speed range sensorless DTFC of IPMSM drives," *IEEE Trans. Energy Convers.*, 2008, 23, (2), pp. 393–402.
- [18] P. Garcia, F. Briz, D. Raca, and R. D. Lorenz, "Saliency tracking-based sensorless control of AC machines using structured neural networks," *IEEE Trans. Industry Applications*, vol. 43, no. 1, pp. 77–86, Jan./Feb. 2007.
- [19] F. Briz, A. Diez and M. W. Degner , "Dynamic operation of carrier-signal-injection-based sensorless direct field-oriented ac drives ," *IEEE Trans. Industry Applications*, vol. 36, no. 5, pp. 1360–1368, September-October. 2000.
- [20] H. Kim, K.-K. Huh, Robert D. Lorenz and T. M. Jahns, "A novel method for initial rotor position estimation for IPM synchronous machine drives," *IEEE Trans. Industry Applications*, vol. 40, no. 5, pp. 1369–1378, September-October. 2004.
- [21] Y. Jeong, R. D. Lorenz, T.M. Jahns, S. Sul, " Initial rotor position estimation of an IPM motor " , *Record of IEEE-IEMDC-2003*, pp. 1218-1223.
- [22] J. Holtz and J. Quan, "Sensorless vector control of induction motors at very low speed using a nonlinear inverter model and parameter identification," *IEEE Trans. Industry Applications*, vol. 38, no. 4, pp. 1087–1095, July-Aug. 2002.
- [23] N. Bianchi and S. Bolognani, "Influence of rotor geometry of an IPM motor on sensorless control feasibility, " *IEEE Trans. Industry Applications*, vol. 43, no. 1, pp. 87–96, Jan./Feb. 2007.

- [24] W. Leonhard, *Control of Electrical Drives*, 3rd Edition, Berlin: Springer-Verlag, 2001.
- [25] I. Boldea and S. A. Nasar, *Electric Drives*, 2nd Edition, New York: CRC Press, Taylor and Francis, 2005.
- [26] D. W. Novotny and T. A. Lipo, *Vector Control and Dynamics of AC Drives*, New York: Oxford University Press, 1996.
- [27] P. Vas, *Sensorless Vector and Direct Torque Control*, New York: Oxford University Press, 1998.
- [28] M. P. Kazmierkowski, R. Krishnan, and F. Blaabjerg (Eds.), *Control in Power Electronics: Selected Problems*, Amsterdam: Academic Press, Elsevier Science, 2002, Chap. 5 & 9.
- [29] Z. Chen, M. Tomita, S. Doki, and S. Okuma, "An extended electromotive force model for sensorless control of interior permanent magnet synchronous motors," *IEEE Trans. Industrial Electronics*, vol. 50, no. 3, pp. 288–295, April 2003.
- [30] S. Morimoto, K. Kawamoto, M. Sanada, and Y. Takeda, "Sensorless control strategy for salient-pole PMSM based on extended EMF in rotating reference frame," *IEEE Trans. Industry Applications*, vol. 38, no. 4, pp. 1054–1061, July/Aug. 2002.
- [31] S. Morimoto, M. Sanada, and Y. Takeda, "Mechanical sensorless drives of IPMSM with online parameter identification," *IEEE Trans. Industry Applications*, vol. 42, no. 5, pp. 1241–1248, Sept./Oct. 2006.
- [32] S. Koonlaboon and S. Sangwongwanich, "Sensorless control of interior permanent-magnet synchronous motors based on a fictitious permanent-magnet flux model," in *Conf. Record IEEE-IAS 2005 Annual Meeting, Hong Kong*, vol. 1, pp. 311–318.
- [33] I. Boldea, M. C. Paicu and G.-D. Andreescu, "Active flux concept for motion-sensorless unified ac drives," *IEEE Trans. Power Electronics*, vol. 23, no. 5, pp. 2612–2618, Sept. 2008.

Chapter 3

“Active Flux” Sensorless Vector Control of IPMSM

Abstract

This chapter presents a novel strategy for the vector control of IPMSM drives with space vector modulation (SVM), without signal injection. First, the method is developed, implemented and then tested and described. This novel „active flux” concept was proposed before in Chapter 2. The active flux, defined as the flux that multiplies i_q current in the dq -model torque expression of all ac machines, is easily obtained from the stator flux vector and has the rotor position orientation. Therefore, notable simplification in the rotor position and speed estimation is obtained. For IPMSM, a stator flux observer is employed based on combined current and voltage models, with speed dependent smooth transition between them using a PI compensator of flux error. The overall performance of the motion-sensorless control depends strongly on the accuracy of the rotor position and speed estimation from the active flux. All the factors that may lead to inaccurate estimation in the proposed active flux such as: inverter nonlinearities, magnetic saturation and stator resistance variation are analyzed and their compensation methods are discussed and some of them proven by digital simulations. The stability of the active flux observer is also analyzed. Mainly, this chapter demonstrates, through digital simulations and experimental results, the effectiveness of the active flux observer under half full rated torque operating conditions in 2 rpm-1000 rpm speed range.

3.1. Introduction

The vector control theory is based on the pioneering work of F. Blaschke and K. Hasse [1]-[2].

In the ac control drives, adoption of motors of IPMSM type is continuously increasing.

The earliest vector control principles for ac permanent magnet synchronous machines resembled the control of a fully compensated DC machine. The idea was to control the current of the machine in space quadrature with the magnetic flux created by the permanent magnets. The torque is then directly proportional to the product of the flux linkage created by the magnets and the current. In an ac machine the rotation of the rotor demands that the flux must rotate at a certain frequency. If the current is then controlled in space quadrature with the flux, the current must be an ac current in contrast with the dc current of a dc machine.

The magnet flux lies on the d -axis and if the current is controlled in space quadrature with the magnet flux it is aligned with the q -axis. This gives a commonly used name for this type of the control, $i_d = 0$ - control.

Vector control of permanent magnet (PM) synchronous motors requires the knowledge of the rotor magnet axis position. As a rule, PM motors are equipped with a mechanical transducer, such as encoder or resolver, able to provide that information, from which the rotor speed feedback is computed by the time-derivative. The presence of the transducer involves cost, encumbrance, wiring, alignment procedures, and others tedious disadvantages. For this reason, development of a "sensorless" strategy, that means removal of the position transducer and replacement of its function by a proper detection method, is an attractive goal in many practical applications, besides being a challenging research task.

Furthermore, in the last few years the search for position sensorless control has emerged, thus involving very low or even zero speed operation [3]-[10].

The methods for sensorless position estimation can be divided into two main categories: approaches using back-electromotive-force (EMF) estimation with fundamental excitation and spatial saliency image tracking methods using excitation in addition to the fundamental. The saliency tracking methods [11]-[15] are suitable for zero-speed operation, whereas the back-EMF-based methods fail at low speed [24]-[26].

The saliency and signal injection methods estimate the rotor position based on the feature of a salient-pole PMSM such that the inductance varies depending on the rotor position. These methods suppose a high frequency voltage or current injected signal from the inverter in order to detect inductance variation. Thus, using these methods, the position can be estimated even at standstill and low-speed.

On the other hand, the fundamental excitation method although it does not need any additional signal it does not operate at zero speed. A lot of different estimation methods belong to this category. Some of them, using the Kalman filter, MRAS [23] or the INFORM method [14] allow low and zero speed operation, but are apparently too complex and expensive to be used in practical systems. Other methods extract rotor flux information from measured electrical stator voltage and stator currents. Nevertheless, it is quite critical to estimate position at low speed region, since the flux signals are contaminated by noises, stator resistance variation with temperature, dc-offset and drifting terms in the feedback currents [3], [12].

The sensorless strategy implemented in this paper belongs to this fundamental excitation method and it is based on the concept of the "active flux" (or "torque producing flux"), which "turns all the salient-pole machines into nonsalient-pole ones". Its main advantage is that the proposed sensorless technique can be applied to universal ac drives. The "active flux" concept was developed in [27] and [28].

This chapter is focused on rotor position and speed estimation of IPMSM from "active flux" observer, in order to achieve very low speed operation.

The implemented active flux based observer ensures proper motion-sensorless operation down to 2 rpm with half full rated torque, without signal injection.

Experimental results in correlation with the simulation ones demonstrate the performance of the active flux observer under steady-state and transient conditions.

3.2. Mathematical Model of the Saturated IPMSM

An inherent property of IPMSM is a significant degree of saliency. Since an interior permanent magnet synchronous motor (IPMSM) is used in this paper, the mathematical model is developed for this type of machine.

In order to reduce the complexity some assumptions are made to develop the machine model [21]. These assumptions are common in electrical machines models, and do not reduce the correctness of the model developed here because it is valid in the usual operation range of the PMSM. The assumptions are:

- the spatial stator phase winding distribution is assumed to be sinusoidal, so the mmf produced by the stator can be considered sinusoidal;
- no thermal effect for stator resistance
- and the permanent magnet flux;
- no saturation effect for inductances;
- no core losses in the machine;

With these assumptions the machine may be modeled.

The mathematical model of a saturated IPMSM in the dq synchronous reference frame is given by:

$$\bar{V}_s = R_s \cdot \bar{i}_s + \frac{d\bar{\psi}_s}{dt} + j\omega_r \cdot \bar{\psi}_s \quad (3.1)$$

$$\bar{\psi}_s = (L_d + \psi_{PMd})i_d + jL_q(i_q) \cdot i_q \quad (3.2)$$

$$T_e = \frac{3}{2} \cdot p_1 \cdot [\psi_{PMd} + (L_d - L_q(i_q)) \cdot i_d] \cdot i_q \quad (3.3)$$

where \bar{V}_s is the stator voltage, \bar{i}_s is the stator current, R_s is the stator resistance, L_d, L_q are the dq axes inductances, $\bar{\psi}_s$ is the stator flux, ψ_{PMd} is the PM flux linkage on d axis, T_e is the electromagnetic torque, ω_r is the electrical rotor speed and p_1 is the number of pole pairs.

3.3. Active Flux Concept for IPMSM

The "active flux" concept, as presented before in Chapter 2, turns all salient-pole rotor ac machines into fictitious nonsalient-pole ones such that the rotor position and speed estimation become simpler.

For IPMSM case in which axis d corresponds to the rotor pole axis, as it shown in the steady state vector diagram in Fig. 3.1, the active flux $\bar{\psi}_d^a$ has the form:

$$\psi_d^a = \psi_{PMd} + (L_d - L_q(i_q))i_d; \quad L_d < L_q(i_q) \quad (3.4)$$

with the torque expression:

$$T_e = 1.5p_1\psi_d^a i_q \quad (3.5)$$

As demonstrated in [27], $\bar{\psi}_d^a$ represents the torque producing flux and then the model of IPMSM "looses" magnetic anisotropy and manifests itself by the inductance $L_q(i_q)$ (torque current is i_q as in (3.5)):

$$\bar{V}_s = R_s \bar{i}_s + (s + j\omega_r)L_q(i_q)\bar{i}_s + (s + j\omega_r)\bar{\psi}_d^a \quad (3.6)$$

Thus, the active flux vector $\bar{\psi}_d^a$ observer, in stator coordinates, is:

$$\bar{\psi}_d^{as} = \int (\bar{V}_s - R_s \bar{i}_s + \bar{V}_{comp}) dt - L_q(i_q) \bar{i}_s \quad (3.7)$$

thus yields:

$$\bar{\psi}_d^{as} = \bar{\psi}_s - L_q(i_q) \bar{i}_s \quad (3.8)$$

The simplicity of (3.8) in any reference frame looks striking, but it is just natural. It should be noticed that if in stator frame the stator flux $\bar{\psi}_s$ is estimated, the active flux estimation is straightforward, with magnetic saturation influence present in $L_q(i_q)$, which greatly simplifies its accountancy in the model.

$\bar{\psi}_d^{as}$ axis falls along rotor axis d and thus:

$$\bar{\psi}_d^{as} = \psi_d^a \cos \theta_{\psi_d^a} + j \psi_d^a \sin \theta_{\psi_d^a} \quad (3.9)$$

Equation (3.8) leads to the estimation of both ψ_d^a amplitude and angle $\theta_{\psi_d^a}$ with respect to stator phase a ($\theta_{\psi_d^a} = \theta_{er}$ (electrical angle rotor position)) for IPMSM.

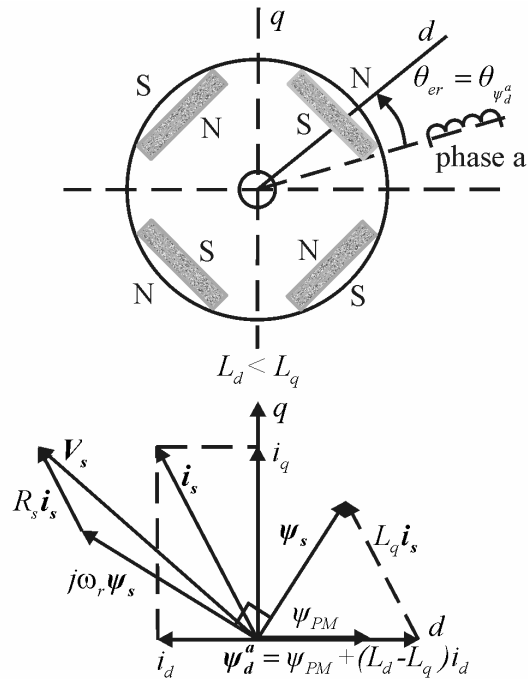


Fig. 3.1. IPMSM and its vector diagram pointing out the active flux $\bar{\psi}_d^a$

3.4. Vector Control System

Fig. 3.3 illustrates the proposed vector control system for IPMSM, which consists in space vector modulator block (SVM), vector control implementation scheme, active flux observer and rotor position-speed estimator.

The voltage source-inverter (VSI) switching signals ($S_{a,b,c}$) are generated by the space vector modulation (SVM) block, which employs the dead time and inverter nonlinearities compensations, otherwise distortions and discontinuities in the stator-voltage vector waveform occur. This compensation is indispensable for accurate active flux estimation, especially at very low speed.

The vector control system uses the voltage model in stator flux reference (3.1).

To obtain a smooth speed reference signal and to avoid the overshooting, a PT1 filter based on the following relation is implemented:

$$\frac{k_{p_PT1}}{(T_{i_PT1} \cdot s + 1)} \tag{3.10}$$

where, for our case: $k_{p_PT1} = 1$, $T_{i_PT1} = 0.025$.

The speed controller is of PI type with anti-windup and torque limiter. Its proportional gain is $k_{pW} = 0.1$ and the integral gain is $k_{iW} = 20$ (Fig. 3.2).

In the vector control scheme accurate speed control depends on how well the current vector is regulated.

Most of the reported work on control of IPMSM took an assumption of $i_d = 0$ in order to produce a maximum torque and to avoid the demagnetization of the magnet material and to use the i_q current component for torque control over speed range.

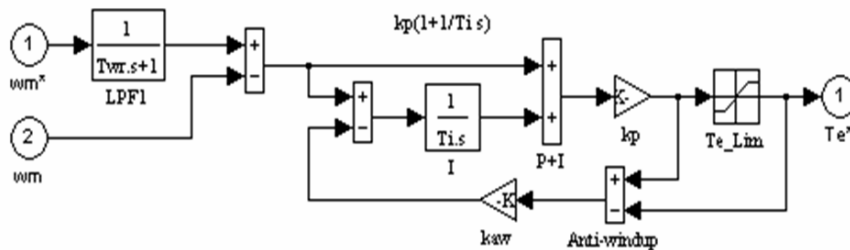


Fig. 3.2. PI anti-windup controller

The speed controller produces the reference q -axis current i_q :

The two PI current control loops have been implemented in a synchronous rotating dq reference frame having a better performance than stationary frame regulators, as they operate on dc quantities and hence can eliminate steady-state errors. They have the integral time constants proportional with electrical time constants, i.e., $1/k_i \approx L_{d,q}/R$.

The controllers are started from zero initial states, thus the scheme gives a meaningful estimate right away.

The design of the current controller employs the relation (Fig. 3.3):

$$k_p(1 + \frac{k_i}{s}) \tag{3.11}$$

The proportional and integral gains for the PI controller on the d axis are $k_{pd} = 50$, $k_{id} = 100$, respectively for the PI controller on the q axis $k_{pq} = 30$, $k_{iq} = 100$ and were chosen by trial and error.

The output voltages (V_d^* , V_q^*) are compensated (by motion emfs $V_{d_decoupling} = -\hat{\omega}_{\psi_d^a} L_q i_q^*$ and $V_{q_decoupling} = \hat{\omega}_{\psi_d^a} (L_d i_d^* + \psi_{PM})$) in order to eliminate the cross coupling between d and q axis.

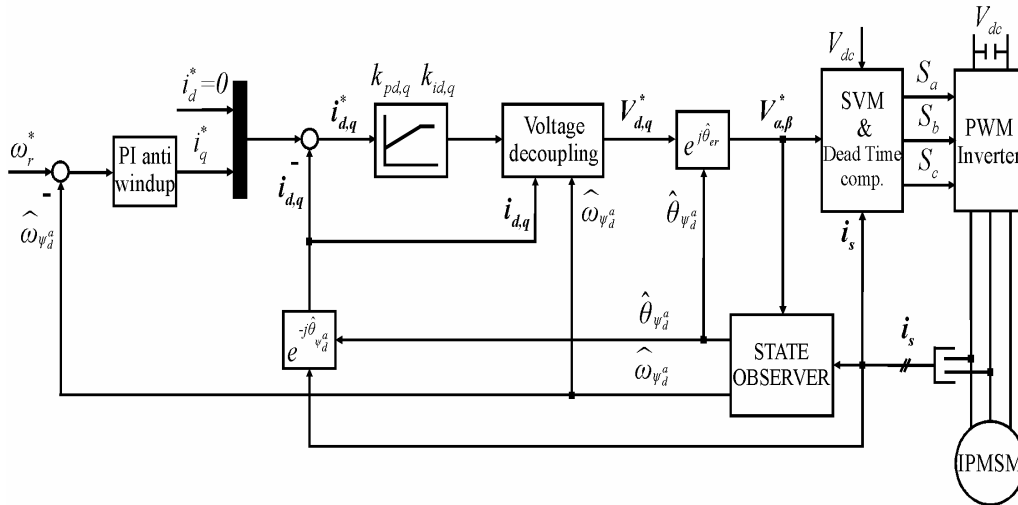


Fig. 3.3. The proposed vector control system for IPMSM

Even more, the voltage references V_d^* and V_q^* should satisfy the following limit to avoid the voltage saturation:

$$V_d^{*2} + V_q^{*2} \leq V_{\max}^2 \tag{3.12}$$

The maximum stator voltage V_{\max} is determined from the available dc link voltage V_{dc} and pulse width modulation (PWM) strategy (in our case space vector modulation (SVM)) and thus $V_{\max} = \frac{V_{dc}}{\sqrt{3}}$.

These voltages in rotor reference frame, which are in fact the outputs of the current controllers, are transformed in to stationary stator reference frame ($\alpha\beta$) using the rotor position as follows:

$$\begin{aligned} V_{\alpha}^* &= V_d^* \cos \hat{\theta}_{\psi_d^a} - V_q^* \sin \hat{\theta}_{\psi_d^a} \\ V_{\beta}^* &= V_d^* \sin \hat{\theta}_{\psi_d^a} + V_q^* \cos \hat{\theta}_{\psi_d^a} \end{aligned} \quad (3.13)$$

These stationary reference frame voltage commands are used to generate the inverter control signals.

Thus for motion- sensorless algorithm, the main block is the rotor position estimator, which makes the difference from the standard sensor-used vector control system.

In practical use, the estimated speed $\hat{\omega}_{\psi_d^a}$ is filtered through a low-pass filter to reduce the influence of noise. The filtered estimated speed is then used in the control system.

The estimated angle $\hat{\theta}_{\psi_d^a}$ was used for supplying all vector transformations between the abc and dq frames.

This completes the general description of the proposed sensorless vector control system in Fig. 3.3.

3.5. State Observers

3.5.1. The Active Flux Observer

The operating principle for this observer is to extract the active flux information from the two inputs of the stator-current (\vec{i}_s^S) and stator-voltage command in the stationary reference frame ($V_{\alpha}^*, V_{\beta}^*$). Instead of its command, the

actual voltage can be used at the cost of additional hardware. By using the implementation of the space vector modulator (SVM) including dead time and voltage drops on inverter power devices compensation, the voltage generated by the inverter system closely corresponds to the voltage command from the current regulator. The terminal-voltage measurement is, therefore, not required and the voltage command can be used successfully as voltage information. Of course, to generate precise terminal voltage according to the command, the dc link voltage information should be available and the sensing equipment for link voltage is required.

The active flux observer implementation scheme is presented in Fig. 3.4 and it consists in a stator flux observer in stator coordinates from which the term $L_q(i_q)\bar{i}_s^S$ is subtracted (3.7).

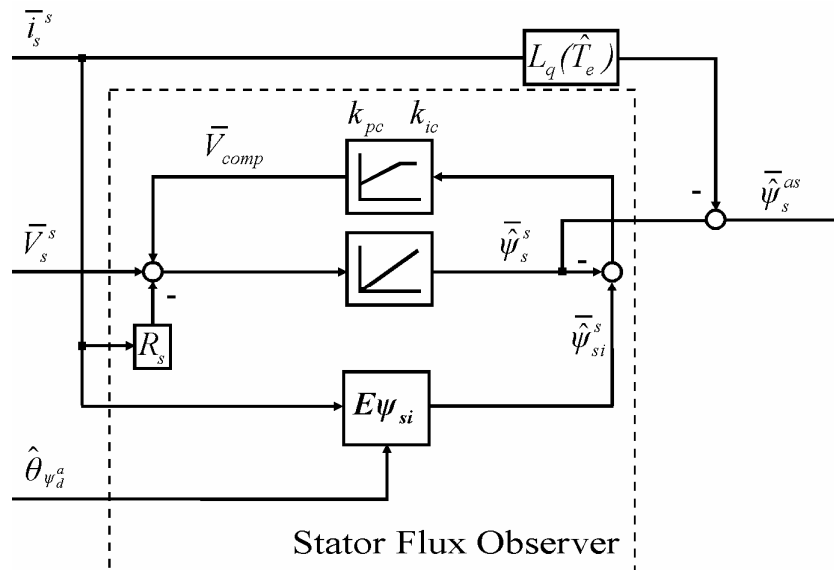


Fig. 3.4. The stator flux observer

The stator flux observer (the parallel model) combines advantages of the current model estimator in rotor reference (upper side) at low speeds with the voltage model estimator in stator reference (lower side) at medium-high speeds, using a compensation loop driven by the stator flux estimation error.

The voltage compensation employs the following equation, as it can be observed in Fig. 3.4:

$$\bar{V}_{comp} = (k_p + \frac{k_i}{s})(\bar{\psi}_{si}^s - \bar{\psi}_{su}^s) \quad (3.14)$$

The proportional and integral gains for the compensation PI term ($k_{pc} = 4, k_{ic} = 4$) may be calculated such that, at zero frequency, the current model stands alone, while at high frequency the voltage model prevails. An adequate choice of k_i and T_i is based on the given observer poles ω_1 and ω_2 :

$$k_i = -(\omega_1 + \omega_2); \quad T_i = \frac{k_i}{\omega_1 \omega_2} \quad (3.15)$$

Typical values of ω_1 and ω_2 are: $\omega_1 = -(1 \div 10) \text{ rad/s}$, $\omega_2 = (1 \div 10)|\omega_1|$.

The accuracy of active flux estimation is very limited at low speed due to noise, dc-offset and drifting terms in the feedback currents, inverter nonlinearities, magnetic saturation and stator resistance variation, which deviates from its nominal value.

The PI compensator eliminates the dc-offset and drifting terms from current measurement chains and also the error in integrator initial conditions. Also, the offset drift instability associated to pure integrators is not a problem since the corection loop compensates for it. The compensator also achieves a smooth transition depending on speed between the weight of the current model based flux estimator and the weight of the voltage model based flux estimator.

The voltage drop on the power devices of the inverter has to be subtracting from the dc link voltage when operating at low frequency (low voltage amplitude), otherwise distortion and discontinuities in the voltage waveform occur. Also the dead time compensation has to be account for.

As it was presented in literature (see Chapter 1), at low speed, the accuracy of flux and consequently of rotor position and speed depend on accurate estimation of model parameters, which vary as a function of temperature, saturation and load. In the case of a model parameter mismatch, an unstable operation occurs.

Thus, the observer is sensitive to the stator resistance error, especially at low speeds when the back electromotive force (EMF) decreases and the stator resistance voltage drop becomes significant. Thus, any small error in the stator resistance (due to the variation with the temperature) perturbs the stator flux estimation and implicitly the active flux estimation. A compensation method will be detailed in paragraph 3.5.1.4.

In the experimental tests the stator resistance value was set to $R_s = 4\Omega$ (hot temperature value) and dead time and voltage drops compensation were included, but incomplete compensation was performed due to the fact that the characteristics of power switches were not precisely known. This is highlighted by the large errors in the estimated rotor position during operation at low speed (see the paragraph from this chapter containing the experimental results).

There are methods to overcome all these drawbacks. In what follows, they are presented and some of them are tested through digital simulations. But first of all, let us prove the active flux observer stability.

3.5.1.1. Stability

The performance of a sensorless drive depends of the accuracy of its observer. If the observer is affected by cumulative errors, noise and delays then inaccurate estimations are provided. This can easily lead the drive to instability especially at low speeds.

As it was demonstrated, the active flux (Fig. 3.4) can be derived from the stator flux using (3.8). Therefore, the analysis of active flux stability reduces to the demonstration of a stable stator flux observer.

Observer design

First, the observer is desired to be model as:

$$\begin{aligned} \dot{x} &= Ax + Bu \\ y &= Cx \end{aligned} \tag{3.16}$$

where u is the $m \times 1$ input vector to the system, y is its $p \times 1$ output vector, while x is an $n \times 1$ state vector. A is an $n \times n$ matrix, while B and C are $n \times m$ and $p \times n$ matrices, respectively.

Taking into consideration (3.1), mathematically, the observer can be expressed as:

$$\frac{d}{dt} \begin{pmatrix} \hat{\psi}_{sa} \\ \hat{\psi}_{s\beta} \end{pmatrix} = \begin{pmatrix} V_{sa} \\ V_{s\beta} \end{pmatrix} - R_s \begin{pmatrix} i_{sa} \\ i_{s\beta} \end{pmatrix} + k_{pc} \begin{pmatrix} \hat{\psi}_{sai} - \hat{\psi}_{sa} \\ \hat{\psi}_{s\beta i} - \hat{\psi}_{s\beta} \end{pmatrix} + \begin{pmatrix} x_{11} \\ x_{12} \end{pmatrix} \quad (3.17)$$

$$\frac{d}{dt} \begin{pmatrix} x_{11} \\ x_{12} \end{pmatrix} = k_{ic} \begin{pmatrix} \hat{\psi}_{sai} - \hat{\psi}_{sa} \\ \hat{\psi}_{s\beta i} - \hat{\psi}_{s\beta} \end{pmatrix} \quad (3.18)$$

where $\begin{pmatrix} x_{11} \\ x_{12} \end{pmatrix}$ is another state vector used to model the PI compensator. Thus, the

system is one of fourth order:

$$\begin{aligned} \frac{d}{dt} \begin{pmatrix} \hat{\psi}_{sa} \\ \hat{\psi}_{s\beta} \\ x_{11} \\ x_{12} \end{pmatrix} &= - \begin{pmatrix} k_{pc} & 0 & -1 & 0 \\ 0 & k_{pc} & 0 & -1 \\ k_{ic} & 0 & 0 & 0 \\ 0 & k_{ic} & 0 & 0 \end{pmatrix} \begin{pmatrix} \hat{\psi}_{sa} \\ \hat{\psi}_{s\beta} \\ x_{11} \\ x_{12} \end{pmatrix} + \begin{pmatrix} k_{pc} & 0 \\ 0 & k_{pc} \\ k_{ic} & 0 \\ 0 & k_{ic} \end{pmatrix} \begin{pmatrix} \hat{\psi}_{sai} \\ \hat{\psi}_{s\beta i} \end{pmatrix} \\ &+ \begin{pmatrix} 1 & 0 \\ 0 & 1 \end{pmatrix} \begin{pmatrix} V_{sa} \\ V_{s\beta} \end{pmatrix} - \begin{pmatrix} R_s & 0 \\ 0 & R_s \end{pmatrix} \begin{pmatrix} i_{sa} \\ i_{s\beta} \end{pmatrix} \end{aligned} \quad (3.19)$$

Also, the relation between the estimated stator flux vector, in stator coordinates, from the current model and the stator current vector can be modeled as:

$$\begin{pmatrix} \hat{\psi}_{sai} \\ \hat{\psi}_{s\beta i} \end{pmatrix} = \begin{pmatrix} \cos \hat{\theta} & \sin \hat{\theta} \\ -\sin \hat{\theta} & \cos \hat{\theta} \end{pmatrix} \begin{pmatrix} L_d & 0 \\ 0 & L_q \end{pmatrix} \begin{pmatrix} \cos \hat{\theta} & -\sin \hat{\theta} \\ \sin \hat{\theta} & \cos \hat{\theta} \end{pmatrix} \begin{pmatrix} i_{sa} \\ i_{s\beta} \end{pmatrix} - \psi_{PM} \begin{pmatrix} \cos \hat{\theta} \\ -\sin \hat{\theta} \end{pmatrix} \quad (3.20)$$

In the Lyapunov stability analysis it is assumed that there is no input in the system, hence in general:

$$\dot{x} = Ax \quad (3.21)$$

Consequently, combining (3.19) and (3.20) and assuming orientation and accurate machine parameters, yields:

$$\dot{X} = \frac{d}{dt} \begin{pmatrix} \hat{\psi}_{sa} \\ \hat{\psi}_{s\beta} \end{pmatrix} = -CAC^T \begin{pmatrix} \hat{\psi}_{sa} \\ \hat{\psi}_{s\beta} \end{pmatrix} = -CAC^T X \quad (3.22)$$

$$Y = \begin{pmatrix} \hat{\psi}_{sa} \\ \hat{\psi}_{s\beta} \\ x_{11} \\ x_{12} \end{pmatrix} = C^T \begin{pmatrix} \hat{\psi}_{sa} \\ \hat{\psi}_{s\beta} \end{pmatrix} = C^T X$$

where:

$$A = \begin{pmatrix} k_{pc} & 0 & -1 & 0 \\ 0 & k_{pc} & 0 & -1 \\ k_{ic} & 0 & 0 & 0 \\ 0 & k_{ic} & 0 & 0 \end{pmatrix} \quad \text{and} \quad C = \begin{pmatrix} 1 & 0 & 0 & 0 \\ 0 & 1 & 0 & 0 \end{pmatrix} \quad (3.23)$$

Also C^T is the transpose matrix of C.

Furthermore, the state error dynamics are:

$$\frac{d}{dt} \begin{pmatrix} \tilde{\psi}_{sa} \\ \tilde{\psi}_{s\beta} \end{pmatrix} = -CAC^T \begin{pmatrix} \tilde{\psi}_{sa} \\ \tilde{\psi}_{s\beta} \end{pmatrix} \Leftrightarrow \dot{\tilde{X}} = -CAC^T \tilde{X} \quad (3.24)$$

Lyapunov's stability

Lyapunov's **theorem** says [29]:

Let $V(x)$ be a continuously differentiable definitely positive function of the system states $x(t)$ on a neighborhood of the equilibrium point. This function may also be time-varying.

- (a) If its time derivative $\dot{V}(x)$ is semi-definitely negative, then this equilibrium point is stable in the sense of Lyapunov
- (b) If $\dot{V}(x)$ is definitely negative, then this point is asymptotically stable in the sense of Lyapunov. (Such $V(x)$ is called the Lyapunov function).

Note that „ $V(x)$ is definitely positive” means $V(0) = 0$ and $V(x) > 0$ for $x \neq 0$.

Let us now apply the Lyapunov's theorem to our observer system.

First, let the candidate positive definite Lyapunov function be:

$$V = \frac{1}{2} \tilde{X}^T \tilde{X} > 0 \quad (3.25)$$

where $\tilde{X}^T = (\tilde{\psi}_{sa} \quad \tilde{\psi}_{s\beta})^T$.

Then, the time derivative of (3.25) is given by:

$$\dot{V} = \tilde{X}^T \dot{\tilde{X}} = -\tilde{X}^T CAC^T \tilde{X} \quad (3.26)$$

Using (3.23), $CAC^T = k_{pc} \begin{pmatrix} 1 & 0 \\ 0 & 1 \end{pmatrix}$. Thus, for any $k_{pc} > 0$, CAC^T is definitely positive, then \dot{V} is definitely negative, and the system is asymptotically stable in the sense of Lyapunov.

The gains k_{pc} and k_{ic} in matrix A can be carefully selected via the pole placement method. For our case, $k_{pc} = 4$ and $k_{ic} = 4$.

3.5.1.2. Inverter Nonlinearities

Additional problems arise when the voltage at the machine terminals differs from its commanded value. The most important sources of voltage distortion are: the inverter dead time and the voltage power devices drops during the on state.

Dead-time compensation

The implementation of dead-time nonlinearities in a sensorless drive is mandatory [17].

Let us define the total time error resulting from dead time, turn-on and turn-off times:

$$T_{\Delta} = T_d + T_{on} - T_{off} \quad (3.27)$$

where T_d is the dead time, which guarantees that both power devices in an inverter leg never conduct simultaneously, T_{on} is the power devices turn-on delay time and T_{off} is the power devices turn-off delay time.

If T_{Δ} modifies, the duty cycle D_a will be modified with $\Delta = T_{\Delta}/T_s$, where T_s is the sampling time period. Thus, for all three phases, the real duty cycles are:

$$\begin{aligned} D_a &= D_a^* - \Delta \operatorname{sgn}(i_a) \\ D_b &= D_b^* - \Delta \operatorname{sgn}(i_b) \\ D_c &= D_c^* - \Delta \operatorname{sgn}(i_c) \end{aligned} \quad (3.28)$$

where the superscript „*“ denotes reference values.

The voltage vector produced by inverter can be determined as:

$$\vec{V}_{sdt}^* = \vec{V}_s^* - \vec{V}_{\Delta} \quad (3.29)$$

where \vec{V}_{sdt}^* is the output voltage vector required by the control algorithm, \vec{V}_s^* is the reference voltage vector.

The voltage error vector \bar{v}_Δ is defined as:

$$\begin{aligned}\bar{v}_\Delta &= V_{\Delta\alpha} + jV_{\Delta\beta} \\ v_{\Delta\alpha} &= V_{dc}\Delta(\text{sgn}(i_a) - \frac{1}{3}(\text{sgn}(i_a) + \text{sgn}(i_b) + \text{sgn}(i_c))) \\ v_{\Delta\alpha} &= V_{dc}\Delta \frac{1}{\sqrt{3}}(\text{sgn}(i_b) - \text{sgn}(i_c))\end{aligned}\quad (3.30)$$

The dead time compensation is already included in the SVM used in all control implementations on the dSpace platform.

Power devices voltage drops compensation

Also, the threshold voltages of the power semiconductor devices introduce another disturbance which is also nonlinear [18]. It becomes significant at low amplitudes of the stator voltage, i.e. at low speed.

Thus, the voltage contribution of only one phase (the phase-to-N voltage), taking into account the voltage drop is described by:

$$\begin{aligned}v_{an} &= D_a V_{dc} - D_a v_T - (1 - D_a) v_D & \text{if } i_a > 0 \\ v_{an} &= D_a V_{dc} - D_a v_D - (1 - D_a) v_T & \text{if } i_a < 0\end{aligned}\quad (3.31)$$

where v_T and v_D are the voltage drops across the transistor and the diode, respectively:

$$v_T = v_{T0} + r_T \cdot |i_a| \quad (3.32)$$

$$v_D = v_{D0} + r_D \cdot |i_a| \quad (3.33)$$

here v_{T0} and v_{D0} are the threshold voltages and r_T and r_D are the drain-to-source resistance and diode resistance during on-state, respectively.

Combining (3.31), (3.32) and (3.33) yields:

$$v_{an} = D_a V_{dc} - (D_a - 1/2)(v_D - v_T) - \text{sgn}(i_a)(v_D + v_T)/2 \quad (3.34)$$

Assuming that the transistor and diode have almost identical voltage drop, i.e., $v_T \cong v_D$, the second term in (3.34) may be neglected and thus:

$$v_{an} = D_a V_{dc} - \text{sgn}(i_a)(v_D + v_T)/2 \quad (3.35)$$

Taking account for (3.32) and (3.33), the inverter phase a voltage becomes:

$$v_{an} = D_a V_{dc} - \text{sgn}(i_a)(v_{D0} + v_{T0})/2 - i_a (r_D + r_T)/2 \quad (3.36)$$

As it can be observed, the term $(r_D + r_T)/2$ acts as a load resistance which can be compensated by adding it to the real stator resistance R_S .

Consequently, the voltage drop on the phase a is given by:

$$v_{tha} = \text{sgn}(i_a)(v_{D0} + v_{T0})/2 + i_a (r_D + r_T)/2 \quad (3.37)$$

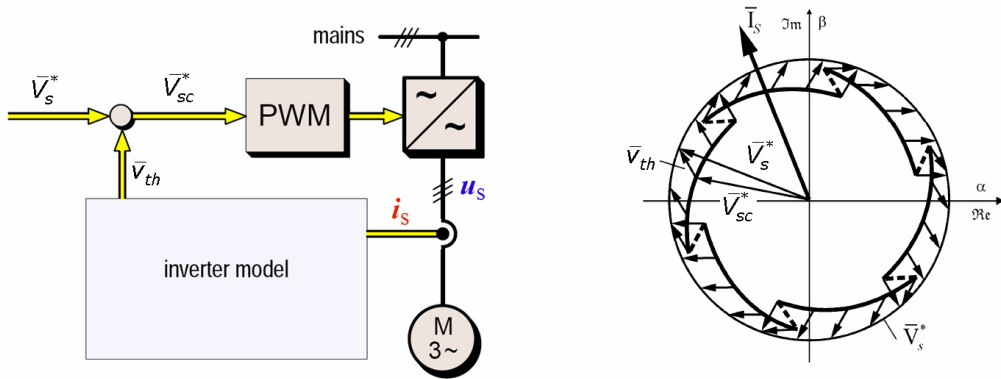


Fig. 3.5. The stator voltage command including the voltage drops on inverter power devices

Assuming here again that the reference voltage vector is \bar{V}_s^* and the voltage vector modelling the voltage drops in inverter is \bar{v}_{th} , then the stator voltage command \bar{V}_{sc}^* (Fig. 3.5) yields:

$$\bar{V}_{sc}^* = \bar{V}_s^* - \bar{v}_{th} \quad (3.38)$$

This compensation technique [16] is simple and gives relatively good results, even if it suffers from the drawback that power devices parameters are sometimes uncertain.

3.5.1.3. The inductance variation due to magnetic saturation

If the magnetic saturation $L_q(i_q)$ is ignored and the inductance is assumed to be a constant parameter, it seems that the control performances become worse and the control system may become unstable because the inductance value is used in the control algorithm, more specific in the flux observer of IPMSM [20]-[22].

In the stator flux observer the PI controller, which performs the compensation (3.14), may be tuned such as the voltage model is dominant while the current model has less influence. In this way the errors that affect the current model, mainly inductance estimation errors, will have little overall influence on the observer behavior. However, in the active flux observer (3.8) the magnetic saturation must be accounted for, if accurate active flux estimation is desired.

So, magnetic saturation, with mild cross-coupling effect for IPMSM (with inset rotor magnets) is considered by the function $L_q(\hat{T}_e)$:

$$L_q = L_{qn} / (1 + k_T |\hat{T}_e| / T_{en}) \quad (3.39)$$

where L_{qn} is the L_q unsaturated value, k_T is a torque coefficient, \hat{T}_e is the estimated torque and T_{en} is the rated torque value.

The current model based flux estimator in (Fig. 3.4) and the active flux (3.8) employ $L_q(\hat{T}_e)$. The L_d inductance is considered constant (PM is in the d -axis) and the cross-coupling effect is rather small since the currents do not exceed 150%

rated value in order to limit the inverter ratings and costs, as usual in industrial drives.

Fig. 3.6 illustrates, by digital simulations, the influence of the magnetic saturation of L_q in the active flux observer, for full step-load response at 2 rpm, with and without considering the saturation. In simulation, the machine model includes always the magnetic saturation according to (3.39).

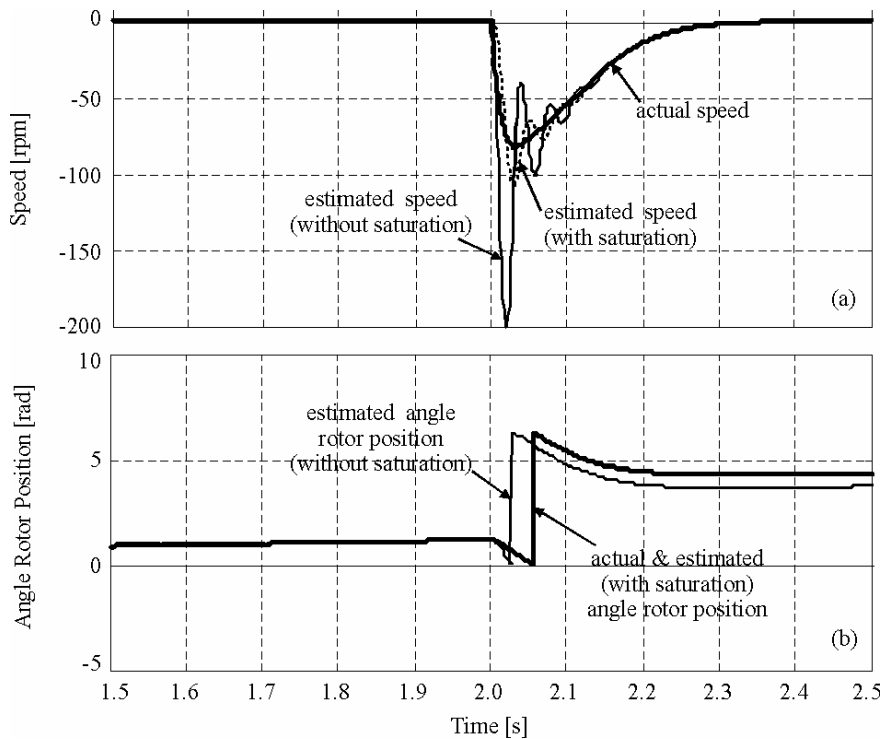


Fig. 3.6. Influence of L_q magnetic saturation in the active flux observer for sensorless operation at lowest speed of 2 rpm (0.1Hz) and step of 100% rated torque: a) actual speed, estimated speed with saturation and estimated speed without saturation, b) actual rotor position, estimated rotor position with saturation and estimated rotor position without saturation – simulation results

It is evident that the estimated speed from the active flux observer with considered saturation is much closer to the actual speed; also, the estimated rotor position is much closer to the actual rotor position.

This is of conclusive evidence that magnetic saturation is a must in the motion observer for successful robust control, especially during the transients.

3.5.1.4. The resistance variation

The resistive voltage becomes the significant term at low speed. The variations of the stator resistance take place due to temperature changes.

The problem of the variation of stator resistance is manifested by errors in the estimated flux linkage vector and in the electromagnetic torque, which causes unstable operation of the drive.

Several control schemes have been proposed to overcome the problem of stator resistance variation, reporting good performance for an induction motor drive [13], [18], [19] and [26], but recently also for the PMSMs [24] and [25].

Extensive simulation has been performed to investigate the effect of stator resistance variation on the performance of the observer. In all simulations presented in Fig. 3.7-Fig. 3.12, the following speed and torque profiles have been applied (see Fig. 3.7). Speed profile: 0–2 s: startup followed by steady-state operation at 1000 rpm; 4–6 s: deceleration followed by very-low-speed operation at 2 rpm. Torque profile: 0–2 s: no load; 2–6 s: 50% rated load torque applied. In simulation, the stator resistance of the IPMSM remains always unchanged, only in the active flux observer its nominal value changes. Also, the drive is controlled using the signal provided by the encoder and the active flux observer is used only to see how it reacts at stator resistance detuning. Note that, here, the stator flux observer employes the series model in order to make use of the error between the measured and estimated stator current.

Fig. 3.8 and Fig. 3.9 give the $\alpha\beta$ stator flux components (actual and estimated) and error between actual and estimated stator flux magnitude for +50% stator resistance detuning. As it can be seen, at high speed, the observer is practically insensitive to rotor resistance detuning because the back emf of the machine is significantly larger than its resistive voltage drop. In contrast, the low

speed operation is more affected. The errors in the stator flux estimation will determine larger errors in the rotor position and speed estimation, which may cause instability at low speeds.

To mitigate the undesirable effects of stator resistance variations on the sensorless drive, an online resistance estimator is proposed [26].

$$\hat{R}_s = R_{s0} - \gamma \int (\hat{\psi}_{d\alpha}^a \tilde{i}_\beta - \hat{\psi}_{d\beta}^a \tilde{i}_\alpha) dt \quad (3.40)$$

where the coefficient $\gamma > 0$, $\tilde{i}_\alpha = \hat{i}_\alpha - i_\alpha$, respectively $\tilde{i}_\beta = \hat{i}_\beta - i_\beta$ are the errors between estimated and actual stator current components and R_{s0} is the initial stator resistance estimate which can be measured offline.

The adaptation error is selected to be similar to the torque estimation error because the resistance error affects the active power balance and, therefore, torque estimation.

The evolution of estimated \hat{R}_s for +50% initial detuning ($R_{s0} = 1.5 * R_s$; $R_s = 3.3\Omega$) is shown in Fig. 3.10. The resistance adaptation was activated from $t=0$ s for the same speed and torque profiles.

It can be observed that at high speeds, in no-load operation, the adaptation law (3.40) is not able to estimate the resistance. At low speed the stator resistance estimator is very effective as it is able to identify the actual stator resistance value and now the actual and estimated components of the stator flux are overlapped (Fig. 3.11) and the errors in the stator flux magnitude estimation converge to zero (Fig. 3.12). Similar behavior was obtained for -50% (not shown).

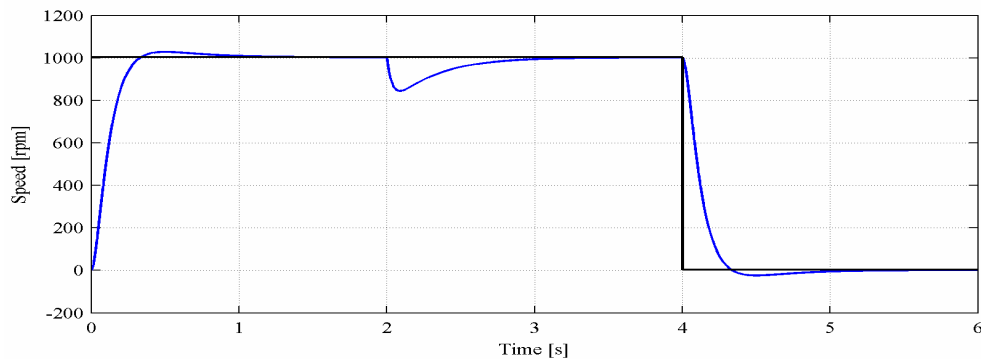


Fig. 3.7. Actual (blue) and reference speed

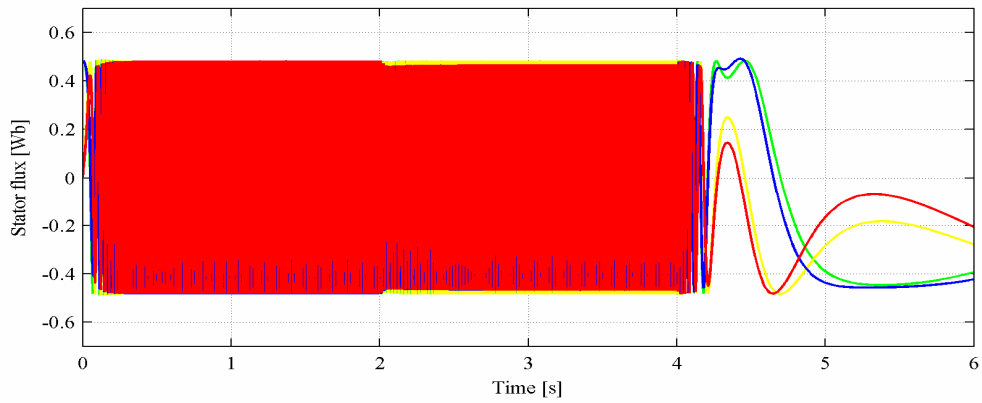


Fig. 3.8. $a\beta$ stator flux components: actual (green and yellow) and estimated (blue and red)

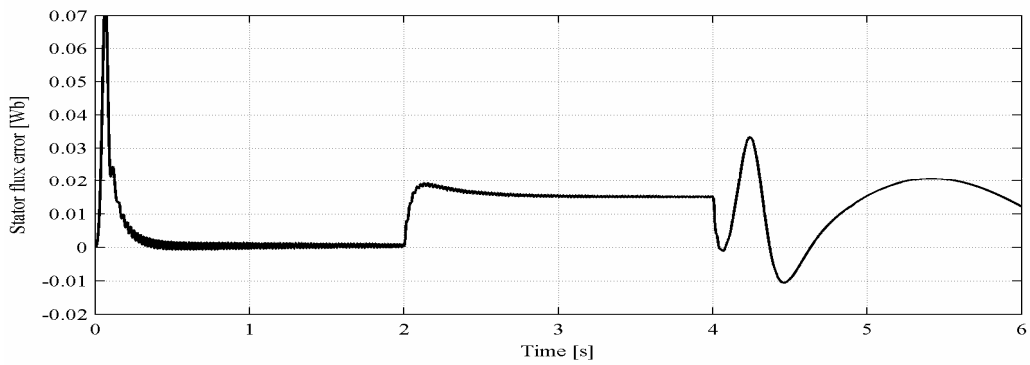


Fig. 3.9. Error between actual and estimated stator flux magnitude

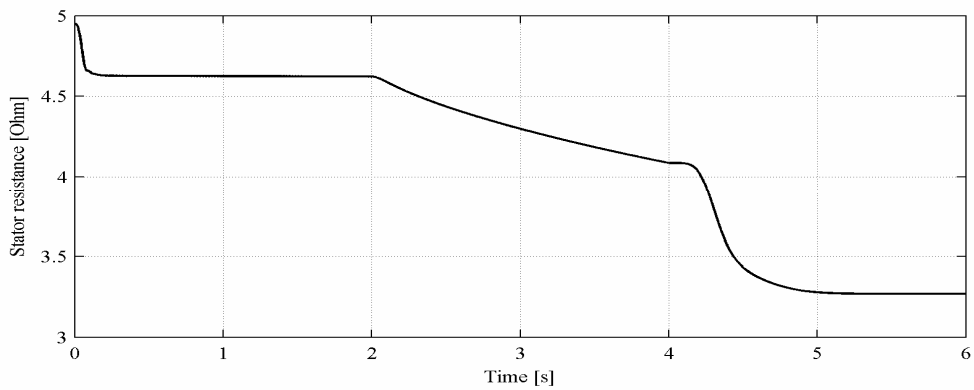


Fig. 3.10. Stator resistance

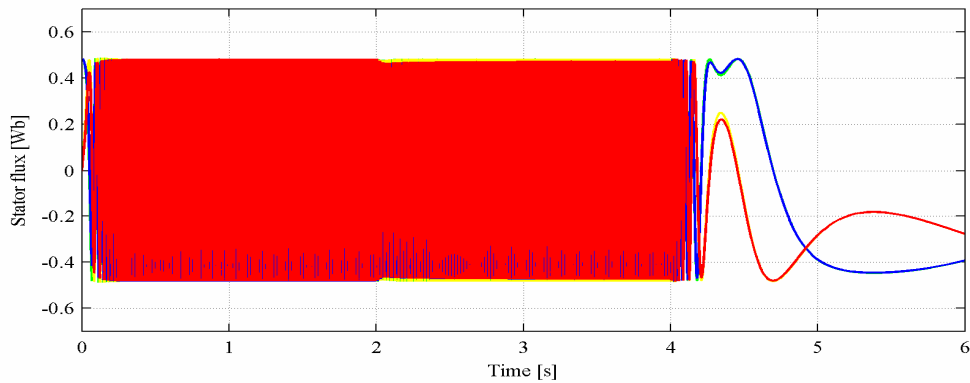


Fig. 3.11. $\alpha\beta$ stator flux components: actual (green and yellow) and estimated (blue and red)

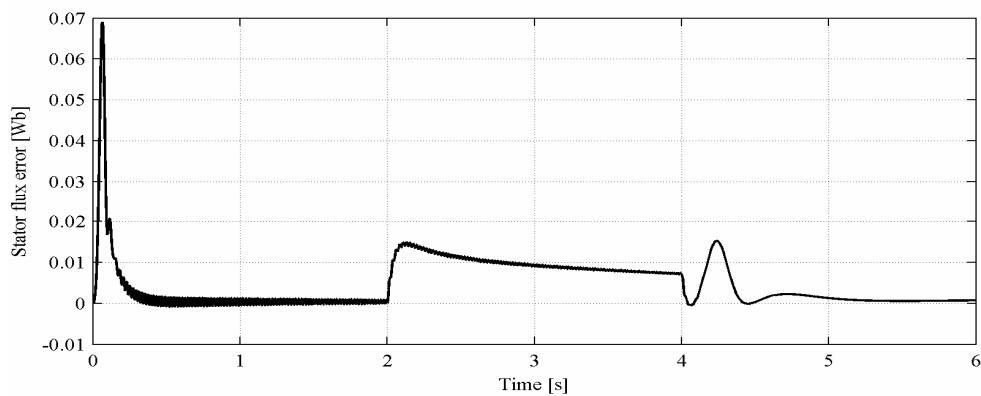


Fig. 3.12. Error between actual and estimated stator flux magnitude

3.5.2. Position-Speed Estimator and Torque Estimator

Because the active flux vector falls along the rotor d -axis, its position angle is identical to the rotor position and thus greatly simplifies the rotor position and speed estimation. A phase-locked-loop estimator is used, in general, to extract the rotor position and speed from the active flux vector.

In Chapter 2 a PLL (phase-locked-loop) estimator was used for rotor position-speed estimation. In what follows, however, the estimators (3.41)-(3.43) are chosen, to reduce errors in speed $\hat{\omega}_r$ estimation from $\hat{\theta}_{er}$ estimation:

$$\hat{\omega}_{\psi_d^a} = d\hat{\theta}_{\psi_d^a} / dt \quad (3.41)$$

$$\hat{\theta}_{\psi_d^a} = \text{atan}(\hat{\psi}_{d\beta}^a / \hat{\psi}_{da}^a) \quad (3.42)$$

$$\hat{\omega}_{\psi_d^a} = \frac{\hat{\psi}_{dak-1}^a \hat{\psi}_{d\beta k}^a - \hat{\psi}_{d\beta k-1}^a \hat{\psi}_{dak}^a}{h(\hat{\psi}_{dak}^a{}^2 + \hat{\psi}_{d\beta k}^a{}^2)} \quad (3.43)$$

where h is the sampling period, and the index $k-1$ in (3.43) denotes variables delayed with one sampling period.

The rotor position-speed estimator and torque estimator implementation is illustrated in Fig. 3.13.

The rotor speed estimation $\hat{\omega}_{\psi_d^a}$ in the whole speed range is required in the speed controller. A low pass filter is applied to the estimated speed to reduce the noise.

This filter is a PT1, where the proportional gain is $k_{p_PT1} = 1$, respectively the integral gain is $T_{i_PT1} = 3.3 \text{ ms}$.

The transformations between the reference frames in both feedforward and feedback paths in Fig. 3.3 can be affected by inaccurate rotor position estimation. Position estimation errors will be thoroughly checked.

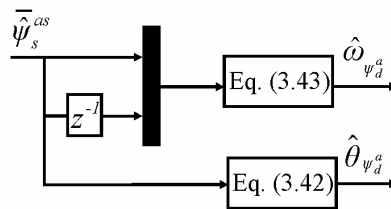


Fig. 3.13. The position-speed estimator

If the active flux vector is correctly estimated, the electromagnetic torque \hat{T}_e is simply computed based on (3.5).

3.6. Digital Simulation Results

3.6.1. Overall simulated control system description

The entire simulated sensorless control was developed in Matlab Simulink package for an easy translation into the dSpace system for experiments.

Its implementation is shown in Fig. 3.14.

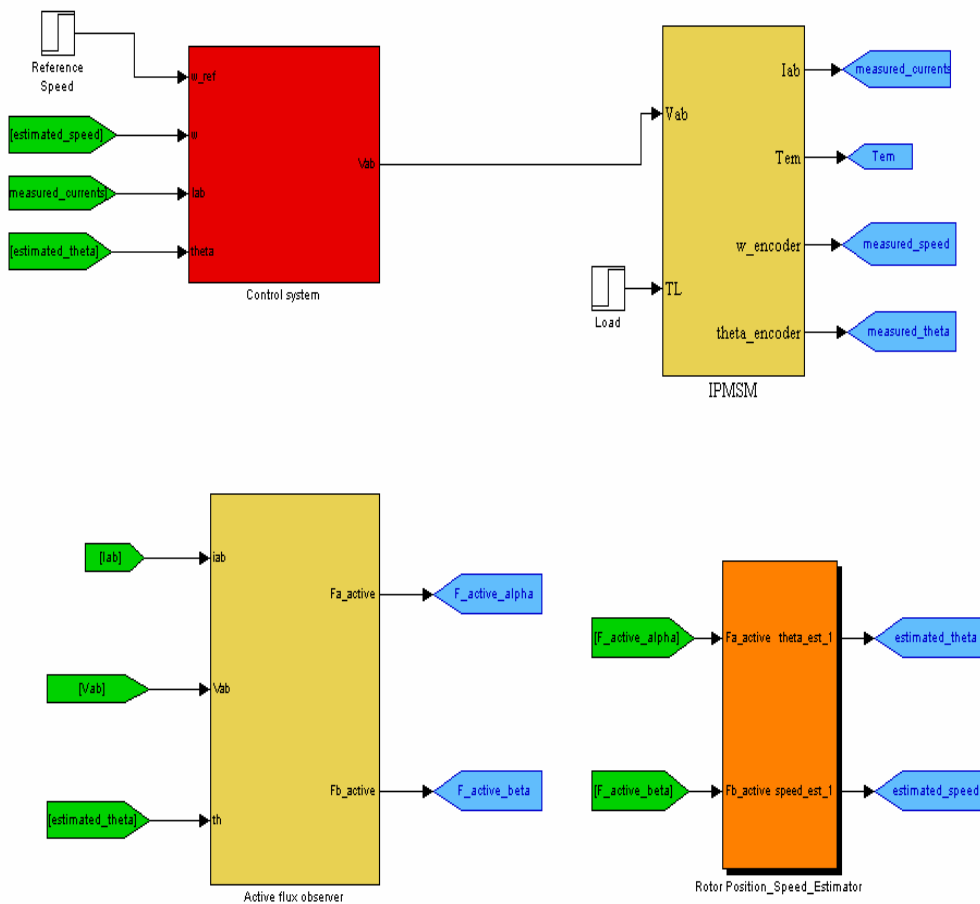


Fig. 3.14 IPMSM simulated system overview

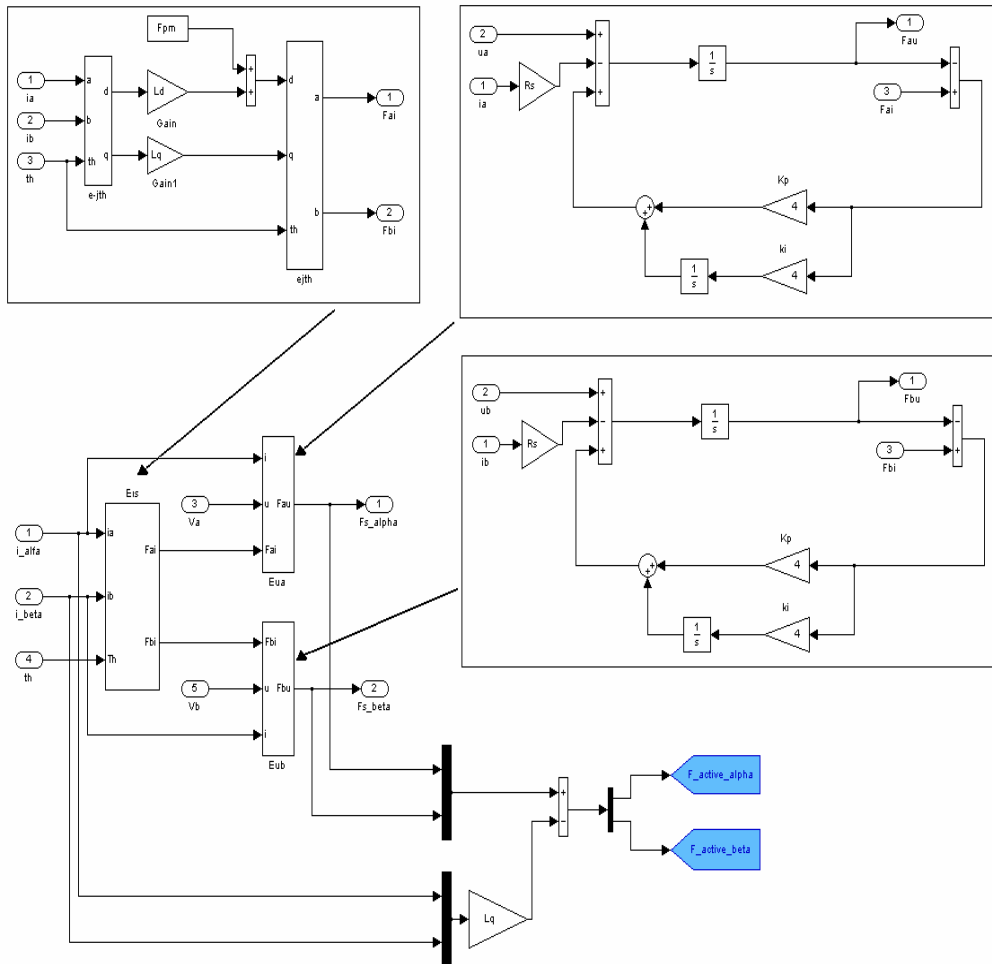


Fig. 3.16 Active flux observer obtained by the stator flux observer with combined voltage-current models

Furthermore, due to the fact that the active flux axis corresponds to the rotor d-axis, these two components are used in the rotor position and speed estimator.

The encoder device is thus replaced by this rotor position and speed estimator.

Here, the used control strategy is the classical vector control maintaining $I_d = 0$. How the vector control itself is implemented in Matlab is illustrated in Fig. 3.17.

The prescribed signals are speed and torque. They have a step waveform obtained by using a dedicated block from Matlab.

The control block mainly consists in a speed controller and dq current controllers with emf compensator (where $V_{d_decoupling} = -\hat{\omega} \psi_d^a L_q i_q$, respectively $V_{q_decoupling} = \hat{\omega} \psi_d^a (L_d i_d + \psi_{PM})$).

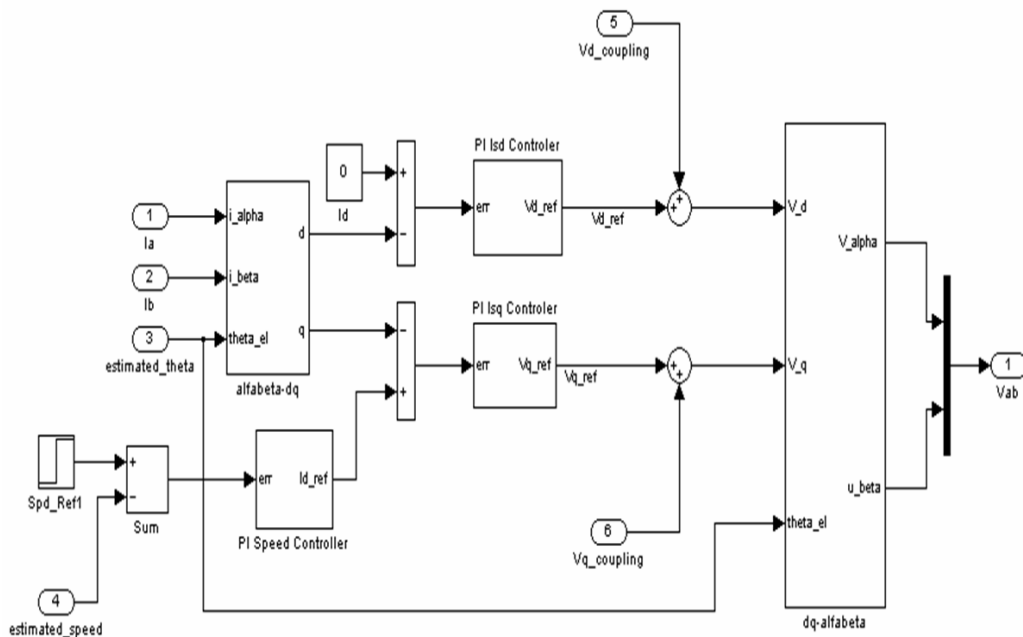


Fig. 3.17 Simulated vector control block

The speed controller generates the torque command through the I_q current. The current controllers consist of two PI controllers in order to control these currents with zero steady state error. These controllers are of anti-windup type.

The anti-windup strategy uses the saturation block to limit the PI output and to avoid the integrator saturation (Fig. 3.8). Its gain decides the system rapidity to overcome the saturation.

The actual currents (I_d and I_q) in rotor reference frame, used in current control, could be obtained by measuring two phase currents and then transforming them from stator coordinates in to rotor coordinates using the relationship:

$$I_d = \frac{2}{3} \left[I_a \cos\left(\hat{\theta}_{\psi_d^a}\right) + I_b \cos\left(\hat{\theta}_{\psi_d^a} - \frac{2\pi}{3}\right) - (I_b + I_c) \cos\left(\hat{\theta}_{\psi_d^a} + \frac{2\pi}{3}\right) \right] \quad (3.44)$$

$$I_q = -\frac{2}{3} \left[I_a \sin\left(\hat{\theta}_{\psi_d^a}\right) + I_b \sin\left(\hat{\theta}_{\psi_d^a} - \frac{2\pi}{3}\right) - (I_b + I_c) \sin\left(\hat{\theta}_{\psi_d^a} + \frac{2\pi}{3}\right) \right] \quad (3.45)$$

where $\hat{\theta}_{\psi_d^a}$ is the estimated electrical rotor position.

Then, the voltages, which are in fact the outputs of the current controllers, are transformed into stationary stator reference frame using the estimated rotor position as follows:

$$V_\alpha = V_d \cos\hat{\theta}_{\psi_d^a} - V_q \sin\hat{\theta}_{\psi_d^a} \quad (3.46)$$

$$V_\beta = V_d \sin\hat{\theta}_{\psi_d^a} + V_q \cos\hat{\theta}_{\psi_d^a} \quad (3.47)$$

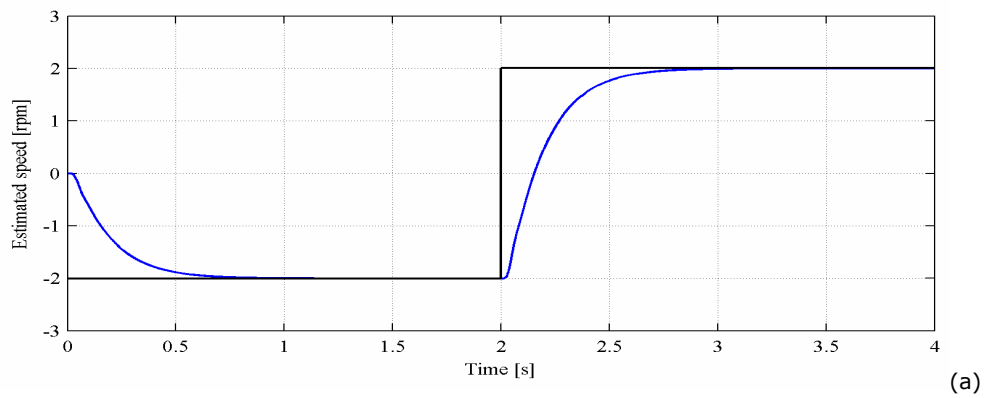
These stationary reference frame voltage commands are used to generate the inverter control signals, so these voltage commands are applied to the machine phases.

In what follows, the way the motor reacts when the classical vector control is applied will be presented. No information provided by an encoder is used, thus the entire control system works sensorless.

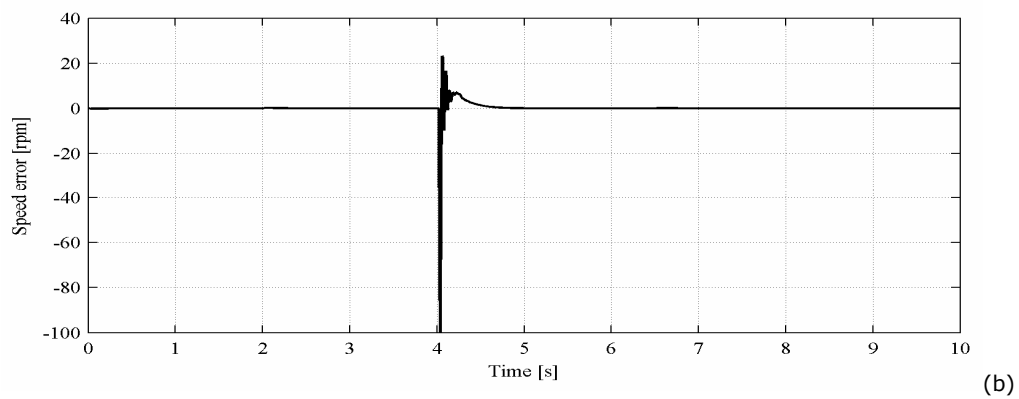
The motor will be tested under various operating modes. The above figure illustrates how the motor speed follows the reference speed. We did not concentrate to obtain good motor dynamics. Our scope here was to demonstrate that the active concept is a simpler and better method to obtain sensorless motion control at very low and close to zero speed, without using the injection signal method. All the next figures present the digital simulation results obtained the sensorless vector control applied to IPMSM.

The simulation test in Fig. 3.18 presents start up from 0 to -2 rpm, then transients from -2 rpm to 2 rpm at $t=2$ s, followed by a full step torque load at $t=4$ s and a speed step at 5 rpm at $t=6.5$ s.

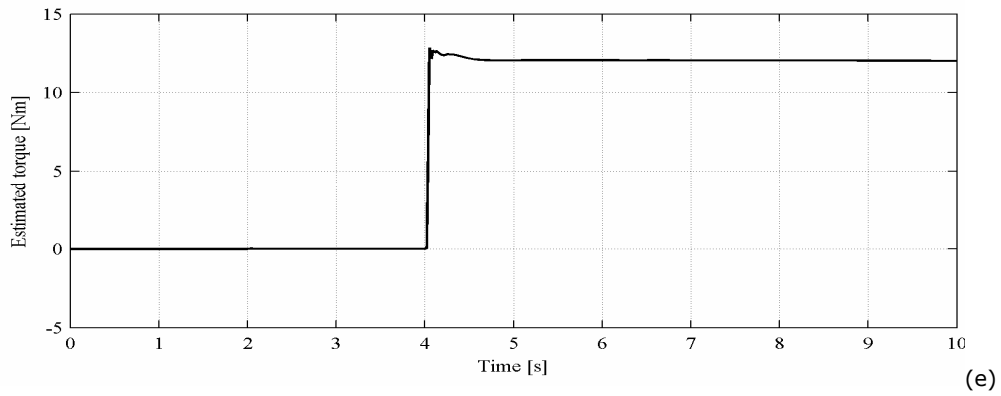
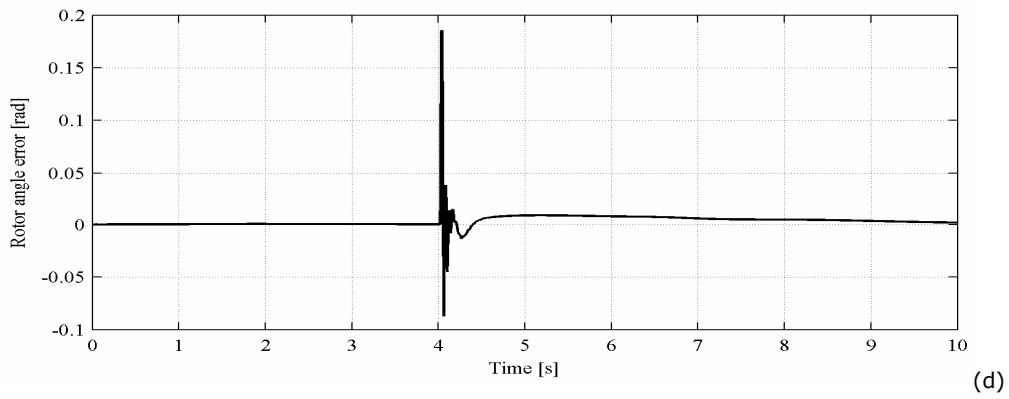
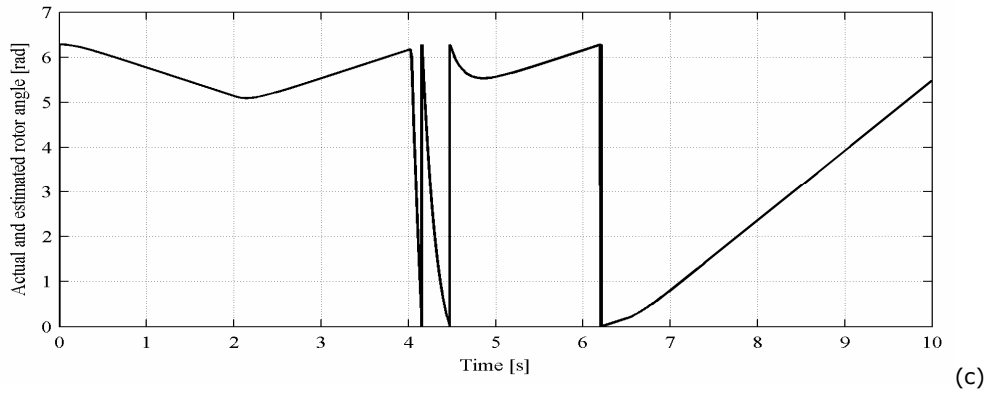
The intended purpose of this test was to demonstrate that the active flux concept can perform at very low speed.



(a)



(b)



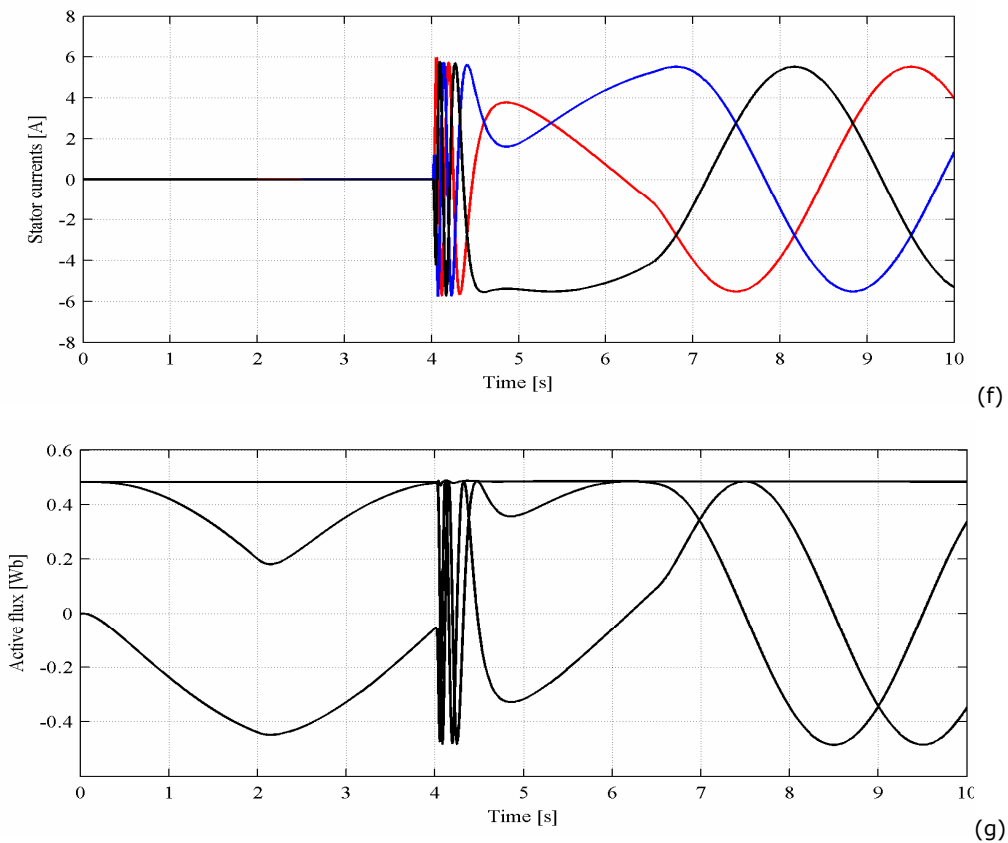


Fig. 3.18. Transients from -2 rpm to 2 rpm at $t=2$ s, followed by a full step torque load at $t=4$ s and a speed step at 5 rpm at $t=6.5$ s; from top to bottom: (a). zoom of reference and estimated speed during speed reversal; (b). error between actual and estimated speed; (c). actual and estimated rotor angle (overlapped); (d). error between actual and estimated rotor angle; (e). estimated torque; (f). stator currents i_{abc} ; (g). active flux and its two

components: ψ_{da}^a and $\psi_{d\beta}^a$

As it can be seen in Fig. 3.18a the speed response is good below 1 s and having no overshoot. However during loading, the speed error is quite large (100 rpm).

Having such good active flux estimation (Fig. 3.18g), one can expect that also the rotor position estimation to be as good as the active flux is. This is confirmed by the two overlapped actual and estimated angle rotor position in Fig. 3.18c. Thus, the proposed active flux concept is proven.

Fig. 3.18e, respectively Fig. 3.18f illustrate the torque developed by the machine and respectively how smooth and sinusoidally the currents are (this is due to the fact that in simulation everything is ideal and the inverter nonlinearities were not modelled).

The next simulation test presents startup from zero to -1000 rpm, then transients from -1000 rpm to 1000 rpm at $t=2$ s, followed by a full step torque load at $t=4$ s and at last a no loading operation started at $t=7$ s, followed by a speed step to 2000 rpm at $t=9.5$ s.

This test was performed in order to also validate the high speed operation based on active flux concept.

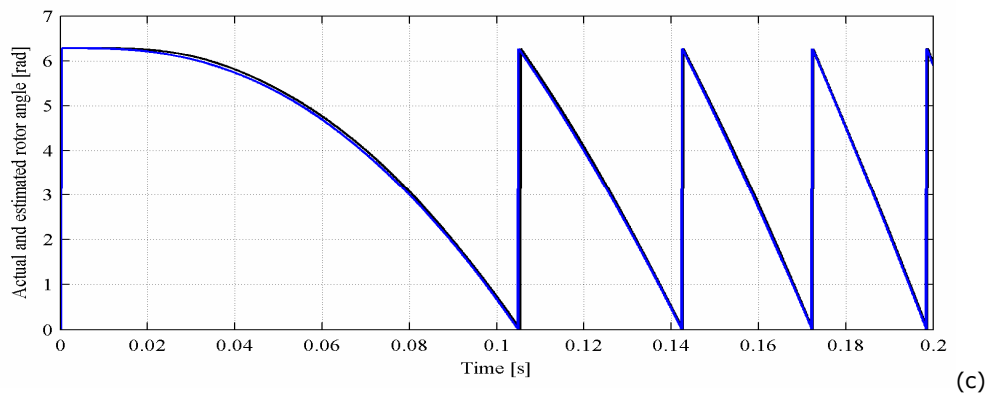
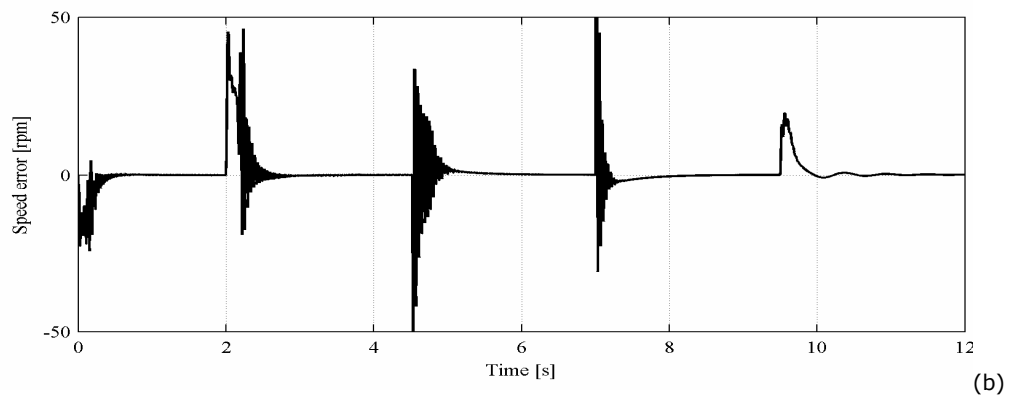
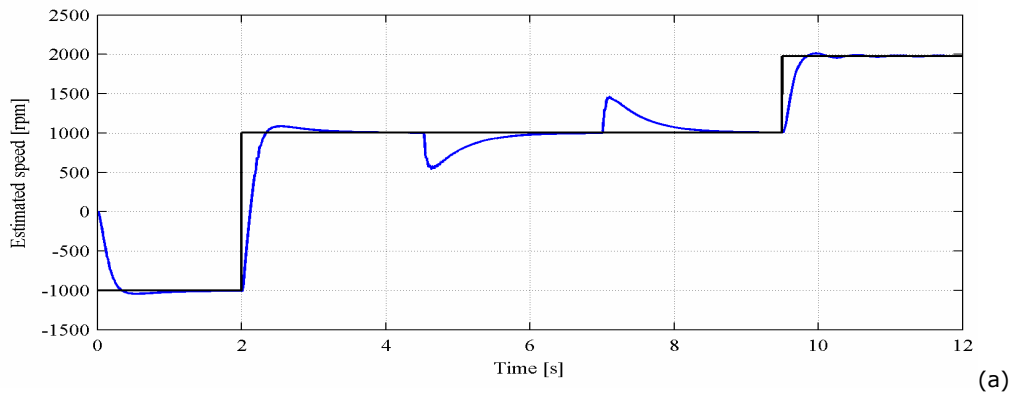
The speed error is presented in Fig. 3.19b. It can be observed that this speed error is large only during transients (maximum 50 rpm).

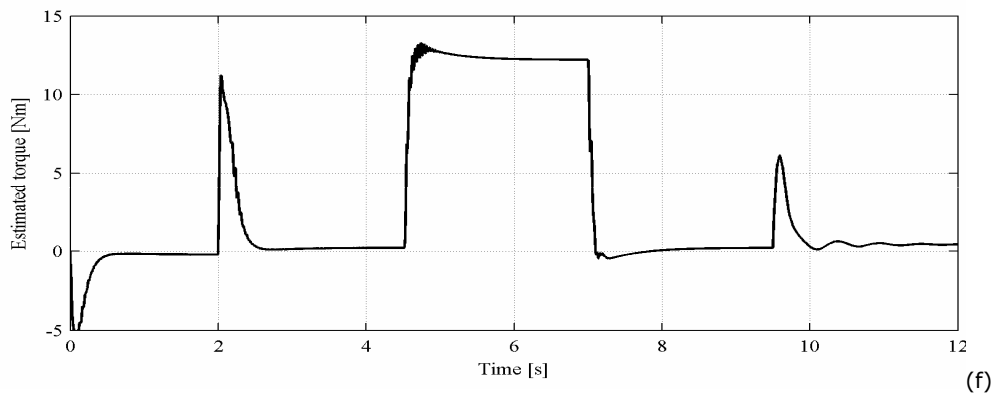
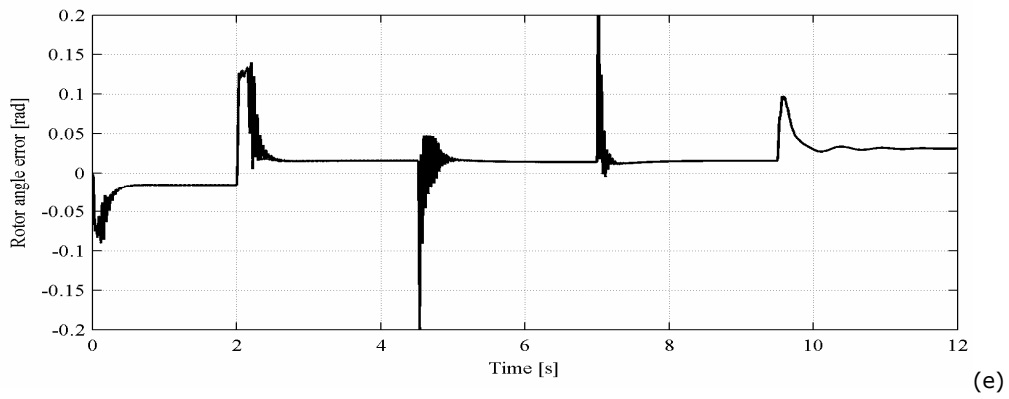
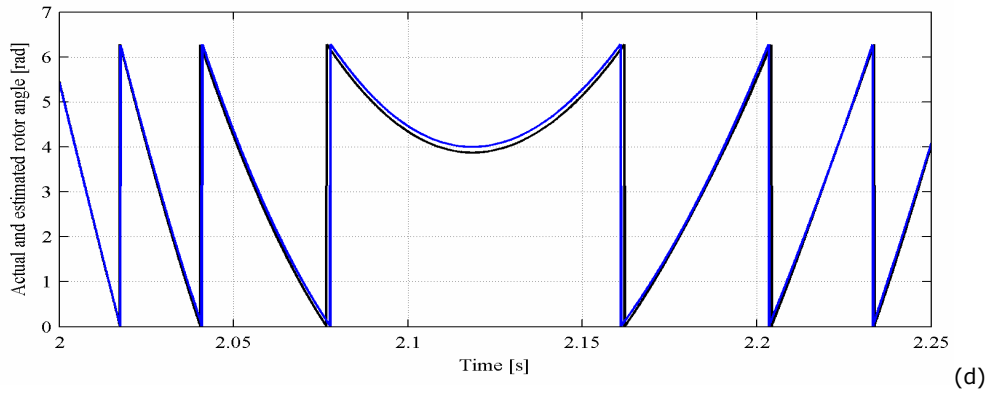
Fig. 3.19c and Fig. 3.19d present a zoom of the two rotor angles (the actual and the estimated one) during the most critical instants of time: the start-up from 0 to -1000 rpm and the speed reversal from -1000 rpm to +1000 rpm. It can be seen how well the estimated rotor angle (blue line) follows the actual one (the maximum rotor position error is 0.2 rad).

In general, it is not so important that the estimated angle differs with a few percents from the actual one, but is paramount to avoid the failure of the start-up. It is possible that the machine to be desynchronized if the estimated angle is not good enough.

Fig. 3.19g illustrates the stator three phase currents waveforms during this test. As it can be seen, the currents are not larger than the admitted ones.

Fig. 3.19h presents the hodograph of the active flux $\alpha\beta$ components. It is circular, as the theory says. This is a method of correction and verification. If the hodograph has not a circular waveform, then the estimated rotor position from its two components will not be correct.





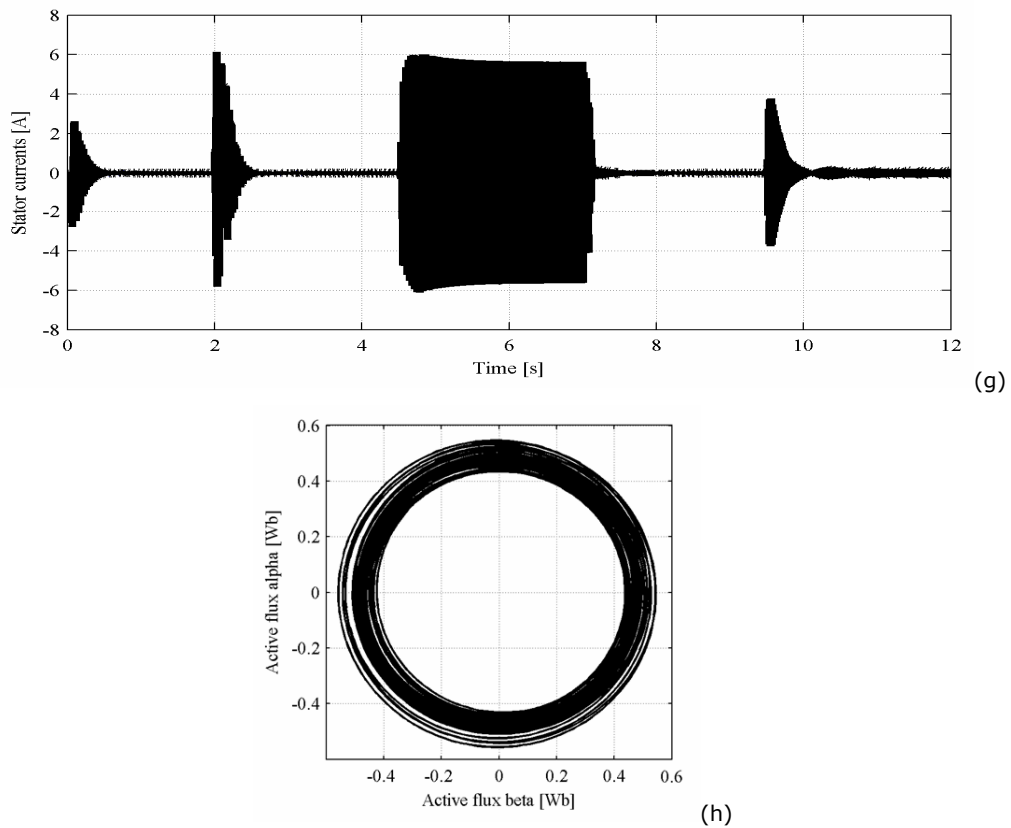


Fig. 3.19. Transients from -1000 rpm to 1000 rpm at $t=2$ s, followed by a full step torque load at $t=4$ s then an unload at $t=7$ s and followed by a speed step to 2000 rpm at $t=9.5$ s; from top to bottom: (a).reference and estimated speed; (b). error between actual and estimated speed; (c). actual and estimated rotor angle (overlapped) during start up; (d). actual and estimated rotor angle (overlapped) during speed reversal; (e). error between actual and estimated rotor angle; (f). estimated torque; (g). stator currents i_{abc} ; (h). active flux hodograph

All these simulation results demonstrate a good behavior of the simulated sensorless control system and validate the theoretical background of the active flux concept and give confidence in pursuing the experimental work.

3.7. Experimental Results

Now, looking at the above presented simulation results, one can expect that the control system will have at least the same good behavior during the practical implementation (without encoder).

The proposed sensorless vector control has been validated on the IPMSM presented in Chapter 6, which is fully dedicated to the experimental test rig.

This was possible by developing the system control algorithm in MATLAB-Simulink, followed by its implementation on a dSpace PPC 1103 single controller board.

Experimentally it has been observed that, as the theory says, at low speed, the control was sensitive to the dead time and voltage drops on the inverter power devices and to the stator resistance. Thus, without the implementation of the compensation methods of voltage drops on inverter power devices and of inverter dead time, the experimental results at very low speed of 2 rpm could not be obtained.

For the sensorless control system, knowing the initial rotor position is mandatory in the integrator of the active flux observer from (3.7).

The startup procedure is mandatory and it aligns the machine to a known position before start-up, by triggering for a short time period the voltage vector $\vec{V}_1(1,0,0)$ along a -axis that creates a stator flux, which moves the rotor to zero rotor position. This startup procedure could not be acceptable in some applications because the rotor moves, moreover, in an unpredictable direction. This represents a drawback of this procedure.

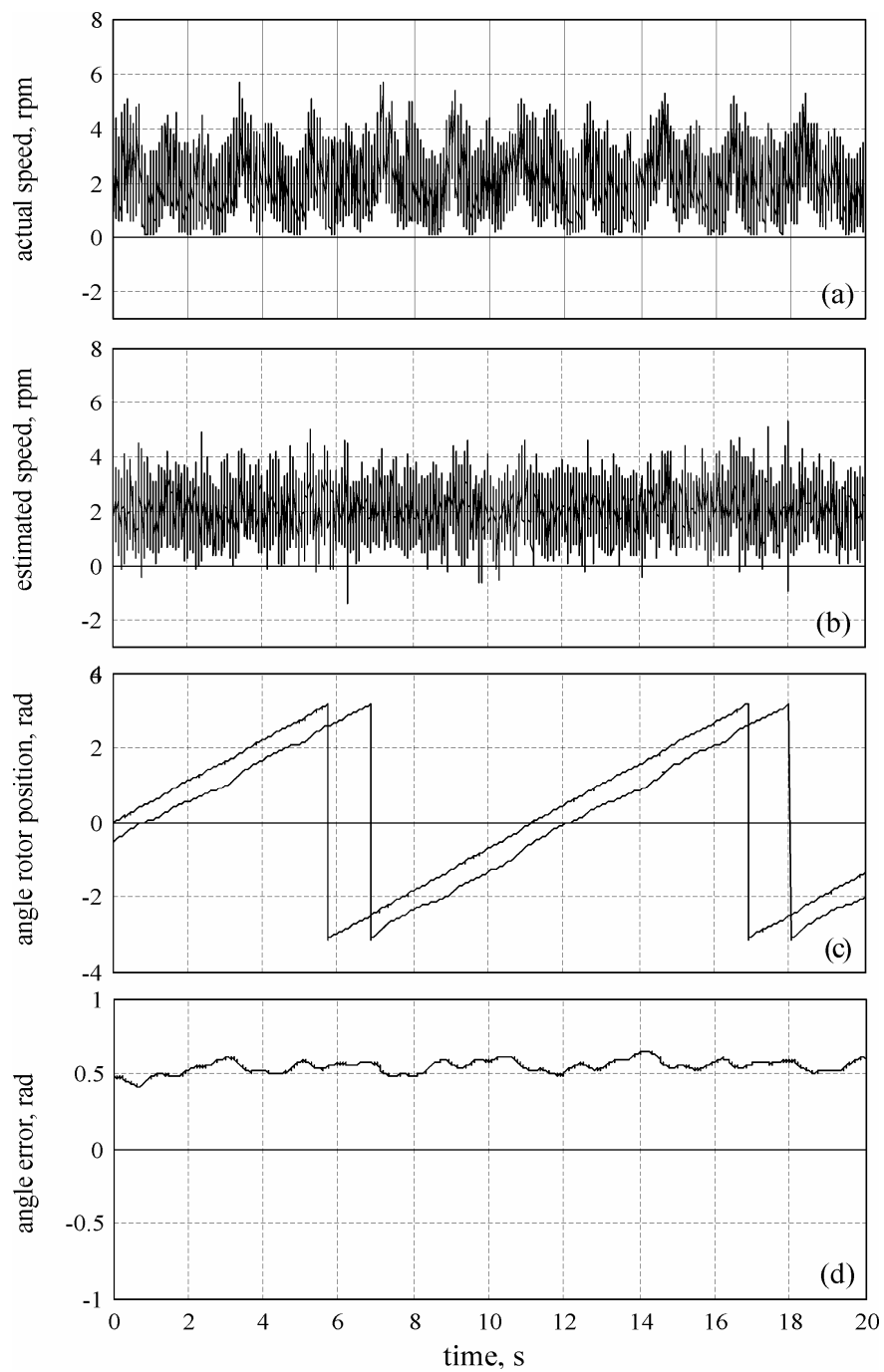
When fast start-up without encoder is desired, the initial rotor position has to be well known, otherwise the angle from the Park transformation is wrongly introduced and the system may not start.

The experiments are deliberately chosen to show both steady state and dynamic operation of the proposed control method.

The following test runs have been performed to check the proposed concept:

- Steady state operation at lowest speed (2 rpm) and 50% rated torque

The lowest speed achieved with the implemented sensorless control system is 2 rpm, operating under a step disturbance of 50% rated torque.



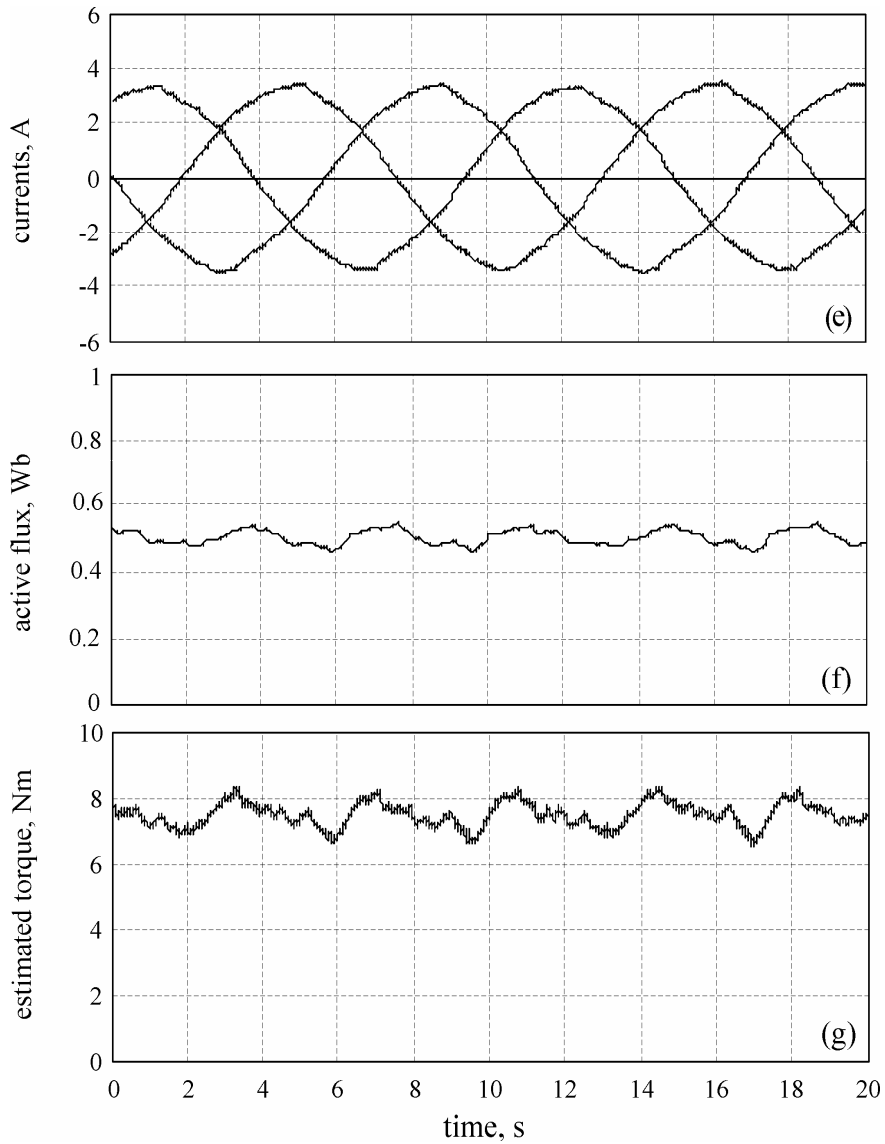


Fig. 3.20. Steady state sensorless operation at lowest speed of 2 rpm (0.1Hz) and 50% rated torque; from top to bottom: (a). actual speed, (b). estimated speed, (c). angle rotor position (actual and estimated), (d). error between estimated and actual angle rotor position (e). measured currents, (f). estimated torque and (g). active flux

The rotor position estimation errors are visible, but acceptable. The estimated angle rotor position fluctuates around actual one. The fluctuation causes small current distortion and speed variation.

Further improvements in position estimation precision are both necessary and feasible.

- Step speed reduction from 5 rpm to 3 rpm at 50% rated torque

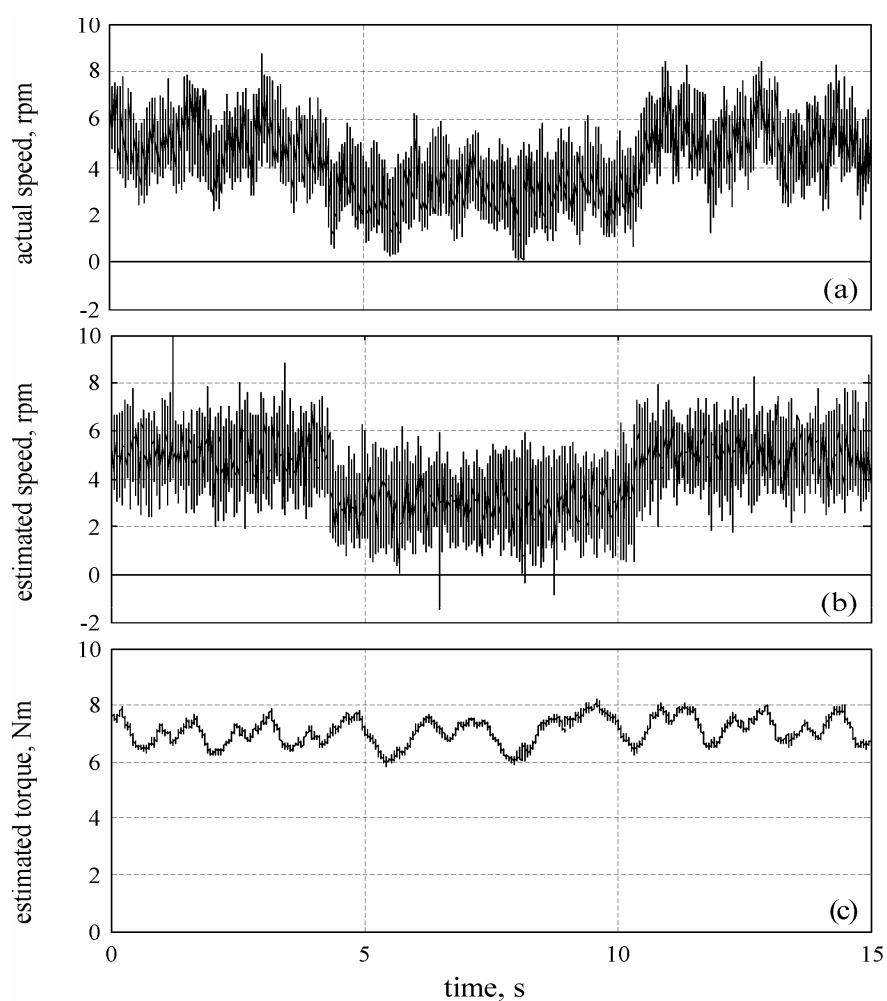


Fig. 3.21. Transients from 5 rpm to 3 rpm at 50% rated torque; from top to bottom: (a). actual speed, (b). estimated speed and (c). estimated torque

- Steady state operation at 5 rpm with full load torque

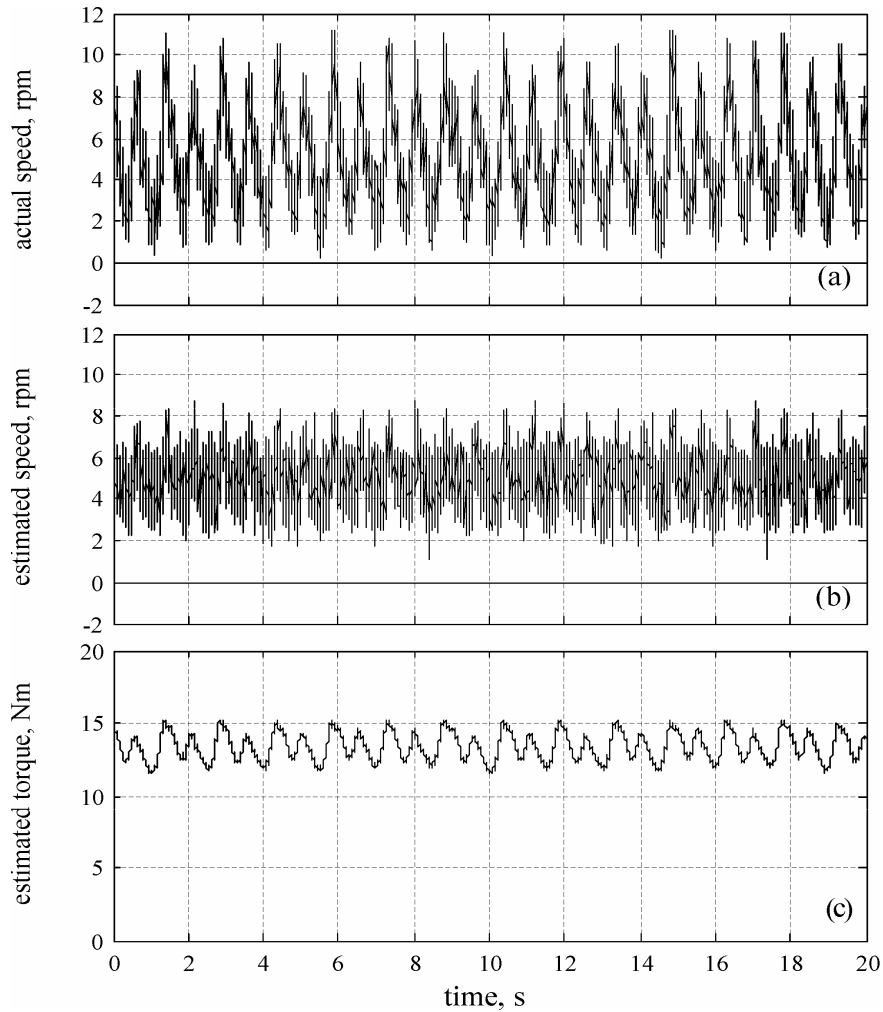
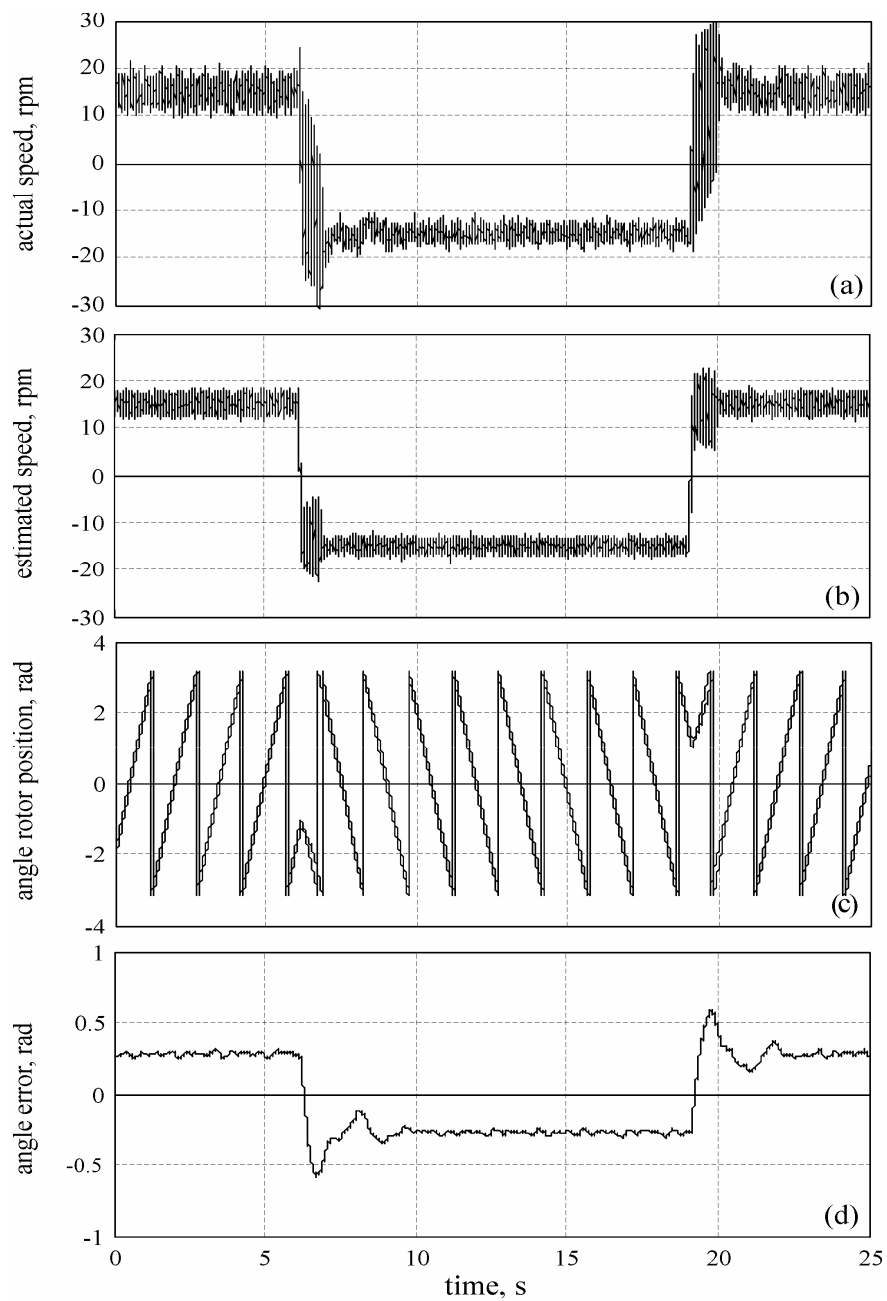


Fig. 3.22. Stationary 5 rpm at 100% rated torque; from top to bottom: (a). actual speed, (b). estimated speed and (c). estimated torque

- ± 15 rpm speed reversal at 50% rated torque

For a sensorless control system, the crossing zero point is the most challenging test. The presented speed-reversal results in Fig. 3.23 show a good transition through zero speed.



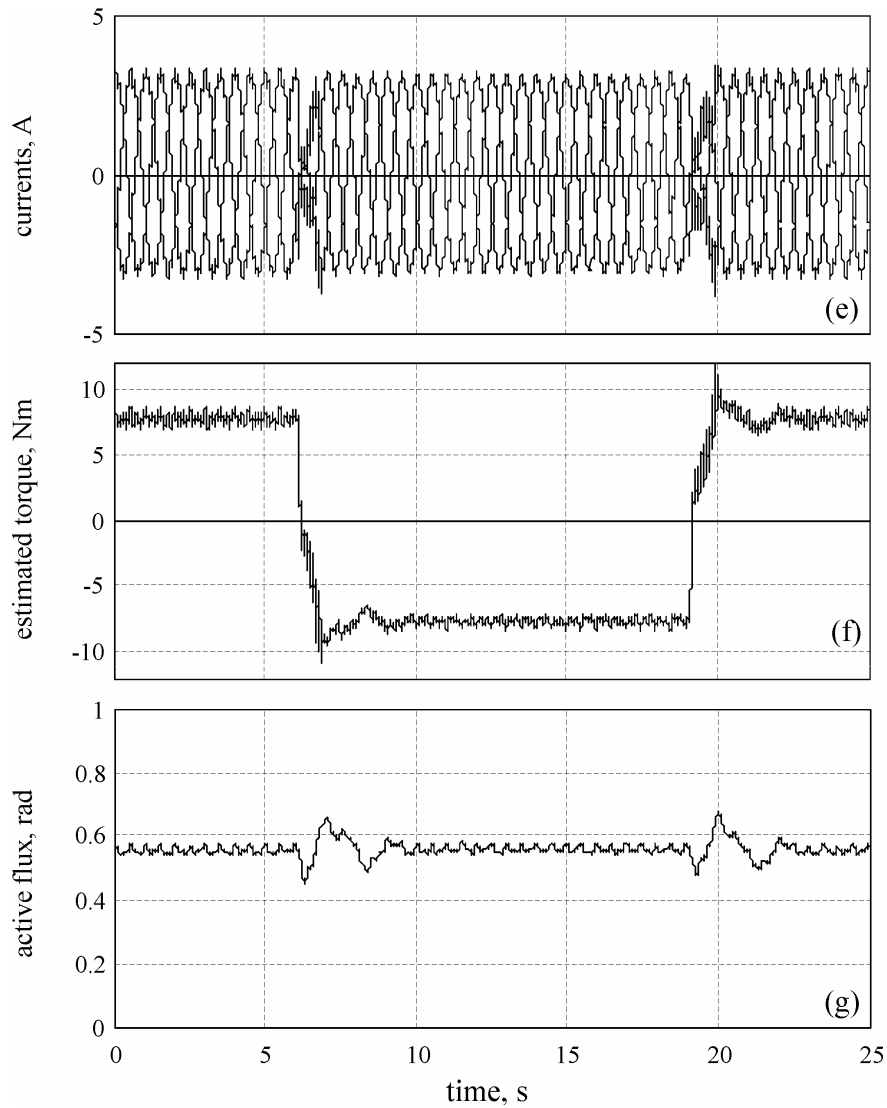
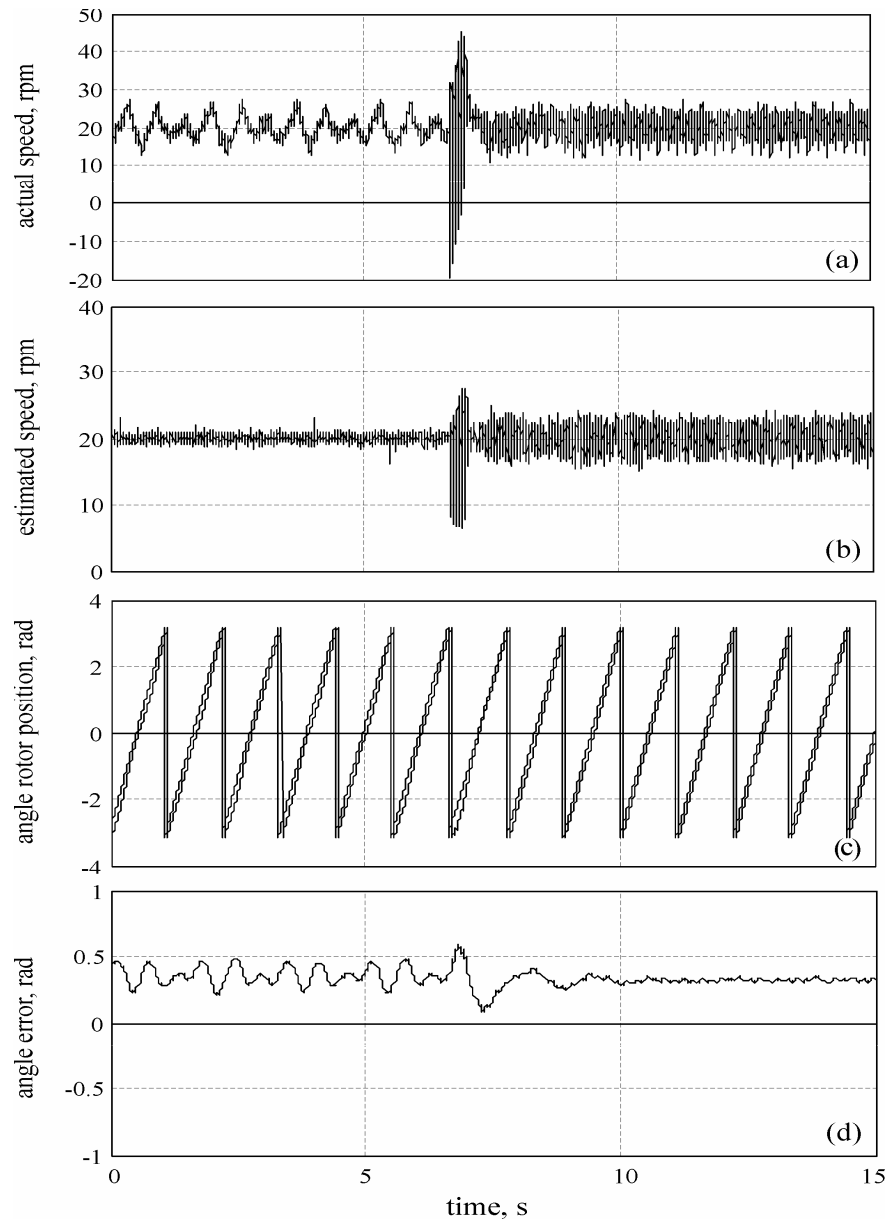


Fig. 3.23. Speed reversal at ± 15 rpm and 50% rated torque; from top to bottom: (a). actual speed, (b). estimated speed, (c). angle rotor position (actual and estimated), (d). error between estimated and actual angle rotor position (e). measured currents, (f). estimated torque and (g). active flux

- Response at nominal rated torque step during operation at 20 rpm



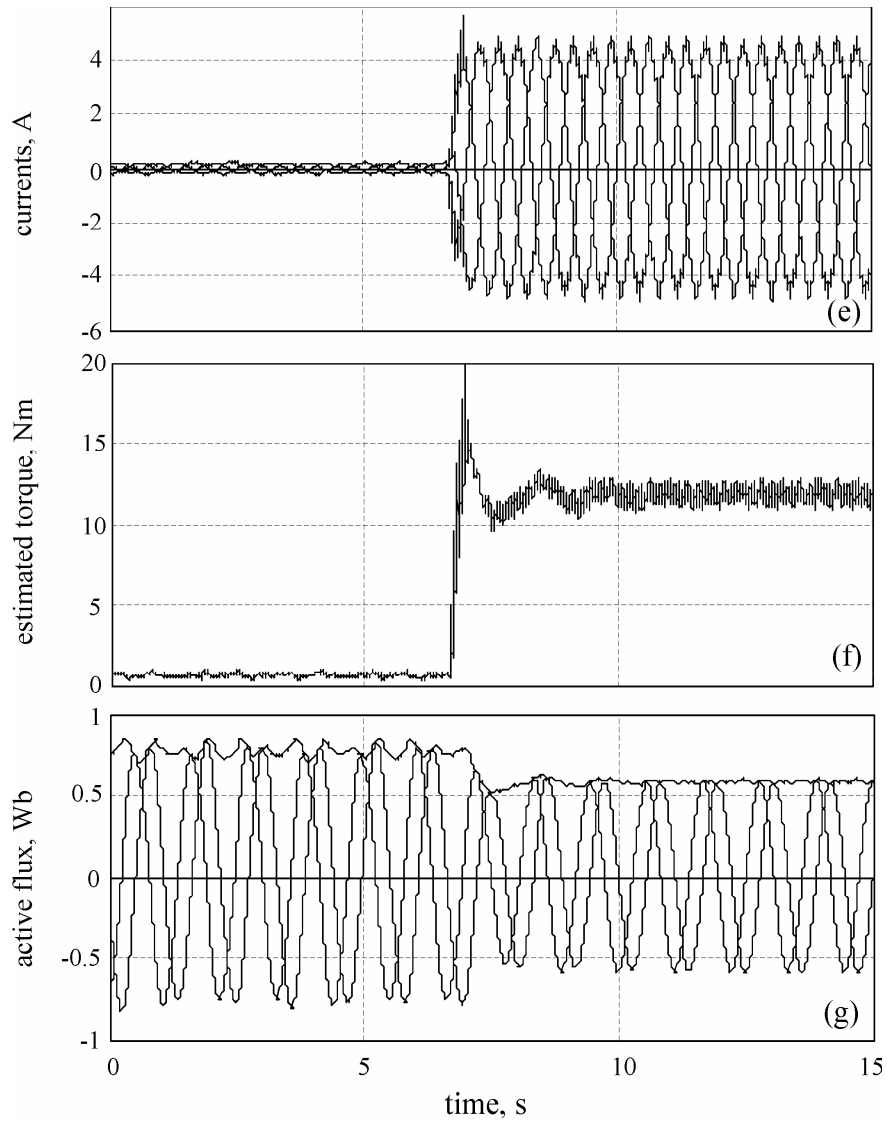


Fig. 3.24. Torque transients at 20 rpm and full load; from top to bottom: (a). actual speed, (b). estimated speed, (c). angle rotor position (actual and estimated), (d). error between estimated and actual angle rotor position (e). measured currents, (f). estimated torque and (g). active flux

In vector control with $i_d^* = 0$, ideally, the active flux $\hat{\psi}_d^a = \psi_{PM}$ from (3.4). In Fig. 3.24, this is acceptable with load, but at no load $\hat{\psi}_d^a > \psi_{PM}$, with the following explanation: at no load and 20 rpm, through PI compensator, the voltage model dominates in the stator flux observer because the current is small, and at no load $\hat{\psi}_d^a \approx \hat{\psi}_s$ from (3.8). Moreover, at no load and 20 rpm, the stator voltage is very small and incomplete inverter nonlinearities compensation (voltage drop on power switches and dead time) determines errors in the estimated stator voltage ($V_{\alpha\beta}^*$) at the integrator input (Fig. 3.4), thus errors occur in $\hat{\psi}_s$. On the other hand, under loading conditions (Fig. 3.24), the stator voltage increases and the errors from the inverter nonlinearities have lower weight and the stator current becomes important in (3.7) and thus $\hat{\psi}_d^a$ is better estimated.

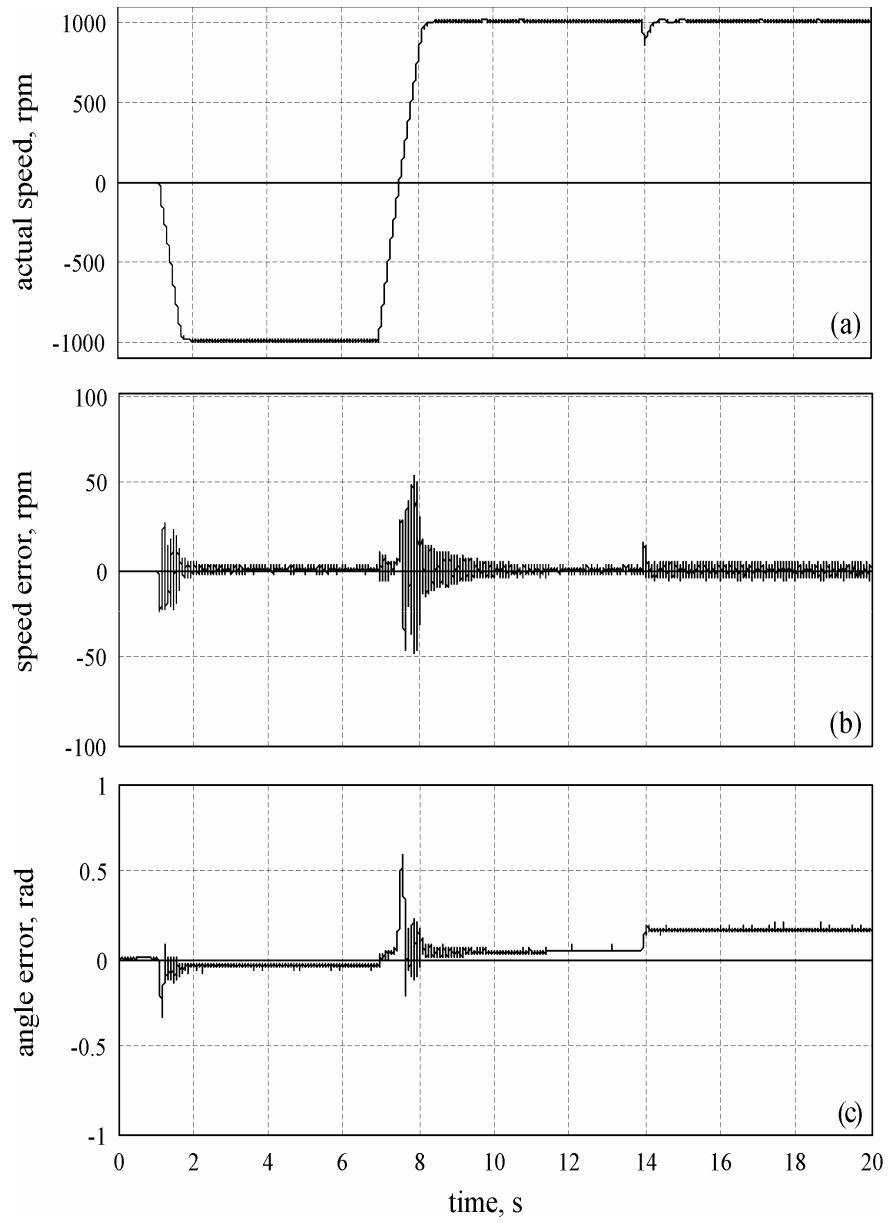
- Start up response from zero to 1000 rpm, followed by ± 1000 rpm speed reversal, plus 60% step torque loading response

It has been observed that when the speed reference or load torque changes rapidly, a position (speed) estimation error occurs.

The rotor position estimation error and the rotor speed estimation error increase when the speed reference or load disturbance change quickly, as it is shown in Fig. 3.23 - Fig. 3.25. Also during steady state the rotor speed estimation errors are less than 7-13 rpm, during transients they go up to 50 rpm.

At high speeds (Fig. 3.25), the back electromotive force (EMF) will approach the available inverter voltage and can make proper current regulation difficult due to a lack of the necessary voltage margin, which explains the presence of spikes in the current (torque) waveforms.

The hodograph in Fig. 3.27 is almost circular as it should. Comparing the results obtained by simulation with the experimental ones, the correlation is straightforward.



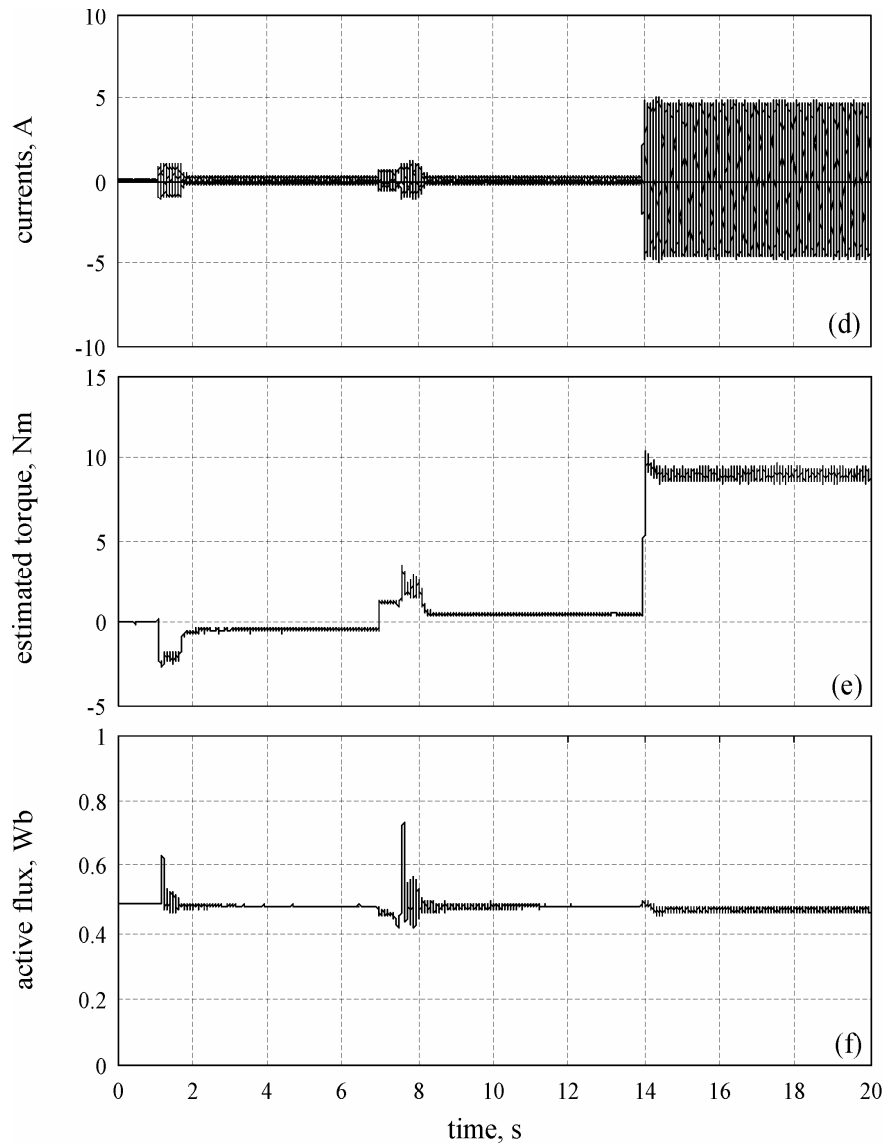


Fig. 3.25. Startup response from 0 to -1000 rpm, speed reversal at ∓ 1000 rpm and torque transients at 1000 rpm at 60% rated torque; from top to bottom: (a). actual speed, (b). error between estimated and actual speed, (c). angle rotor position (actual and estimated), (d). error between estimated and actual angle rotor position (e). measured currents, (f). estimated torque and (g). active flux

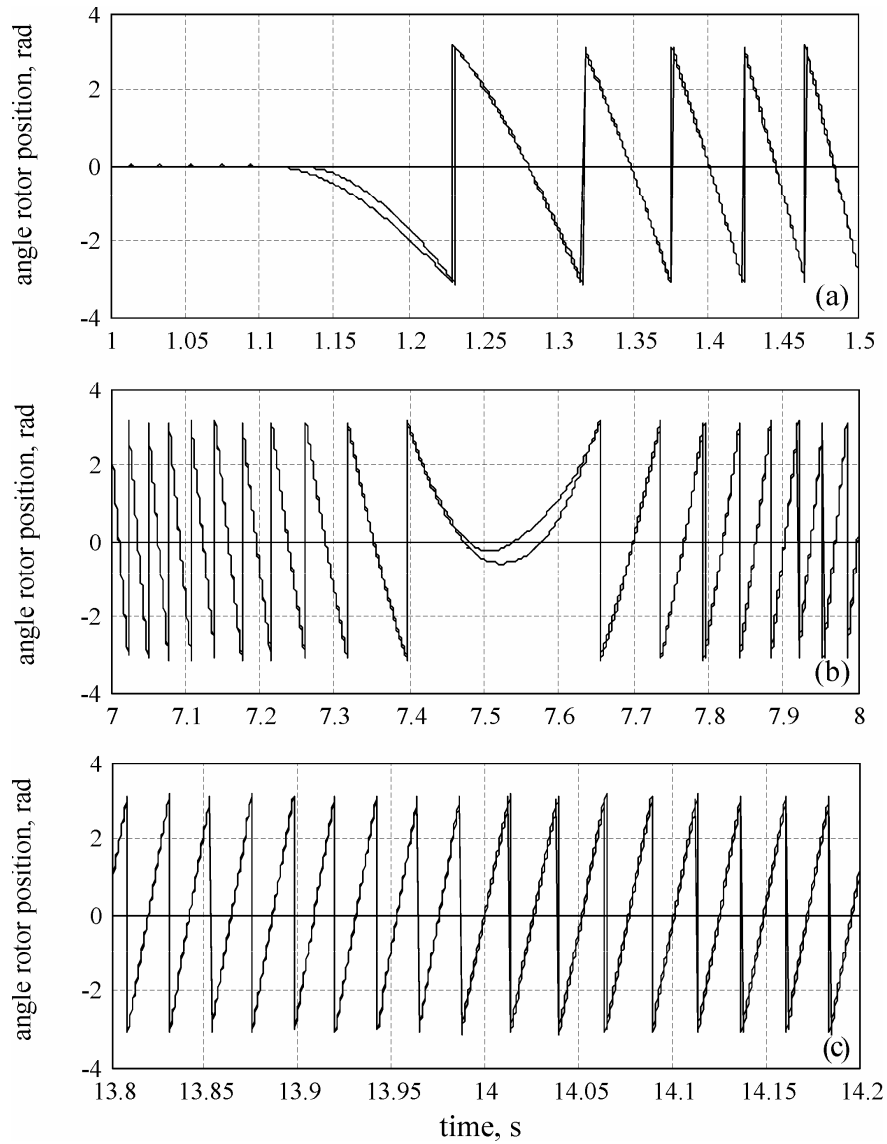


Fig. 3.26. Start up response from 0 to -1000 rpm, speed reversal at ± 1000 rpm and torque transients at 1000 rpm at 60% rated torque; from top to bottom: (a). actual and estimated angle rotor position at start up, (b). at speed reversal and (c). at step torque load

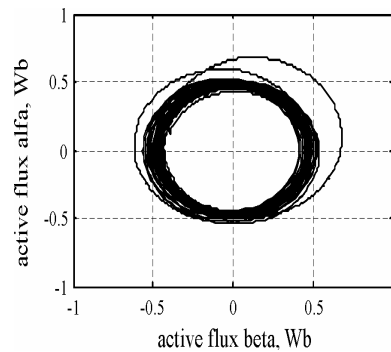


Fig. 3.27. Start up response from 0 to -1000 rpm, speed reversal at ∓ 1000 rpm and torque transients at 1000 rpm at 60% rated torque: active flux beta versus active flux alpha hodograph

3.8. Conclusion

This chapter focuses on performance motion sensorless control of IPMSM via stator flux estimation using the “active flux” concept.

The stability of the proposed active flux observer is analyzed.

The compensation methods of all factors which can cause inaccurate active flux estimation are also discussed and some of them proven by digital simulation.

The current vector control strategy, using the proposed observer and without signal injection, was applied to the IPMSM sensorless drive in a speed range down to 2 rpm and up to 1000 rpm.

In conclusion, note that the proposed sensorless vector control was demonstrated first by digital simulations and then through experimental results to be able to deliver accurate estimation both in steady state and during transients even at 2 rpm (0.1 Hz) operation with 50% load torque.

The proposed solution is a general approach that can be used in sensorless control of universal ac drives.

References

- [1] F. Blaschke, "The principle of field orientation as applied to the new transvector closed-loop control system for rotating-field machines," *Siemens Review*, vol. 34, no. 5, pp. 217–220, May 1972.
- [2] K. Hasse, "Speed control methods for fast-reversing drives using controlled rectifier fed induction motors with squirrel cage otors", *Regelungstechnik-und-Prozess-Datenverarbeitung*, Febr. 1972.
- [3] J. Holtz and J. Quan "Sensorless vector control of induction motors at very low speed using a nonlinear inverter model and parameter identification," *IEEE Trans. Ind. Appl.*, vol. 38, no. 4, pp. 1087–1095, July-Aug. 2002.
- [4] S. Shinnaka, "New sensorless vector control using minimum-order flux state observer in a stationary reference frame for permanent-magnet synchronous motors," *IEEE Trans. Ind. Electron.*, vol. 53, no. 2, pp. 388–398, April 2006.
- [5] C. Mademlis, I. Kioskeridis, and N. Margaris, "Optimal efficiency control strategy for interior permanent-magnet synchronous motor drives ," *IEEE Trans. En. Conv.*, vol. 19, no. 4, pp. 715–723, Dec. 2004.
- [6] S. Ostlund and M. Brokemper "Sensorless rotor-position detection from zero to rated speed for an integrated PM synchronous motor drive," *IEEE Trans. Ind. Appl.*, vol. 32, no. 5, pp. 1158-1165, Sept.-Oct. 1996.
- [7] E. Urlep and K. Jezernik, "Low and zero speed sensorless control of nonsalient PMSM," in *Conf. Record IEEE-ISIE 2007*, pp. 2238–2243.
- [8] C. Silva, G. M. Asher, and M. Sumner, "Hybrid rotor position observer for wide speed range sensorless PM motor drives including zero speed," *IEEE Trans. Ind. Electron.*, vol. 53, no. 2, pp. 373–378, 2006.
- [9] A. Consoli, G. Scarcella, and A. Testa, "Industry applications of zero speed sensorless control techniques for PMSMs," *IEEE Trans. Ind. Appl.*, vol. 37, no. 2, pp. 513–521, 2001.
- [10] N. Bianchi, S. Bolognani, J.-H. Jang, and S.-K. Sul, "Advantages of inset PM machines for zero-speed sensorless position detection," *IEEE Trans. Ind. Appl.*, vol. 44, no. 4 pp. 1190–1198, July-Aug. 2008.

- [11] F. Briz, M. W. Degner, P. Garcia, and R. D. Lorenz, "Comparison of saliency-based sensorless control techniques for ac machines," *IEEE Trans. Ind. Appl.*, vol. 40, no. 4, pp. 1007–1115, 2004.
- [12] J.M. Guerrero, M. Leetmaa, F. Briz, A. Zamarron, and R.D. Lorenz "Inverter nonlinearity effects in high-frequency signal-injection-based sensorless control methods," *IEEE Trans. Ind. Appl.*, vol. 41, no. 2, pp. 618-626, March-April 2005.
- [13] J. Holtz, "Sensorless control of induction machines - with or without signal injection?," *IEEE Trans. Ind. Electron.*, vol. 53, no. 1, pp. 7-30, Febr. 2006.
- [14] E. Roseischi and M. Schroedl, "Optimized INFORM measurement sequence for sensorless PMSM: drive with respect to minimum current distortion," *IEEE Trans. Ind. Appl.*, vol. 40, no. 2, pp. 591–598, 2004.
- [15] S. Ogasawara, H. Akagi "Implementation and position control performance of a position-sensorless IPM motor drive system based on magnetic saliency" *IEEE Transactions on IA*, vol. 34, Issue 4, July-Aug. 1998, pp. 806-812.
- [16] J.-W. Choi, and S.-K. Sul, "Inverter output voltage synthesis using novel dead time compensation", *IEEE Trans. Power Electron.*, vol. 11, no. 2, pp. 221-227, March 1996.
- [17] Y. Murai, T. Watanabe and H. Iwasaki, "Waveform distortion and correction circuit for PWM inverters with switching lag-times," *IEEE Trans. Ind. Applicat.*, vol. 23, no. 5, pp. 881-886, Sept./Oct. 1987.
- [18] J. Holtz, and A. Khambadkone, "Vector controlled induction motor drive with a self-commissioning scheme", *IEEE Trans. Ind. Electron.*, pp. 322-327, 1991.
- [19] H. Kubota, and K. Matsuse, "Speed sensorless field oriented control of induction motor with rotor resistance adaptation", *IEEE Trans. Ind. Applicat.*, vol. 30, no. 5, pp. 1219- 1224, Sept/Oct. 1994.
- [20] N. Imai, S. Morimoto, M. Sanada, and Y. Takeda, "Influence of magnetic saturation on sensorless control for interior permanent-magnet synchronous motors with concentrated windings", *IEEE Trans. Ind. Applicat.*, vol. 42, no. 5, pp. 1192-1200, Sept.-Oct. 2006.
- [21] S. Morimoto, M. Sanada, and Y. Takeda, "Effects and compensation of magnetic saturation in flux-weakening controlled permanent magnet

- synchronous motor drives", *IEEE Trans. Ind. Applicat.*, vol. 30, no. 6, pp. 1632-1637, Nov.-Dec. 1994.
- [22] P. Guglielmi, M. Pastorelli, G. Pellegrino, and A. Vagati, "Position-sensorless control of permanent-magnet-assisted synchronous reluctance motor", *IEEE Trans. Ind. Applicat.*, vol. 40, no. 2, pp. 615-622, Mar.-Apr. 2004.
- [23] M. Dybkowski, T. Orłowska-Kowalska, "Low-speed performance of the stator current based MRAS Estimator with FL controller in the sensorless induction motor drive," in *Proc. OPTIM-2008*, pp. 161-169, Brasov, 22-23 May 2008.
- [24] B. Nahid-Mobarakeh, F. Meibody-Tabar, and F.-M. Sargos, "Mechanical sensorless control of PMSM with online estimation of stator resistance," *IEEE Trans. Ind. Appl.*, vol. 40, no. 2, pp. 457-471, Mar.-Apr. 2004.
- [25] Z. Xu, and M.F. Rahman, "An improved stator flux estimation for a variable structure direct torque controlled IPM synchronous motor drive using a sliding observer," in *Conf. Record of IEEE-IAS 2005*, pp. 2484-2490.
- [26] C. Lascu, G.-D. Andreescu, "Sliding-mode observer and improved integrator with DC-offset compensation for flux estimation in sensorless-controlled induction motors", *IEEE Trans. Ind. Electron.*, vol. 53, no. 3, pp. 785-794, June 2006.
- [27] I. Boldea, M. C. Paicu and G.-D. Andreescu, "Active flux concept for motion-sensorless unified ac drives," *IEEE Trans. Power Electronics*, vol. 23, no. 5, pp. 2612-2618, Sept. 2008.
- [28] I. Boldea, M. C. Paicu, G.-D. Andreescu, and F. Blaabjerg, "'Active flux' orientation vector sensorless control of IPMSM," in *Proc. OPTIM-2008*, pp. 161-169, Brasov, 22-23 May 2008.
- [29] B. Kısacanin, and G. C. Agarwari, *Linear control systems*, ERC Press, New York, 2001.

Chapter 4

“Active Flux” DTFC-SVM Sensorless Control of IPMSM

Abstract

This chapter proposes an implementation of a motion-sensorless control system based on the “active flux” using direct torque and flux control with space vector modulation (DTFC-SVM) for IPMSM. To obtain a sensorless control without signal injection, the rotor position and speed estimation is based on the concept of “active flux” (or “torque producing flux”), which turns all the salient-pole rotor ac machines into fully nonsalient-pole ones. A notable simplification in the rotor position observation of salient-pole rotor ac machines is thus obtained because the active flux position is identical to rotor position. A model of the motion-sensorless control system for DTFC-SVM was first developed in Matlab-Simulink. The digital simulation results validate the active flux concept theory and ensure that the experimental results will be as good as from the simulation ones. Then the control system is implemented on dSpace platform. Indeed, experimental results demonstrate the effectiveness of the proposed sensorless control system. With the active flux observer, the drive system operates from the very low speed of 2 rpm with half full load, up to 1400 rpm. Higher speed is possible, in principle, with flux weakening.

4.1. Introduction

The direct torque and flux control (DTFC) has become an accepted vector control method beside the current vector control. The DTFC was first applied to asynchronous machines, and has later been applied also to synchronous machines.

The basic principle of DTFC is to select stator voltage vectors according to the differences between the reference and actual torque and flux linkages. Current

controllers followed by pulse width modulators (PWM) are not used in DTFC system, and the parameters of the motor are also not used, except for the stator resistance.

Compared to the conventional current vector control method, the DTFC has the following features:

- there are no current control loops, hence the current is not regulated directly;
- coordinate transformation is not required and thus the use of DTFC should be beneficially in motion-sensorless implementations;
- stator flux vector and torque estimation is required;
- fast torque response;
- the magnitude of the torque ripple in DTFC drive is slightly smaller than that in current vector control drive;
- less parameter dependence.

Nevertheless, the large torque and flux ripples were its main drawbacks. Many researchers have attempted to improve the ripples as shown in [1]-[3]. By using multilevel inverters [4], the resolution of the voltage vectors can be improved and hence, more smooth torque and flux responses. However, due to the increased number of power switches, the system cost and complexity increase. A modified DTFC scheme that utilizes space vector modulation (SVM) was reported in [1]. In this method, fixed switching frequency and lower torque and flux ripples were achieved with the help of a proportional-integral (PI) controller and the SVM technique.

However, this scheme is relatively noisy [5]. A variable structure DTFC controller was introduced in [6]. This scheme reduces too the torque and ripples significantly but it parameter dependant and requires gain scheduling.

This chapter proposes a new DTFC method based on SVM for IPMSM drives. The torque and flux linkage are controlled independently via two PI controllers, and the reference voltage vectors are generated by the SVM unit. When compared to the classical DTFC scheme, the proposed method suppresses the torque and flux ripples significantly.

Flux estimation with current model is used at low frequencies and requires the stator current and the rotor speed data. The drawbacks of this method are its susceptibility to the changes of the rotor parameters at high speeds and its need of a speed sensor. For sensorless flux estimation, the voltage model is preferred. This

model has a very high accuracy at high speeds. However, at low speeds due to the very low stator voltage, decrease of the ohmic voltage and component voltage diminishes the error of the integration process increases. Accuracy of the flux estimation depends on the accuracy of the measured current, voltage and real parameters.

In practice, the structure of the flux sensors and the error due to noise or a small DC shift of the transitional region, results in error accumulation at the integrator. In order to avoid that effect, an integrator with a LP filter is used instead of a pure integrator [7].

Therefore, the driver performance decreases especially at frequencies close to the cut-off frequency of the filter.

In the last few years, various signal-injection magnetic saliency-based sensorless control algorithms, even processing of certain pulse width modulation voltage sequences, involving low even zero speed, have been proposed for IPMSMs [9]-[20]. An initial position estimation sequence is added [19], [20].

In very low-speed (sub 3-10 rpm) servo-drives performance, the inherent signal injection algorithms complexity is to be accepted, because low-speed operation is quite critical using electromotive-force (emf) techniques for the rotor position estimation based on fundamental model [21]-[29], without signal injection. At very low speed, the stator voltage is very small and thus, flux or rotor position estimations using stator voltage become very difficult to obtain.

All very low-speed, flux and position observers must be provided with a compensator of inverter nonlinearity, and with techniques for online estimation of the stator resistance.

This chapter aims yet another fundamental model sensorless control method for ac drives focusing on rotor position and speed estimation of IPMSM from a novel so called "active flux" observer, presented in Chapter 2 in an effort to simplify its online computation and to provide very low speed operation without any signal injection.

As it was demonstrated, the active flux is aligned to rotor d -axis implying that its speed is identical to the rotor speed, which is a strong asset in speed estimation at all speeds. Also, the active flux observer is very similar in all traveling field machines, which should be instrumental in developing easier unified motion sensorless ac drives.

Thus, main claims of this chapter lay into active flux based state observer implementation, but this time using DTFC-SVM control. The methodology has been verified experimentally on a sensorless DTFC-SVM IPMSM drive, and has been proven to work at very low operating speed (2 rpm) at half full rated load, as in the case of vector control presented in Chapter 2, and to have good estimation accuracy both in speed transients and in steady state. The proposed method is intended to general ac drives that allow a little hesitation at start and do not require sustained operation under 2 rpm.

4.2. Active Flux Concept for the IPMSM

As presented before in Chapter 2, the active flux vector $\bar{\psi}_d^a$, developed in [27] is defined as the flux that multiplies i_q in the dq -model torque expression of all ac machines:

$$T_e = 1.5p_1\psi_d^a i_q \quad (4.1)$$

For the IPMSM case, the module ψ_d^a , has the form:

$$\psi_d^a = \psi_{PMd} + (L_d - L_q(i_q))i_d; \quad L_d < L_q(i_q) \quad (4.2)$$

where p_1 is the number of pole pairs, i_d , i_q are the dq stator current components, L_d , $L_q(i_q)$ are the dq inductances, and ψ_{PMd} is the PM flux. ψ_d^a represents the total torque producing flux in (4.1).

As it can be observed from (4.1), the active flux vector $\bar{\psi}_d^a$ has the d -axis orientation, i.e, its position electrical angle is the rotor position $\theta_{er} = \theta_{\psi_d^a}$ and its speed is the rotor speed $\omega_r = \omega_{\psi_d^a}$, in any operation mode.

Eq. (4.2) is simply rewritten as (4.3) and then as (4.4):

$$\bar{\psi}_d^a = \psi_{PM} + L_d i_d + (jL_q(i_q)i_q) - L_q i_d - (jL_q(i_q)i_q) \quad (4.3)$$

$$\bar{\psi}_d^a = \bar{\psi}_s - L_q \bar{i}_s \quad (4.4)$$

The key result (4.4), valid in any reference frame, highlights that the active flux vector $\bar{\psi}_d^a = (\bar{\psi}_s, \bar{i}_s)$ is calculated by using $\bar{\psi}_s$ and \bar{i}_s , that are the stator flux and current vectors, respectively.

By using (4.4), the IPMSM voltage model in rotor reference frame “looses” magnetic anisotropy and manifests itself by the inductance $L_q(i_q)$ (torque current is i_q):

$$\bar{V}_s = R_s \bar{i}_s + (s + j\omega_r) L_q(i_q) \bar{i}_s + (s + j\omega_r) \bar{\psi}_d^a \quad (4.5)$$

where \bar{V}_s is stator voltage vector and R_s is the stator resistance. This is a definitive sign that the active flux IPMSM model is now a pure nonsalient rotor pole model, both for steady state and transients. The magnetic saturation influence is present in $L_q(i_q)$.

4.3. DTFC-SVM Sensorless Control System

This section gives an overview of a direct torque and flux controlled permanent magnet synchronous motor drive.

The key element of a direct torque controlled drive is the estimation of the stator flux linkage.

Fig. 4.1 illustrates the proposed DTFC-SVM sensorless control system for IPMSM, which contains the DTFC-SVM control, active flux observer, position-speed observer, and torque estimator.

DTFC-SVM guarantees fast torque response and smooth control of the drive, especially at low speeds.

The DTFC structure is based on the IPMSM voltage model in stator-flux reference frame [8], given by:

$$\bar{V}_s = R_s \bar{i}_s + d\psi_s / dt + j\omega_{\psi_s} \psi_s, \quad \text{with } \bar{\psi}_s = \psi_s + j0 \quad (4.6)$$

$$V_d = R_s i_d + d\psi_s / dt, \quad V_q = T_e R_s / (1.5p_1\psi_s) + \omega_{\psi_s} \psi_s \quad \text{with } T_e = 1.5p_1\psi_s i_q \quad (4.7)$$

where T_e is the torque and ω_{ψ_s} is the stator-flux speed that is different from ω_r during transients. Eq. (4.7) ensures the decoupling procedure: the flux closed-loop is controlled by $V_d \sim \Delta\psi_s$, the torque closed-loop is controlled by $V_q \sim T_e$, provided ψ_s is regulated for a constant value and there is a feed-forward compensation of the $\omega_{\psi_s}\psi_s$ term.

The DTFC-SVM system, shown in Fig. 4.2, ensures a decoupled-control of flux and torque, and fast torque responses.

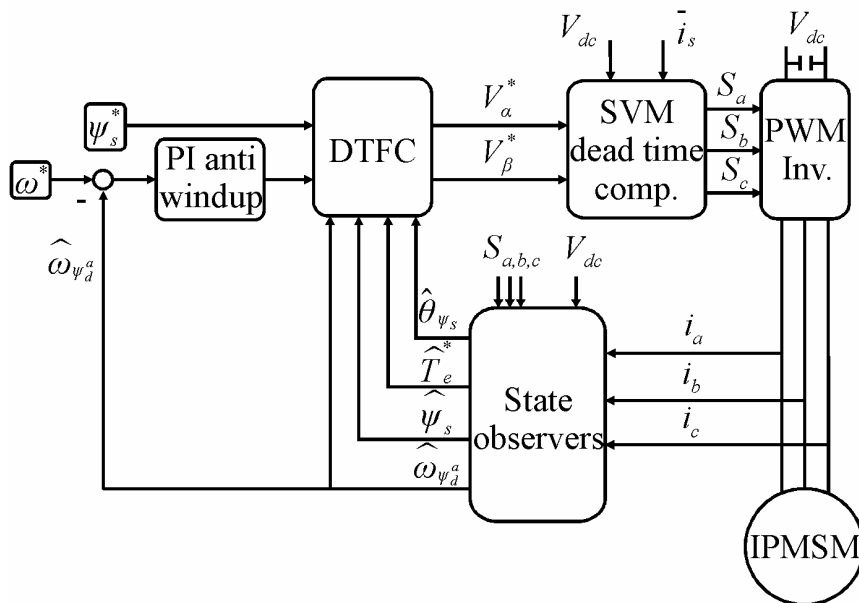


Fig. 4.1. Proposed DTFC-SVM sensorless control system for IPMSM.

It involves two parallel closed-loops with PI controllers operating in stator-flux reference frame: the torque control loop with (T_e^*, \hat{T}_e) and the stator-flux magnitude control-loop with $(\psi_s, \hat{\psi}_s)$. They provide the stator voltage reference in stationary frame (\bar{V}_s^*) by using the estimated stator-flux angle ($\hat{\theta}_{\psi_s}$) in the rotator operator.

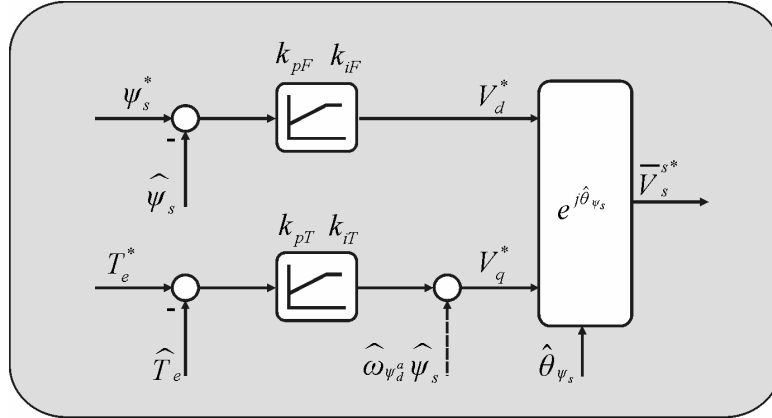


Fig. 4.2. DTFC-SVM structure in stator-flux reference frame.

The voltage source-inverter switching signals (S_a, S_b, S_c) are generated by the space vector modulation (SVM) block, which replaces the switching table in the conventional DTFC scheme and which employs dead time and inverter nonlinearities compensations to realize a suitable stator-voltage vector reference. This way, the torque and current pulsations result low. This compensation is indispensable for accurate active flux estimation, especially at very low speed.

For IPMSM, using trial and error procedure, the proportional and integral gains for the PI controller on the d -axis are $k_{pF} = 10$, $k_{iF} = 10 \text{ sec}^{-1}$, and for the PI controller on the q -axis are $k_{pT} = 3$, $k_{iT} = 30 \text{ sec}^{-1}$. The PI controllers have the form: $k_p(1 + k_i / s)$.

The speed controller is identical to that in the vector control system, also of PI type with anti-windup and torque limiter, and with a first order low-pass filter on speed reference ω_r^* . The PI gains are $k_{pw} = 0.1$ and $k_{iw} = 10 \text{ sec}^{-1}$.

DTFC method has been proven more robust than vector control method in sensorless control since it does not use Park operator, typical in vector control. Consequently, the estimated position error is not so important. Using the SVM block, the torque and current pulsations are significantly reduced.

4.4. State Observers

4.4.1. Active Flux Observer

As it was said before in Chapter 2 and Chapter 3, the main purpose of the active flux observer is to estimate the active flux vector using the measured stator current and the estimated stator voltage.

The active-flux observer implementation scheme is shown in Fig. 4.3 and consists in a stator flux observer $\hat{\psi}_s^s$ in large speed range based on combined voltage-current model, from which the term $L_q(i_q)^s$ is subtracted.

If the initial conditions of the integrators are respected and no offset exists in the voltage measurement and machine parameters have the correct values, the stator flux estimation is very accurate. The voltage drops on the stator resistance dominates the integrator input at low speeds, when the supply voltage V_s is low, also. For better results the initial value of the integrators are important.

The stator flux observer combines advantages of the current-model estimator in rotor reference at low speed, with the voltage-model estimator in stator reference at medium-high speed, employing a PI compensator that decides the flux estimation dynamic behavior in frequency domain.

The voltage model is generally regarded to perform well at high frequencies. However, due to possible errors in the estimated value of the stator resistance and errors in the measurement of the stator voltage and current, the integration becomes inaccurate.

Therefore either the current model or some other stabilization method has to be used to ensure good performance even at higher frequencies.

At very low speed including zero speed ($\omega_e \rightarrow 0$), the PI compensator gain, characterized in frequency domain by $k_{pc} - jk_{ic} / \omega_e$, has very high value. Thus, the stator flux estimation $\hat{\psi}_s^s$ follows the stator flux reference given by the open-loop current model $\hat{\psi}_{sj}^s$, to reduce the flux error.

At medium-high speed, the PI compensator gain practically remains only with the proportional component (low k_{pc}) and now, the correction loop could be considered an open one. Thus, the stator flux estimation $\hat{\psi}_s^s$ is given only by the

voltage model. The dc-offset ($\omega_e = 0$) from the measured current and voltage chains is totally compensated.

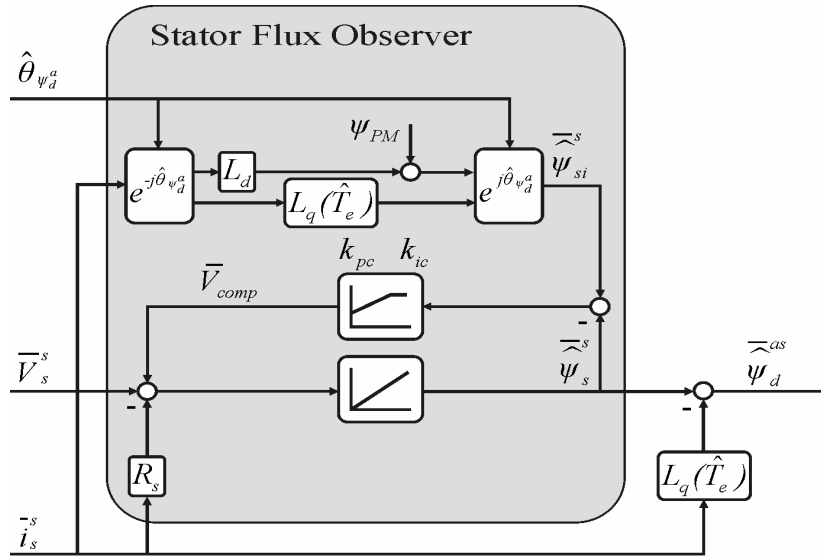


Fig. 4.3 Active flux observer

In conclusion, the frequency behavior of the PI compensator provides for the stator flux estimation a smooth transition, depending on speed, between the open-loop current model - sensitive to magnetic parameter variations (ψ_{PM}, L_d and $L_q(i_q)$), and the closed-loop voltage model - with mildly R_s influence.

The PI compensator gains are tuning by pole allocation method choosing double pole at 2 rad/s, resulting $k_{pc} = 4$, $k_{ic} = 4$, and $R_s = 4\Omega$ is set for hot temperature value.

Finally, the magnetic saturation has to be taken into consideration for an accurate active flux estimation [22]. Thus, here it is considered in the function $L_q(i_q)(\hat{i}_s^s)$:

$$L_q = L_{qn} / (1 + k_T |\hat{T}_e| / T_{en}) \tag{4.8}$$

where L_{qn} is the L_q nominal value, k_T is a torque coefficient, \hat{T}_e is the estimated torque and T_{en} is the rated torque value.

4.4.2. Position-Speed Estimator and Torque Estimator

As the active flux vector falls along the rotor d -axis, its speed is identical to the rotor speed, which greatly simplifies the speed estimation.

As presented in Chapter 3, to extract the rotor position and speed from the active flux vector, a solution is to employ derivative estimator based on (4.9)-(4.11) :

$$\hat{\omega}_{\psi_d^a} = d\hat{\theta}_{\psi_d^a} / dt \quad (4.9)$$

$$\hat{\theta}_{\psi_d^a} = \text{atan}(\hat{\psi}_{d\beta}^a / \hat{\psi}_{da}^a) \quad (4.10)$$

$$\hat{\omega}_{\psi_d^a} = \frac{\hat{\psi}_{dak-1}^a \hat{\psi}_{d\beta k}^a - \hat{\psi}_{d\beta k-1}^a \hat{\psi}_{dak}^a}{h(\hat{\psi}_{dak}^a{}^2 + \hat{\psi}_{d\beta k}^a{}^2)} \quad (4.11)$$

where h is the sampling period, and the index $k - 1$ in (4.11) refers to one sampling time period delayed.

The drawback of this solution is that the speed estimation accuracy is strictly dependent on the accuracy of the active flux components estimation. The accuracy of active flux depends on the electromagnetic parameters and the noise and offset of the measured signals. To remove the noise from the estimated speed a low pass filter (LPF) (4.12), small time-constant, is applied to the estimated speed to reduce noise:

$$H_{LPF} = k_{pF} / (T_{iF} \cdot s + 1) \quad (4.12)$$

where $k_{pF} = 1$, $T_{iF} = 0.003$ sec.

If the active flux vector is correctly estimated, the electromagnetic torque \hat{T}_e is simply computed based on (4.1).

From the active flux observer, the rotor position estimation is used in rotator operators in Fig. 4.3, and the rotor speed estimation is used for the speed control loop. So if the vector control system can be affected by inaccurate rotor position

estimation $\hat{\theta}\psi_d^a$, in DTFC-SVM (Fig. 4.2), none of them are used, this fact being an inherent advantage of DTFC motion-sensorless control.

4.5. Digital Simulation Results

For theoretical validation of the active flux concept, a Matlab-Simulink simulation model has been built and run.

Fig. 4.4 illustrates the Matlab-Simulink implementation of the DTFC basic scheme.

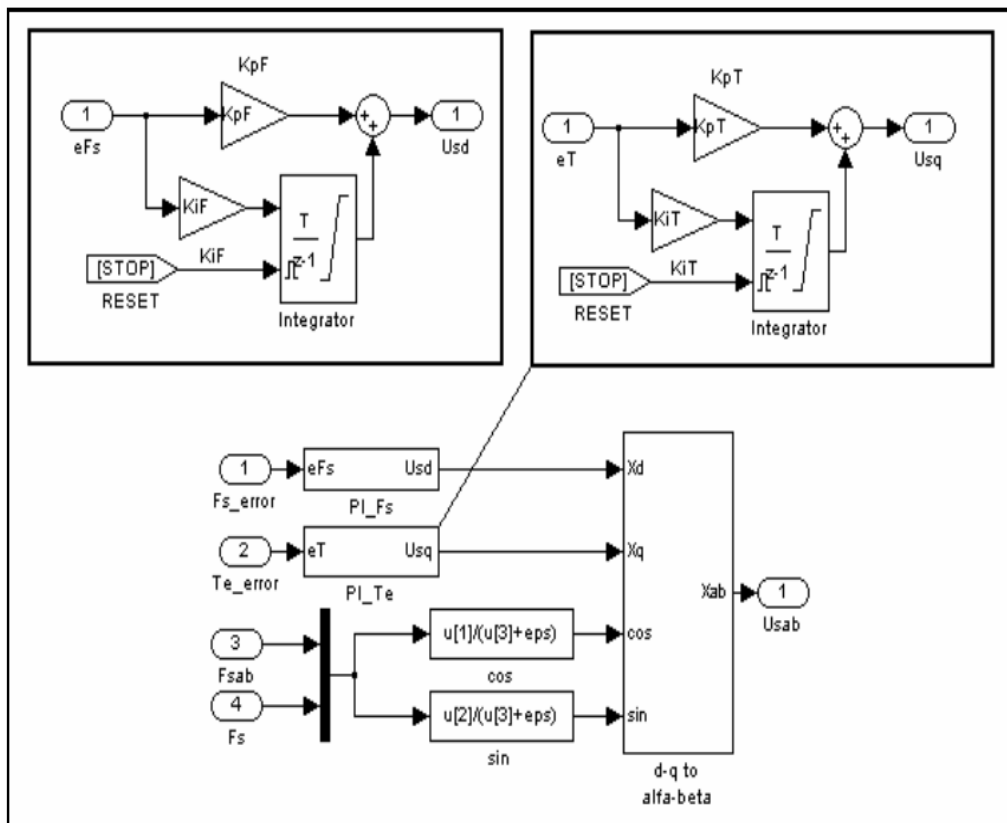


Fig. 4.4. Matlab-Simulink implementation of DTFC basic scheme

Of course, for the sensorless implementation, the rotor position and speed estimation has been of important interest.

In order to obtain accurate rotor position and speed estimations, the active flux (the angle as well as the magnitude) has to be estimated as good as possible.

The operation at low speeds involves small currents. When the currents are small, the sensorless control becomes difficult.

The performances of the DTFC sensorless control technique are evaluated in terms of transient responses: startup, speed reversal and load torque variation.

In order to prove by digital simulation results the motion-sensorless based on active flux concept of the IPMSM using DTFC-SVM, the following tests were performed:

- Startup with full torque to -2 rpm followed by transients from -2 rpm to 2 rpm at $t=2$ s and then a speed step at 5 rpm at $t=3.5$ s

Usually, in practice, operation with the motor loaded than unloaded is desired.

To see how the control system responses when is fully loaded from standstill this simulation test was performed under this condition.

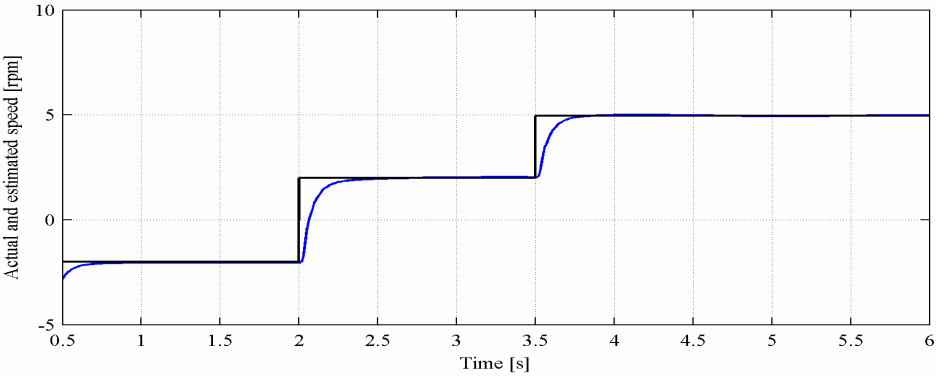
As it can be seen in Fig. 4.5b the speed error is large (almost 200 rpm), but this is only at start up, the machine being full loaded.

In steady state and even during speed reversal from -2 rpm to 2 rpm and from 2 rpm to 5 rpm the speed error is very small (around 5 rpm).

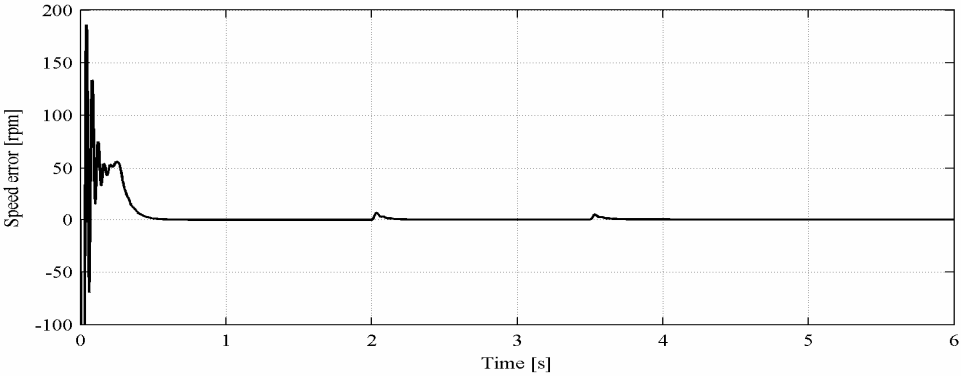
Also the rotor position estimation is very good: actual and estimated angle rotor position in Fig. 4.5c being overlapped and the rotor position error being below 0.02 rad with the exception of start up when is almost 0.15 rad.

Thus, the proposed active flux concept is proven.

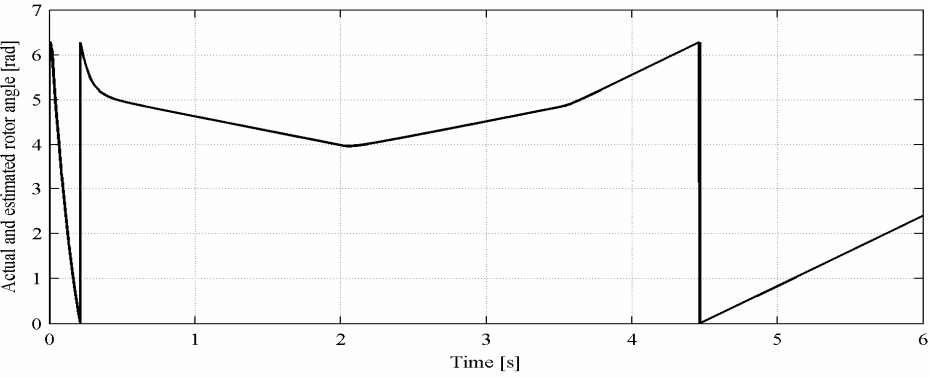
Fig. 4.5e shows the torque developed by the machine and respectively in Fig. 4.5f the currents which are very sinusoidal and smooth are illustrated.



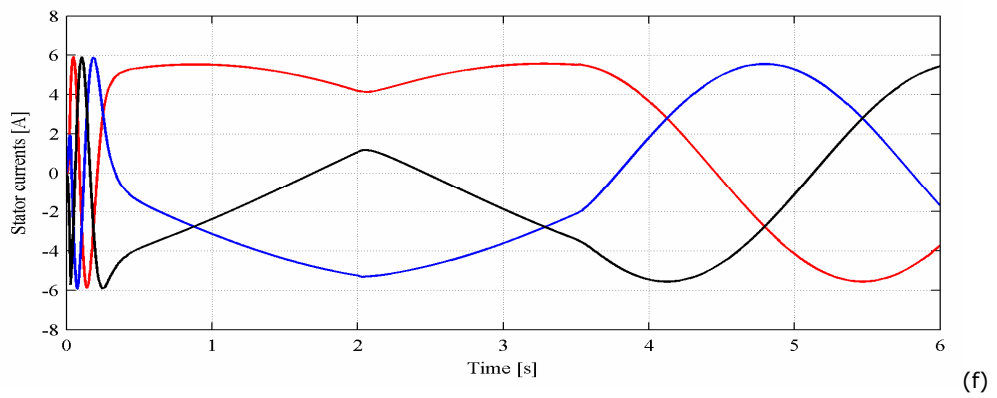
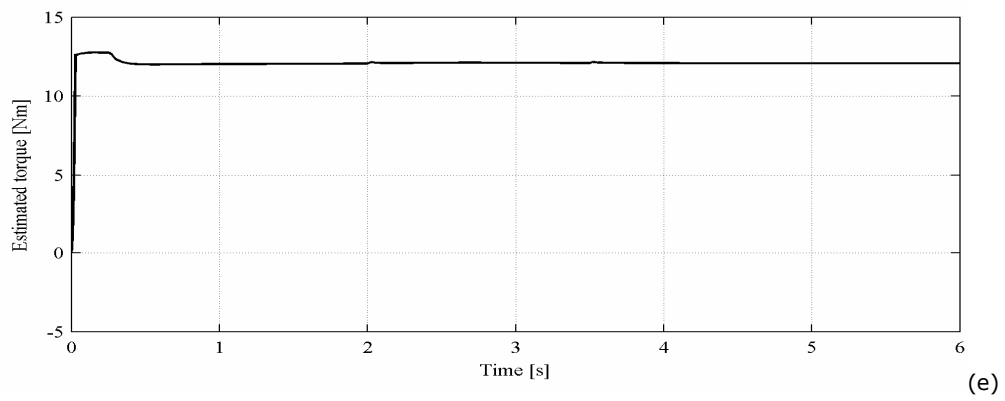
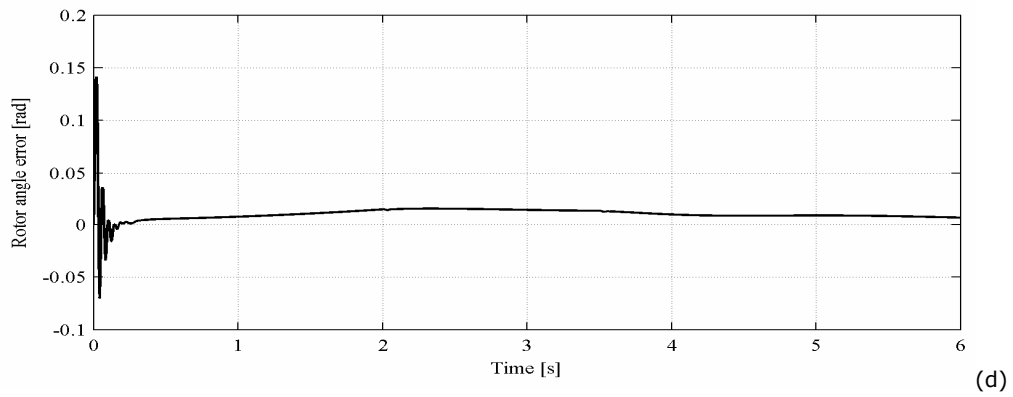
(a)



(b)



(c)



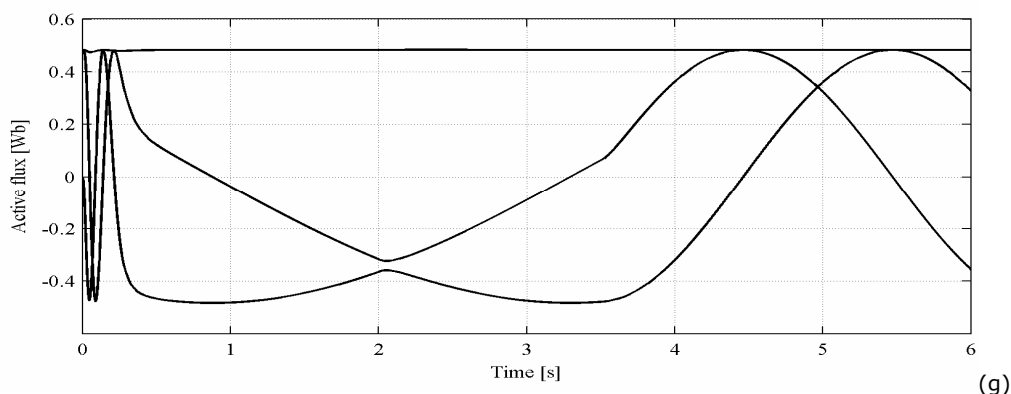


Fig. 4.5. Startup with full torque to -2 rpm followed by transients from -2 rpm to 2 rpm at $t=2$ s and then a speed step at 5 rpm at $t=3.5$ s; from top to bottom: (a).reference and estimated speed; (b). error between actual and estimated speed; (c). actual and estimated rotor angle (overlapped); (d). error between actual and estimated rotor angle; (e). estimated torque; (f). stator currents i_{abc} ; (g). active flux and its two components: $\psi_{d\alpha}^a$ and $\psi_{d\beta}^a$

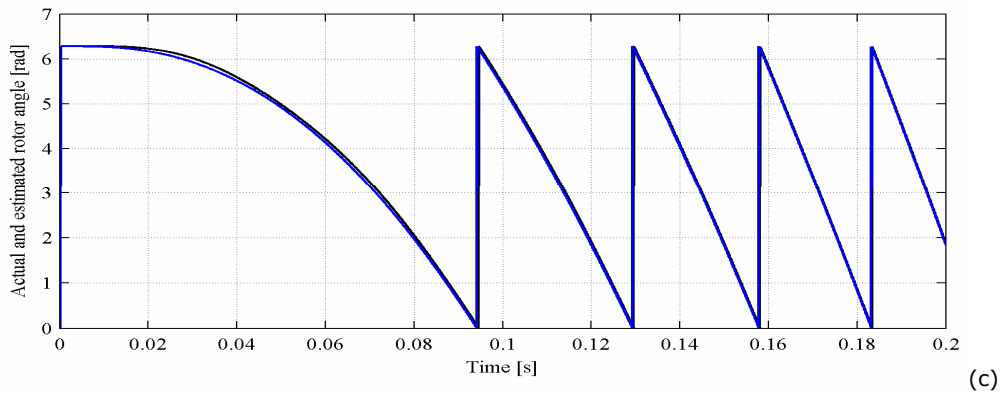
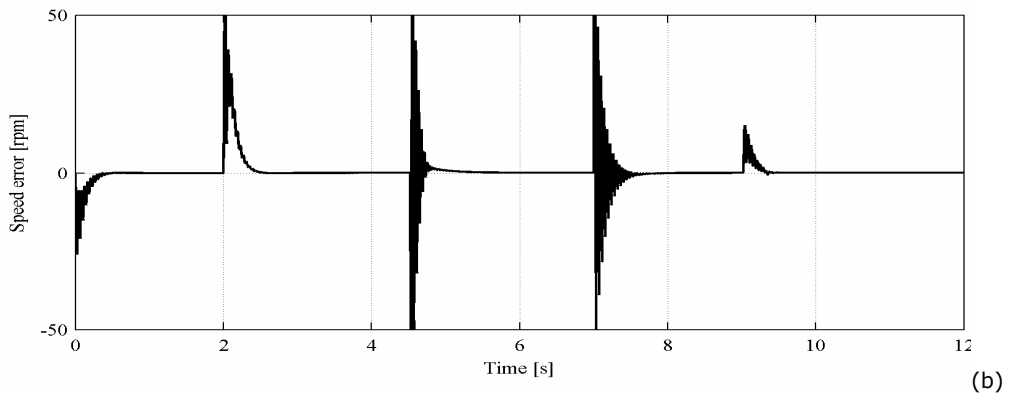
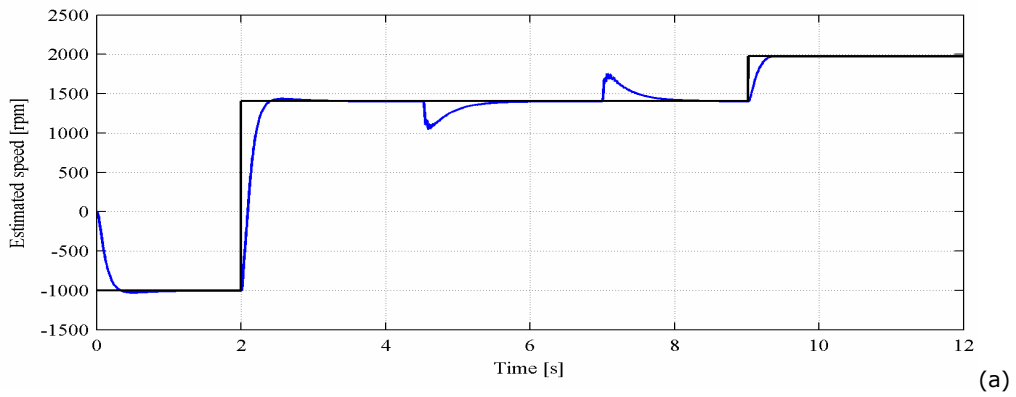
- Transients from -1400 rpm to 1400 rpm at $t=2$ s, followed by a full step torque load at $t=4.5$ s then an unload at $t=7$ s and followed by a speed step to 2000 rpm at $t=9$ s

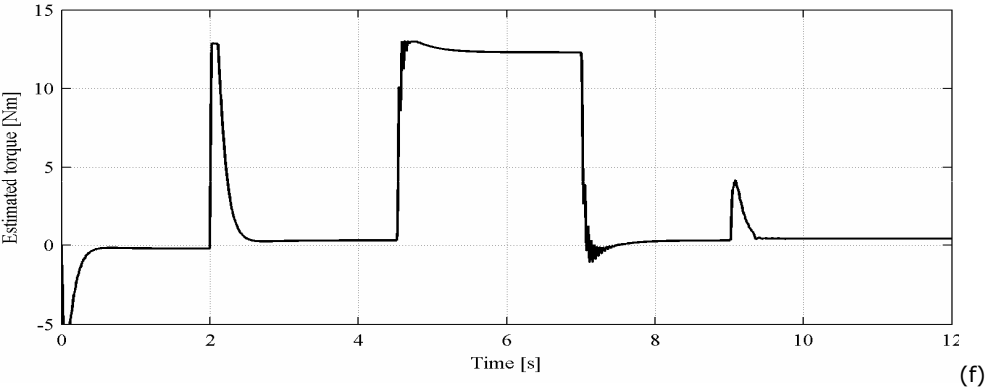
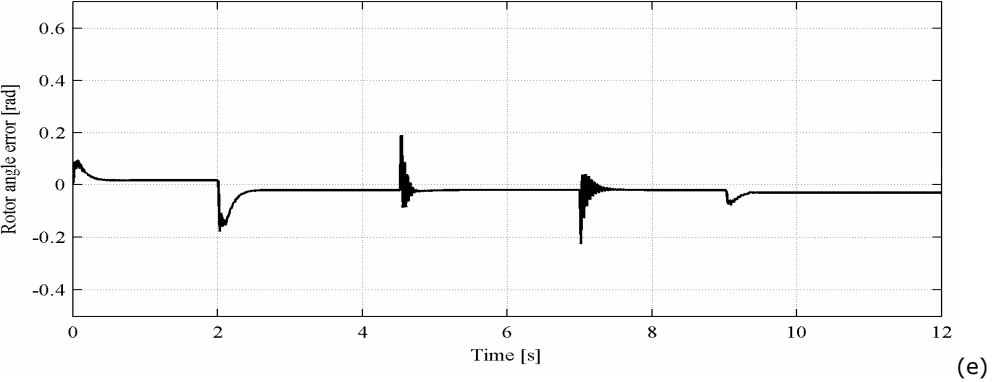
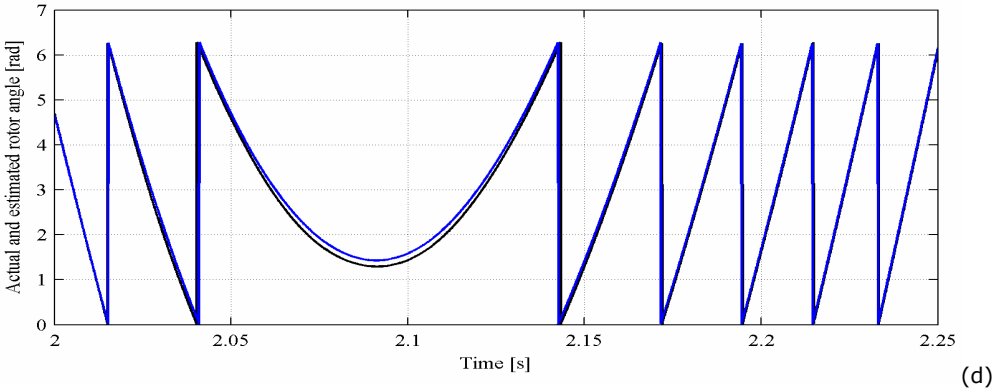
This test was performed in order to also validate the high speed operation based on active flux concept.

The speed error is presented in Fig. 4.6b. It can be observed that this speed error is large only during transients (maximum 50 rpm, as in the case of vector control system).

Fig. 4.6c and Fig. 4.6d present a zoom of the two rotor angles (the actual and the estimated one) during the most critical instants of time: the start-up from 0 to -1400 rpm and the speed reversal from -1400 rpm to +1400 rpm. It can be observed that the estimated rotor angle (blue line) follows the actual one (the maximum angle rotor position error is 0.22 rad).

As it can be seen, the stator three phase currents are not larger than the admitted ones (Fig. 4.6g) and the hodograph of the active flux is circular (Fig. 4.6h).





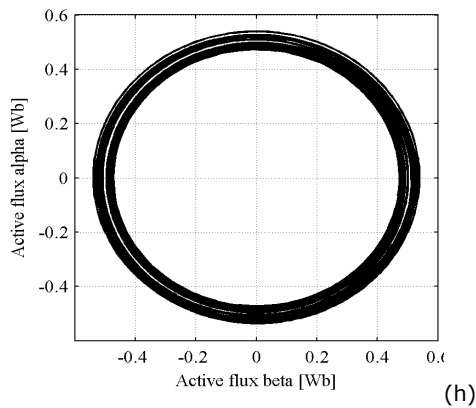
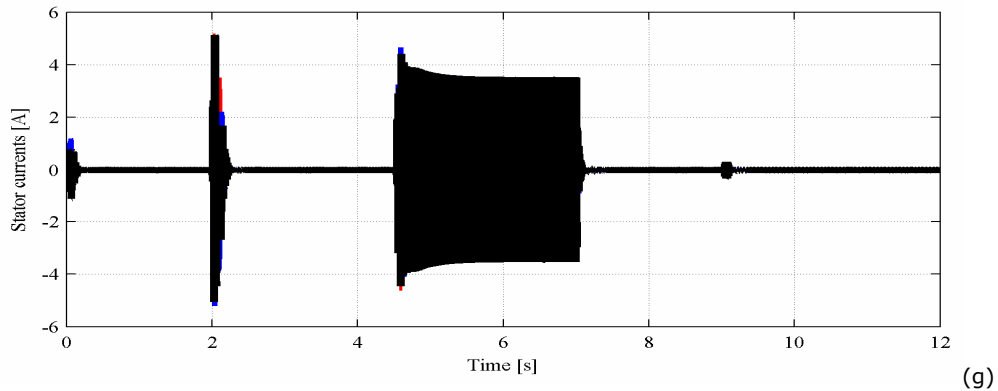


Fig. 4.6. Transients from -1400 rpm to 1400 rpm at $t=2$ s, followed by a full step torque load at $t=4.5$ s then an unload at $t=7$ s and followed by a speed step to 2000 rpm at $t=9$ s; from top to bottom: (a).reference and estimated speed; (b). error between actual and estimated speed; (c). actual and estimated rotor angle (overlapped) during start up; (d). actual and estimated rotor angle (overlapped) during speed reversal; (e). error between actual and estimated rotor angle; (f). estimated torque; (g). stator currents i_{abc} ; (h). active flux hodograph

In conclusion, the simulations results confirm that the sensorless DTFC system based via active flux model gives a good tracking performance for different speeds with and without load.

4.6. Experimental Results

Once, the digital simulations seem to give confidence into the proposed sensorless DTFC-SVM system for IPMSM drive, the experimental work was pursued.

The proposed sensorless direct torque and flux control (DTFC-SVM) is validated on the experimental setup presented in Chapter 6.

Here, again, we confront with the same problems as in the vector control system: the stator voltage applied to machine is lower than the commanded one because of dead-time losses and the stator resistance variation, especially at low speeds.

So, the implementation of the compensation methods of voltage drops on inverter power devices and of inverter dead time, presented in Chapter 3, play again an important role in achieving very low speed operation of 2 rpm.

The startup procedure presented in Chapter 3 is also necessary to align the rotor at zero.

In all experimental tests the sensorless control system was used.

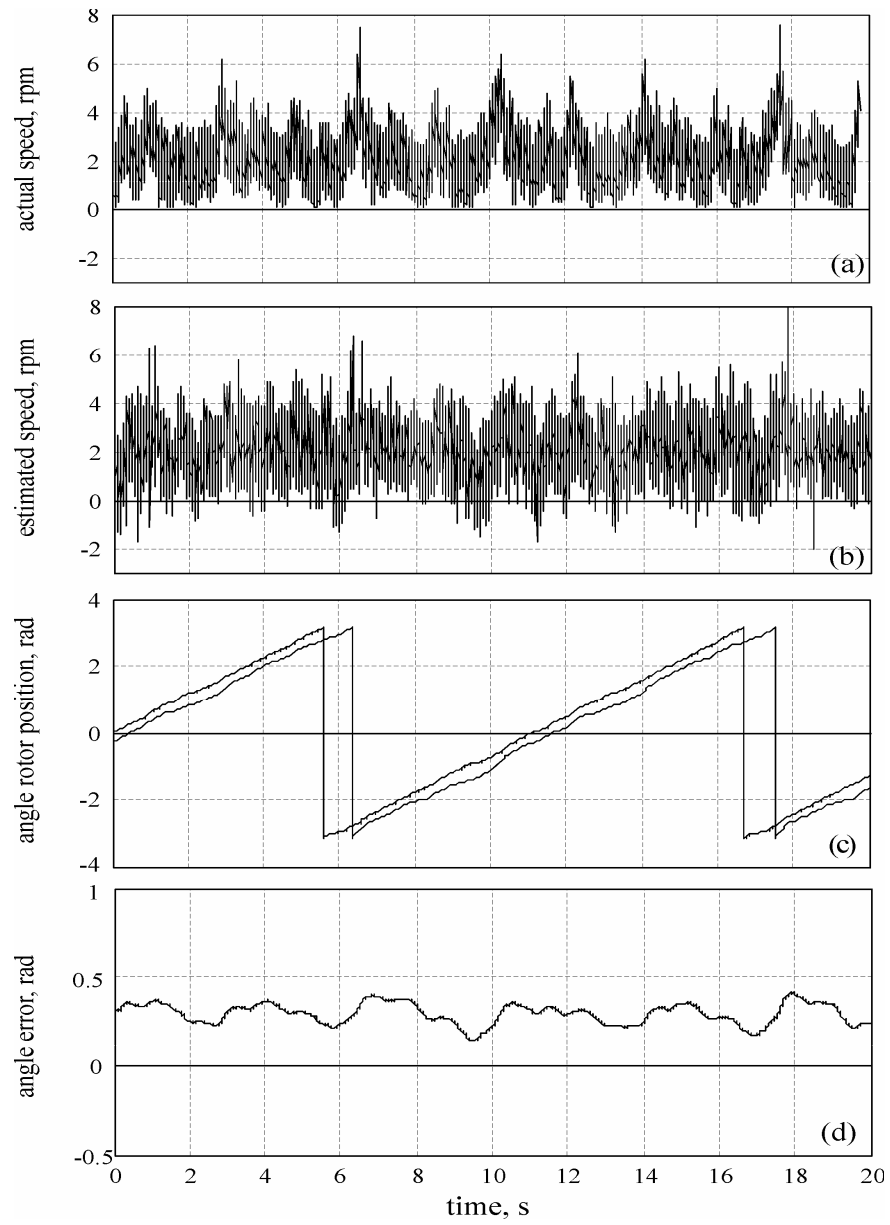
As we expected from theory, during experiments, it was observed that the control was sensitive to dead-time and voltage drops on the inverter power devices (the stator voltage applied to machine is lower than the commanded one because of them), and to the stator resistance, especially at low speeds.

For a good image of how the sensorless control system works, various tests considered to be relevant have been performed, in a speed range from very low speed to high speed of 1400 rpm.

All the experiments have been carried out with a limited value (50%) of rated motor torque because we did not have a stable loading machine at very low speed (2 rpm or so) for more than 50% rated torque.

The following experiments are performed to check the concepts and performance of the proposed motion-sensorless control system:

- Steady state operation at lowest speed (2 rpm) and 50% rated torque



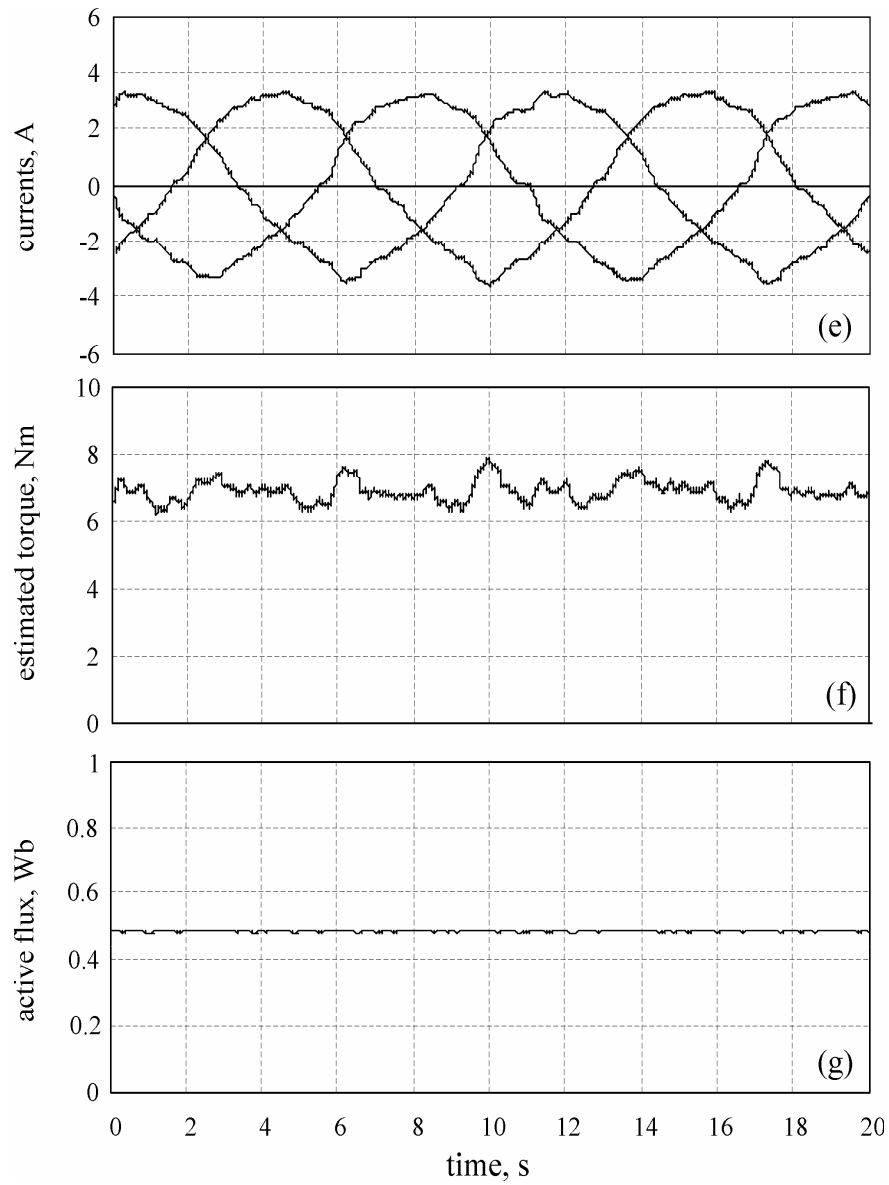


Fig. 4.7. Steady state sensorless operation at lowest speed of 2 rpm (0.1Hz) and 50% rated torque; from top to bottom: (a). actual speed, (b). estimated speed, (c). angle rotor position (actual and estimated), (d). error between estimated and actual angle rotor position (e). measured currents, (f). estimated torque and (g). active flux

- Step speed reduction from 5 rpm to 2 rpm at 50% rated torque

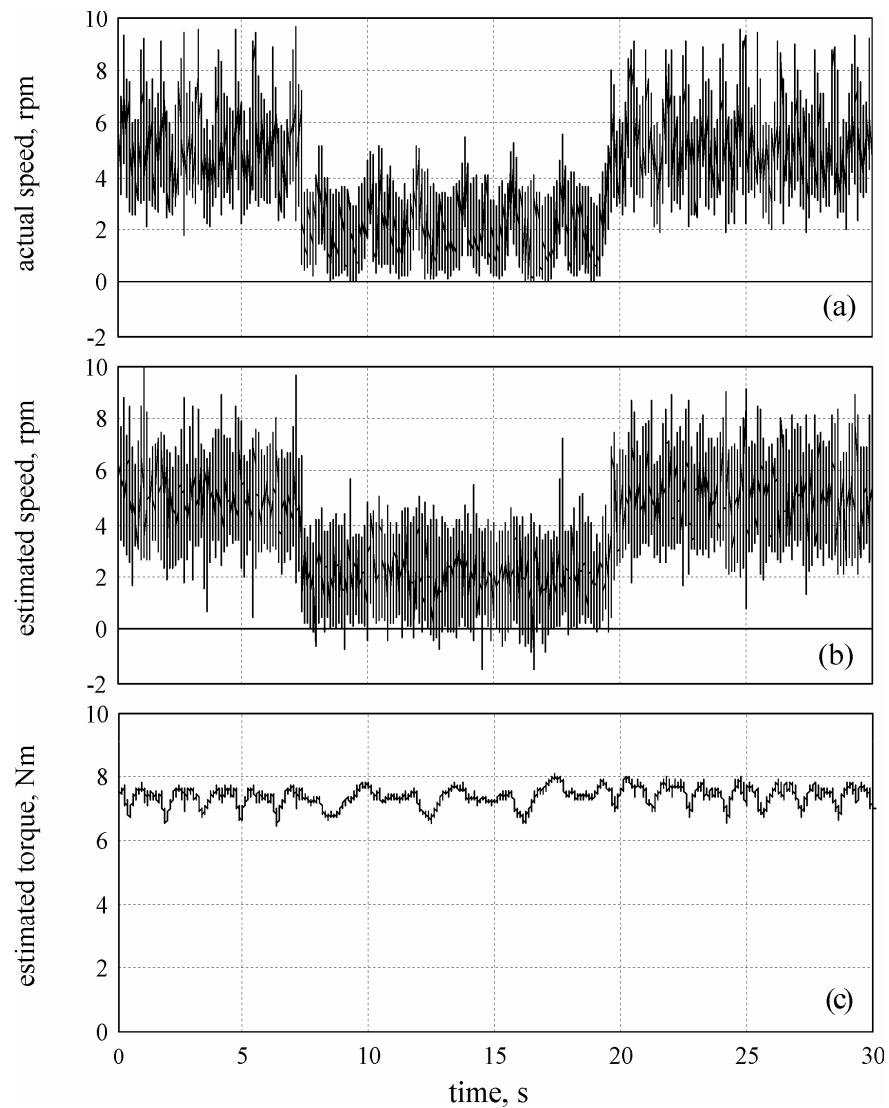
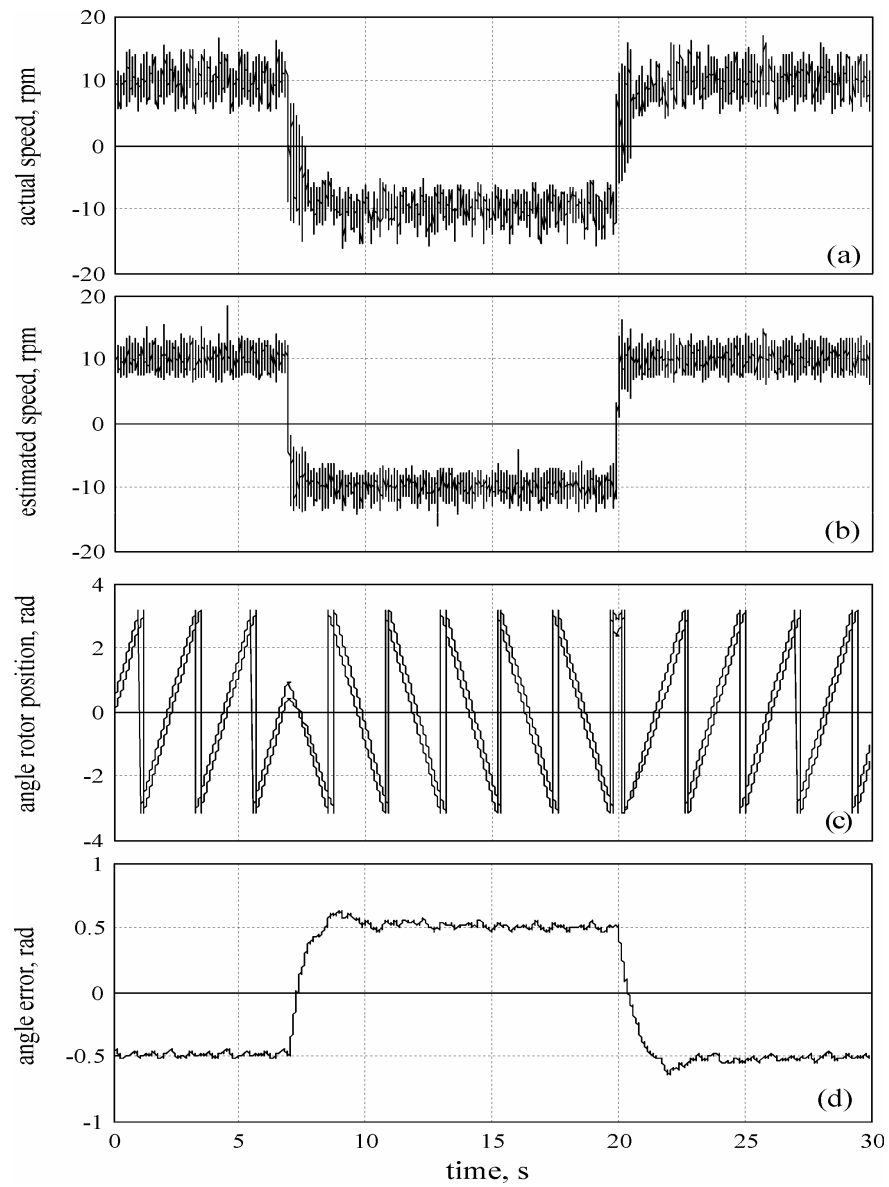


Fig. 4.8. Transients from 5 rpm (0.25 Hz) to 2 rpm (0.1 Hz) at 50% rated torque; from top to bottom: (a). actual speed, (b). estimated speed and (c). estimated torque

- ± 10 rpm speed reversal at 50% rated torque



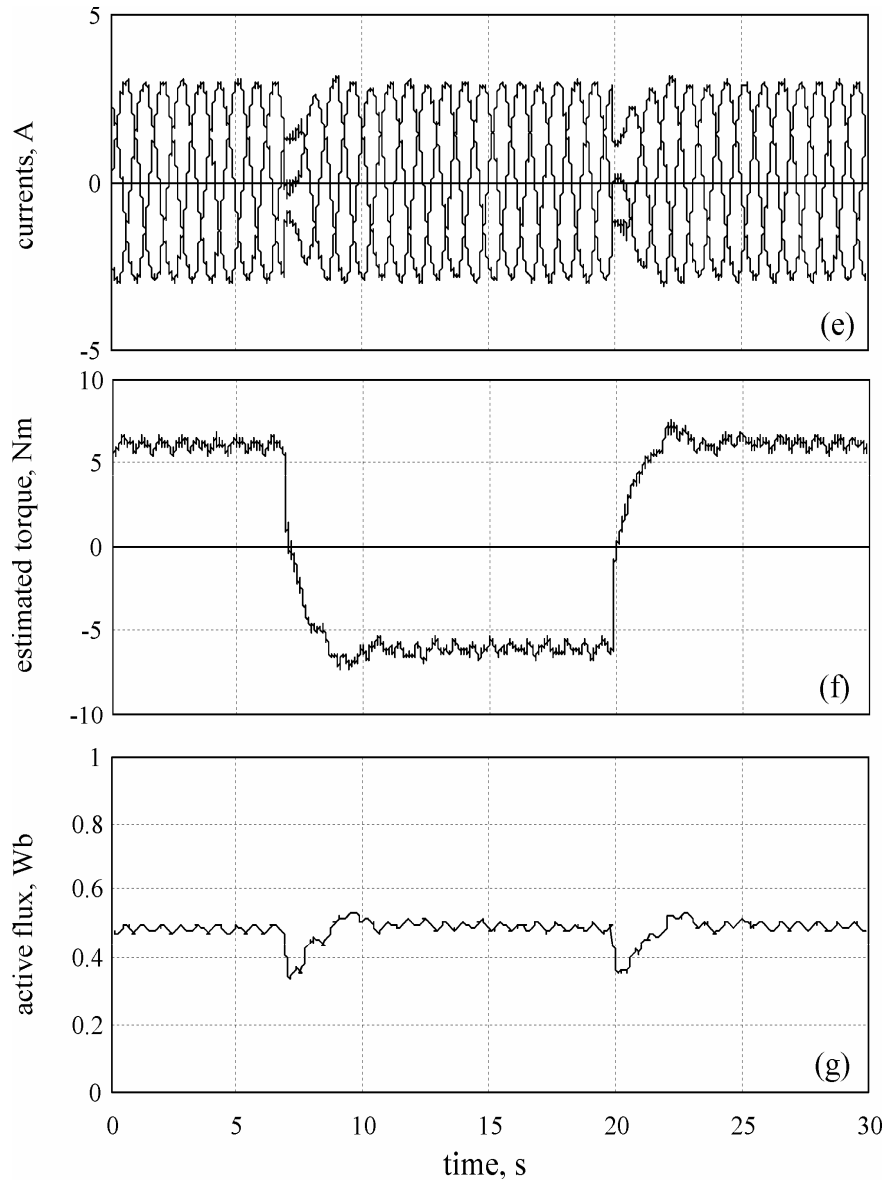
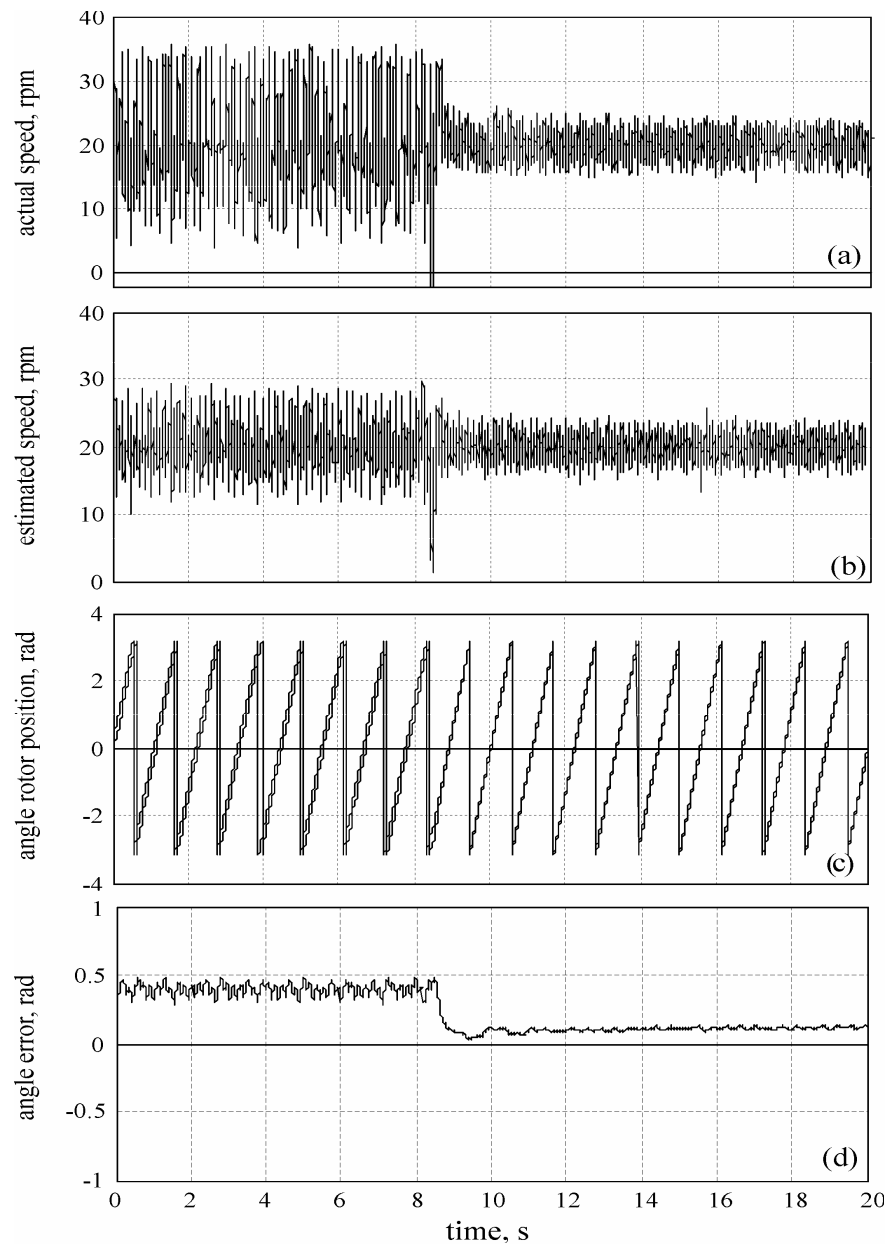


Fig. 4.9. Speed reversal at ∓ 10 rpm (0.5 Hz) and 50% rated torque; from top to bottom: (a). actual speed, (b). estimated speed, (c). angle rotor position (actual and estimated), (d). error between estimated and actual angle rotor position (e). measured currents, (f). estimated torque and (g). active flux

- Step torque response at 20 rpm



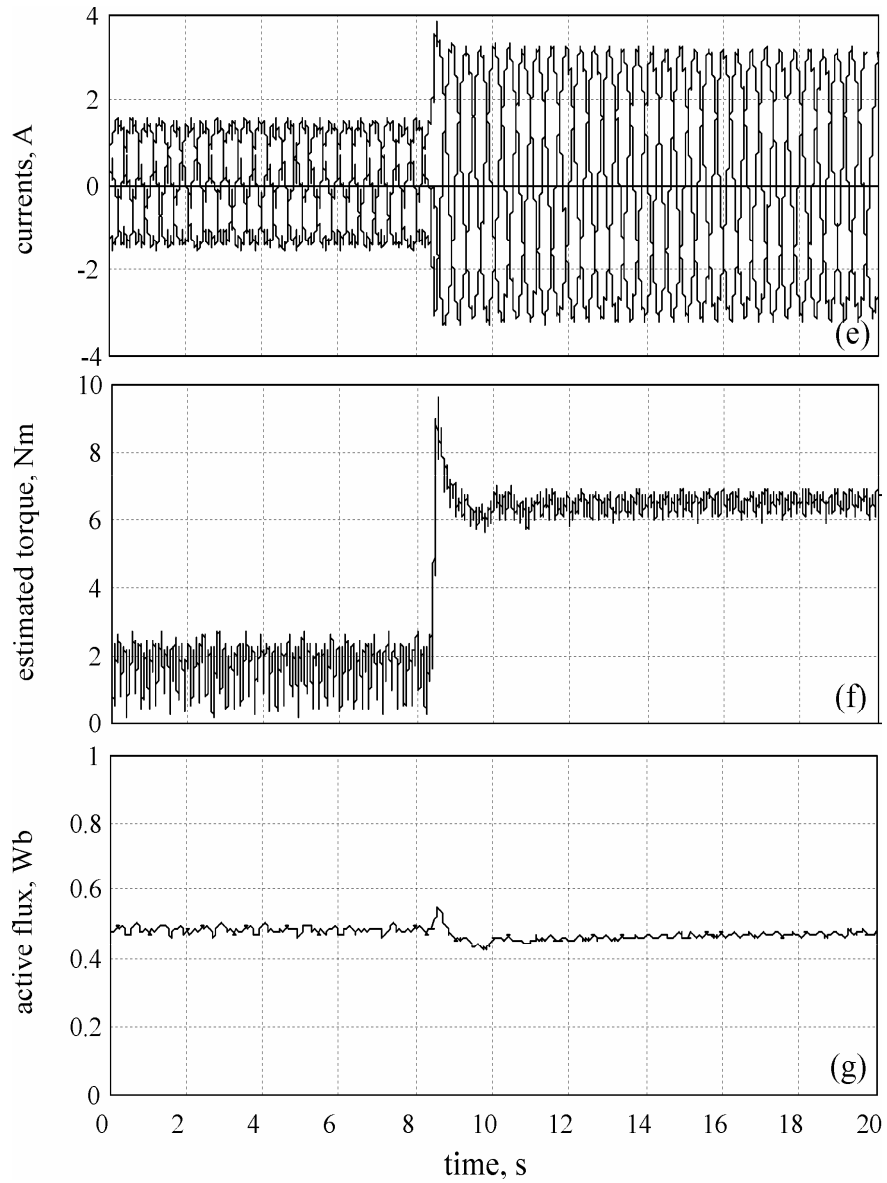
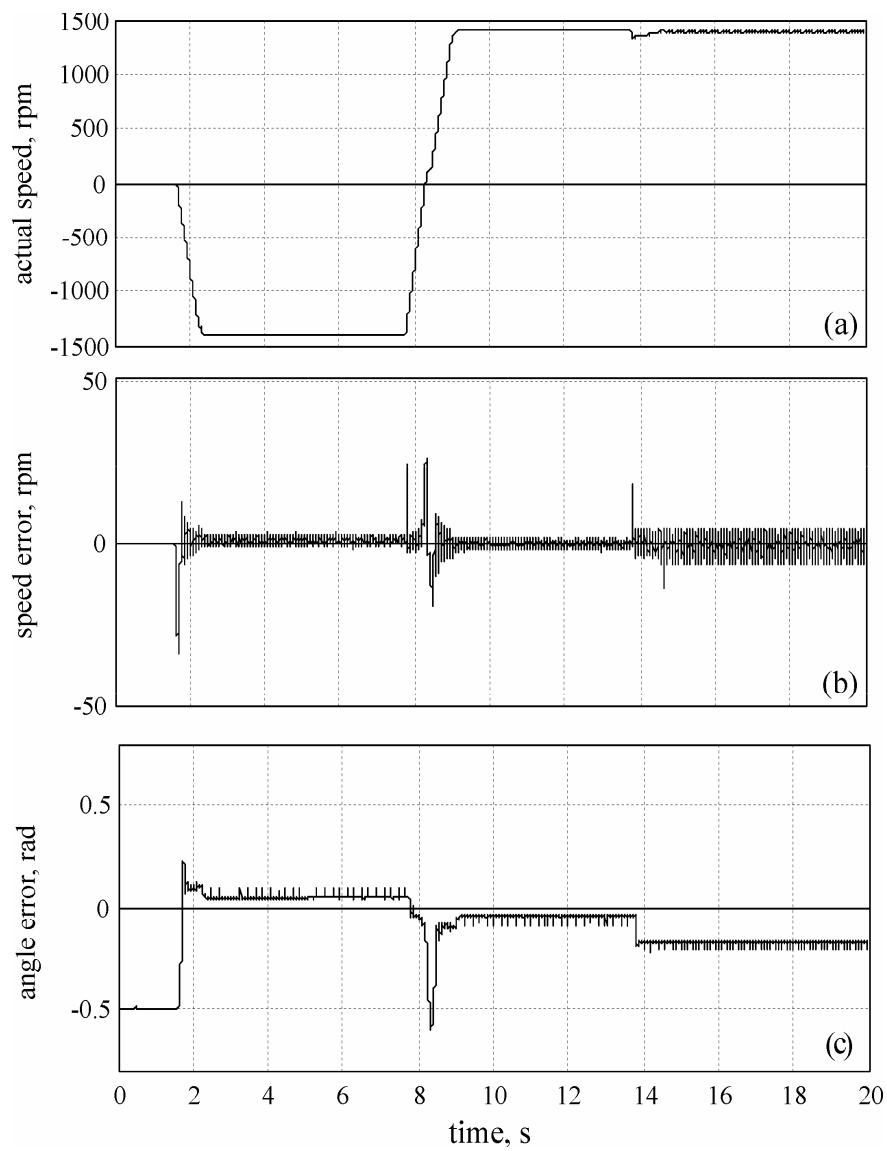


Fig. 4.10. Torque transients at 20 rpm (1 Hz) and 50% rated torque; from top to bottom: (a). actual speed, (b). estimated speed, (c). angle rotor position (actual and estimated), (d). error between estimated and actual angle rotor position (e). measured currents, (f). estimated torque and (g). active flux

- Start up response from zero to 1400 rpm, followed by ± 1400 rpm speed reversal, plus 50% step torque loading response



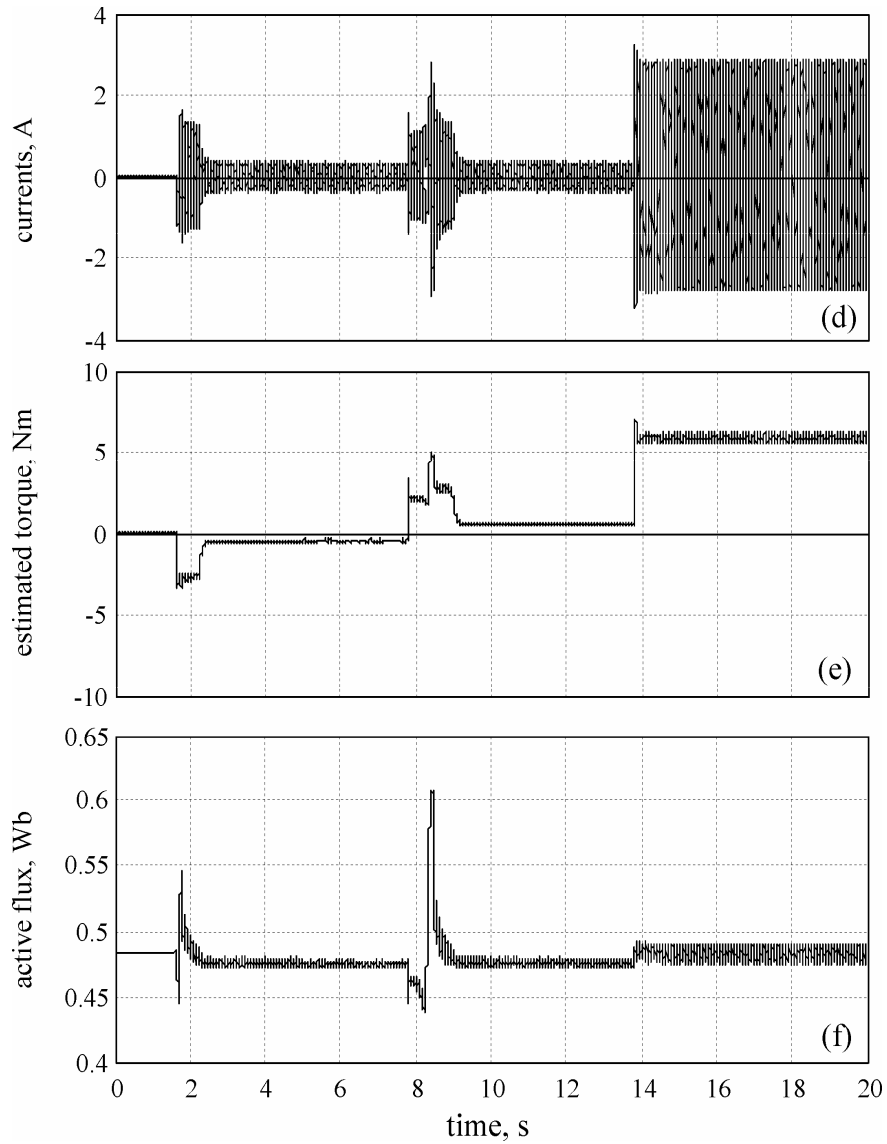


Fig. 4.11. Startup response from 0 to -1400 rpm (70 Hz), speed reversal at \mp 1400 rpm and torque transients at 1400 rpm at 50% rated torque; from top to bottom: (a). actual speed, (b). error between estimated and actual speed, (c). angle rotor position (actual and estimated), (d). error between estimated and actual angle rotor position (e). measured currents, (f). estimated torque and (g). active flux

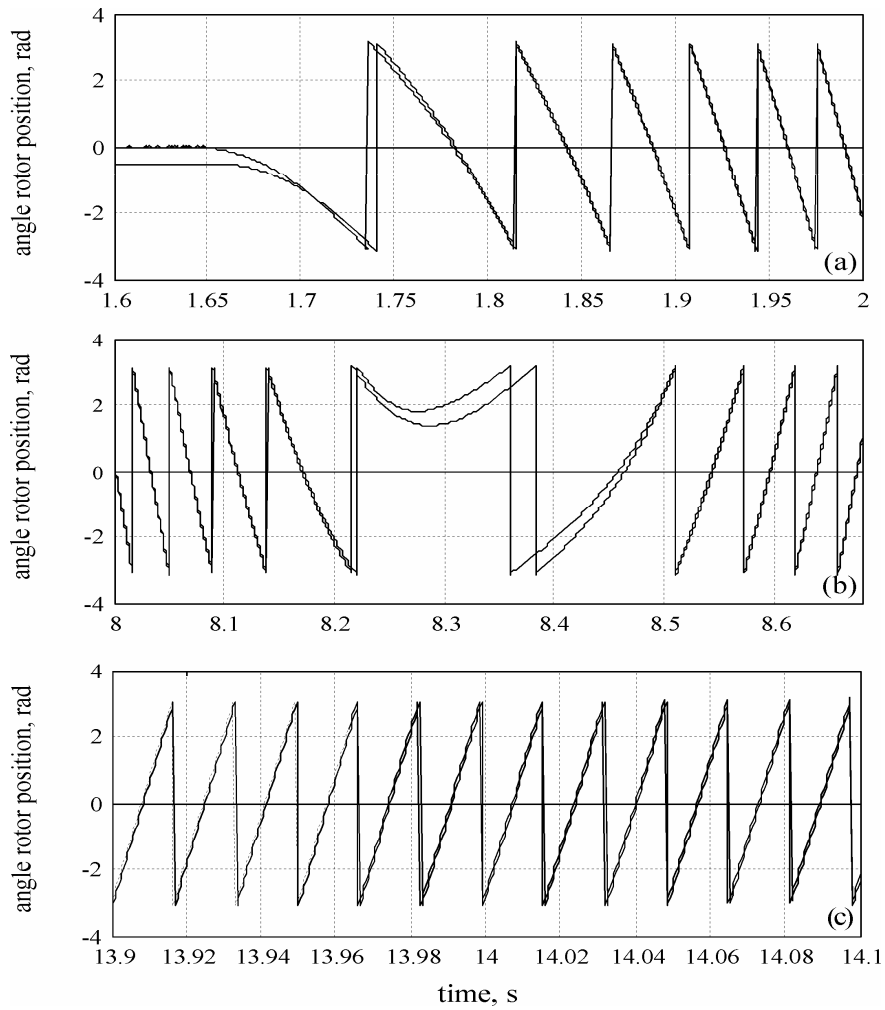


Fig. 4.12. Start up response from 0 to -1400 (70 Hz) rpm, speed reversal at \mp 1400 rpm and torque transients at 1400 rpm at 50% rated torque; from top to bottom: (a). actual and estimated angle rotor position at start up, (b). during speed reversal and (c). during step torque load

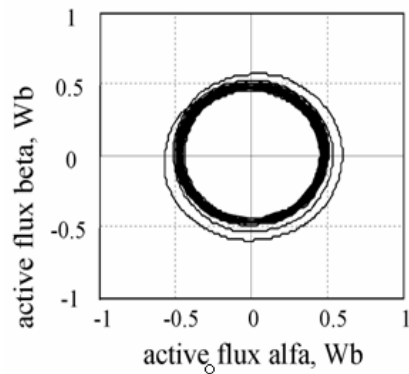


Fig. 4.13. Start up response from 0 to -1400 rpm, speed reversal at \mp 1400 rpm and torque transients at 1000 rpm at 60% rated torque: active flux beta versus active flux alpha hodograph

The DTFC motion-sensorless control for IPMSM is experimentally proven by stable steady state operation at lowest speed limit of 2 rpm (0.1 Hz) and 50% rated load torque with good performance (see Fig. 4.7), taking into account that the novel concept of active flux is employed, and not signal injection methods.

In DTFC case, the rotor position estimation enters only in the current model based stator flux estimator, which is important only at low speeds. Thus, the position error at medium and high speeds is not important at all. The speed estimation error really counts in the speed control loop. Note that, if the rotor position error is rather constant, then the speed is correctly estimated.

Even with partial compensation of the VSI nonlinearities, the currents and the torque are not quite smooth and the measured speed has some pulsations, but in acceptable limits for general variable speed drive applications.

These could be due to the cogging torque, partial-compensated nonlinearities, and other non-modeled disturbances.

To check the dynamics at very low speeds, operation from 5 rpm to 2 rpm is tested with good results (Fig. 4.8).

Fig. 4.9 shows good results obtained from a speed reversal operation at \pm 10 rpm and 50% of rated torque. Here, the currents are smooth, the torque shows some pulsations, but they are again, reasonable.

Torque transients at 20 rpm for step-loading from 0 to 50% rated torque, with an acceptable overshooting are presented in Fig. 4.10.

Start up response from 0 to -1400 rpm, speed reversal at ± 1400 rpm, and torque transients at 1400 rpm at 50% rated torque are all shown in Fig. 4.11-Fig. 4.13 with good expected dynamics at high speeds.

Fig. 4.12 illustrates the actual (provided by the encoder) and the estimated rotor position angle. Only at startup a small difference between the two waveforms (actual and estimated) can be observed.

In this case, the implemented observer operates for acceptable parameter values and has small errors. In encoderless systems, the duration of position angle computation, is decisive. If the estimated angle has large oscillations comparatively with the encoder angle, then the system will not operate properly. This is visibly during operation at high speeds, where the angle estimator should be very fast and without large oscillations.

The speed estimation error really counts because a speed feedback is used for speed loop control. The speed estimation errors are up to 30 rpm during speed transients, but they go down to less than 2-5 rpm during steady state.

Note that if the rotor position error is constant, then the speed estimation will be correct.

The intended purpose of all these experiments is to validate the concept of "active flux" for motoring and generating. Changing the speed sign and maintaining the torque sign involve operation of IPMSM in generating (see Fig. 4.10).

Comparing the experimental results with the results obtained through digital simulation, it can be said that, excepting low speeds where, due to the large rotor position error, the results can not be compared, at high speeds almost the same results are obtained. Much more, we can even say that the experimental results are better if we refer to the speed error during during speed reversal from -1400 rpm to +1400 rpm (around 25 rpm in experiments and 50 rpm in simulation).

In summary, note that DTFC, as it was demonstrated for the vector control in Chapter 3, is capable to sustain 2 rpm (0.1Hz) operation with 50% load torque, and in general, good low speed transients operations.

At low speed, by showing a lower value of the position error, DTFC has been proven more robust than vector control.

4.7. Conclusion

The novel state-observer for flux, rotor position and speed is developed based on the concept of active flux, particularized for motion-sensorless for IPMSM drive using DTFC-SVM. No signal injection is involved.

The IPMSM drive performs with good results in a wide speed range down to 2 rpm and up to 1400 rpm.

Through experimental tests, sustained sensorless operation at low speed down to 2 rpm is obtained, with stable operation to 50% rated load torque step perturbation. The rotor position errors are visible, but limited. They occur, however, only in the active flux observer at very low speeds because DTFC is performed.

For making a comparison between theory and practice, digital simulations of the motion-sensorless control system are also presented. Both of them validate the active flux concept for motion-sensorless DTFC-SVM for IPMSM drive.

References

- [1] L. Tang, L. Zhong, M. F. Rahman and Y. Hu, "A Novel Direct Torque Control for Interior Permanent Magnet Synchronous Machine Drive System with Low Ripple in Flux and Torque and Fixed Switching Frequency," *IEEE Trans. Power Electron.*, vol. 19, pp. 346-354, March 2004
- [2] C. G. Mei, S. K. Panda, J. X. Xu and K. W. Lim, "Direct Torque Control of Induction Motor – Variable Switching Sensors," *Conf. Rec. IEEE-PEDS*, pp. 80-85, July 1999, Hong Kong.
- [3] C. Lascu, I. Boldea and F. Blaabjerg, "A Modified Direct Torque Control for Induction Motor Sensorless Drive," *IEEE Trans. Ind. Applicat.*, vol. 36 no.1, pp.122-130, Jan/ Feb 2000.
- [4] C. Martins, X. Roboam, T. A. Meynard and A. S. Caryalho, "Switching Frequency Imposition and Ripple Reduction in DTC Drives by Using a Multilevel Converter," *IEEE Trans. Power Electron.*, vol. 17, issue 2, pp. 286-297, March 2002.
- [5] G. S. Buja and M. P. Kazmierkowski, "Direct torque control of PWM inverter-fed AC motors – a survey," *IEEE Trans. Ind. Electron.*, vol. 51, pp. 744-757, 2004.
- [6] Z. Xu and M. F. Rahman, "A variable structure torque and flux controller for a DTC IPM synchronous motor drive," *Power Electron. Conf., PESC 2004 IEEE 35th Annual Meeting*, vol.1, pp. 445-450, June 2004.
- [7] S. Ozcira, N. Bekiroglu, and E. Aycicek: "Direct Torque Control of Permanent Magnet Synchronous Motor Using LP Filter", in *Conf. Record IEEE-ICEM 2008*.
- [8] G.-D. Andreescu, C. I. Pitic, F. Blaabjerg, and I. Boldea: "Combined flux observer with signal injection enhancement for wide speed range sensorless DTFC of IPMSM drives," *IEEE Trans. Energy Convers.*, vol. 23, no. 2, pp. 393–402, 2008.
- [9] Kim, T., Lee, H.-W., and Ehsani, M.: "Position sensorless brushless DC motor/generator drives: review and future trends", *IET Electr. Power Appl.*, vol. 1, no. 4, pp. 557–564, 2007.

- [10] O. Wallmark, and L. Harnefors: "Sensorless control of salient PMSM drives in the transition region", *IEEE Trans. Ind. Electron.*, vol. 53, no. 4, pp. 1179–1187, 2006.
- [11] O. Wallmark, and L. Harnefors: "Sensorless control of salient PMSM drives in the transition region", *IEEE Trans. Ind. Electron.*, vol. 53, no. 4, pp. 1179–1187, 2006.
- [12] A. Piippo: "A method for sensorless estimation of rotor speed and position of a permanent magnet synchronous machine", US Patent Application 11/972667, July 2008.
- [13] S. Bolognani, M. Zigliotto, and M. Zordan: "Extended-range PMSM sensorless speed drive based on stochastic filtering", *IEEE Trans. Power Electron.*, vol. 16, no. 1, pp. 110–117, 2001.
- [14] P.L. Jansen and R.D. Lorenz, "Transducerless position and velocity estimation in induction and salient ac machines," *IEEE Trans. Ind. Appl.*, vol. 31, no. 2, pp. 240–247, 1995.
- [15] E. Roseischi and M. Schroedl, "Optimized INFORM measurement sequence for sensorless PMSM: drive with respect to minimum current distortion," *IEEE Trans. Ind. Appl.*, vol. 40, no. 2, pp. 591–598, 2004.
- [16] M. E. Haque, L. Zhong, and M. F. Rahman, "A sensorless initial rotor position estimation scheme for a direct torque controlled interior permanent magnet synchronous motor drive," *IEEE Trans. Power Electron.*, vol. 18, no. 6, pp. 1376–1383, 2003.
- [17] I. Boldea, C. I. Pitic, C. Lasca, G.-D. Andreescu, L. Tutelea, F. Blaabjerg, and P. Sandholdt, "DTFC-SVM motion-sensorless control of PM-assisted reluctance synchronous machine as starter-alternator for hybrid electric vehicles," *IEEE Trans. Power Electron.*, vol. 21, no. 3, pp. 711–719, 2006.
- [18] J. Holtz: "Sensorless control of induction machines—With or without signal injection?," *IEEE Trans. Ind. Electron.*, vol. 53, no. 1, pp. 7–30, 2006.
- [19] Y. Jeong, R.D. Lorenz, T.M. Jahns, and S. Sul, "Initial Rotor Position Estimation of an Interior Permanent Magnet Synchronous Machine Using Carrier-Frequency Injection Methods," *Trans. Ind. Appl.*, vol. 41, no. 1, pp. 38–45, Jan.-Febr. 2005.

- [20] J. Holtz, "Initial rotor polarity detection and sensorless control of PMSMs," in Conf. Record IEEE-IAS 2006.
- [21] P. Guglielmi, M. Pastorelli, G. Pellegrino, and A. Vagati, "Position-sensorless control of permanent-magnet-assisted synchronous reluctance motor", IEEE Trans. Ind. Applicat., vol. 40, no. 2, pp. 615-622, Mar.-Apr. 2004.
- [22] A. Vagati, M. Pastorelli, G. Franceschini, and V. Drogoreanu, "Flux-observer-based high-performance control of synchronous reluctance motors by including cross saturation," IEEE Trans. Ind. Appl., vol. 35, no. 3, pp. 597-605, May-June 1999.
- [23] M. Schrodli, M. Hofer, W. Staffler, "Extended EMF- and parameter observer for sensorless controlled PMSM-machines at low speed," in Conf. Record EPE2007, pp. 1-8 .
- [24] Y. Inoue, K. Yamada, S. Morimoto, and M. Sanada, "Improvement of Position Estimation Accuracy in IPMSM Sensorless Drives with On-Line Parameter Identification," IEEE Trans. Ind. Appl., vol. 128, no. 7, pp. 867-873, 2008.
- [25] E. Urlep and K. Jezernik, "Low and zero speed sensorless control of nonsalient PMSM," in Conf. Record IEEE-ISIE 2007, pp. 2238-2243.
- [26] S. Koonlaboon and S. Sangwongwanich, "Sensorless control of IPMSM based on a fictitious PM flux model," in Conf. Record IEEE-IAS 2005, pp. 311-318.
- [27] I. Boldea, M. C. Paicu, and G.-D. Andreescu, "Active flux concept for motion sensorless unified ac drives," IEEE Trans. Power Electron., vol. 23, no. 5, pp. 2612-2618, Sept. 2008.
- [28] I. Boldea, M. C. Paicu, G.-D. Andreescu, and F. Blaabjerg, "'Active Flux' DTFC-SVM Sensorless Control of IPMSM," IEEE Trans. En. Conv., (to be published).
- [29] M. C. Paicu, I. Boldea, G.-D. Andreescu, and F. Blaabjerg, "Very low speed performance of active flux based sensorless control: IPMSM vector control versus direct torque and flux control," IET-EPA, (to be published).

Chapter 5

Wide Speed Range Sensorless Control of PM-RSM via “Active Flux Model”

Abstract

This chapter presents two improved control strategies for the sensorless control of permanent magnet reluctance synchronous motor (PM-RSM) in a wide speed range. The first control strategy is a novel torque referencing strategy which includes a reference torque calculator that is capable to develop maximum available motor torque for an optimal current pair (i_d, i_q) below base speed (maximum torque/ampere), but also in flux weakening region (above base speed) where voltage limitations impose constraints on the allowable (i_d, i_q) currents. The second control strategy is an alternative to the first control, but having the advantage to be much simpler and involving less off-line computational effort. The motion sensorless control of the PM-RSM is obtained via model-based stator flux estimation using the “active flux” concept. Comprehensive digital simulations for wide speed range sensorless control of a PM-RSM drive, operating down to 1 rpm and up to 12000 rpm demonstrate the effectiveness of both proposed sensorless control strategies. The conclusion was that both of them perform the same. Thus, in the experiments the second sensorless control strategy has been performed, being much simpler. Experimental results between 30 rpm and 3000 rpm are in agreement with digital simulations and validate the theoretical background. By these experimental results the proposed here strategies provide stable and reliable operation up to a speed equal eight times the machine base speed. Also the vector control system was developed and the experimental results employing it were compared with the ones obtained by using one of the two proposed control strategies.

5.1. Introduction

The PM-RSM (Fig. 5.1) is an interior permanent magnet synchronous motor (IPMSM) with weak PMs (emf < 0.25 p.u.), but with large magnetic saliency ($L_d/L_q > 3/1$), which is credited with large constant power speed range (CPSR = 3/1) for reasonably low motor torque and inverter current overrating.

Moreover, due to weak magnets and high magnetic saliency, the no load voltage even at 6/1 CPSR is only 1.5 p.u., which avoids any dedicated over voltage protection in the inverter when the latter is off by faulty operation.

On the other hand, tooth/wound surface PMSMs with reach stator mmf space harmonics content (12 slot/10 pole for example) show a high synchronous inductance L_s ($L_s > 1.0$ in p.u.) and thus, have been proved suitable for a true 3/1 CPSR. This is very good for a surface PM rotors when considering that the demagnetizing current i_{dk} ($\psi_{PM} = L_s i_{dk}$) is notably smaller than the rated current, and thus the machine efficiency stays good during flux weakening region.

However, L_s is still large not only in axis d but also in axis q which limits the true CPSR to 3/1 or so. Moreover, as the torque in SPMSM is produced solely by the PM flux (emf = 0.8-0.9 p.u.) at no load, the voltage at maximum speed, say with CPSR = 3/1, is 2.4-2.7 p.u., which requires dedicated over voltage inverter protection for inverter complete shut-off by faulty operation. On top of this, for same no load faulty operation, full PM flux leads to high core losses, which are not accepted in some applications, e.g., automotive.

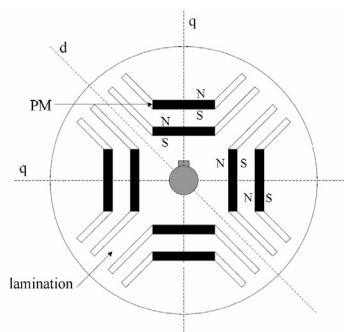


Fig. 5.1. The sensorless vector control system

Consequently, we can safely consider that the PM-RSM still retains solid advantages for wide CPSR ($CPSR > 3/1$).

Motion sensorless control of PM-RSM emerged rigorously lately, involving very low [1]-[2] and very high speed [3]. In the last case, it is difficult to make the acquisition of speed signal from the incremental encoder.

Analytical expressions for current references, which maximize the ratio of the torque and the current, were first formulated by Jahns et al (1986) [4]. This kind of control is generally called the *maximum torque per ampere control* or *minimum current control*.

Thus, below base speed, or at lower than maximum torque available at a given speed, maximum *torque/current control* was used to minimize approximately the losses [5]-[16].

At a certain base speed ω_b , the voltage V reaches the maximum voltage available from the inverter. If the speed must be increased above this frequency, the flux magnitude must be decreased. This procedure is called *the flux weakening*. The speed range above ω_b is called therefore *the field weakening range* or *the constant power area*.

So, separately, for flux weakening, above base speed, maximum *torque/flux control* was exercised successfully [17]-[26].

If a PM-RSM is controlled with current vector control based on minimizing the stator current, the modulus of the stator flux linkage varies as a function of the torque. Therefore also the base frequency varies as the torque is changed. With control principles based on keeping the modulus of the stator flux linkage constant below the base speed, the field weakening is accomplished easily by changing the flux linkage's modulus in inverse proportion to the speed.

In essence, the following criteria will be considered: maximization of the nominal torque as a function of ψ_{PM} , i_d and i_q with the voltage and the current limited to nominal values and also the current should be such that the torque to current ratio is maximized (i.e. the minimum current control is considered).

For the motion sensorless control, the "active flux" observer was used, from which more accurate rotor position and speed estimation are obtained.

The "active flux" concept (or "torque producing flux"), which "turns all the salient-pole machines into nonsalient-pole ones", was developed in [2].

To extend the torque/speed range, automatic rearrangement of (i_d^*, i_q^*) is provided.

This chapter aims as main contribution, to combine the maximum torque/ampere control with the "sliding" towards maximum torque/flux when the voltage ceiling is surpassed, into a single control strategy, accounting also for magnetic saturation variation. To do so, a „self-reconfigurable" torque referencer ($i_d^* + i_{d\text{FW}}^*, i_q^*$ versus T_e^*) is introduced, while the "active flux" model [2] is used in the state observer.

A second strategy, which is computationally simpler, is also proposed: a novel (i_d^*, i_q^*) pair referencer valid from zero to maximum speed, which implicitly switches gradually from maximum torque/flux (for maximum torque/speed envelope) to maximum torque/copper losses (for lower loads and speeds).

Digital simulations for a built PM-RSM prototype using both control strategies show proper motion-sensorless control from 1 rpm to 12000 rpm without signal injection, evidentiating flux weakening at high speeds and current (flux) reduction at low torque.

The rationality of theory analysis has been also proved by experimental results, which validate satisfactorily the proposed solutions.

5.2. Mathematical Model of PM-RSM Including Magnetic Saturation Effects

The PM-RSM is rather a good saliency interior PM rotor synchronous machine. The PMs are placed in the q -axis, while the d -axis shows higher magnetic permeance ($L_d > L_q$).

In the general synchronous machine model, the flux-current relation is linear with constant inductance. But, because of magnetic saturation, flux can not be expressed as function of inductance.

So, the magnetization function represents the flux-current function $\psi_d(i_d) = L_d(i_d)i_d$. Recalling the general model and replacing $\psi_d(i_d) = L_d(i_d)i_d$, the general synchronous machine model, including magnetic saturation effects, is:

$$\bar{V}_s = R_s \cdot \bar{i}_s + \frac{d\bar{\psi}_s}{dt} + j\omega_r \cdot \bar{\psi}_s \quad (5.1)$$

$$\bar{\psi}_s = L_d(i_d) \cdot i_d + j(L_q \cdot i_q - \psi_{PMq}) \quad (5.2)$$

$$T_e = \frac{3}{2} \cdot p_1 \cdot [\psi_{PMq} + (L_d(i_d) - L_q) \cdot i_q] \cdot i_d = \frac{3}{2} \cdot p_1 \cdot \text{Re}(j \cdot \bar{\psi}_s \cdot \bar{i}_s^*) \quad (5.3)$$

where V_s is the stator voltage, i_s is the stator current, R_s is the stator resistance, L_d, L_q are the dq axes inductances, ψ_s is the stator flux, ψ_{PMq} is the PM flux linkage, T_e is the electromagnetic torque, ω_r is the electrical rotor speed and p_1 is the number of pole pairs. The magnetic saturation is considered only in the d -axis $L_d(i_d)$, with L_q constant.

It is evident that the saturated model is almost identical with the linear model, with the only difference that any controller or observer based on those models has to be speed and inductance adaptive.

5.3. Sensorless Vector Control System

Fig. 5.2 illustrates the proposed vector control system for controlling the PM-RSM, where the stator current is controlled in the rotor reference frame.

As in usual vector control, the two PI current control loops have been implemented in a rotating dq reference frame for better performance than stationary frame regulators, as they operate on dc quantities.

The design of the controllers employs the relation (5.4):

$$k_p(1 + \frac{k_i}{s}) \quad (5.4)$$

In the case of PM-RSM, a high i_q current is required in order to cancel the q -axis flux, while the i_d current component is use for torque control over speed range.

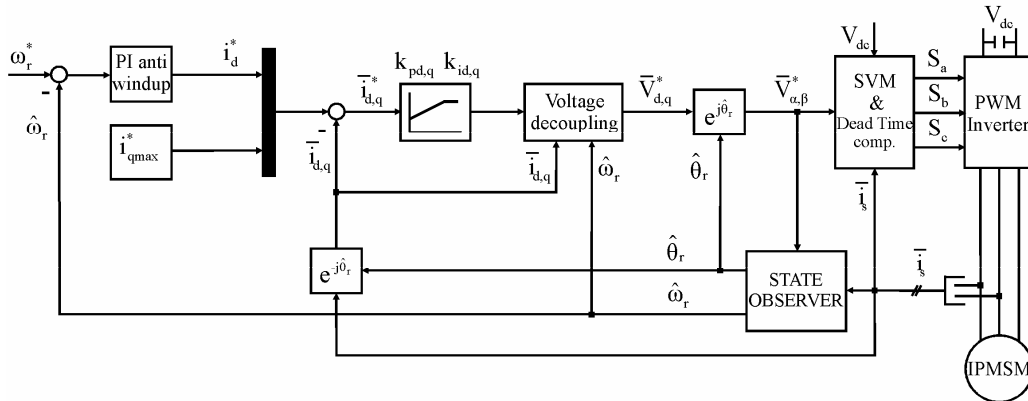


Fig. 5.2. The sensorless vector control system

The maximum value for $i_q \max$ current is 22 A, experimentally derived. Stronger magnets would allow larger $i_q \max$. Thus, over the entire speed range the $i_q \max$ current is kept constant at a value of 22 A.

The system command is given by the speed. The estimated speed $\hat{\omega}_r = \hat{\omega} \psi_q^a$ is used as feedback signal in the PI speed controller.

The estimated angle $\hat{\theta}_r = \hat{\theta} \psi_q^a + \frac{\pi}{2}$ was used for supplying all vector transformations between the abc and dq frames.

5.4. Wide Speed Range Sensorless Control System (strategy 1)

Fig. 5.3 illustrates the proposed sensorless control system for PM-RSM, which consists of a torque referencing strategy scheme (Fig. 5.4), a space vector modulator block (SVM), an active flux observer and rotor position-speed estimator.

The SVM block generates the switching signals for the voltage source inverter. The state observers provide rotor position, rotor speed and torque estimation in order to achieve sensorless control of the PM-RSM drive.

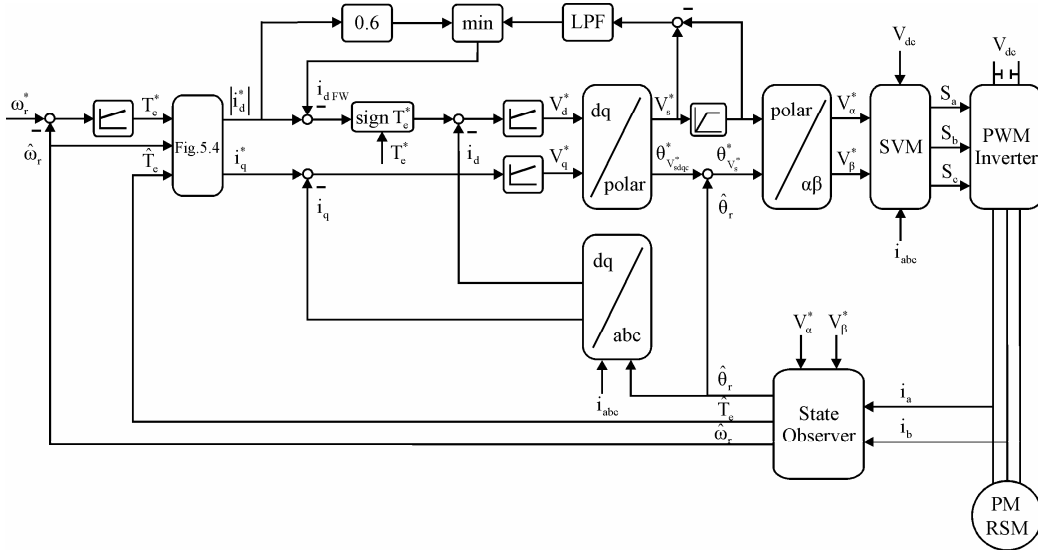


Fig. 5.3. The proposed sensorless control strategy 1 for torque-dq current referencer

For torque referencing strategy (Fig. 5.4), a speed controller provides the reference torque.

For a certain speed the torque can be achieved with a variety of different dq current pairs.

There is an optimum operating point $(i_{d_opt}^*, i_{q_opt}^*)$ in which for a demanded torque, the phase current amplitude is minimized.

The upper part of the Fig. 5.4 shows that the d axis current component i_d^* is obtained by minimizing the output of two curves: the magnetic saturation curve $(L_d(i_d))$ and $i_{d_opt}^*(T_e^*)$ curve (Fig. 5.29, respectively Fig. 5.30 from Appendix), which is obtained by Finite Element Method (FEM) design, based on maximum torque/current criterion.

The $\psi_{s \lim}^*(|\hat{\omega}_r|)$ curve is simply obtained:

$$\begin{aligned} \psi_{s \lim}^* &= \frac{V_{s \max}}{\omega_b}, \text{ for } |\hat{\omega}_r| \leq \omega_b, \\ \psi_{s \lim}^* &= \frac{V_{s \max}}{|\hat{\omega}_r|}, \text{ for } |\hat{\omega}_r| > \omega_b \end{aligned} \tag{5.5}$$

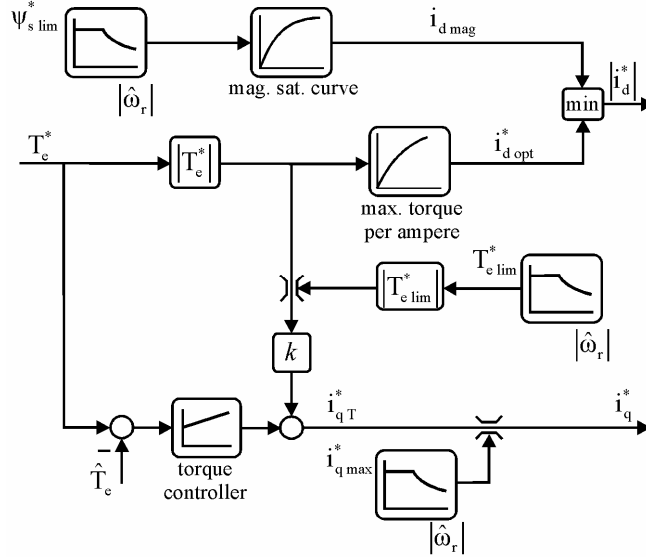


Fig. 5.4. The torque-current referencers

The lower part of the Fig. 5.4, illustrates how the q axis current component i_q^* is obtained.

To improve the system dynamic behavior, a feedforward signal, limited by torque reference speed dependent, was added to the output signal of the PI torque controller (Fig. 5.4); $k = 0.9$ is the feedforward coefficient which is less than $i_{q_max}^* / T_{e_lim}^*$. The q axis current reference is then limited by the maximum q allowable current.

The voltage limitation (flux weakening) block from Fig. 5.3 ensures through $i_{d_FW}^*$ that the voltage reference satisfies the maximum voltage constraint by a substantial reduction of the magnetizing current i_d^* through $i_{d_FW}^*$, must be imposed. The coefficient 0.6 means $i_{d_FW}^* = 40\% i_d^*$ voltage limit. Thus, the created voltage margin allows for increasing the available torque producing current component i_d^* .

Using the torque control strategy described so far, the reference current components i_d^* and i_q^* always ensure that the magnitude of the stator current vector does not exceed the maximum current I_{Smax} :

$$\sqrt{i_d^2 + i_q^2} \leq I_{Smax} \quad (5.6)$$

In conclusion, below base speed, the current limit (5.7) and the rated flux level ψ_s^* determine the operating point corresponding to the maximum torque.

Above base speed, the torque control strategy is based on the flux weakening control method because here we need to reduce the stator flux magnitude in order to satisfy the voltage constraint:

$$\sqrt{V_d^2 + V_q^2} \leq V_{s\max} \quad (5.7)$$

$V_{s\max}$ is the maximum voltage of the inverter.

The operating point of the maximum possible torque corresponding to a certain speed value is defined by the intersection of the voltage limit curve and the current limit curve.

To obtain fast torque dynamics when operating at the voltage limit, in [18]-[20], for an induction machine case, a temporary voltage margin is created in a dynamic condition by deviating the trajectory (angle δ) of the stator flux linkage vector to flux values of lower magnitude.

To accomplish this, for PM-RSM, the scheme illustrated in Fig. 5.5 is employed. As it can be seen the speed error $\Delta\omega$ is used as a feedforward signal. The speed error $\Delta\omega$ is used as a feedforward signal enabled by the condition $\Delta V_s \leq 0$ that indicates operation at the maximum available voltage. A signal $\Delta\delta$ (varying between 0 and 60 degrees) is then created and it rotates the stator voltage vector such that the stator flux linkage vector is deviated towards a trajectory of reduced amplitude.

In our PM-RSM case, the temporary voltage margin is almost created by the torque control strategy itself, and thus the scheme presented in Fig. 5.5 does not need to be used here.

To demonstrate this, digital simulations operating at the voltage limit without and with $\Delta\delta$ are presented in Fig. 5.7. It can be noticed that with $\Delta\delta$ correction (Fig. 5.6) the torque response is smoother and 15% faster when operating at 3500 rpm.

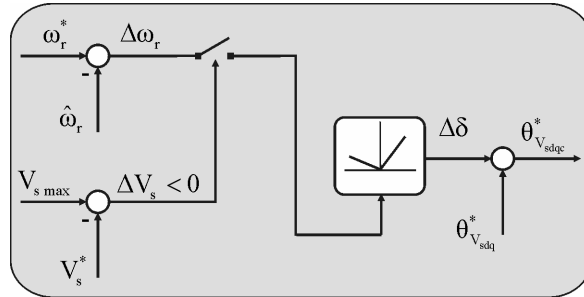


Fig. 5.5. The variation angle scheme

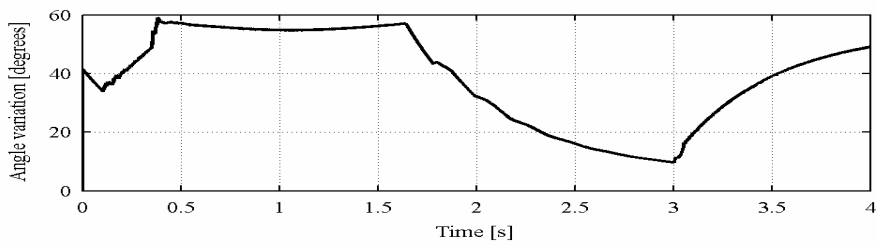
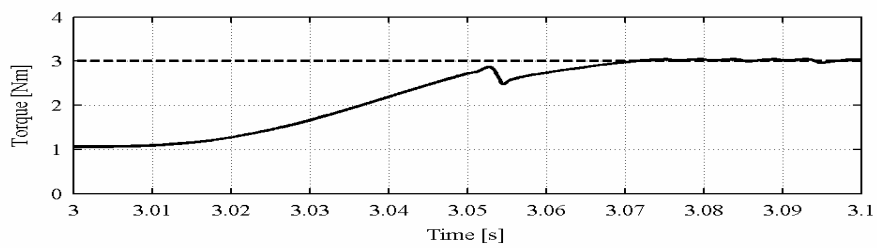


Fig. 5.6. Torque transients from 1 Nm to 3 Nm during operation at the maximum available voltage (3500 rpm): angle variation correction $\Delta\delta$



(a)

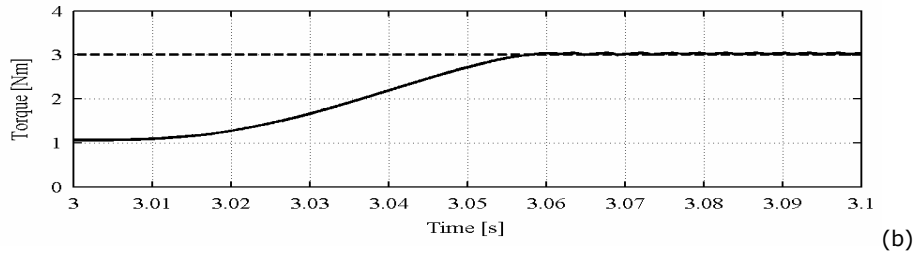


Fig. 5.7. Torque transients from 1 Nm to 3 Nm during operation at the maximum available voltage (3500 rpm): reference (dashed line) and actual torque when operating with (a) and without angle variation correction $\Delta\delta$ (b)

5.5. Wide Speed Range Sensorless Control System (strategy 2)

As the margin of maximum available torque with speed and maximum torque per ampere criteria in the proposed strategy 1 (Fig. 5.4) supposes notable off-line computation effort, this new (i_d^*, i_q^*) referencing strategy 2 is a simplified alternative procedure, but with much less off-line computation effort (Fig. 5.8).

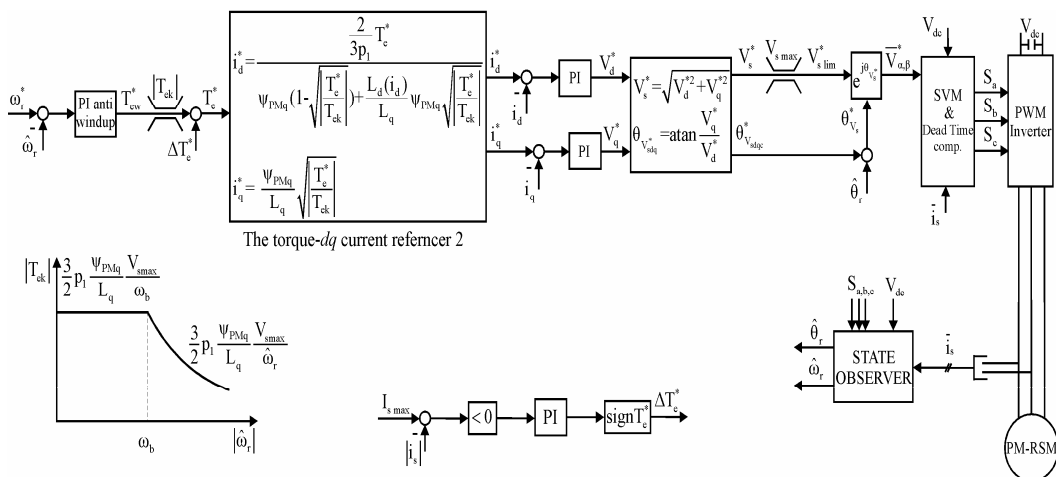


Fig. 5.8. The proposed sensorless control strategy 2 for torque-dq current referencer

Here, for the maximum torque (T_{ek}) as function of ω_r , $i_q^* = i_{qk} = \frac{\psi_{PMq}}{L_q}$ and thus, from (5.1)-(5.3) simply:

$$T_{ek} = \frac{3}{2} p_1 \frac{\psi_{PMq}}{L_q} L_d i_d \approx \frac{3}{2} p_1 \frac{\psi_{PMq}}{L_q} \frac{V_{s\max}}{\omega_b}, \quad \text{for } |\omega_r| \leq \omega_b \quad (5.8)$$

$$T_{ek} = T_{e\max b} \left| \frac{\omega_r}{\omega_b} \right|, \quad \text{for } \omega_r > \omega_b$$

when the required torque $T_e^* < T_{e\max}(\omega_r)$ the i_q^* is reduced with the square root of torque reference:

$$i_q^* = \frac{\psi_{PM}}{L_q} \sqrt{\left| \frac{T_e}{T_{ek}} \right|} \quad (5.9)$$

from torque equation (5.3) for optimum torque per current:

$$i_d^* = \frac{\frac{2}{3p_1} T_e^*}{\psi_{PMq} \left(1 - \sqrt{\left| \frac{T_e^*}{T_{ek}} \right|} \right) + \frac{L_d(i_d)}{L_q} \psi_{PMq} \sqrt{\left| \frac{T_e^*}{T_{ek}} \right|}} \quad (5.10)$$

which replaces the need for the maximum torque per current family of curves ($i_d^*(T_e^*)$, $i_q^*(T_e^*)$) which need apriori calculations or experiments.

As it can be seen in Fig. 5.8, when the current limit is surpassed due to parameter mismatch an additional reference torque correction is added: ΔT_e^* .

Also, when the voltage limit is surpassed (again only due to parameter mismatch), the stator voltage is limited to $V_{s\max}$ but its angle remains given by V_d^* and V_q^* .

Only the magnetization curve $L_d(i_d)$, the rather constant value of L_q and the PM flux ψ_{PMq} are required for control calibration.

5.6. Active Flux Observer for the PM-RSM

As it was mentioned before, this observer is based on the “active flux” concept, as developed in [2] and it leads to the estimation of both “active flux” amplitude $\hat{\psi}_q^a$ and angle $\hat{\theta}_{\psi_q^a}$ with respect to stator phase a .

In contrast with the active flux observer presented so far, here, for PM-RSM case, $\hat{\theta}_{\psi_q^a} = \hat{\theta}_r - \frac{\pi}{2}$ (where $\hat{\theta}_r$ is the electrical angle rotor position)). $\hat{\theta}_{\psi_q^a}$ corresponds to PM rotor position and here it corresponds with the negative axis q .

Thus, for the PM-RSM case, the “active flux” vector $\hat{\psi}_q^a$ observer, in stator coordinates, is:

$$\hat{\psi}_q^{as} = \int (\bar{V}_s^s - R_s \bar{i}_s^s + \bar{V}_{comp}) dt - L_d(i_d) \cdot \bar{i}_s^s \tag{5.11}$$

$$\hat{\psi}_q^{as} = \bar{\psi}_s^s - L_d(i_d) \cdot \bar{i}_s^s \tag{5.12}$$

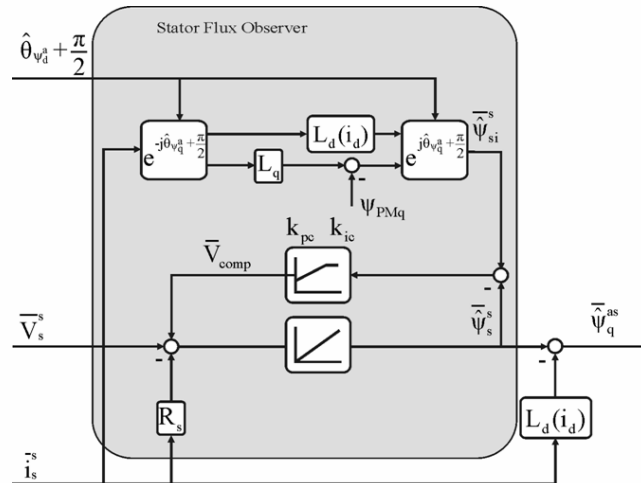


Fig. 5.9. The active flux observer in the PM-RSM case

In this case, the active flux observer implementation scheme (Fig. 5.9), consists in a stator flux observer in stator coordinates from which the term $L_d(i_d) \cdot \vec{i}_s^S$ is subtracted (5.11).

The position and speed estimator is the same with the one presented in the previous chapters ($\hat{\theta}_r = \hat{\theta}_{\psi_q^a} + \frac{\pi}{2}$, $\hat{\omega}_r = \hat{\omega}_{\psi_q^a}$).

5.7. Digital Simulations

The digital simulations have been processed in MATLAB/Simulink package for the PM-RSM model specified in Experimental setup 2 in Chapter 6.

As in the theoretical background two wide speed range control strategies were presented, the intended purpose of this paragraph is to validate and compare them. Thus, two simulation models were developed and in what follows digital simulations results using both control strategies will be presented.

5.7.1. Digital Simulations Results Using the Proposed Wide Speed Range Control Strategy 1

In order to validate the proposed sensorless control strategy 1 of PM-RSM via „active flux” in a wide speed range digital simulation tests at low, medium and high speed were performed and will be next presented:

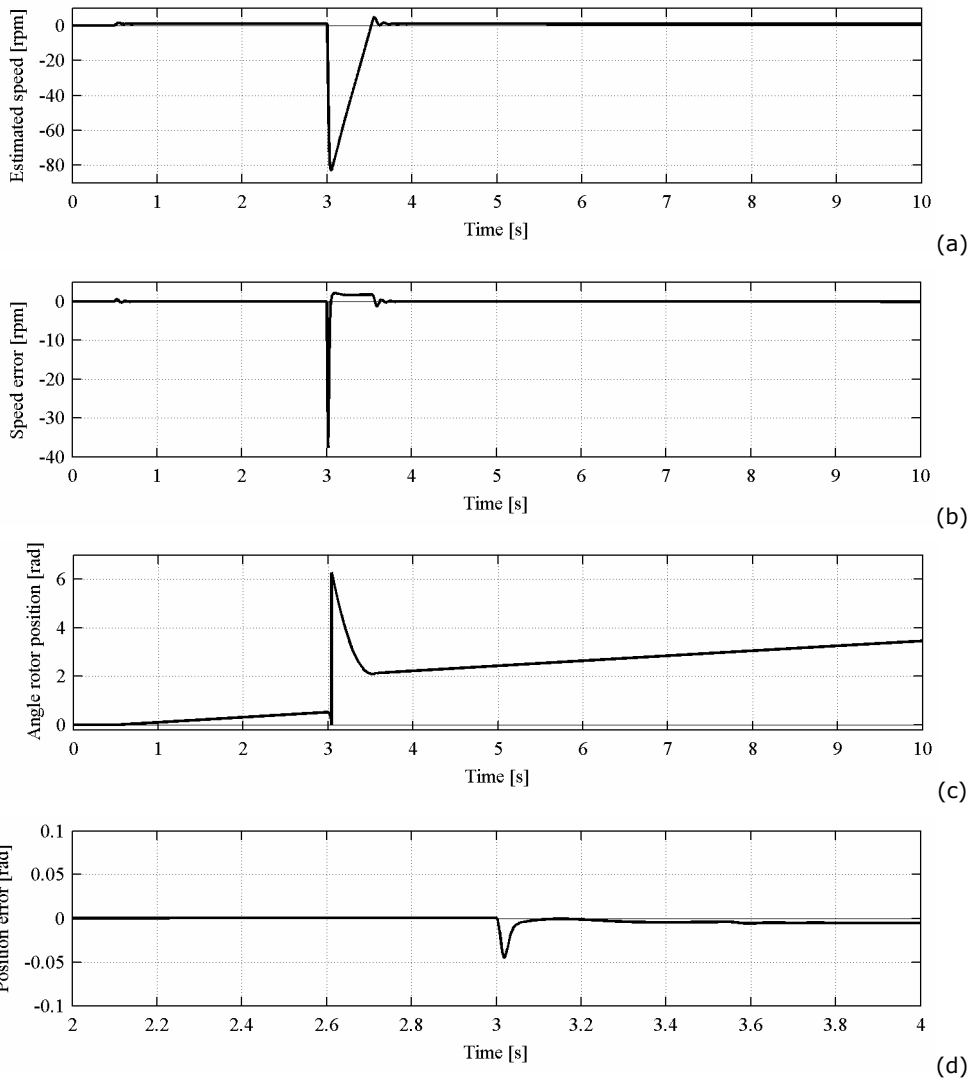
- **low speed operation:** start up at 1 rpm followed by a full step torque load at $t=3$ s using **the proposed sensorless control strategy 1** (Fig. 5.10)

Fig. 5.10a shows a quick speed recovery and a small speed ripple in the estimated speed waveform.

The position estimation during torque transients is very reliable (Fig. 5.10c), the error between the actual and estimated angle rotor being only of 0.04 rad during torque transient (Fig. 5.10d).

Fig. 5.10h shows that the flux increases at flux reference value only during torque transients in order to produce the demanded torque; otherwise it is maintained at the PM flux (low) value.

It can be observed that the motor operates with constant torque because the command speed is below the base speed (Fig. 5.10f).



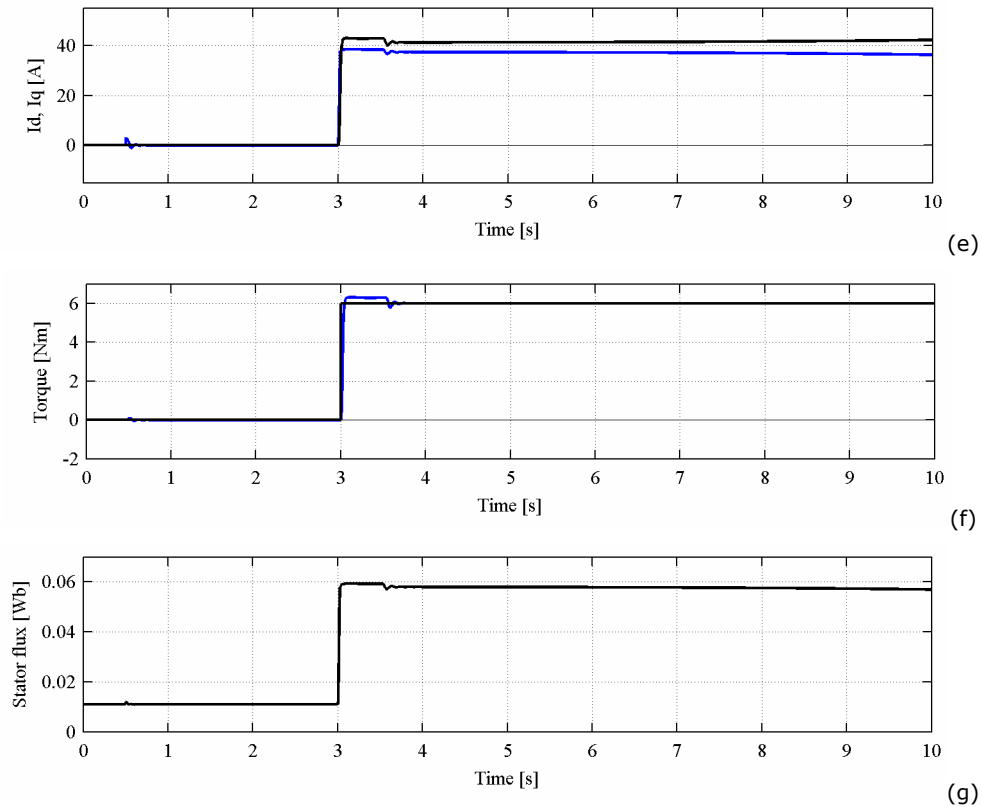


Fig. 5.10. Start up to 1 rpm at $t = 0.5$ s followed by a full step torque load at $t = 3$ s, using **the proposed sensorless control strategy 1**; from top to bottom: (a). estimated speed; (b). error between encoder and estimated speed; (c). angle rotor position; (d). error between actual and estimated angle rotor position; (e). I_d (blue), I_q currents; (f). reference and estimated torque; (g). estimated stator flux

- **medium speed operation**: start up at 6000 rpm followed by a step torque load (of 1.5, which is around 26% rated torque) at $t=4$ s using **the proposed sensorless control strategy 1** (Fig. 5.11)

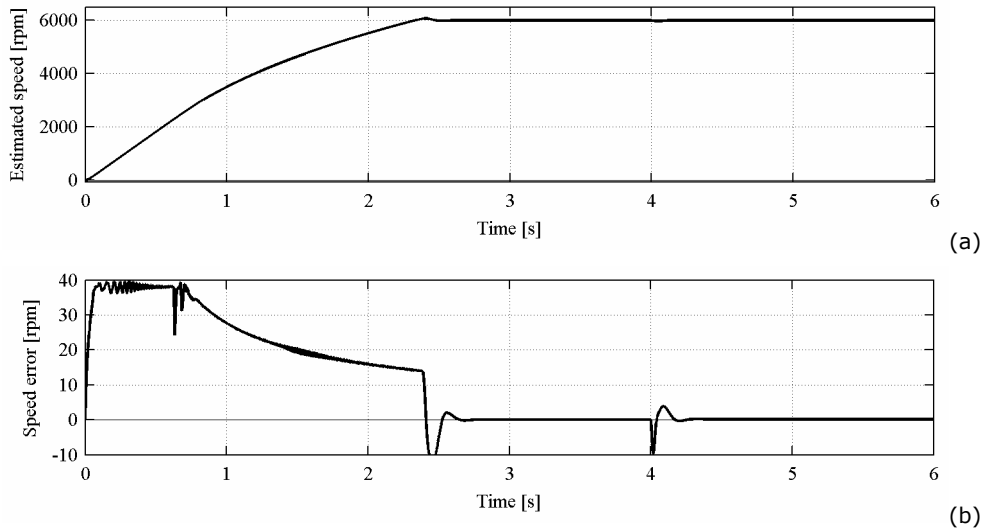
Fig. 5.11a and Fig. 5.11g illustrate the well behaved speed and torque transients.

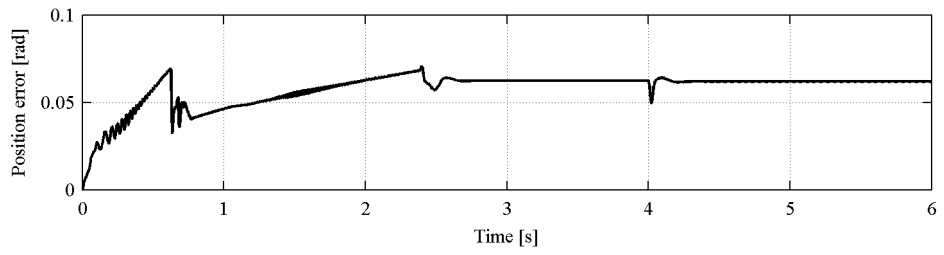
Fig. 5.11h shows how, once the actual speed achieves the reference speed value of 6000 rpm on no-load, the flux is decreased until it achieves the almost PM flux linkage (low) value.

The voltage and current reduction (Fig. 5.11e and Fig. 5.11g) after the command speed reaches steady state shows clearly the optimum torque/current relationship to reduce losses even at high speed, but for low torque when the machine uses the entire available voltage and current.

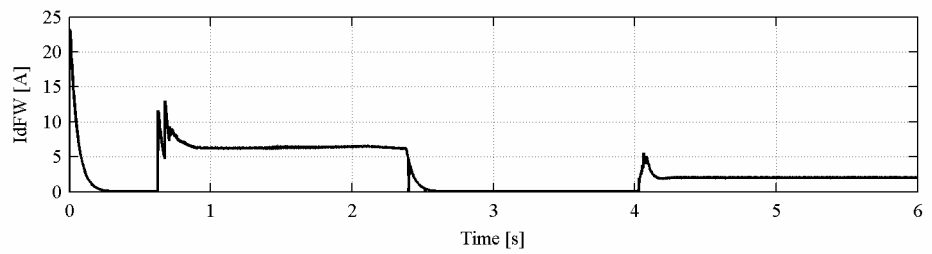
A reduction of the magnetizing current i_d^* through $i_d^*_{FW}$ (Fig. 5.11d) ensures that the voltage reference satisfies the maximum voltage constraint.

In Fig. 5.11c, the position error is small (0.05 rad), which means that the estimated angle rotor position follows very well the actual rotor position even when the speed reference or load disturbance change quickly. As the magnetization curve $\psi_d(i_d)$ is considered, only the stator resistance error influences to some extent the active flux angle (rotor angle) position estimation.

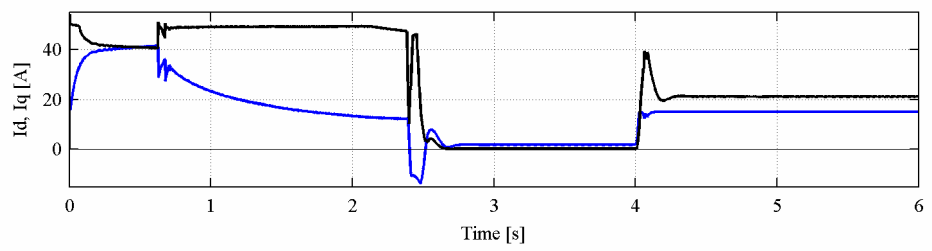




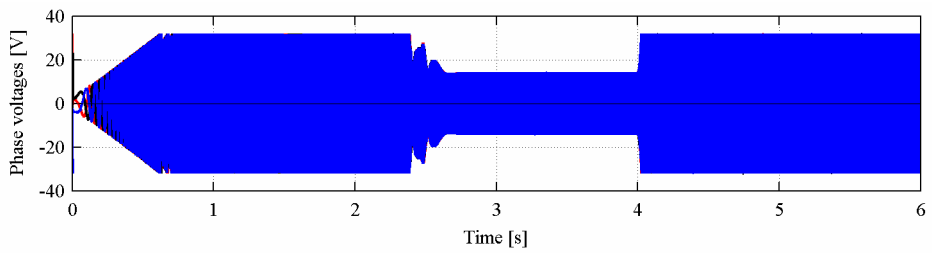
(c)



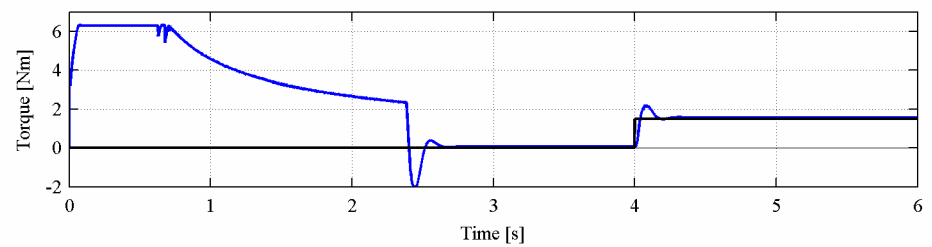
(d)



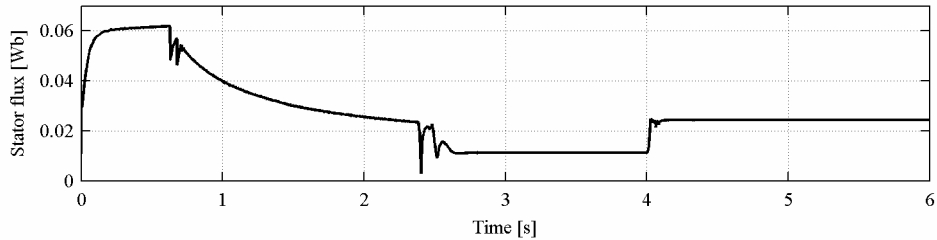
(e)



(f)



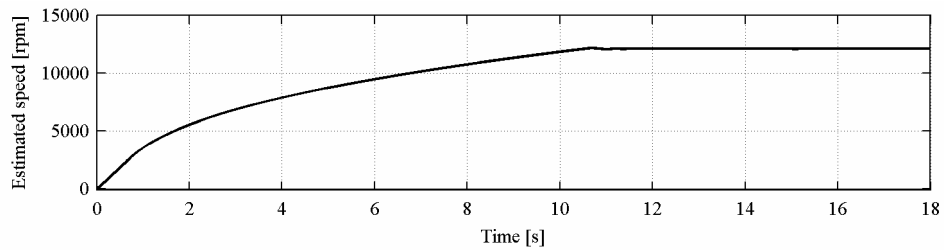
(g)



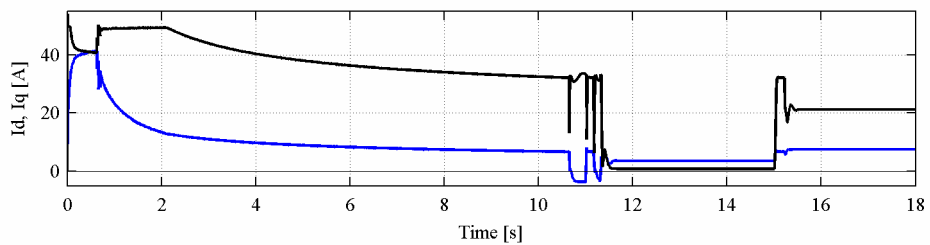
(h)

Fig. 5.11. Start up at 6000 rpm followed by a step torque load (of 26% rated torque) at $t = 4$ s, using **the proposed sensorless control strategy 1**; from top to bottom: (a). estimated speed; (b). error between encoder and estimated speed; (c). error between actual and estimated angle rotor position; (d). I_{dFW} ; (e). I_d (blue), I_q currents; (f). phase voltages; (g). reference and estimated torque; (h). estimated stator flux

- **high speed operation:** start up at 12000 rpm followed by a step torque load of 0.65 Nm (10% rated torque) at $t=15$ s using **the proposed sensorless control strategy 1** (Fig. 5.12)



(a)



(b)

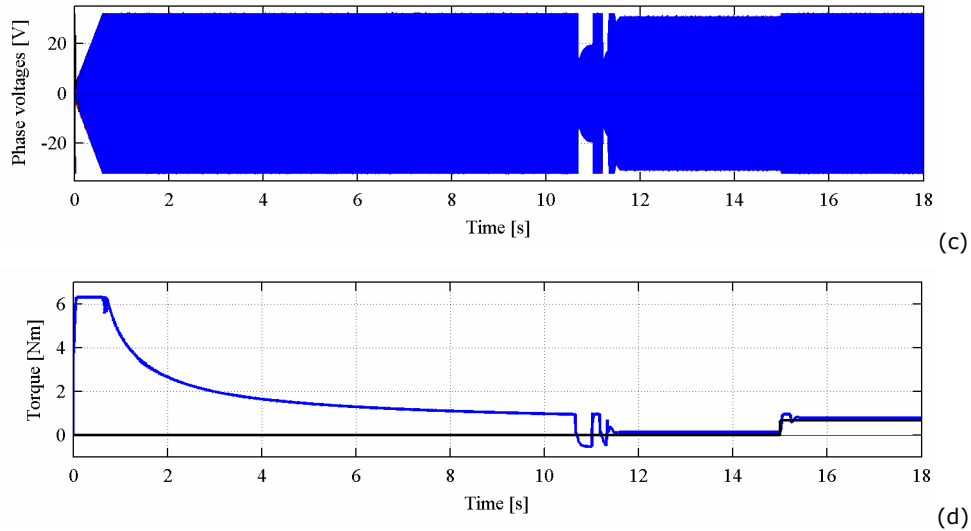


Fig. 5.12. Start up at 12000 rpm followed by a step torque load of 0.65 Nm (around 10% rated torque) at $t=15$ s, using **the proposed sensorless control strategy 1**; from top to bottom: (a). estimated speed; (b). I_d (blue), I_q currents; (c). phase voltages; (d). reference and estimated torque

This digital simulation test was performed with the intended purpose to demonstrate that the machine is capable to run at very high speeds, reaching a speed equal eight times the machine base speed (Fig. 5.12a).

It can be seen that below base speed the torque is maintained at its maximum value and above base speed it decreases with speed (Fig. 5.12d).

At the speed of 12000 rpm, the maximum value for the load torque is 0.65 Nm. Even before loading, the voltage is almost at its maximum available value from the inverter (Fig. 5.12c).

All these digital simulation results at low, medium and high speeds show that the PM-RSM is capable of a wide speed range motion via „active flux” using the proposed control strategy 1 and, in the same time, developing the maximum available torque, for an optimal current pair (i_d, i_q) below base speed, but also in flux weakening region (above base speed) where voltage limitations impose constraints.

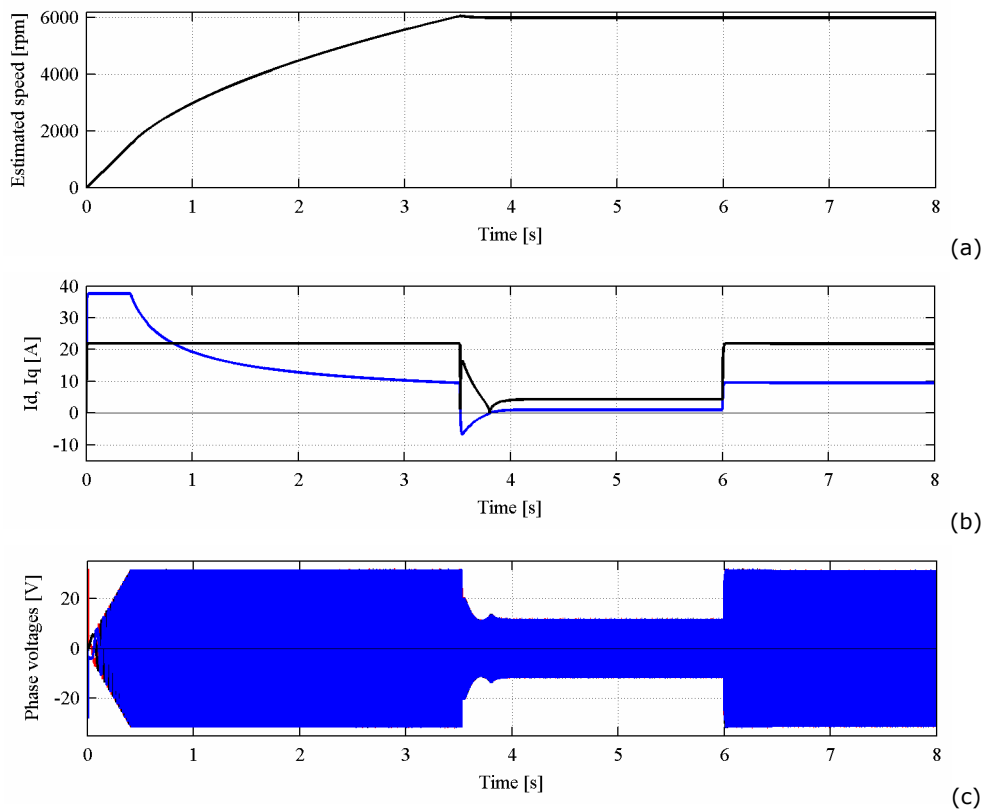
The proportional and integral gains for the PI controllers used in digital simulation are given in TABLE 5.1 (see Appendix).

5.7.2. Digital Simulations Results Using the Proposed Control Strategy 2

In order to also validate the sensorless control strategy 2 and to make a comparison between the two strategies, the same digital simulation test, at medium speed of 6000 rpm and 48 Vdc has to be performed.

Fig. 5.13 illustrating the start up to 6000 rpm transients with step load perturbation at $t=6$ s shows that smooth control of speed and torque can be achieved in the field-weakening region.

The motor operates with constant torque below base speed and then it decreases with speed (Fig. 5.13d).



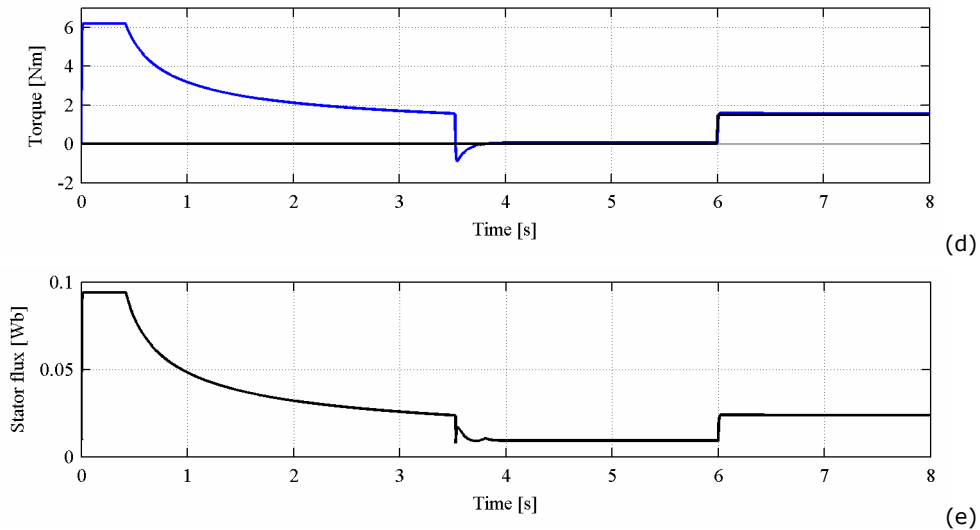


Fig. 5.13. Start up at 6000 rpm followed by a step torque load (of 26% rated torque) at $t = 6$ s, using **the proposed sensorless control strategy 2**; from top to bottom: (a). estimated speed; (b). I_d (blue), I_q currents; (c). phase voltages; (d). reference and estimated torque; (e). estimated stator flux

Comparing these digital simulation results with the ones obtained using the control strategy 1, some conclusions can be traced:

- with both control strategies the optimum torque/current relationship to reduce losses is performed below base speed, but also in flux weakening region (above base speed)
- same torque is developed with both control strategies
- the speed response is faster using the proposed control strategy 1 than using the proposed control strategy 2 (2.5 s, respectively 3.5 s)
- using the proposed control strategy 2, the curves are smoother than using the proposed control strategy 1

It is believed that the above „disadvantage“ could be changed by improving the simpler control strategy 2 (choosing the best gains for the PI controllers).

In conclusion, both proposed control strategies well suite for the wide speed range motion-sensorless control of PM-RSM, the two being equivalent. But, taking account of the off-line computational effort and of the fact that for the control

strategy 1 the $i_{d_opt}^*(T_e^*)$ curve must be precalculated using the Finite Element Method (FEM), the control strategy 2 represents the simplest method to be implemented.

Thus, the proposed control strategy 2 was chosen to perform the experimental work.

In the previous paragraph, through digital simulations, it was demonstrated that the machine can run up to a very high speed of 12000 rpm, representing eight times the machine base speed. In practice, due to mechanical considerations, this could not be possible and we were forced to limit the speed at 3000rpm.

This is the reason why, experiments with the machine being supplied by a single battery (Vdc) instead of four batteries are performed. Thus, if the machine can be driven at 3000 rpm using one battery, for four batteries the speed can be extrapolated at 12000 rpm.

In order for the experimental work, which will be presented in the next paragraph, to be validated also through digital simulation results, the following tests will be presented:

- start up at 1000 rpm followed by a step torque load (of 30% rated torque) at $t = 2$ s using **the proposed sensorless control strategy 2** (Fig. 5.14)

As it can be seen, above base speed (which in the case of using only one battery is 375 rpm) the proposed sensorless control strategy 2 reduces the developed torque proportionally with speed (Fig. 5.14d).

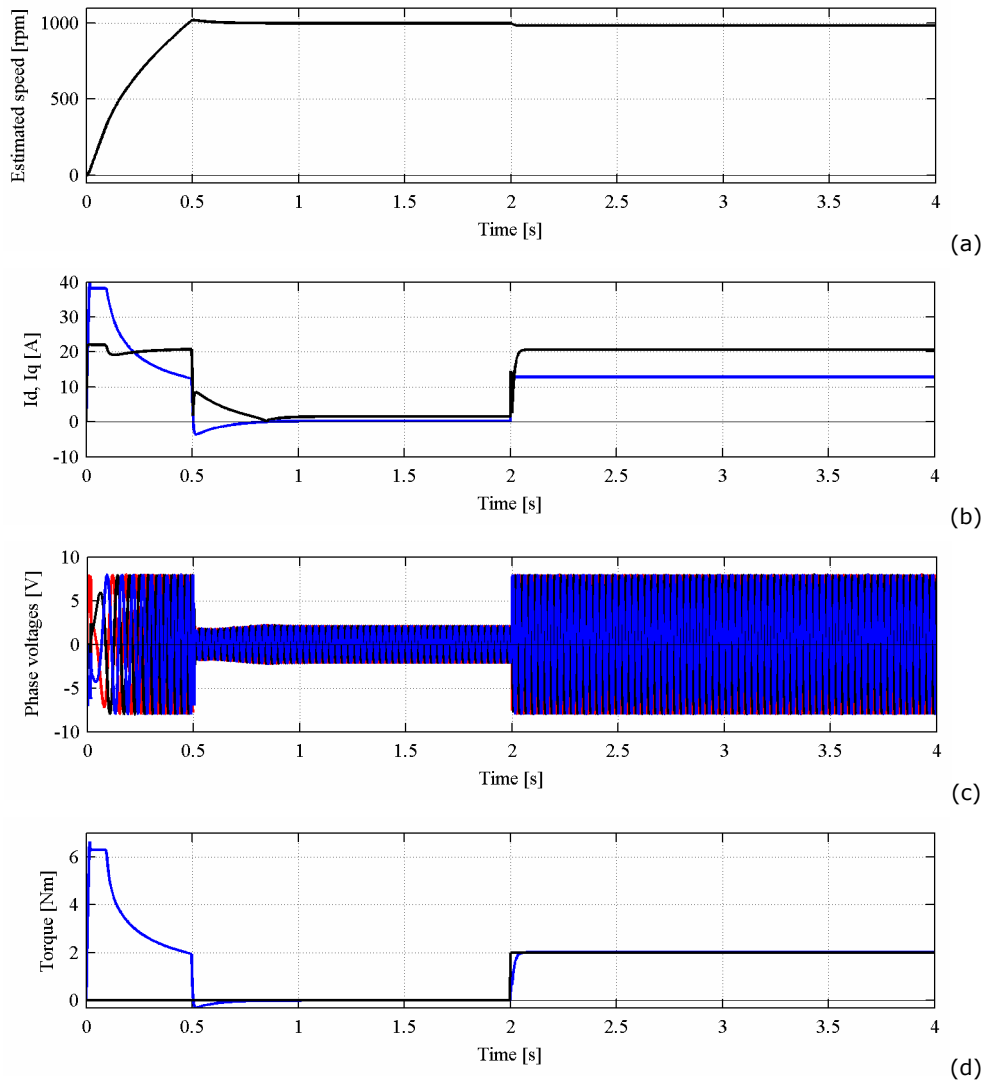
The I_d and I_q responses (Fig. 5.14b) decrease with the increase of speed until the motor speed reaches the speed command of 1000 rpm (Fig. 5.14a).

This field-weakening control mode persists until 0.5 s, then the motor speed reaches the steady state speed of 1000 rpm and the resulting control becomes the maximum torque per ampere control.

Also, the stator flux at no load is maintained at its lower value, which is almost equal with the permanent magnet flux value (Fig. 5.14e).

Corresponding to this speed of 1000 rpm, the developed torque reaches a maximum value of 2 Nm (Fig. 5.14d).

During loading operation, the voltage attains the maximum available value provided by the inverter (Fig. 5.14c).



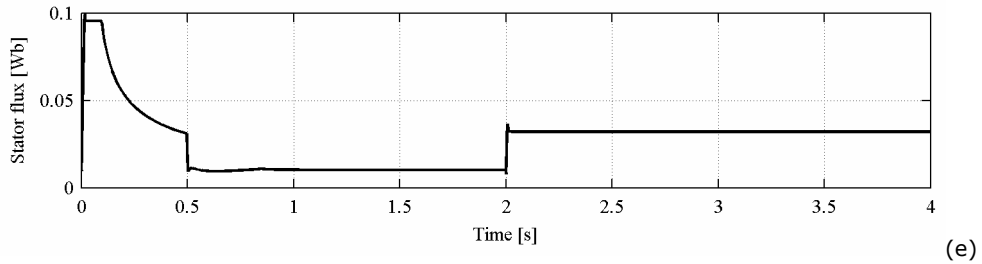
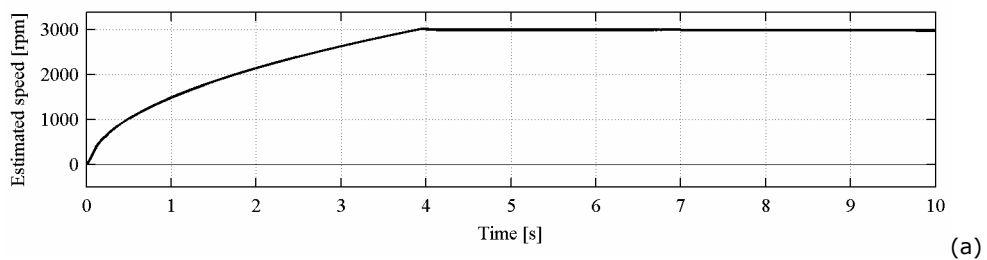


Fig. 5.14. Start up at 1000 rpm followed by a step torque load (of 30% rated torque) at $t = 2$ s, using **the proposed sensorless control strategy 2**; from top to bottom: (a). estimated speed; (b). I_d (blue), I_q currents; (c). phase voltages; (d). reference and estimated torque; (e). estimated stator flux

- start up at 3000 rpm followed by a step torque load of 0.65 Nm (10% rated torque) at $t = 7$ s using **the proposed sensorless control strategy 2** (Fig. 5.15)

Almost the same conclusion can be traced here again, with the mention that at this speed of 3000 rpm, the maximum value for the developed torque is only of 0.65 Nm (almost 10% rated torque)

The proportional and integral gains for the PI controllers used in the digital simulation are given in TABLE 5.2 (see Appendix).



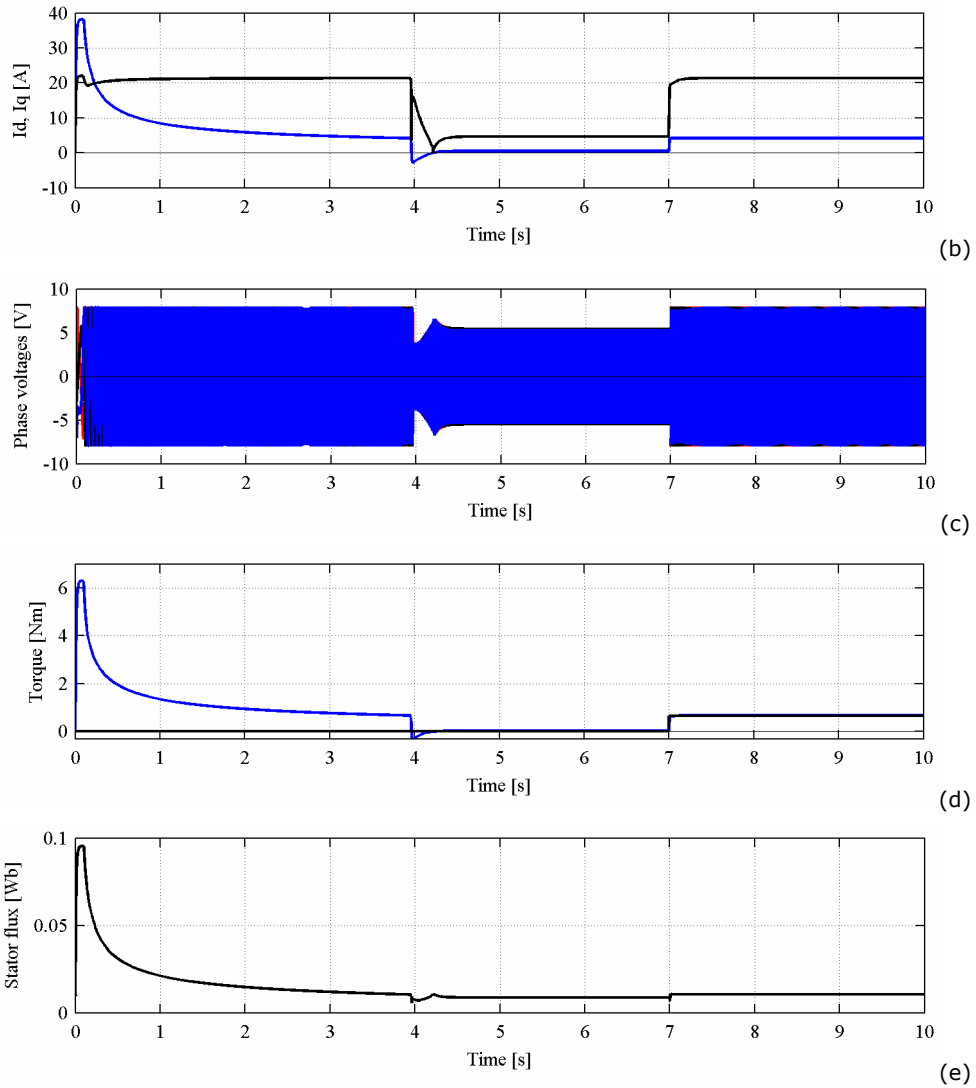


Fig. 5.15. Start up at 3000 rpm followed by a step torque load of 0.65 Nm (10% rated torque) at $t = 7$ s, using **the proposed sensorless control strategy 2**; from top to bottom: (a). estimated speed; (b). I_d (blue), I_q currents; (c). phase voltages; (d). reference and estimated torque; (e). estimated stator flux

5.8. Experimental Work

The claim of this chapter is in essence a novel sensorless control, which is capable to develop maximum available motor torque for an optimal current pair below base speed, but also in above base speed. So, the experimental work is focused on the results obtained after the system implementation.

Since the sensorless vector control system has been developed, it is also here introduced. Finally, the results obtained using both control systems are compared.

Thus, the experimental work can be divided in two major parts: a set of experiments using the sensorless vector control system proposed in Fig. 5.2 and another set using the sensorless control strategy 2 proposed in Fig. 5.8.

All experiments have been carried out on the Experimental setup 2 presented in Chapter 6.

5.8.1. Experimental Results with PM-RSM Using the Vector Control System

5.8.1.1. Stator observers performance at low speed

First, experiments at low speed using the vector control with encoder to calibrate and assess the state observers (active flux, rotor position and speed) were performed.

Two experiments results will be next presented:

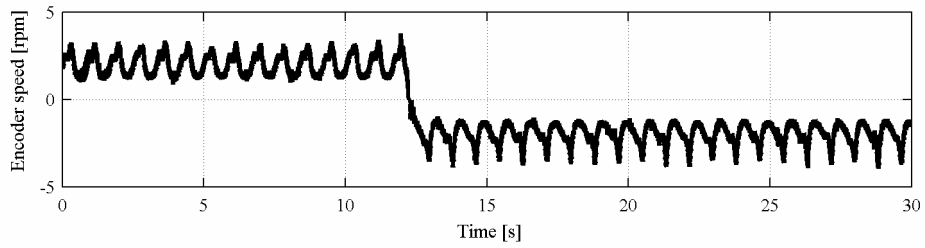
- ± 2 rpm speed reversal using **vector control system with encoder** (Fig. 5.16)

Rather good correlation between estimated and encoder speed are obtained.

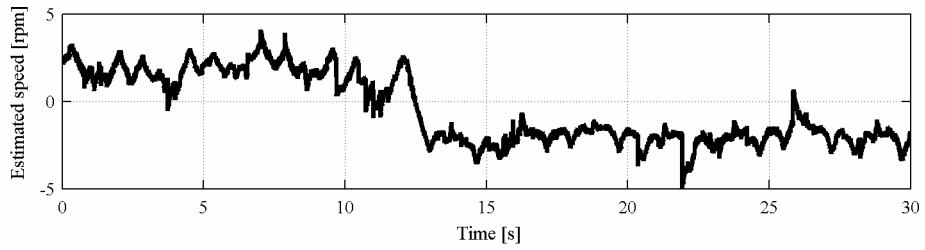
As it can be seen, the stator currents (Fig. 5.16f) and the active flux components (Fig. 5.16e) are quite smooth.

It can be easily seen that the two (actual and estimated) angle rotor positions are overlapped – this proves the validity of the active flux concept (Fig. 5.16c).

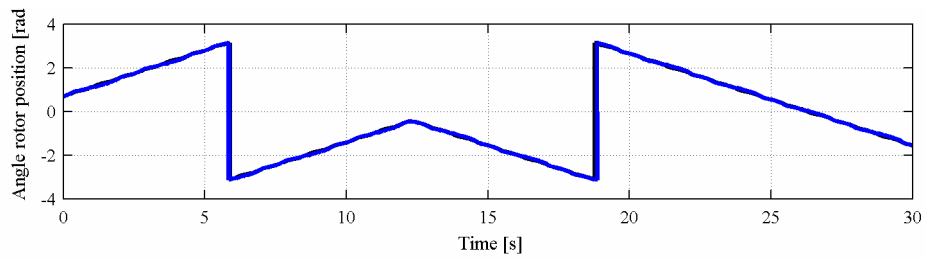
The position error is very small (below 0.1 rad).



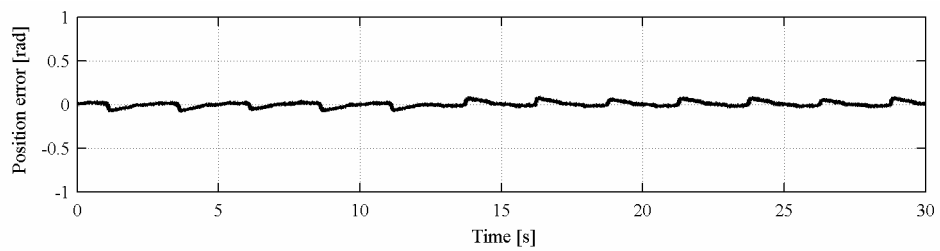
(a)



(b)



(c)



(d)

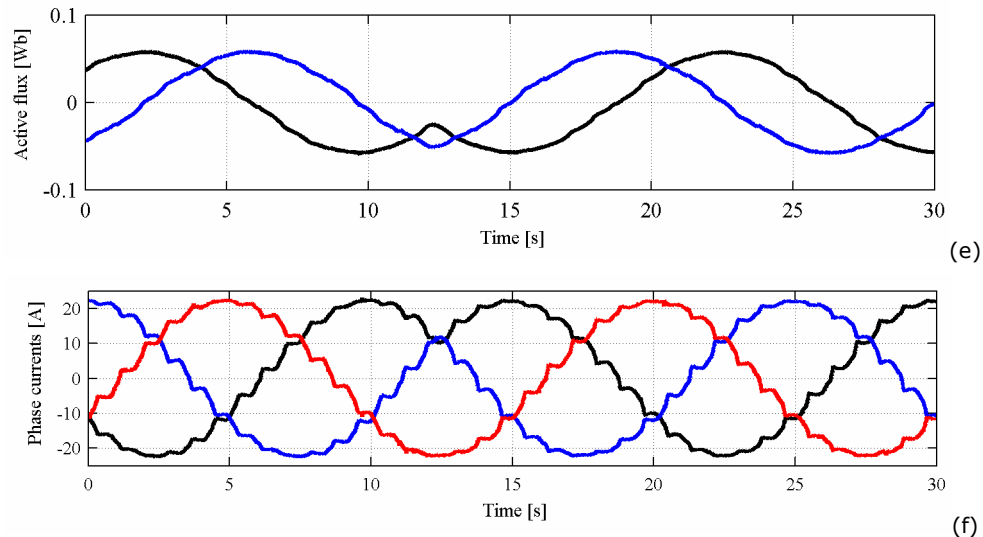


Fig. 5.16. ± 2 rpm speed reversal using **vector control system with encoder**; from top to bottom: (a). encoder speed; (b). estimated speed; (c). angle rotor position (actual and estimated (blue)); (d). error between actual and estimated angle rotor position ; (e). phase currents

- 10 rpm steady state speed using **vector control system with encoder** (Fig. 5.17)

The speed error is between ± 2 rpm in Fig. 5.17b.

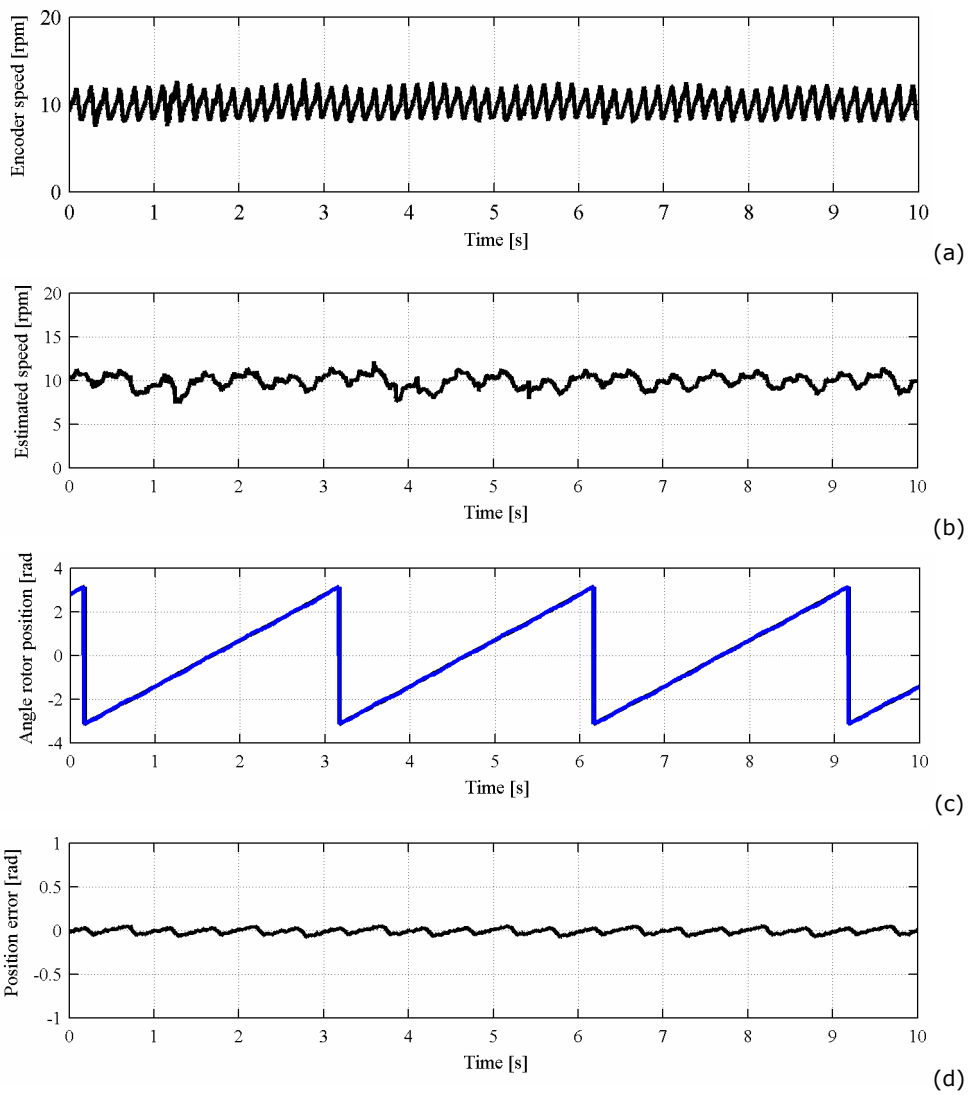
It has to be noted that the position accuracy is very good in spite of current pulsations in phase currents.

As it was expected, the error between the encoder rotor position angle and the estimated one is smaller as the speed increasing (Fig. 5.16d and Fig. 5.17d).

So, once the observers are calibrated, the next step is the implementation of the position and speed estimator based on active flux observer in the sensorless vector control system.

It has to be said that these results were obtained by implementing the compensation methods of voltage drops on inverter power devices and of inverter dead time, presented in Chapter 3. In the obtained experimental results, which will

be presented from now on, without using the motion sensor, these compensations played a very important role.



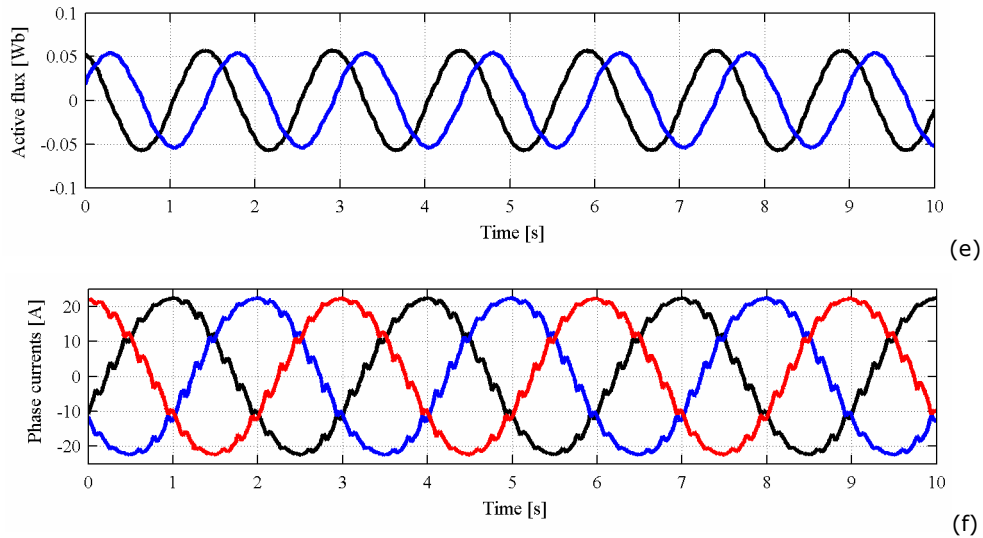


Fig. 5.17. 10 rpm steady state speed using **the vector control system with encoder**; from top to bottom: (a). encoder speed; (b). estimated speed; (c). angle rotor position (actual and estimated (blue)); (d). error between actual and estimated angle rotor position ; (e). phase currents

5.8.1.2. Experimental Results with PM-RSM Using the Sensorless Vector Control System

The flux weakening operation is very effective to attain high speed rotation of a PM-RSM.

Here, the intended purpose is to demonstrate that the vector control (Fig. 5.2) with i_q^* current kept constant at the maximum value of 22 A is itself capable of flux weakening operation and thus, to operate in a wide speed range. This affirmation is sustained by effective experimental results, which will be next presented.

To have a support for a comparison between sensorless vector control system and sensorless control strategy 2, the experiments were performed at the same speeds and almost in the same conditions.

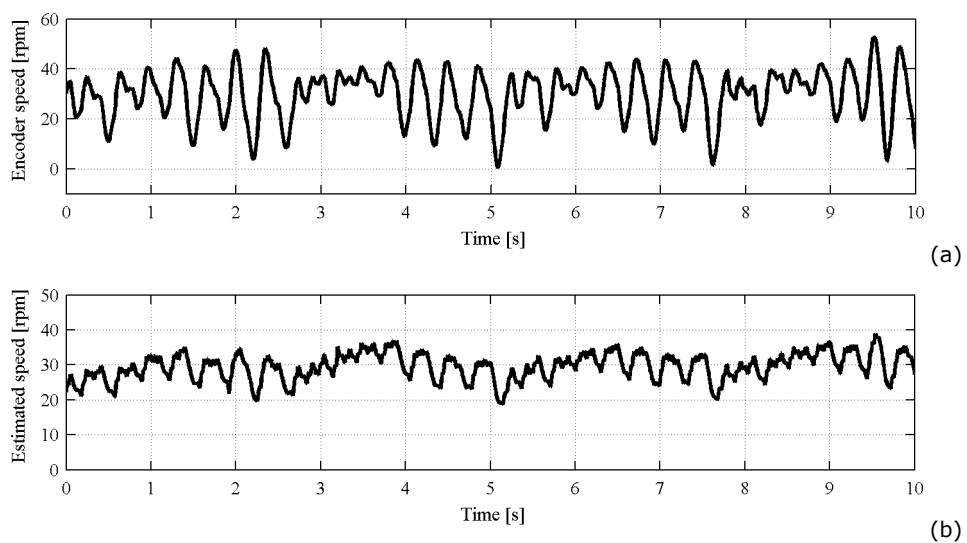
First, the sensorless operation at low speeds using the vector control system is tried to be proven. The lowest speed achieved was 30 rpm (Fig. 5.18).

No loading could be performed at low speeds because the load was an induction machine driven sensorless (in torque control mode) by a bidirectional inverter and in general it was very difficult to control an induction machine sensorless with torque reference.

As it can be seen, the encoder speed waveform has large oscillations (Fig. 5.18a). The estimated speed (Fig. 5.18b) is smoother than the encoder one, but this is due to the large time constant of the estimated speed filter. Actual speed is not filtered.

These are due to the partial compensation of the inverter nonlinearities which is also the reason for the quite large error between actual and estimated angle rotor position (Fig. 5.18d). We assume that, taking into account that the low speed operations are critical, these errors are in acceptable limits.

Also, the phase currents waveforms are reasonable (Fig. 5.18e).



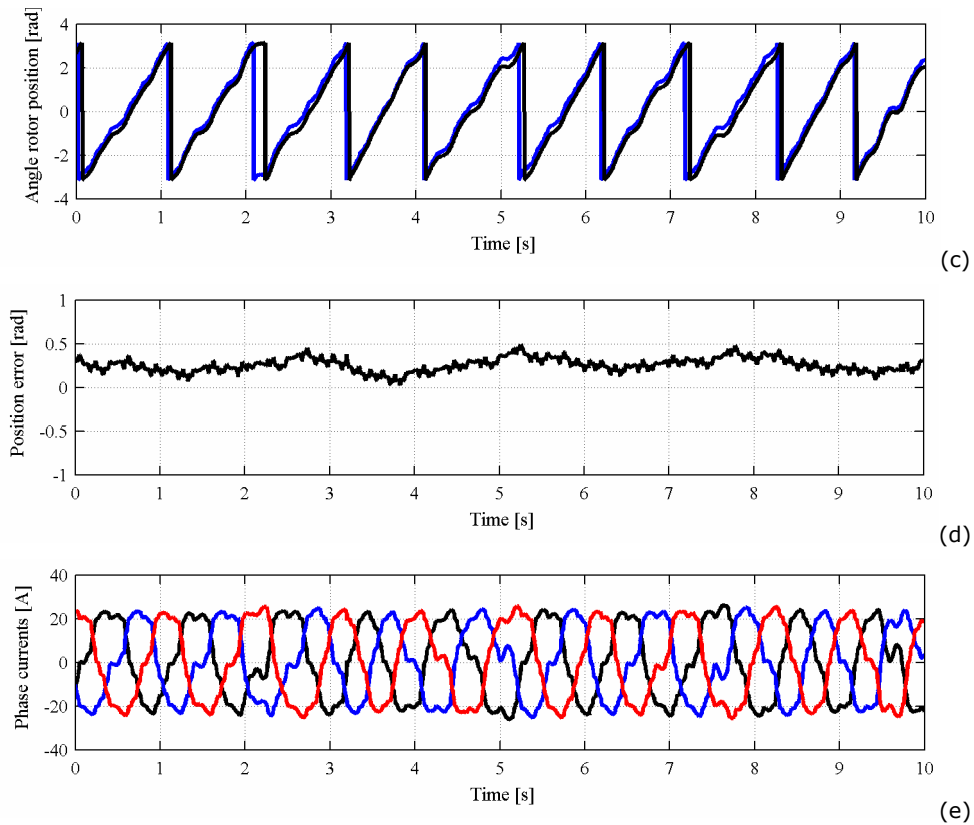


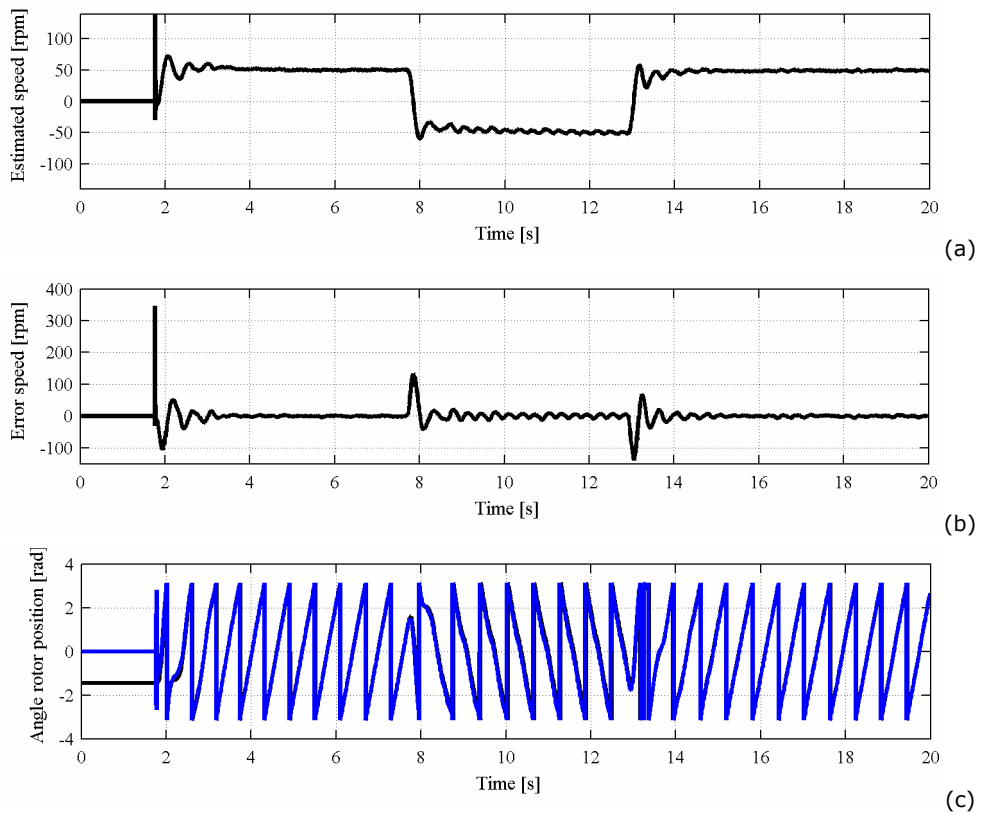
Fig. 5.18. 30 rpm steady state speed using **the sensorless vector control system**; from top to bottom: (a). encoder speed; (b). estimated speed; (c). angle rotor position (actual and estimated (blue)); (d). error between actual and estimated angle rotor position ; (e). phase currents

Next experiment presents ± 50 rpm speed reversal and back to $+50$ rpm using **the sensorless vector control system** (Fig. 5.19).

As it can be observed in the estimated speed waveform (Fig. 5.19a), with the exception of a single spike during start up, the dynamics are very good (less than 0.25 s) during speed reversal. As in the previous case, here again the encoder speed is not as good as the estimated is. In Fig. 5.19b the error between encoder and estimated speed is 120 pm during speed reversal.

In this case, the position error (Fig. 5.19c) is better than in the 30 rpm case (0.1 rad for 50 rpm and 0.25 rad for -50 rpm during steady state).

As it was mentioned before, for mechanical reasons, the machine speed should not exceed 3000 rpm. In order to extend the speed range to the machine maximum capability of 12000 rpm (as it was demonstrated by digital simulations), in the experiments only one battery was used for the machine supply.



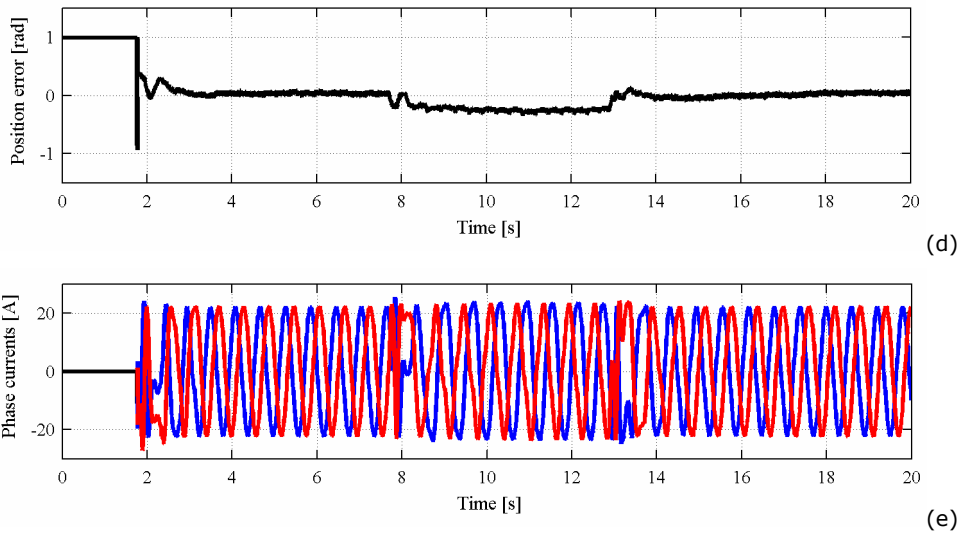


Fig. 5.19. ± 50 rpm speed reversal using **the the sensorless vector control system**; from top to bottom: (a). encoder speed; (b). error between encoder and estimated speed; (c). angle rotor position (actual and estimated (blue)); (d). error between actual and estimated angle rotor position; (e). phase currents

The intended purpose of the next performed experiments at 1000 rpm (Fig. 5.20), respectively at 3000 rpm (Fig. 5.21), is to demonstrate the capability of PM-RSM to obtain maximum torque at a certain speed in the flux weakening region using the sensorless vector control system.

In the experiments the reference speeds were chosen to be above base speed, which in the case of using one battery it becomes 375 rpm.

The first experiment was performed at 1000 rpm. It can be observed that the developed torque is the same as the load torque under steady state condition. Also, the maximum value of the load torque which corresponds to this speed is almost 2Nm, demonstrated by digital simulations and taking a look at Fig. 5.20e, this is in perfect agreement with the experimental results.

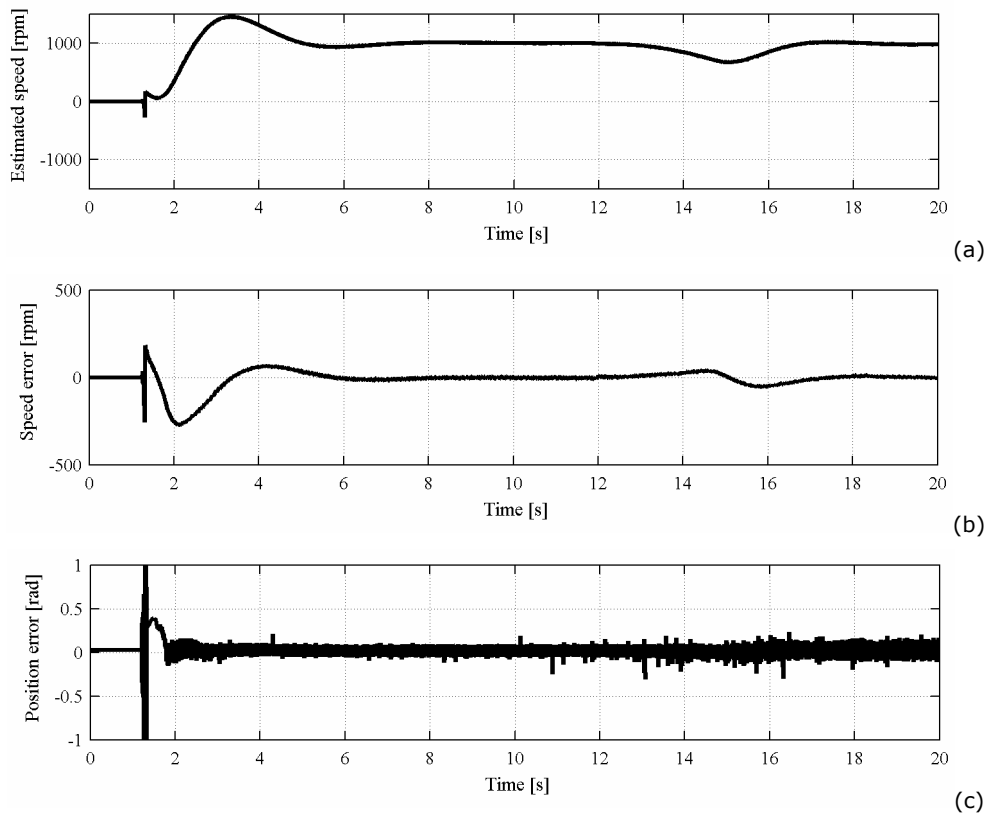
The speed response is quite lent and with a large overshoot, but the purpose in here was not to obtain high machine dynamics. Also, the estimated speed has a

negative spike at startup, but this is favourable because the reference torque will be a bit higher Fig. 5.20a.

However, the position error is very good, below 0.25 rad (Fig. 5.20).

As it was prescribed, the I_q current is kept constant, while the I_d current increases only during loading, when the necessary torque has to be developed (Fig. 5.20d).

This is also the case of the estimated stator flux, which at steady state it is maintained at a low value (almost permanent magnet flux) and then, during loading it increases (Fig. 5.20f).



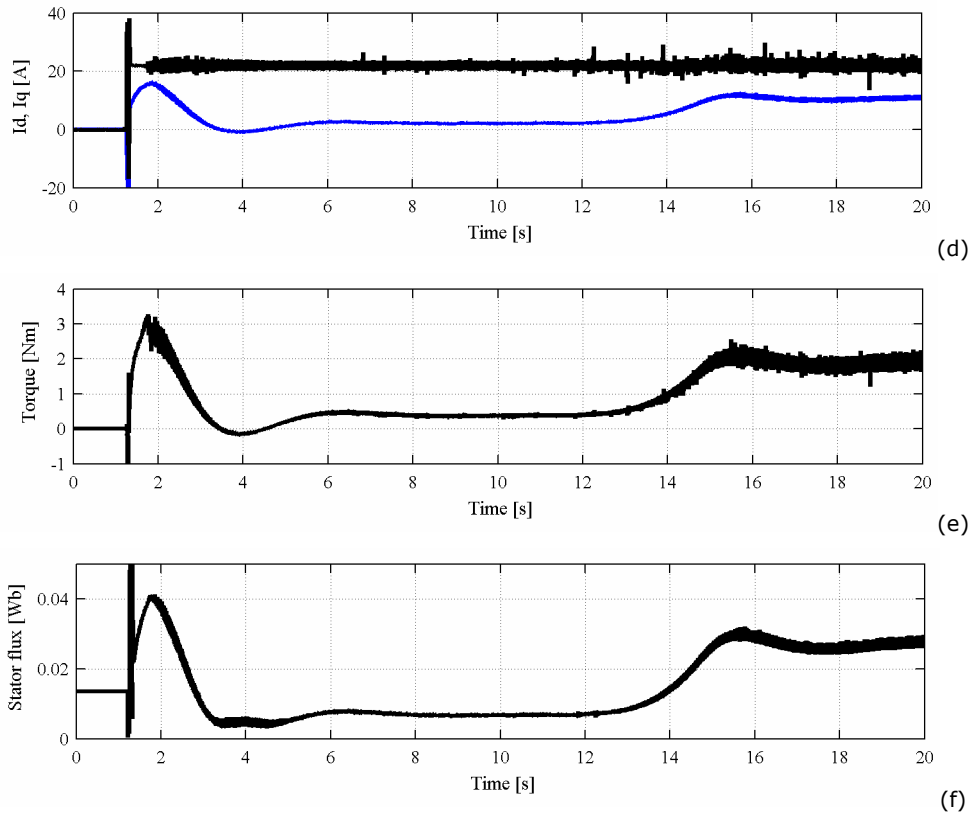


Fig. 5.20. Start up at 1000 rpm followed by a step torque load at 5 s using **the sensorless vector control system**; from top to bottom: (a). estimated speed; (b). error between encoder and estimated speed; (c). error between actual and estimated angle rotor position; (d). I_d (blue), I_q currents; (e). estimated torque; (f). estimated stator flux

The second experiment (Fig. 5.21) proves that the PM-RSM is running at 3000 rpm supplying the machine with only one battery which is equivalent with a speed of 12000 rpm using all four batteries, as it is demonstrated by digital simulations.

However, in practice, using the vector control system the machine could not be loaded. This is in opposite with the case when using the sensorless control strategy 2, when at the machine could be considered a little bit loaded by

connecting the transmission belt between the PM-RSM and the load machine. In the last case a torque of 0.65 (around 10% rated torque) was developed.

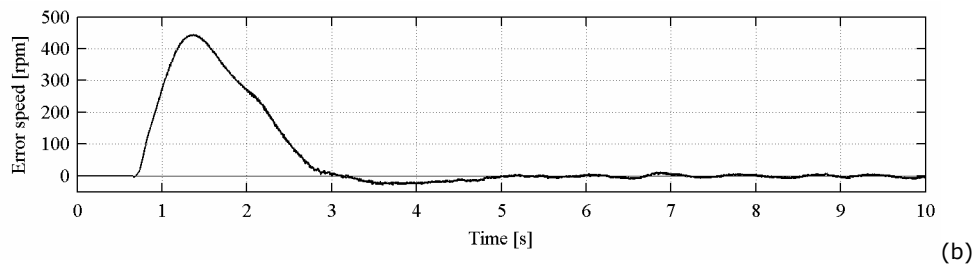
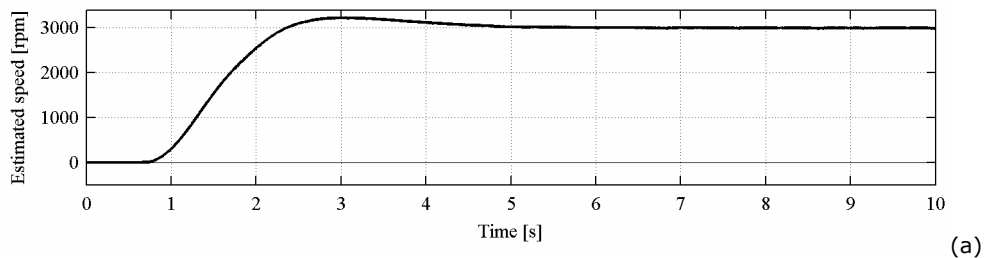
Fig. 5.21e shows the estimated torque of the motor. When the speed of the motor is less than base speed, the torque is more and gets reduced at speeds greater than the rated speed.

The corresponding dq components of current are given in Fig. 5.21d. Since vector control is used the value of i_q is almost 22 A.

Also, since no load is performed, the estimated stator flux remains at the low value Fig. 5.21f.

The conclusion is that using the sensorless vector control system the PM-RSM is capable of flux weakening operation above base speed.

The proportional and integral gains for the PI controllers were chosen by trial and error method and they are given in TABLE 5.3 (see Appendix).



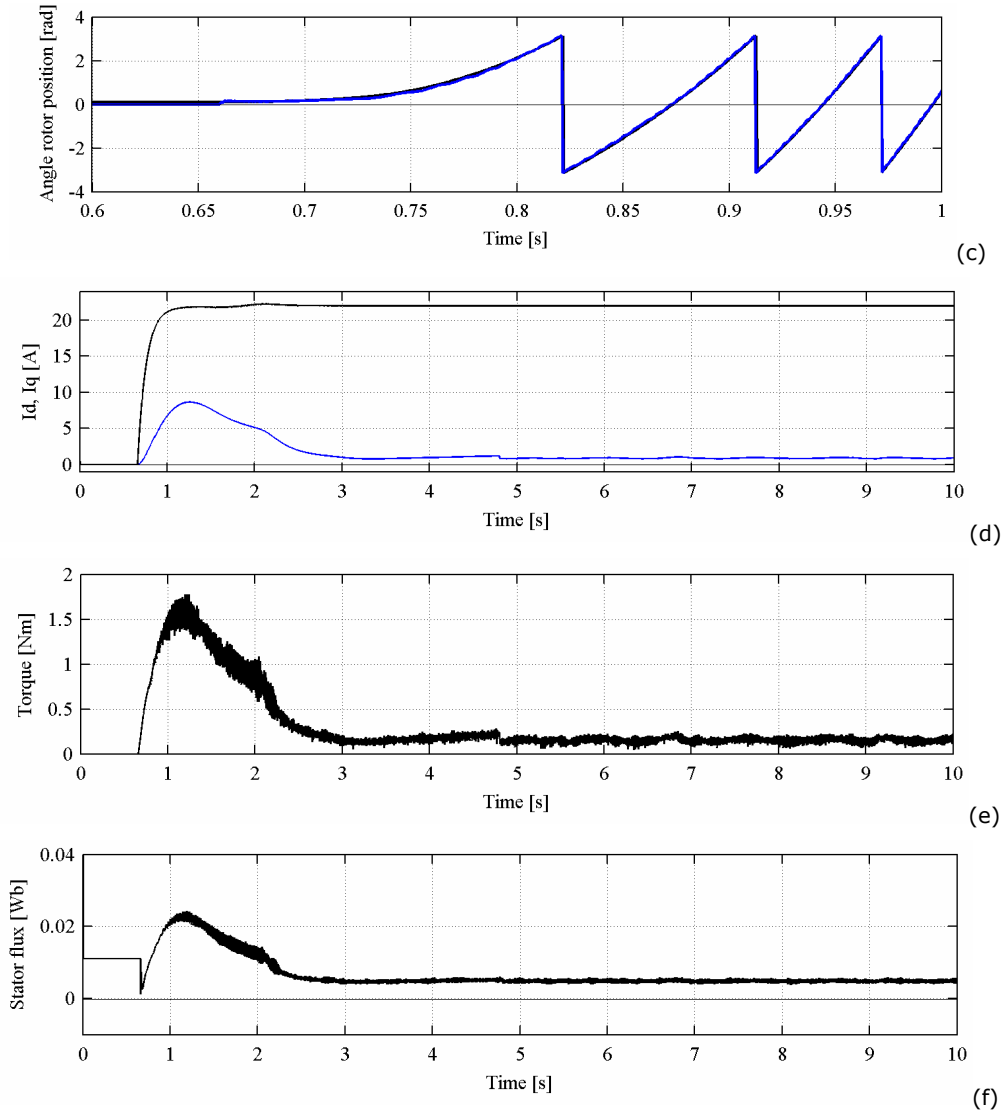


Fig. 5.21. Start up at 3000 rpm using **the sensorless vector control system**; from top to bottom: (a). estimated speed; (b). error between encoder and estimated speed; (c). error between actual and estimated angle rotor position; (d). I_d (blue), I_q currents; (e). estimated torque; (f). estimated stator flux

5.8.2. Experimental Results with PM-RSM Using the Proposed Control Strategy 2

5.8.2.1. Experimental Results with PM-RSM as Motor Using the Proposed Control Strategy 2

The digital simulations results presented at 1 rpm demonstrated that the proposed sensorless control system was able to handle full step torque load. As it was mentioned before, this is not possible in practice due to low performance of the bidirectional inverter at low speeds.

However, the experiments were performed always using the transmission belt between the PM-RSM and the induction load machine. Thus, it can be said that the machine is a little bit loaded and as it could be observed from practice, this load torque was about 0.65 Nm.

So, the experimental results at the lowest achieved speed of 30 rpm, but without load will be next presented in Fig. 5.22.

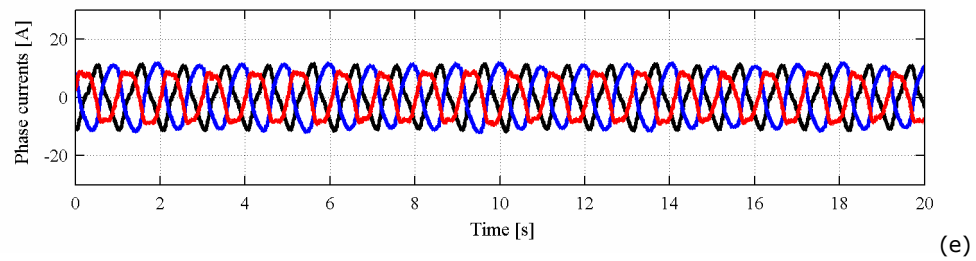
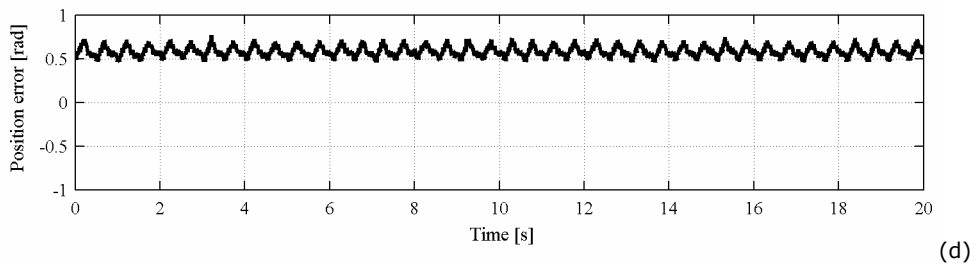
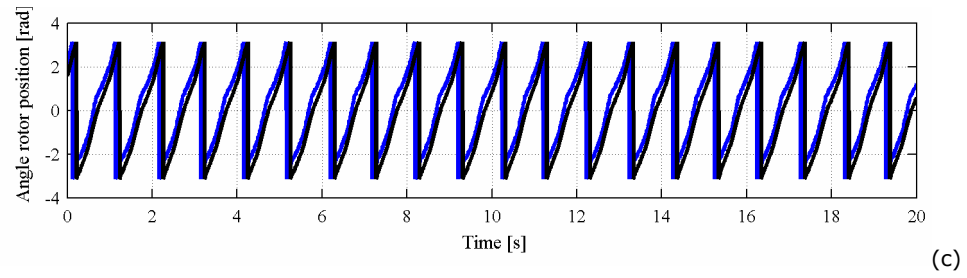
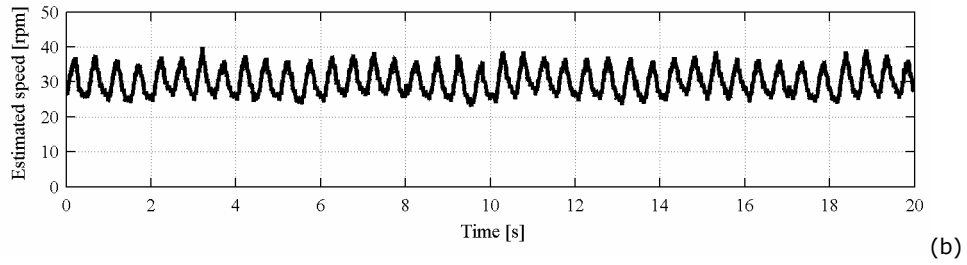
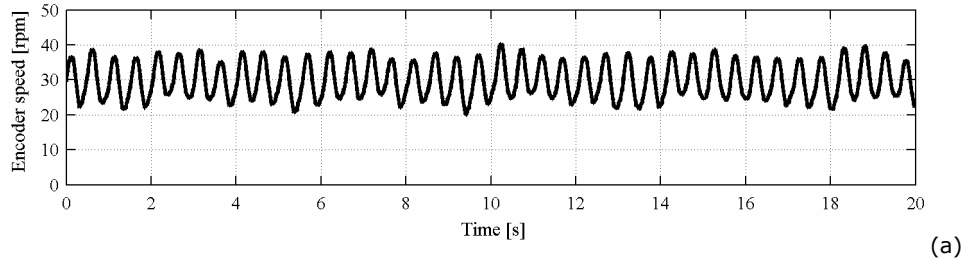
Both encoder and estimated speed have large oscillations of almost 10 rpm according to Fig. 5.22a and Fig. 5.22b. But, it can be observed that the estimated speed is better than the encoder one, due to filtering.

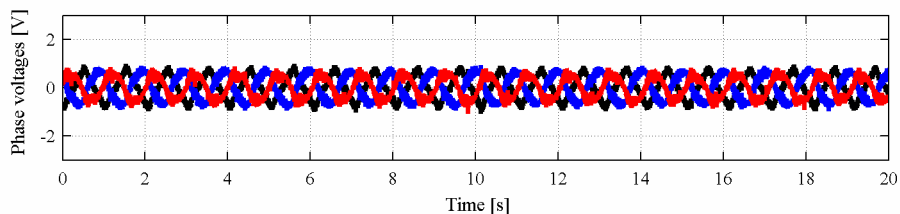
As it is was also mentioned in the others chapters, the performance of the position and speed estimator degrades at low speed, being sensitive to the machine and observer parameters.

Providing so small voltages Fig. 5.22f, it was mandatory for the proposed control system to compensate the voltage drops on the power devices. Even so, the estimated angle rotor position is not smooth, having some pulsations according to Fig. 5.22d and the position error in Fig. 5.22e is quite large (almost 0.6 rad).

From Fig. 5.22e it can be observed that the currents are not smooth and are bigger than they should be due to the fact that the control system tries to counteract the position error.

Comparing these results with the one obtained by using the sensorless vector control system previously presented, it can be concluded that in the last case the position error is lower, whereas with the former one the currents are smaller.





(f)

Fig. 5.22. 30 rpm steady state speed using **the proposed sensorless control strategy 2**; from top to bottom: (a). encoder speed; (b). estimated speed; (c). angle rotor position (actual and estimated (blue)); (d). error between actual and estimated angle rotor position ; (e). phase currents; (f). phase voltages

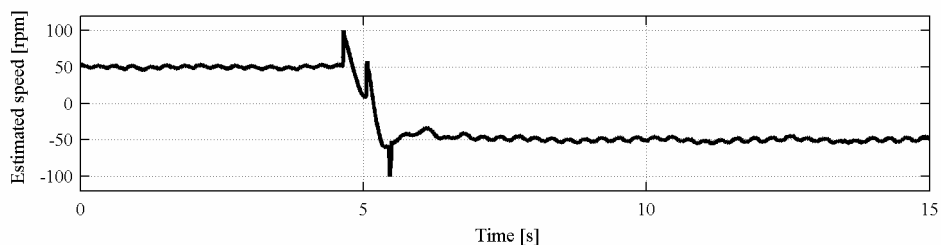
In order to demonstrate that the proposed control system is capable of dynamics at low speed, the next presented experiment performs a speed reversal from + 50 rpm to – 50 rpm Fig. 5.23.

The speed reversal (the speed zero crossing point is critical) is one of the mandatory test to be made to demonstrate the efficacy of the sensorless control system.

The result presented in Fig. 5.23 is considered to be good even if a large spike occurs when the speed crosses zero. One cause may be the interaction between the low pass filter with a large constant time applied to the estimated speed signal and the fast PI speed controller.

Even during steady-state, the errors between the encoder and estimated speed are of 2-3 rpm (Fig. 5.23b), during speed reversal, an overshoot of 50 rpm and a large spike when crossing zero occur in the estimated speed (Fig. 5.23a).

The error of the estimated position reaches a maximum of 0.33 rad.



(a)

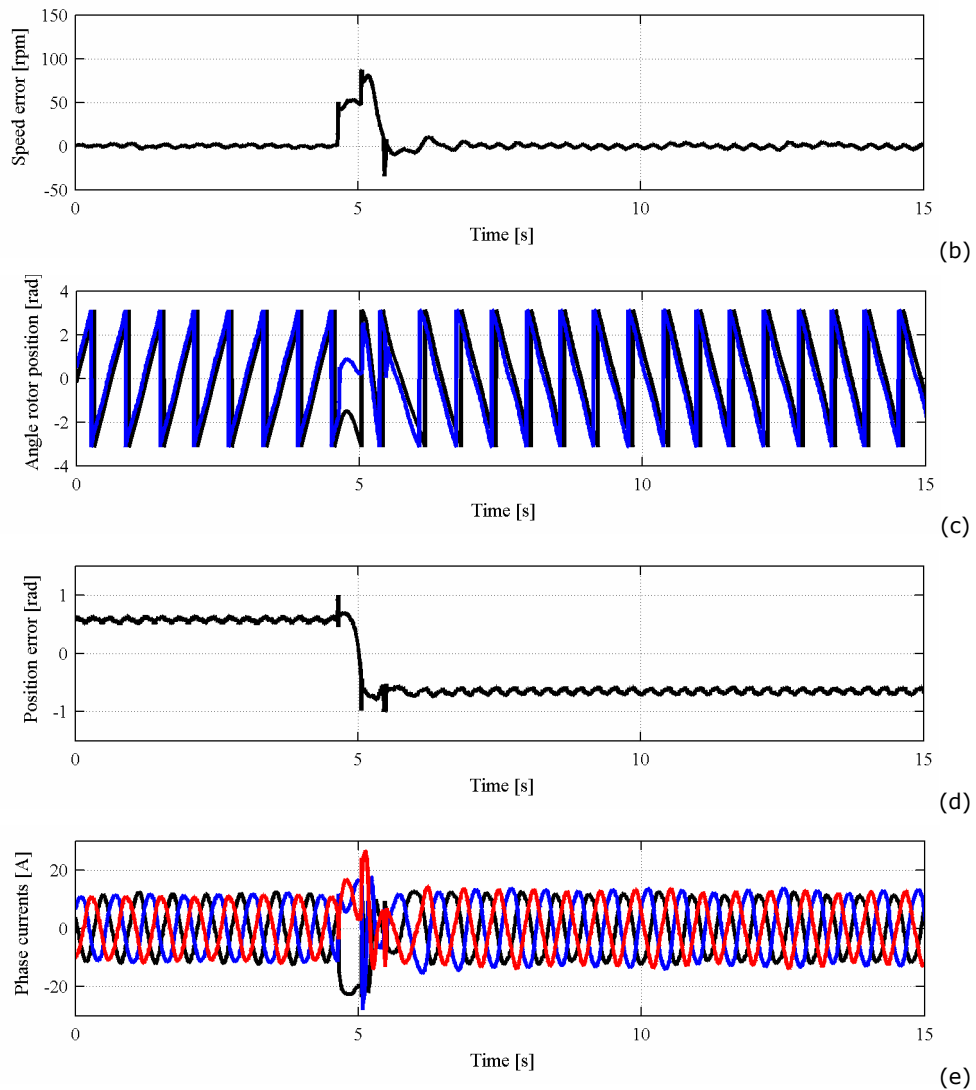


Fig. 5.23. ± 50 rpm speed reversal using **the proposed sensorless control strategy 2**; from top to bottom: (a). encoder speed; (b). error between encoder and estimated speed; (c). angle rotor position (actual and estimated (blue)); (d). error between actual and estimated angle rotor position; (e). phase currents

Here again, comparing this experimental results with the ones obtained using the sensorless vector control system, from the results are obviously better in the last case.

But again, we believe that the former ones could be improved. The important thing that we want to put in evidence here is that both control system are able to handle low speed operation.

In order to demonstrate the capability of the PM-RSM to operate in the flux weakening meanwhile developing maximum torque for a certain speed using an optimal current pair, experimental results are given for two speeds of operation, both of them above base speed.

Thus, within the third experiment, the performances of the proposed control system are evaluated for a speed of 1000 rpm. Using a single battery of 12 Vdc, this speed corresponds to a speed of 4000 rpm in the case of using all four batteries, which is above base speed. The experimental results are shown in Fig. 5.24.

It can be observed that at start up negative polarity oscillations in the estimated speed waveform occur, but then it recovers and achieves the target speed in about 2.5 s (Fig. 5.24a).

At 5.3 s the machine is step loaded with the maximum available torque value (approx. 30% of rated torque) corresponding to the speed of 1000 rpm (Fig. 5.24f).

The speed errors are larger during start up (almost 200 rpm) and during loading (50 rpm), while during steady state they are ± 20 rpm (Fig. 5.24b).

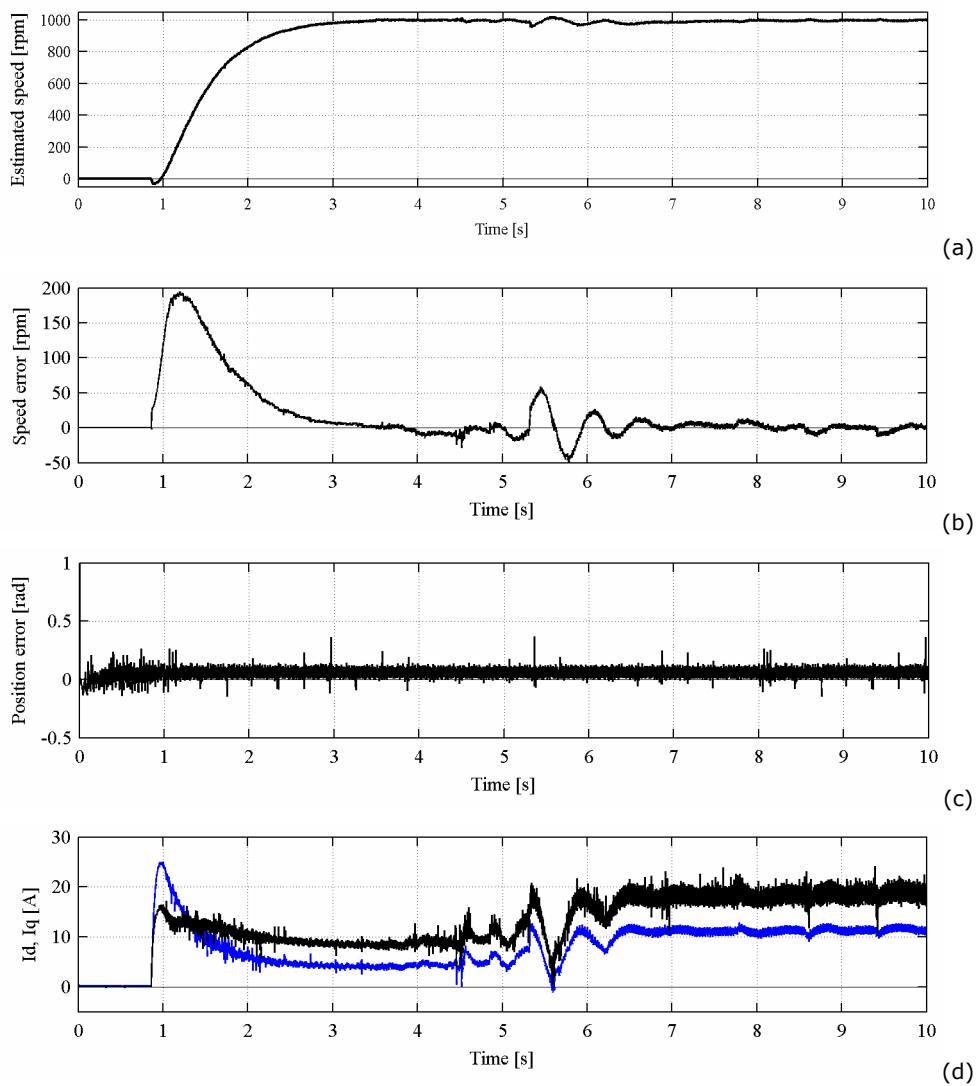
Here, when operating at medium speed the position error is lower than when operating at low speed, due to the fact that now the control system is less sensitive to parameter mismatch and inverter nonlinearities.

It can be also observed that during loading, the voltage attains the maximum available voltage provided by the inverter (Fig. 5.24e).

Also it is obviously that the d -axis current I_d is the torque producing component for the PM-RSM (Fig. 5.24d).

Fig. 5.24f shows the estimated torque of the motor. The starting torque is quite high and the steady state value of torque is reduced to 1.85 Nm at this speed. At this speed the motor is operating in the constant power region.

Also from Fig. 5.24g, it is seen that the estimated stator flux remains at the low value during steady state and during loading increases in order to produce the necessary torque.



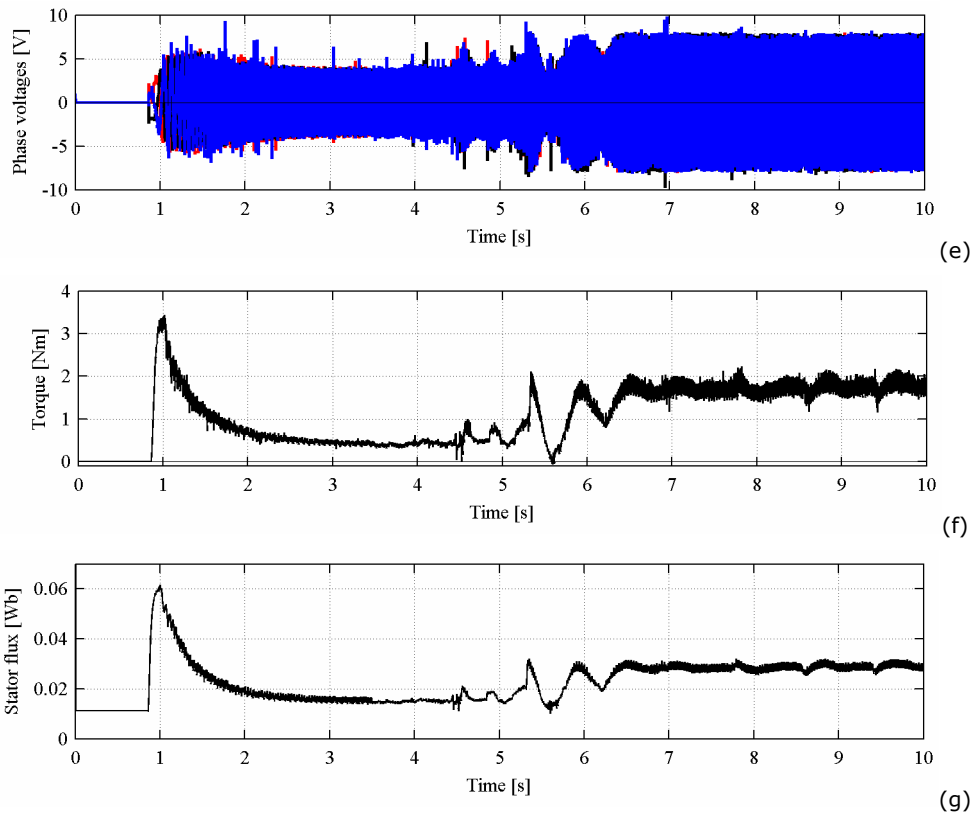


Fig. 5.24. Start up at 1000 rpm followed by a step torque load at 5.3 s using **the proposed sensorless control strategy 2**; from top to bottom: (a). estimated speed; (b). error between encoder and estimated speed; (c). error between actual and estimated angle rotor position; (d). I_d (blue), I_q currents; (e). phase voltages; (f). estimated torque; (g). estimated stator flux

The obtained results are better comparing with the ones obtained using the sensorless vector control system since here, almost the same torque (1.85 Nm compared with 2 Nm) is developed with a smaller total stator current.

To show the operation in the extended speed region the speed command is changed from 0 to 3000 rpm, using a single battery of 12 Vdc.

In the case of using all four batteries, this speed corresponds to a speed of 12000 rpm, which is eight times base speed.

The machine behaves well as expected.

The experimental results are shown in Fig. 5.25.

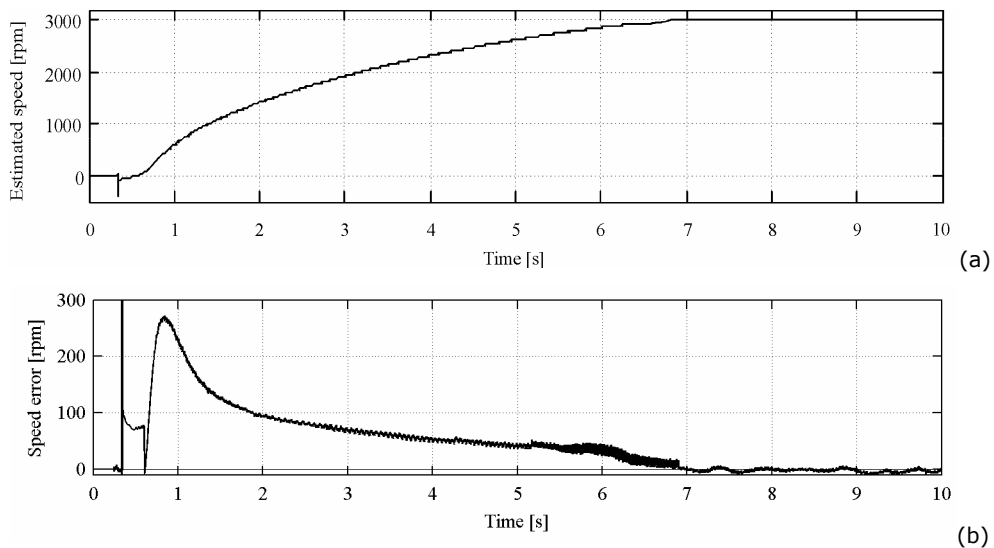
The estimated angle rotor position converges fast to actual angle rotor position during starting (Fig. 5.25c) and the position error is smaller than in the above presented case (Fig. 5.24c).

At 3000 rpm being supplied by a single battery and with the transmission belt between the PM-RSM and the load machine, the machine can not be loaded, the estimated torque being about 0.65 Nm in this case (Fig. 5.25g). This is accordance with the digital simulations results.

In Fig. 5.25d both d and q axis currents are present. However the d axis current is very small since the torque gets very much reduced at higher speed, operating at constant power region.

All these experimental results demonstrate that the transition between the constant torque region and the constant power region is quite fast and smooth at all conditions of operation.

The proportional and integral gains for the PI controllers were chosen by trial and error method and they are given in **TABLE 5.4** (see Appendix).



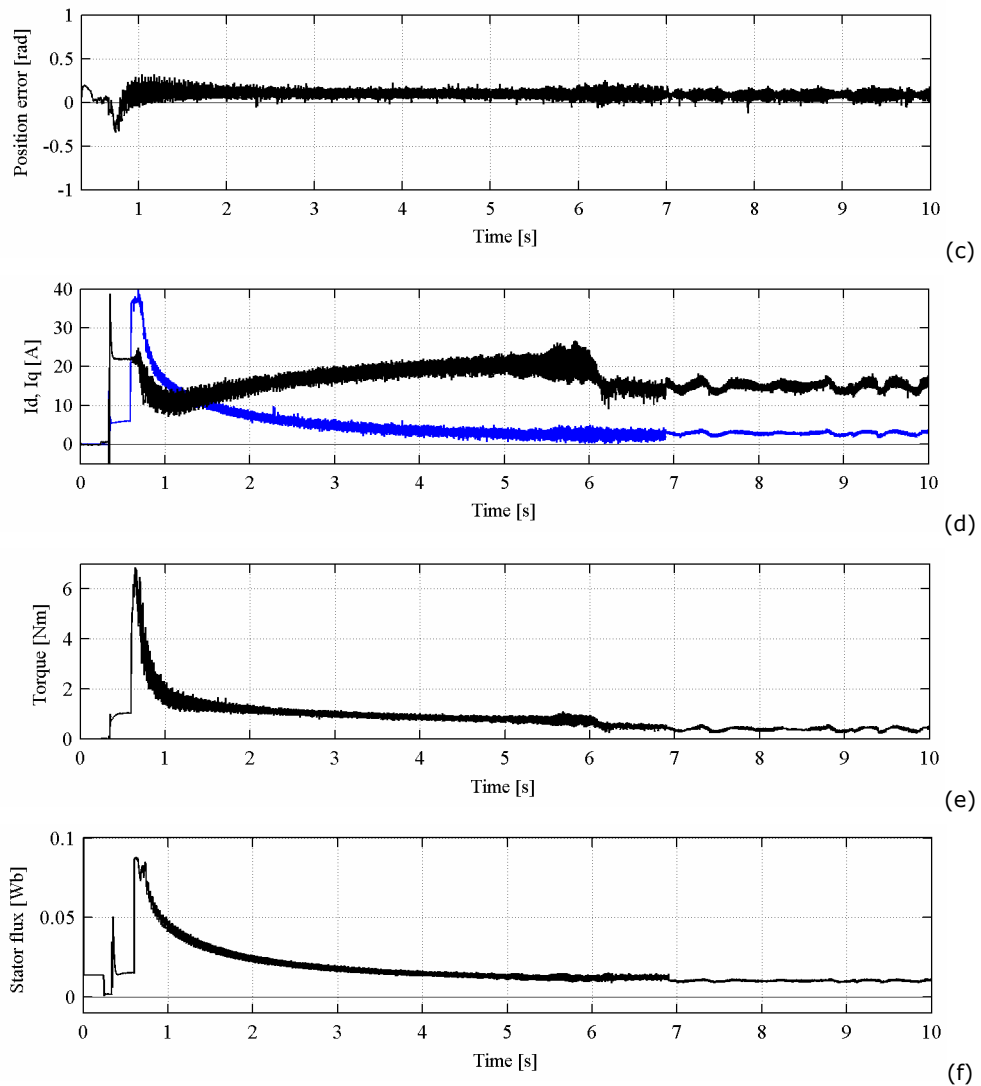


Fig. 5.25. Start up at 3000 rpm using **the proposed sensorless control strategy 2**; from top to bottom: (a). estimated speed; (b). error between encoder and estimated speed; (c). error between actual and estimated angle rotor position; (d). I_d (blue), I_q currents; (e). estimated torque; (f). estimated stator flux

5.8.2.2. Experimental Results with PM-RSM as Generator Using the Proposed Control Strategy 2

The PM-RSM can operate in both modes: motoring or generating. In this paragraph, the purpose is to validate the PM-RSM as generator.

Experimental results at 3000 rpm (Fig. 5.26a) were obtained by driving the PM-RSM torque controlled and the load machine speed controlled. The position used in the coordinate's transformations is the estimated one from the active flux observer.

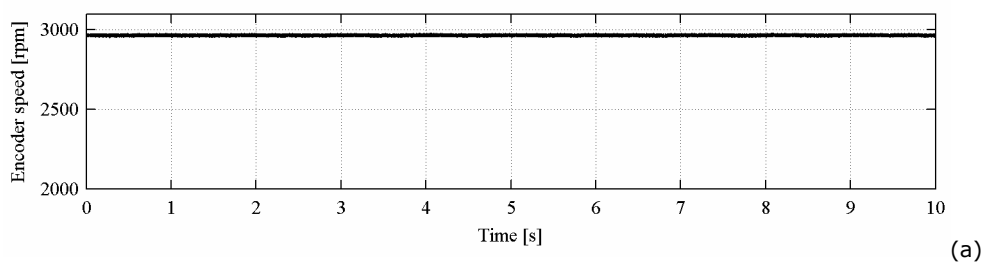
The reference speed is set constant around 3000rpm by the bidirectional inverter, which drives the load machine.

The command torque being negative and the speed positive the PM-RSM operates in generating mode.

The control strategies in generating mode suppose to generate an active power on the batteries either by maintaining the V_{dc} constant or I_{dc} constant or using a more complex strategy which maintains the both V_{dc} and I_{dc} such that the battery could not to be damaged.

In our case, the PM-RSM has been generated power on a single battery with a parallel variable load such that the generated voltage V_{dc} does not exceed 14.4 V (Fig. 5.26c).

For our case, the maximum generated power was 280 W (Fig. 5.26d) for a maximum I_{dc} value of 23.2 A (Fig. 5.26b).



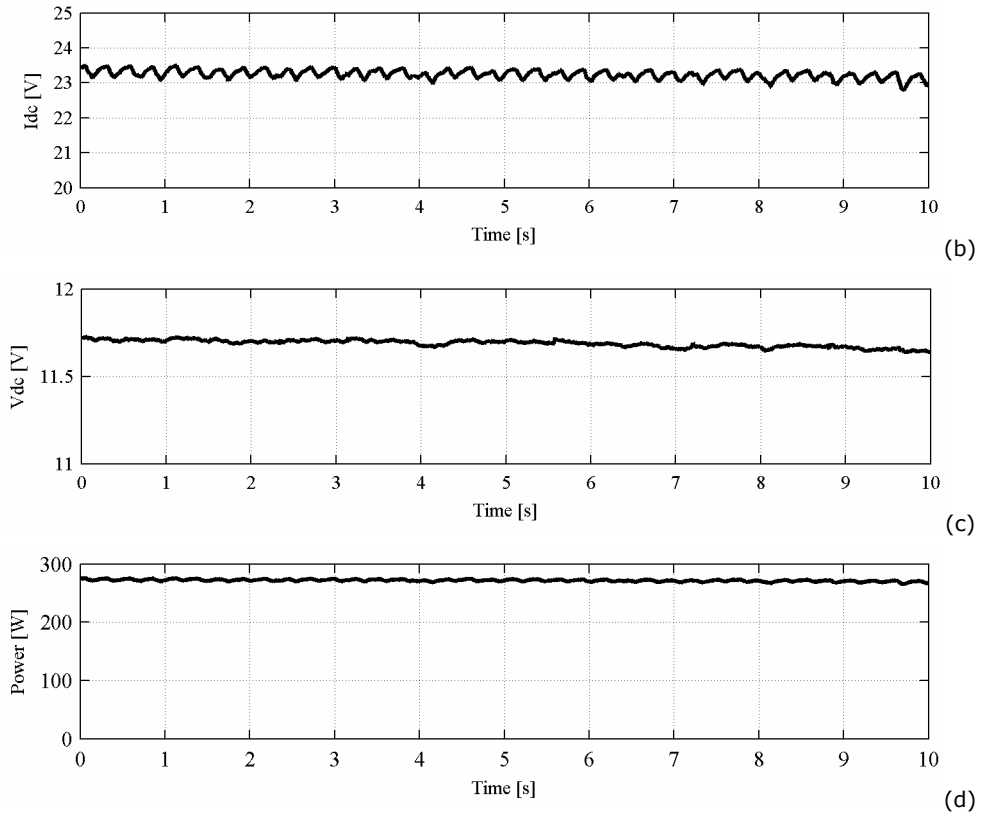


Fig. 5.26. Steady state at 3000 rpm in generating mode; from top to bottom: (a). encoder speed; (b). I_{dc} ; (c). V_{dc} ; (d). active power

5.9. Comparison between the Vector Control and the Proposed Control Strategy 2

In this paragraph, comparisons between the performance of the vector control system and the proposed control strategy 2, both with encoder and in a wide speed range between 30 rpm and 3000 rpm are presented.

It has to be noticed that semnificative loading operation (up to the maximum available torque) was not possible for speeds below 400 rpm due to the low performance of the bidirectional inverter driving the load machine at low speeds.

Here again, the experiments were performed at a voltage that is quarter the rated dc-link voltage of the inverter so as to obtain the eight times base speed and, thus, taking account of the mechanical limits of the PM-RSM.

The experiments were performed under loading and no loading operation modes and their results are presented in Fig. 5.27, respectively in Fig. 5.28.

From Fig. 5.27d it can be seen that using both control systems, the machine can be loaded with almost the same torque value.

Under loading operation mode, the differences in the stator flux and currents waveforms for both control systems are insignificant (Fig. 5.27a,b,c).

In contrast, under no loading operation mode, large differences between the two control systems, over the entire speed range, occur.

Thus, Fig. 5.28a shows that the machine operates with much larger stator flux using the proposed control strategy 2, even if the stator flux is obtained with total stator current lower than in the case of using the vector control system.

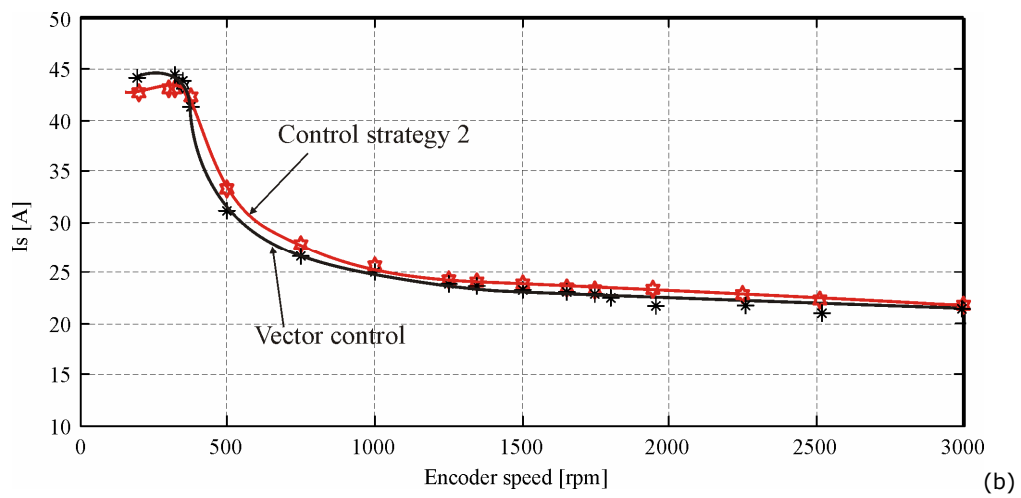
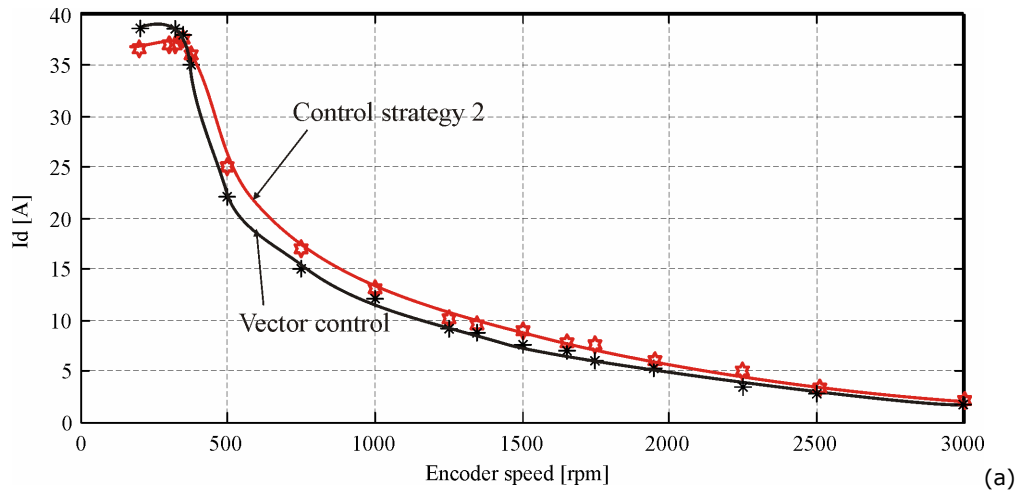
This can be explained by the fact that the vector control system operating mode is to maintain the I_q current at a maximum value of 22 A, independently of the torque value.

During operation in the same conditions as for the vector control system, the proposed control strategy 2 provides an I_q current variable with speed and torque load (Fig. 5.28c).

With both control systems, the I_d current (Fig. 5.27a, respectively Fig. 5.28a) is directly connected with the load torque, but depends a lot of the I_q current previously prescribed. This is the reason why, even with I_q maintained at a constant value of 22 A (in the vector control case) and with I_d having just a little variation around 2 A, the necessary torque is developed.

Both control systems perform well under loading operation mode. However, under no loading operation mode, significant differences between them occur. It is concluded that the proposed control strategy 2 performs better than the vector control system, providing in essence an optimal control characterized by the fact that the maximum torque is no longer achieved with maximum current.

5.9 Comparison between the Vector Control and the Proposed Control Strategy 2 225



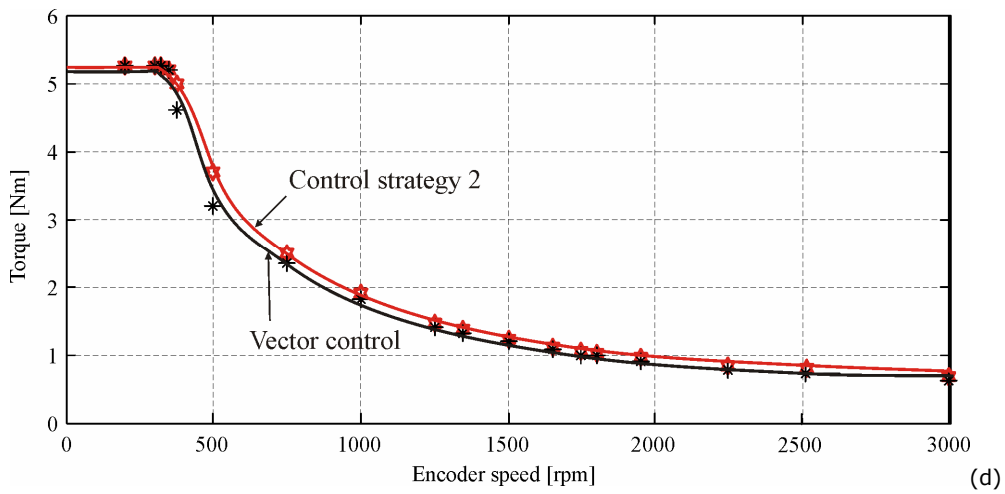
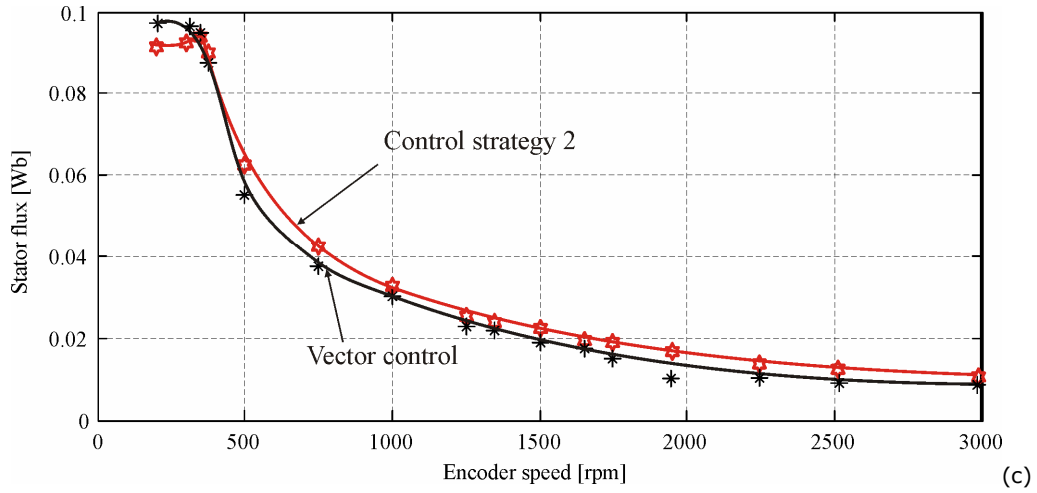
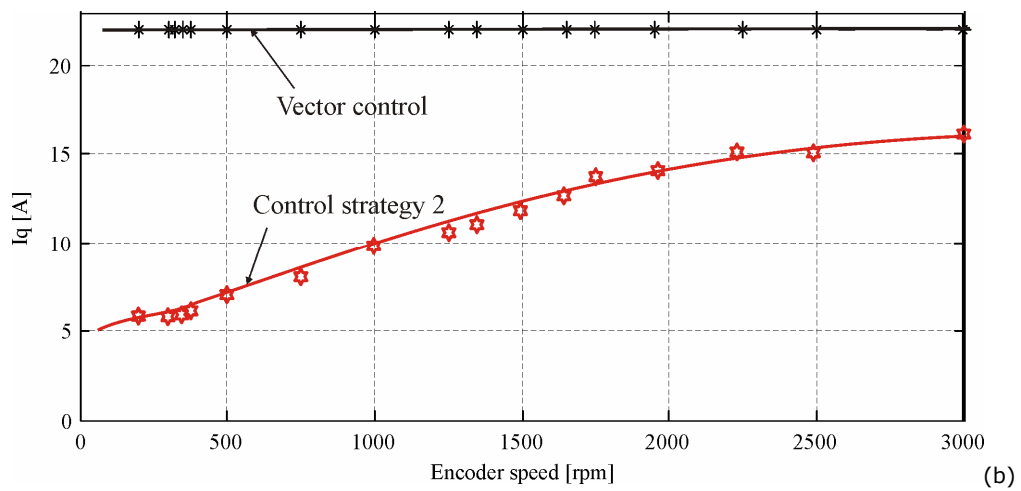
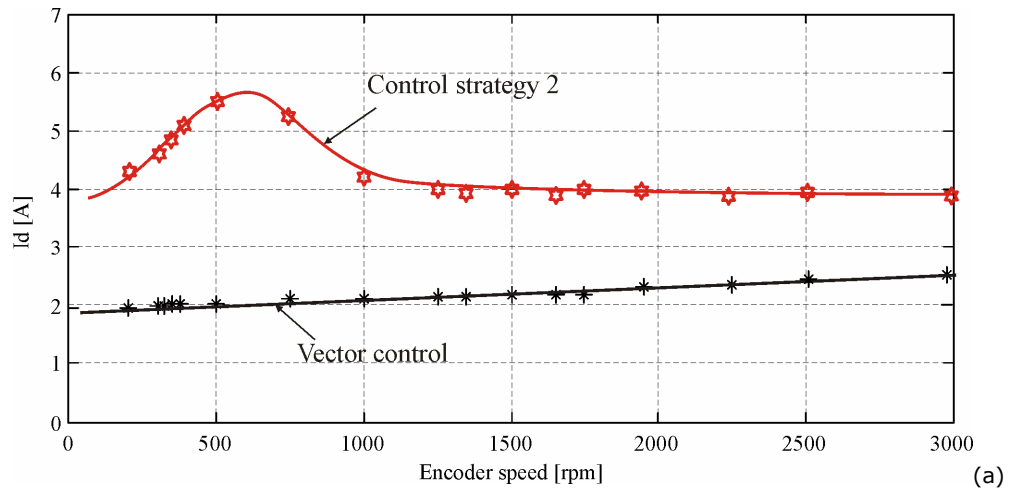


Fig. 5.27. Measurements using both **vector control system** and **proposed control strategy 2** for a wide speed range under **loading** operation; from top to bottom: (a). I_d current; (b). total stator current I_S ; (c). electromagnetic torque; (d). stator flux

5.9 Comparison between the Vector Control and the Proposed Control Strategy 2 227



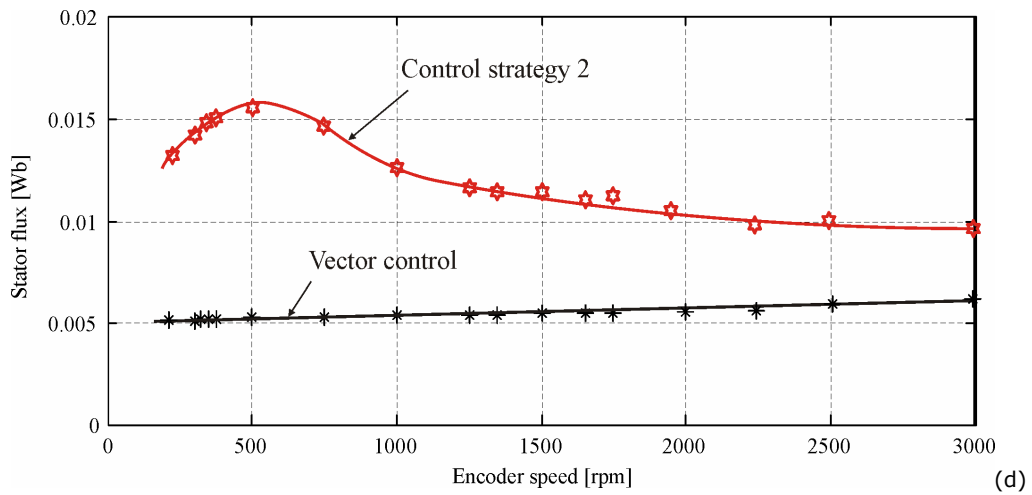
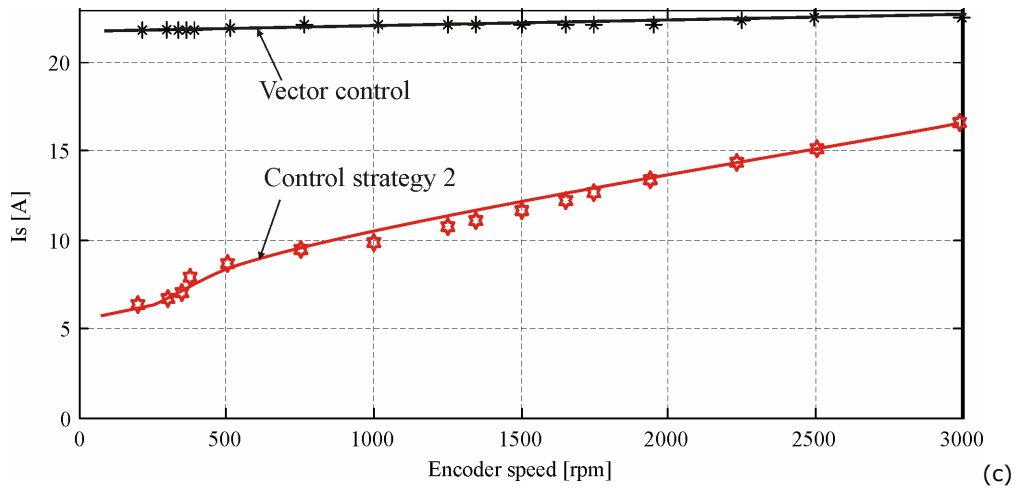


Fig. 5.28. Measurements using both **vector control system** and **proposed control strategy 2** for a wide speed range under **no loading** operation; from top to bottom: (a). I_d current; (b). I_q current; (c). total stator current I_S ; (d). stator flux

5.10. Final Conclusion

Two methods for the motion sensorless control of PM-RSM in wide speed range are presented.

The claim of the first control strategy is a new reference torque calculation and closed loop method that is capable to develop the maximum available torque, for an optimal current pair (i_d, i_q) below base speed, but also in flux weakening region (above base speed) where voltage limitations impose constraints.

At low speed the voltage constraint does not effect the operation of the motor. But at higher speed (FW region) the voltage constraint becomes more effective. To avoid reaching the voltage constraint, the d-axis current should be controlled in such a way that it will weaken the magnetic flux.

Using the proposed control strategy the motor exploits the maximum torque capability in the whole speed range, observing the voltage and current constraints, and good efficiency all over.

The second control strategy is an alternative to the first control, but having the advantage to be much simpler and involving less computational off-line effort.

The theoretical basis of both proposed control strategies has been described in detail and some analytical forms are also provided for reference.

The effectiveness of the two proposed model-based sensorless control strategies is confirmed by digital simulations in a wide speed range down to 1 rpm and up to 12000 rpm, thus, up to a speed equal eight times machine base speed.

The conclusion was that both of them perform the same. Thus, in the experiments the sensorless control strategy 2 has been performed, being much simpler. Its experimental results between 30 rpm and 3000 rpm validate the theoretical background.

Also, a vector control system was developed and operation below and above rated speed has been studied using it. Then a comparasion between vector control system and the control strategy 2 confirmed the effectiveness of the second, especially under loading conditions.

Note. The PM-RSM prototype has rather high magnetic saliency and four flux barriers per pole, which is known to make rotor position tracking more difficult for inset IPMSM.

5.11. Appendix

TABLE 5.1

Gains Used in Digital Simulation Employing the Proposed Wide Speed Range Control Strategy 1

PI speed controller	k_{p_w}	1
	k_{i_w}	20
PI torque controller	k_{p_T}	1
	k_{i_T}	1000
PI i_d controller	$k_{p_i_d}$	10
	$k_{i_i_d}$	400
PI i_q controller	$k_{p_i_q}$	10
	$k_{i_i_q}$	100

TABLE 5.2

Gains Used in Digital Simulation Employing the Proposed Wide Speed Range Control Strategy 2

PI speed controller	k_{p_w}	0.3
	k_{i_w}	10
PI i_d controller	$k_{p_i_d}$	10
	$k_{i_i_d}$	400
PI i_q controller	$k_{p_i_q}$	10
	$k_{i_i_q}$	100

TABLE 5.3

Gains Used in Experimental Work Employing the Vector Control System

PI speed controller	k_{p_w}	0.05
	k_{i_w}	10
PI i_d controller	$k_{p_i_d}$	10
	$k_{i_i_d}$	400
PI i_q controller	$k_{p_i_q}$	10
	$k_{i_i_q}$	100

TABLE 5.4

Gains Used in Experimental Work Employing the Proposed Wide Speed Range Control Strategy 2

PI speed controller	k_{p_w}	0.03
	k_{i_w}	1
PI i_d controller	$k_{p_i_d}$	1
	$k_{i_i_d}$	10
PI i_q controller	$k_{p_i_q}$	1
	$k_{i_i_q}$	100

Magnetic saturation curve identification

In practice, a memorized look-up table with linear interpolation between points was used.

The identification procedure of the $L_d(i_d)$ magnetic saturation curve during self-commissioning is described in what follows:

1) The machine operates in speed closed-loop at (constant) high speed. The measured variables are: $\vec{i}_s^S(i_\alpha, i_\beta)$ and θ_{er} .

2) Eliminating the current flux model from the state observer (Fig. 5.9), the stator flux $\vec{\psi}_s^S$ estimation is provided only by the voltage flux model with PI compensator. Then, the stator flux components (ψ_{sd}, ψ_{sq}) and the stator current components (i_d, i_q) in rotor coordinates are calculated:

$$\hat{\psi}_d + j\hat{\psi}_q = \vec{\psi}_s^S e^{-j\theta_{er}} \quad \text{and} \quad i_d + ji_q = \vec{i}_s^S(i_\alpha, i_\beta) e^{-j\theta_{er}} \quad (5.13)$$

3) Finally, the magnetic saturation curve $L_d(i_d)$, used in current flux model, is computed as illustrated in Fig. 5.29, which, if it is not used, wrong results and conclusions are traced.

Note that at high speed, the flux weakening is inherent and the magnetic saturation curve $L_d(i_d)$ degenerates into straight lines with $L_d = \text{const.}$ and thus, the $\hat{\theta}_{er}$ observer errors are less important.

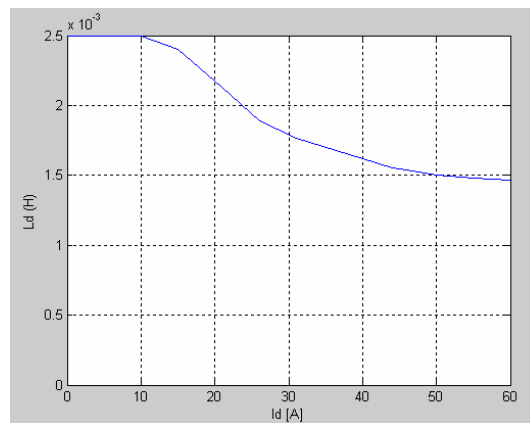


Fig. 5.29. The magnetic saturation curve

In Fig. 5.30, the $i_{d_opt}^*(T_e^*)$, obtained by Finite Element Method (FEM), based on maximum torque/current criterion is presented.

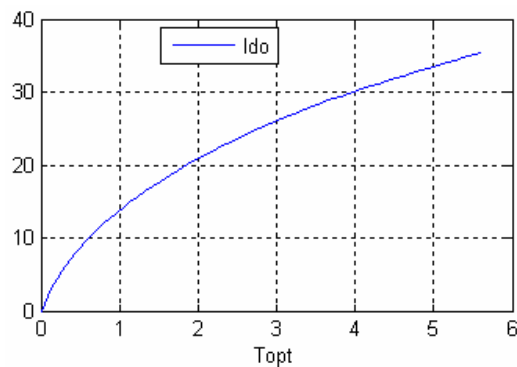


Fig. 5.30. The $i_{d_opt}^*(T_e^*)$ curve (A/Nm)

References

- [1] C. Silva, G. M. Asher, and M. Sumner, "Hybrid rotor position observer for wide speed range sensorless PM motor drives including zero speed," IEEE Trans. Ind. Electron., vol. 53, no. 2, pp. 373–378, 2006.
- [2] I. Boldea, M. C. Paicu, and G. D. Andreescu, "Active flux concept for motion sensorless unified ac drives," IEEE Trans. Power Electron., vol.23, no 5, pp. 2612-2618, 2008.
- [3] M. N. Uddin, and M. A. Rahman, "High-Speed Control of IPMSM Drives Using Improved Fuzzy Logic Algorithms," IEEE Trans. Ind. Electron., vol.54, no 1, pp. 190-199, Febr. 2007.
- [4] T. M. Jahns, G. E. Kliman, and T. W. Neumann, "Interior permanent magnet synchronous motors for adjustable-speed drive," IEEE Trans. Ind. Appl., vol. 22, no 4, pp. 738–747, July/Aug 1986.
- [5] G. Kang, J. Lim, K. Nam, H.B. Ihm and H.G. Kim, "A MTPA control scheme for an IPM synchronous motor considering magnetic flux variation caused by temperature," in Proc. IEEE-APEC 2004, vol. 5, pp. 1617-1621.

- [6] C.T. Pan and S.M. Sue, "A linear maximum torque per ampere control for IPMSM drives over full-load range speed," *IEEE Trans. Energy. Convers.*, vol. 20, no. 2, pp. 359–366, 2005.
- [7] E.M. Rashad, T.S. Radwan, and M. A. Rahman, "A maximum torque per ampere vector control strategy for synchronous reluctance motors considering saturation and iron losses," in *Conf. Record IEEE-IAS 2004*, vol. 4, pp. 2411–2417.
- [8] Z.C. Zhu, Y. S. Chen and D. Howe, "Iron loss in permanent-magnet brushless ac machines under maximum torque per ampere and flux weakening control," *IEEE Trans. Magn.*, vol. 38, no. 5, pp. 3285–3287, 2002.
- [9] C.B. Butt, M.A. Hoque and M.A. Rahman, "Simplified fuzzy-logic-based MTPA speed control of IPMSM drive," *IEEE Trans. Ind. Appl.*, vol. 40, no. 6, pp. 1529–1535, 2004.
- [10] Y. A. R. I. Mohamed and T.K. Lee, "Adaptive self-tuning MTPA vector controller for IPMSM: drive system," *IEEE Trans. Energy. Convers.*, vol. 21, no. 3, pp. 636–644, 2006.
- [11] P. Niazi and H. Toliyat, "Robust maximum torque per ampere (MTPA) control of PM-assisted synchronous reluctance motor," in *Conf. Record IEEE-APEC 2006*, Dallas, TX.
- [12] C. Butt and M.A. Rahman, "Limitations of simplified fuzzy logic controller for IPM motor drive," in *Conf. Record IEEE-IAS 2004*, vol. 3, pp. 1891–1898.
- [13] M.I. Chy and M.N. Uddin, "A novel fuzzy logic flux controls of IPM synchronous motor," in *Conf. Record IEEE-IAS 2007*, pp. 1673–1680.
- [14] M.N. Uddin and M.I. Chy, "Development and implementation of a nonlinear controller incorporating flux control for IPMSM," in *Proc. IEEE-IECON-2007.*, vol. 40, no. 2, pp. 1067–1072, 2007.
- [15] S. Morimoto, M. Sanada, and Y. Takeda, "Effects and compensation of magnetic saturation in flux-weakening controlled permanent magnet synchronous motor drives," *IEEE Trans. Ind. Appl.*, vol. 30, no. 6, pp. 1632–1637, 1994.

- [16] J. Wai, and T.M. Jahns, "A new control technique for achieving wide constant power speed operation with an interior PM alternator machine," in Conf. Record IEEE-IAS 2001, vol. 2, pp. 807-814.
- [17] J.-M. Kim, and S.-K. Sul, "Speed Control of Interior Permanent Magnet Synchronous Motor Drive for the Flux Weakening Operation," IEEE Trans. Ind. Appl., vol. 33, no. 1, pp. 43-48, 1997.
- [18] M. Mengoni, L. Zarri, A. Tani, G. Serra, and D. Casadei, "Stator flux vector control of induction motor drive in the field weakening region," IEEE Trans. Power Electron., vol. 23, no. 2, pp. 941-949, 2008.
- [19] A. Tripathi, A. M. Khambadkone, and S. K. Panda, "Dynamic Control of Torque in Overmodulation and in the Field Weakening Region," IEEE Trans. Power Electron., vol. 21, no. 4, pp. 1091-1098, July 2006.
- [20] H. Abu-Rub, H. Schmirgel and J. Holtz, "Sensorless control of induction motors for maximum steady-state torque and fast dynamics at field weakening," in Conf. Record IEEE-IAS 2006, vol. 1, pp. 96-103.
- [21] L. Xu, B. Guan, J. Hu, "A Robust Sensorless Control Algorithm for Induction Generator Operating in Deep Flux Weakening Region," in Conf. Record IEEE-IAS 2008.
- [22] M. M. Bech, T. S. Frederiksen, and P. Sandholdt, "Accurate Torque Control of Saturated Interior Permanent Magnet Synchronous Motors in the Field-Weakening Region," in Conf. Record IEEE-IAS 2005, vol. 4, pp. 2526-2532..
- [23] P.-Y. Lin, Y.-S. Lai, "Novel Voltage Trajectory Control for Flux Weakening Operation of Surface Mounted PMSM Drives," in Conf. Record IEEE-IAS 2008.
- [24] C. Jo, J.-Y. Seol, and I.-J. Ha, "Flux-Weakening Control of IPM Motors With Significant Effect of Magnetic Saturation and Stator Resistance," IEEE Trans. Ind. Electron., vol. 55, no. 3, pp. 1330-1340, March 2008.
- [25] M. C. Paicu, L. Tutelea, G.-D. Andreescu, I. Boldea, "'Active Flux' Sensorless Vector Control of IPMSM for Wide Speed Range," Journal of Electrical Engineering, JEE, vol. 8, no. 5, Politehnica Publishing House, Timisoara, 2008.
- [26] M. C. Paicu, L. Tutelea, G.-D. Andreescu, I. Boldea, F. Blaabjerg "Wide speed range sensorless control of PM-RSM via "active flux" model" sent for publication to ICCE 2009, San Jose, SUA.

Chapter 6

Experimental Platforms and Software Implementation

Abstract

This chapter presents an extended description of the laboratory setups used for experiments in chapters 2, 3, 4 and 5.

One of the two platforms was realized in the Dspace Lab, Institute of Energy Technology, Aalborg, Denmark. The other one was realized in the Intelligent Motion Control Lab, Faculty of Electrical Engineering, Timișoara, Romania.

Their intended purpose was to prove and gain new information about the control of the synchronous machine, as the main part of the thesis.

In this chapter the two platforms will be separately presented.

Each experimental setup mainly consists in the test machine and the load drive. Besides those main components, there are also the measuring circuits (of the phase currents, of the dc voltage link and of the machine speed and rotor position) and the control system software.

This chapter discusses the experimental setups as well as the implementation of various experimental tests, which were performed in order to validate the proposed sensorless control schemes under various conditions.

6.1. Experimental Setup 1

First of all the experimental setup realized in the Dspace Lab, Institute of Energy Technology, Aalborg, Denmark will be presented. Making use of it, the proposed sensorless control schemes from chapter 2, 3 and 4 will be validated.

Let now make a short presentation of this experimental setup (Fig. 6.1). As you can see in Fig. 6.1b a three-phase 2.2 kW IPMSM is directly coupled to the load machine (Siemens PMSM), which is speed controlled by a frequency inverter (Siemens Simover Masterdrive).

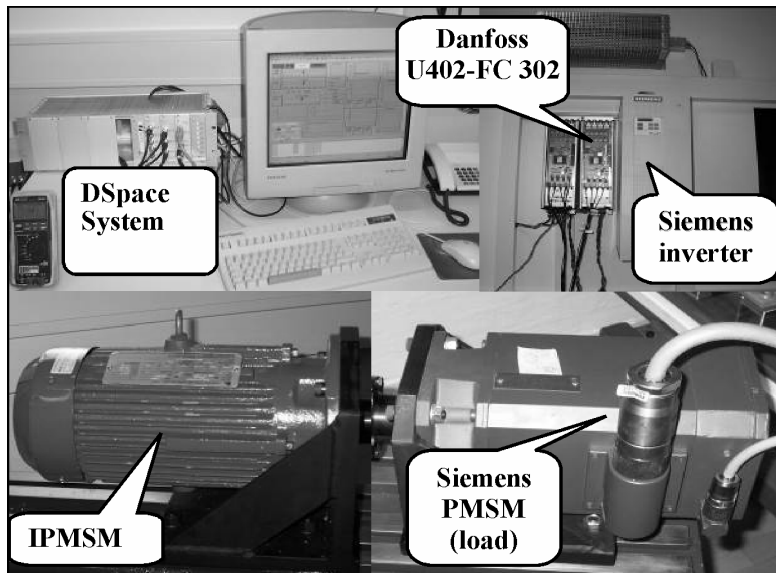
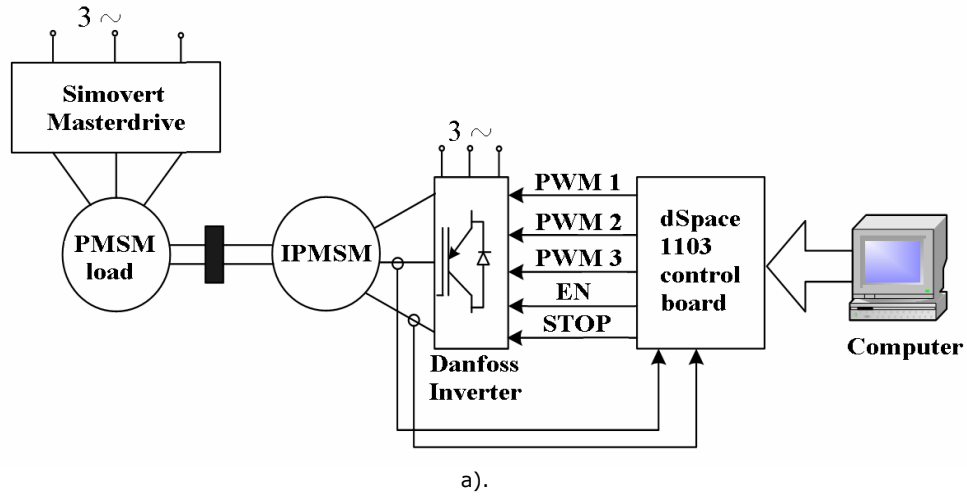


Fig. 6.1. The overview of the experimental setup 1 a). the control block scheme; b).the control real implementation

A three-phase IGBT inverter, supplied at a dc-link voltage of 540V, feeds the IPMSM. The sampling frequency and PWM frequency are set to 10 kHz. The inverter dead time is set to 2 μ s. Phase currents are measured using magnetic current transducers. The actual rotor position and speed are provided by an incremental encoder with 2048 pulses per revolution, only for comparison.

It can be said that the whole experimental setup is divided in few subsystems:

- test machine
- three phase inverter
- load control system
- phase current measurements
- dc voltage link measurements
- rotor speed measurements
- rotor position measurements
- dSpace 1103 platform

6.1.1. Test machine (IPMSM)

The main component in the setup is the interior permanent magnet synchronous motor (IPMSM), manufactured by Yaskawa (see Fig. 6.1b).

TABLE 6.1

IPMSM SPECIFICATIONS

Rated power	2.2 kW
Rated speed	1750 rpm
Rated frequency	87.5 Hz
Rated torque	12 Nm
Rated phase to phase voltage	380 V (rms)
Rated phase current	4.1 A (rms)
Number of pole pairs (p_1)	3
Stator resistance per phase (R_s)	3.3 Ω
d-axis inductance (L_d)	41.6 mH

q-axis inductance (L_{qn})	57.1 mH
Permanent magnet flux (λ_{PM})	0.483 Vs/rad
Total inertia (J)	10.1×10^{-3} kgm ²
Viscous friction coefficient (B)	20×10^{-4} Nm s/rad
Windings connection	star connection

6.1.2. Three phase inverter

The three phase inverter used for this experimental setup is a Danfoss U402 - FC 302 type (Fig. 6.1b).

Control principle:

A frequency converter rectifies AC voltage from mains into DC voltage, after which this DC voltage is converted into an AC current with a variable amplitude and frequency.

The motor is thus supplied with variable voltage and frequency, which enables infinitely variable speed control.

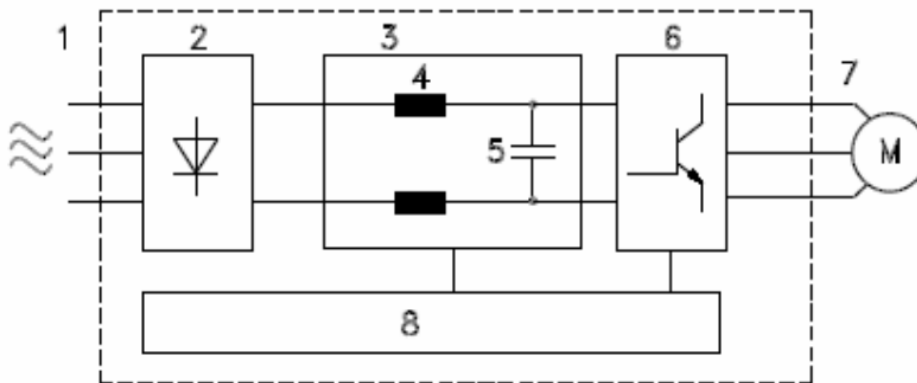


Fig. 6.2. Danfoss principle

where:

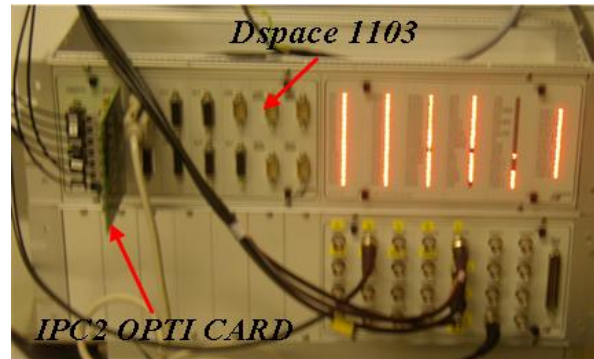
1. Mains voltage: 3 x 200 - 240 V AC, 50 / 60 Hz
 3 x 380 - 500 V AC, 50 / 60 Hz
 3 x 525 - 600 V AC, 50 / 60 Hz.
2. Rectifier: A three-phase rectifier bridge that rectifies AC current into DC current.
3. Intermediate circuit: DC voltage = 1.35 x mains voltage [V].
4. Intermediate circuit coils: Smooth the intermediate circuit current and limit the load on mains and components (mains transformer, wires, fuses and contactors).
5. Intermediate circuit capacitors: Smooth the intermediate circuit voltage.
6. Inverter: Converts DC voltage into variable AC voltage with a variable frequency.
7. Motor voltage: Variable AC voltage, 0-100% of mains supply voltage.
 Variable frequency: 0.5-132/0.5-1000 Hz.
8. Control card: This is where to find the computer that controls the inverter which generates the pulse pattern by which the DC voltage is converted into variable AC voltage with a variable frequency.

The original interface card and control panel were replaced with interface and protection cards (IPC2 – see Fig. 6.3b), produced by IET, Aalborg University.

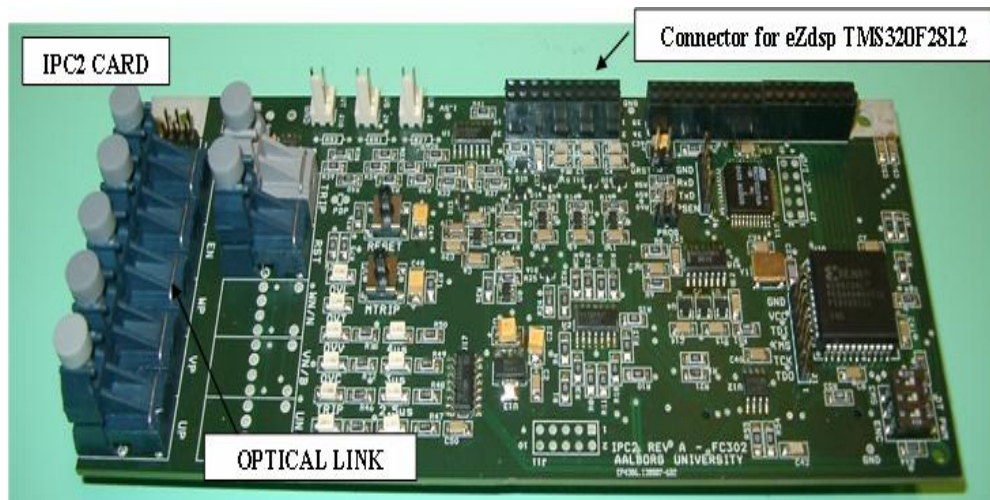
IPC2 is a PCB card with the same dimensions and mounting layout as the original FC 302 control card. It offers the possibility to be connected with an external digital controller (Zdsp TMS 320F2812). The dead time for switches is hardware implemented on IPC board and the user can choose between 1.5-3 μ s.

The interface board is featured with two push-buttons: RESET (RST) and MANUAL TRIP (TRIP) as they are labeled on the card. Any fault that might occur need to be cleared out by pressing RST in order to release the gate signals. The TRIP button forces a trip when pressed.

IPC2 card is connected through optical interface IPC2OPT I card with dSPACE DS1103.



a).



b).

Fig. 6.3. IPC2 interface card for Danfoss U402-FC 302 inverter: a). connected to dSpace platform; b). by itself

6.1.3. Load control system: SIMOVERT MASTER DRIVE

The load machine is a SPMSM. It is from Siemens and the type is ROTEC 1FT6. This machine is fitted with an encoder in order to provide position and velocity

information of the rotor. The rated speed and the rated torque of this machine are 3000 rpm and 14.7 Nm respectively.

It is driven by a commercial inverter operated in open loop torque control mode (SIMOVERT MASTERDRIVE Fig. 6.4).



Fig. 6.4. SIMOVERT MASTERDRIVE

The advantages of the SIMOVERT MASTERDRIVE inverter [1] are:

- can be expanded in a modular fashion: using operator control panels, terminal expansion modules, braking modules, input and output filters
- high speed and torque accuracy
- excellent dynamic performance
- extremely smooth running characteristics at low speeds
- high overload capability
- high power density
- optimum price-performance ratio
- can be simply engineered using PATH, in a user-friendly fashion

The AFE (Active Front End) rectifier/regenerative feedback units belonging to the SIMOVERT MASTERDRIVES series are power electronics devices that are available as cabinet, chassis and as compact units.

The compact units described below are available only in the 400 V mains voltage range.

The units can be operated on three-phase mains with or without an earthed neutral point. The mains voltage range is: 3AC 380 V (- 20 %) to 460 V (+ 5 %)

The core component of the AFE rectifier/regenerative feedback unit consists of a voltage source converter with the CUSA control unit and it generates a controlled DC voltage, the so-called DC link voltage, from a three-phase mains.

This DC link voltage is kept constant almost independently of the mains voltage (also in the event of regenerative feedback). The prerequisite for this is that the DC voltage setpoint is within the operating range defined below.

DC link voltage operating range:

- Minimum: 1.5 times the rms value of the applied mains voltage.
Explanation: the DC link voltage of the AFE inverter must at least be greater than the peak rectified value of the applied mains voltage to ensure that the power system is no longer controlled via the freewheeling diodes of the IGBT switches.
- Maximum: for the 400 V mains voltage range: 740 Vdc

Operating principle:

On the three-phase end, a mains angle-oriented high-speed vector control is subordinate to the DC link voltage control and impresses an almost sinusoidal current on the network so as to minimize system perturbations with the aid of the subsequently connected Clean Power filter.

The vector control also enables setting of the power factor $\cos \phi$, and thus reactive power compensation, but the operating current requirement has priority.

The VSB module (Voltage Sensing Board), functions as the network angle sensor, similarly to the principle of an encoder.

For safety reasons, an AFE rectifier/regenerative feedback unit must be connected to the mains via a main contactor. For this reason, an external 24 V power supply is always needed to supply the VSB module and the AFE unit.

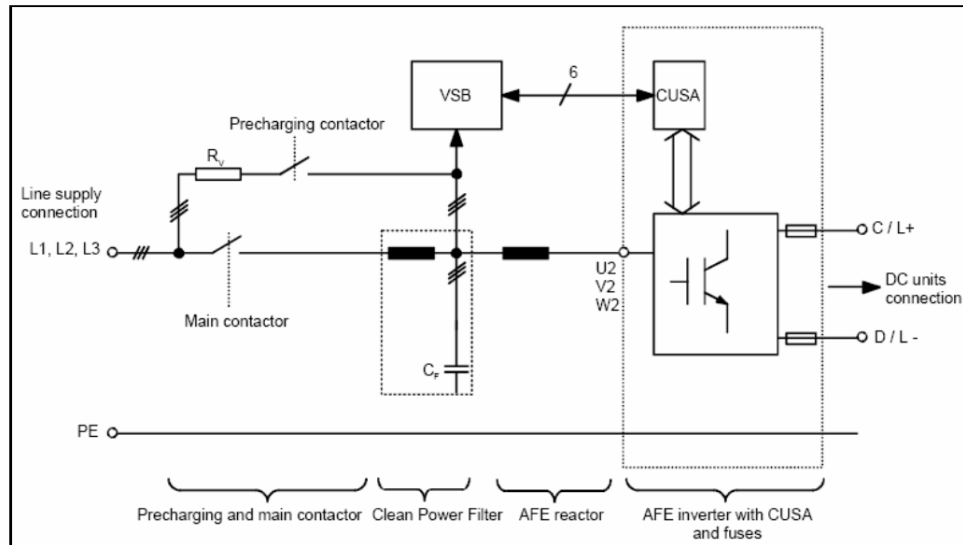


Fig. 6.5. The basic circuit of SIMOVERT MASTERDRIVE

Configuration:

Both one and several inverters can be connected to the output. The maximum connected power of the inverters may amount to 4 times the rated power of the AFE inverter. The total active power drawn from the mains supply must not continuously exceed the rated power of the AFE; the plant must be configured to meet this requirement.

The AFE is suitable for coupling several inverters to a common DC busbar. This allows energy to be transferred between motoring and generating drives, thus providing a power-saving feature.

Line voltage dips can be bridged in voltage step-up operation without altering the DC link voltage value. This can be achieved up to 65 % of rated line voltage without additional components on condition that the power balance can be maintained.

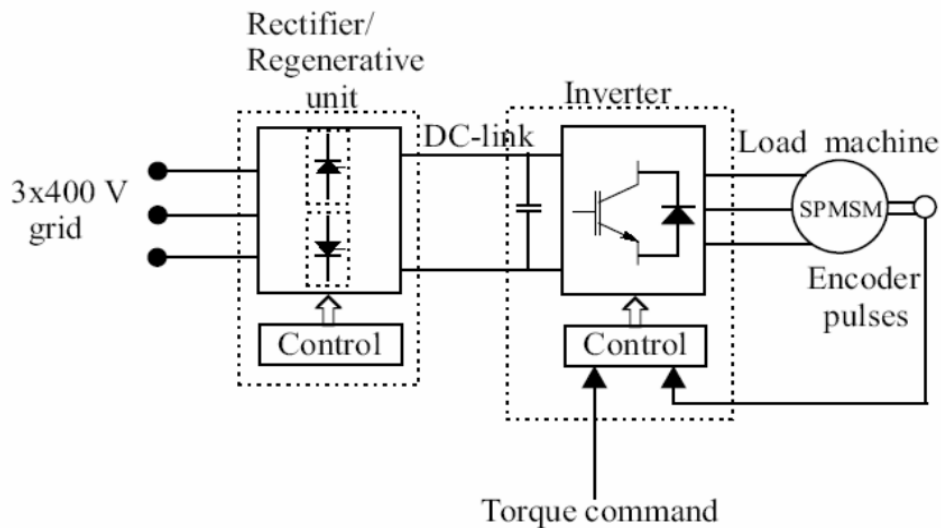


Fig. 6.6. Block diagram illustrating sections of the load control system

To bridge line voltage dips below 65 % of rated line voltage, the auxiliary power supply must be supported by an external UPS or similar to prevent the contactors from dropping out.

Operation and control options :

The unit can be controlled and operated via:

- the parameterization unit (PMU)
- an optional operator control panel (OP1S)
- the terminal strip
- a serial interface

In combination with automation systems, the AFE rectifier/regenerative feedback unit is controlled via optional interfaces (e.g. PROFIBUS) and technology boards (e.g. T100, T300).

Control of the rectifier/regenerative unit and the inverter is provided by Siemens. In addition, those units are provided with software so that the user can programme them via parameters in order to adapt to a specific application. Key-pads with displays are also included so that the user can programme them easily.

The torque command, which is needed to control the torque of the load machine, can be given to the inverter from the key-pad or using an analog voltage signal (0-10 V).

In conclusion, the torque value is sent from DACch1 of Dspace 1103 interface via a galvanic separation unit ISO-SIMO (see Fig.7.19) to SIMOVERT drive.

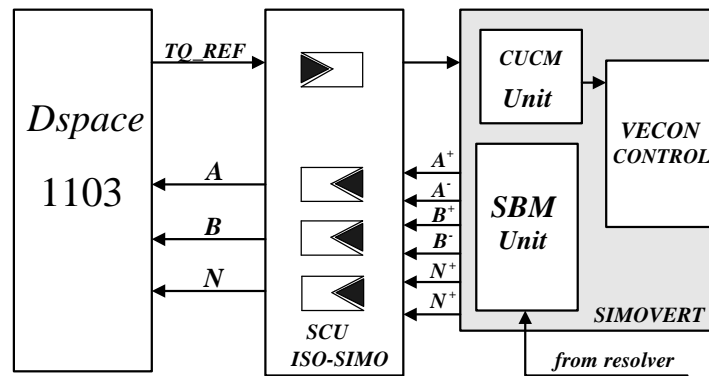


Fig. 6.7. The Simulink software Connections of SIMOVERT drive system to the DS1103 controller card

6.1.4. Acquisition system

6.1.4.1. Voltage and current sensors

The stator phase currents and the DC voltage link were acquired to fulfill the control system requirements.

The three current sensors are LEM LA 55-P type.

The sensors must be tuned so that the transmitted data to the dSpace platform to be accordingly to the actual data and to correspond in totality with the control strategy requirements.

Thus, an adequate signal conditioning box is also included between the current sensors and dSpace acquisition board such that at 10A measured current the sensor output will be 10V, required for the control system's A/D channels.

For the DC voltage link measurement a box with a voltage transducer of LEM LV 25-P type with appropriate signal conditioning such as 500 V measured voltage the output of the sensor is 10 V, required for the control system's A/D channels is also included.

6.1.4.2. Encoder

To prove the sensorless position estimation techniques, the PMSM motor was equipped with an incremental encoder.

Among position sensors, incremental encoders are most widely used because they are relatively cheap and accurate. The incremental encoders can provide absolute position information through the use of so-called Z pulse which is generated only once per revolution, and due to this reason it is practically impossible to start the PMSM motor using this signal.

The chosen device is a RENCO encoder type RCM15, which has a resolution of 2048 pulses per revolution and provides the real rotor position and speed. The output is a usual A QUAD B (A+, A-, B+, B-, INDEX+, INDEX-) which can be directly connected to the control system as it provides encoder interfaces (see Fig. 6.8).

The features of this encoder are:

- 2 data channels in quadrature
- once around index marker pulse.
- 3 commutation channels optically & electrically isolated.
- RS-422 interface (data & comm.).
- self aligning, self centering, self gapping.
- frequency response to 300 KHz.
- differential index, commutation, and data channels.
- PC Board connector for easy installation.

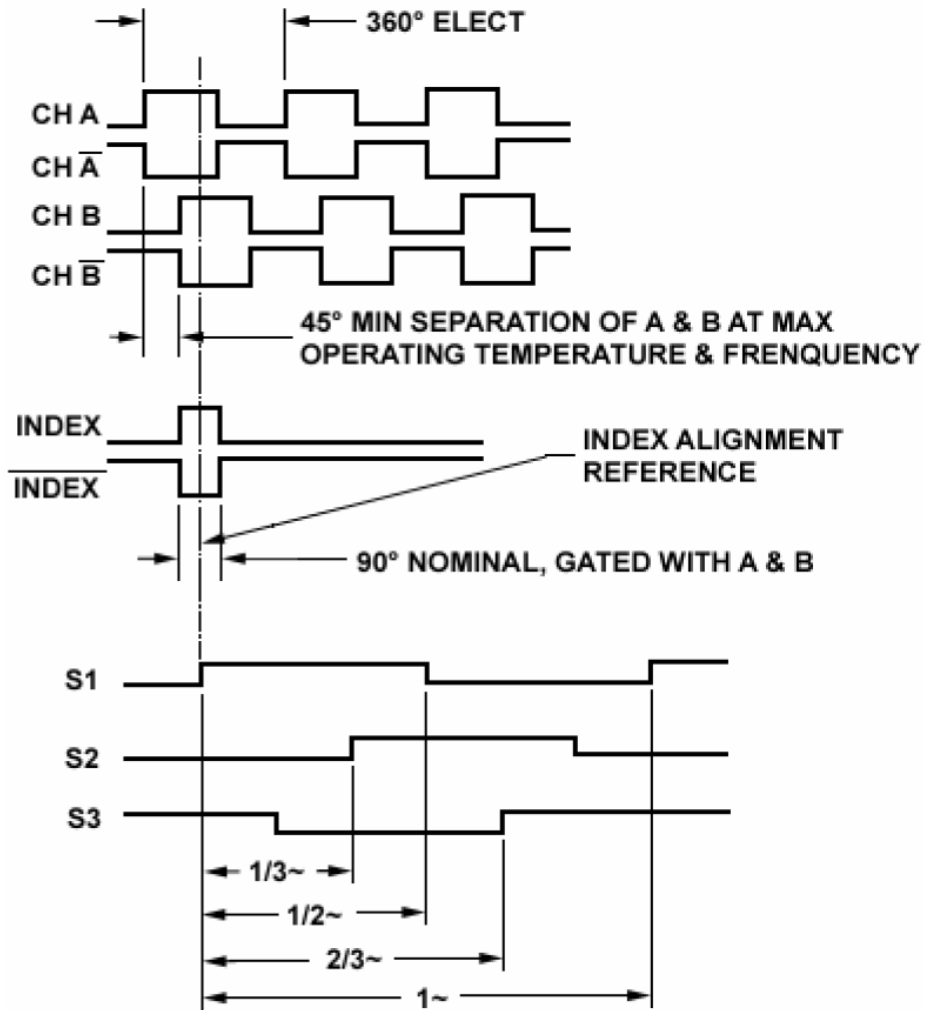


Fig. 6.8. Output configuration of the encoder

6.1.5. dSpace DS1103 platform

The DS1103 PPC, based on the Texas Instruments TMS320F240 DSP fixed - point processor, is especially designed for the control of electric drives.

Among other I/O capabilities, the DSP provides 3 -phase **PWM generation** making the subsystem useful for **drive applications**.

It features both high computational capability and comprehensive I/O periphery, built for real-time control system with just one controller board (Fig. 6.9).

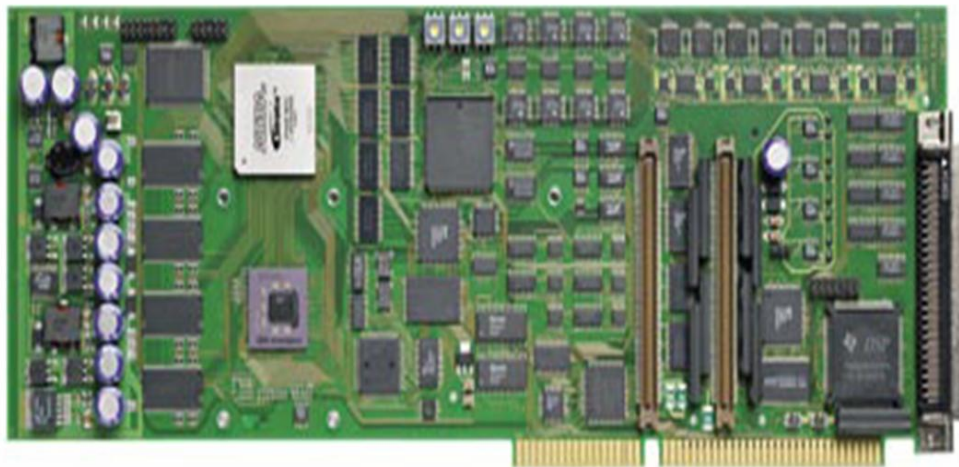


Fig. 6.9. DS1103 PPC Controller Board [2]

Used with Real-Time Interface (RTI), the controller board is fully programmable from the Simulink® block diagram environment. The user can configure all I/O graphically by dragging RTI blocks from Matlab® libraries. This is a quick and easy way to implement your control functions on the board and also reduces the implementation time to minimum.

Among other I/O capabilities, the DSP provides three-phase PWM generation making the subsystem useful for drive applications.

Dspace 1103 platform has been used in all experiments included in this thesis.

An overview of the functional units of Dspace 1103 is shown in Fig. 6.10.

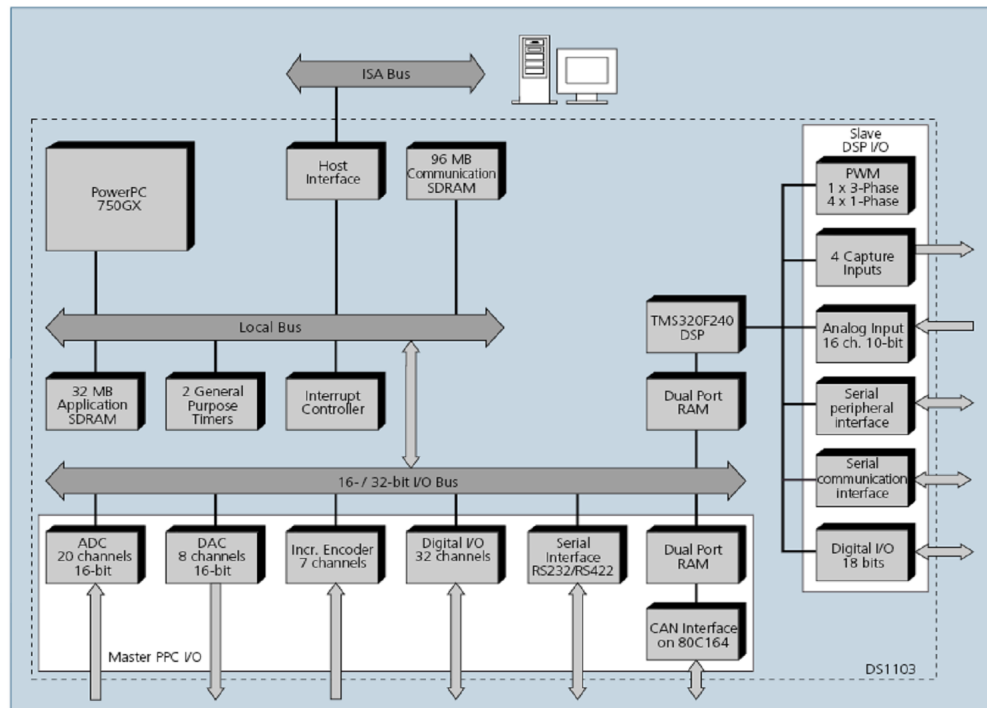


Fig. 6.10. Block diagram of Dspace 1103 [4]

The experimenting software, called Control Desk, allows real-time management of the running process by providing a virtual control panel with instruments and scopes (see Fig. 6.11).

When the soft is ready and it has no errors, it can be compiled in dSpace using the command BUILD. After the compilation, the soft is loaded in this interface Control Desk (see Fig. 6.11). Now, this interface contains all system parameters and allows their visualization, acquisition and changing.

A further subsystem, based on Siemens 80C164 micro-controller (MC), is used for connection to a CAN bus.

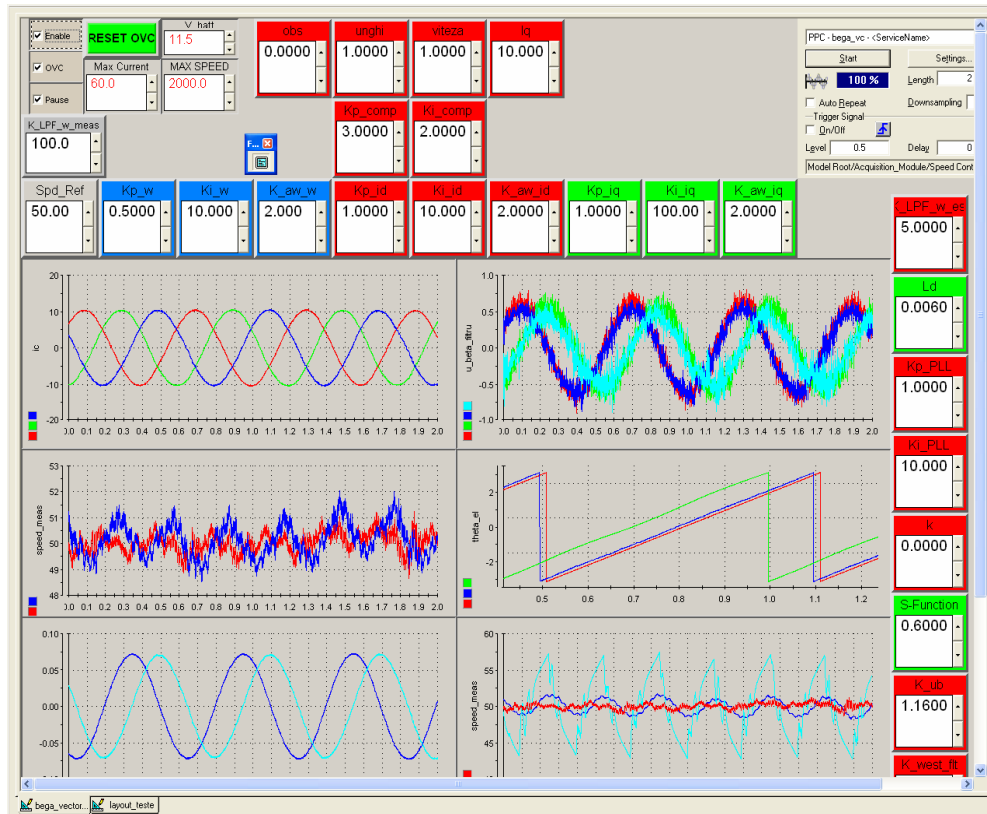
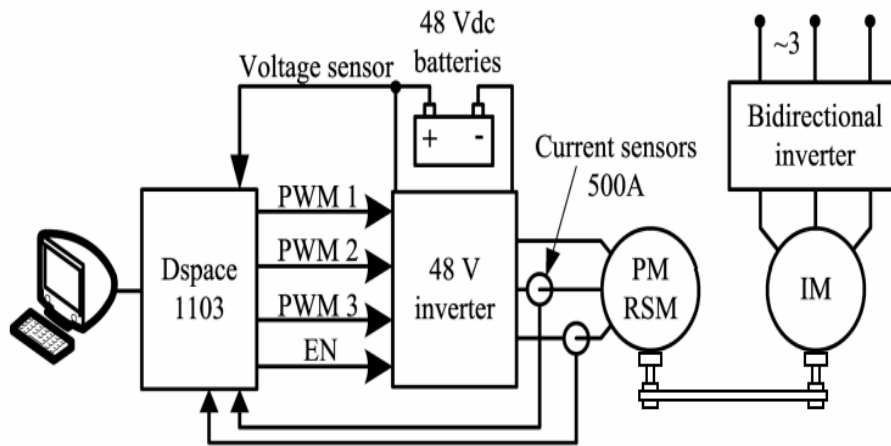


Fig. 6.11 dSpace Control Desk environment [3]

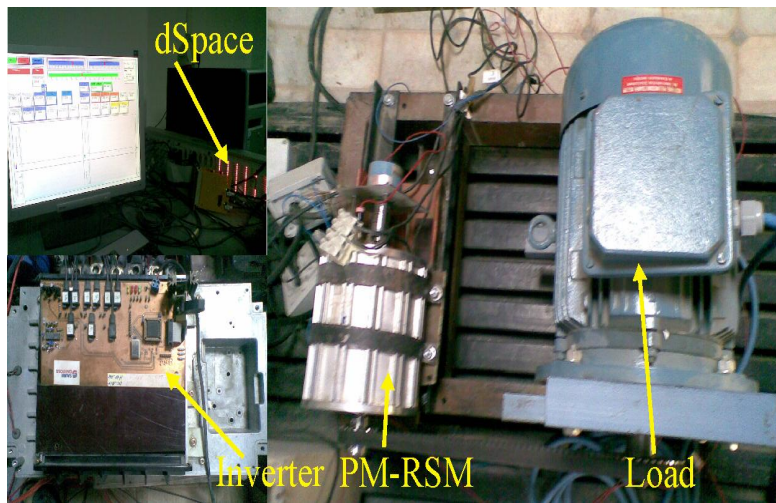
6.2. Experimental Setup 2

This experimental setup was realized in the Intelligent Motion Control Lab, Faculty of Electrical Engineering, Timisoara, Romania, in order to validate the proposed sensorless control schemes from chapter 5.

The setup is presented in Fig. 6.12.



a).



b).

Fig. 6.12. The overview of the experimental setup 1 a). the control block schem e; b).the control real implementation

As it can be seen in Fig. 6.12b a three-phase 2.2 kW PM-RSM is coupled via a transmission belt ($n_{IM}/n_{PM-RSM}=1/2$) with a three phase 5.5kW induction machine (IM), which is DTC sensorless driven by an ABB ACS600 bidirectional converter.

A three-phase MOSFET inverter, supplied at a dc-link voltage of 48V, feeds the PM-RSM.

6.2.1. Three phase inverter

The inverter is a 350A MOSFET inverter with 20 kHz switching frequency manufactured by Sauer Danfoss, Denmark.

The inveter name-plate data are:

BPI	5435
INPUT	48 V _{DC} -35% / -20%
OUTPUT	0...32 V _{AC} 0 350A

6.2.2. Dc-Link Power supply

Four 55Ah BOSCH valve regulated lead-acid batteries connected in series provide the DC link voltage power supply.

6.2.3. Test machine (PM-RSM)

The main component in the setup is a permanent magnet assisted reluctance synchronous motor (PM-RSM) prototype manufactured at Electromotor SA Timisoara (Fig. 6.12b).

It has a typical uniformly slotted stator with a three-phase ac winding, with a rotor with multiple flux barriers filled partially with PMs to reduce q -axis armature flux.

TABLE 6.2**PM-RSM SPECIFICATIONS**

Rated power	750 W
Rated speed	1500 rpm
Rated frequency	50 Hz
Rated torque	6.3 Nm
Rated phase to phase voltage	22 V (rms)
Rated phase current	50 A (rms)
Number of pole pairs (p_1)	2
Stator resistance per phase (R_s)	0.037 Ω
Stator resistance per phase including wires resistance (R_s)	0.065 Ω
d -axis inductance ($L_d(i_d)$)	2.5 mH (saturated value)
q -axis inductance (L_q)	0.5 mH
Permanent magnet flux (ψ_{PM})	0.011 Vs/rad
Total inertia (J)	1×10^{-3} kgm ²
Viscous friction coefficient (B)	1×10^{-4} Nm s/rad

6.2.4. Load control system

The load for the PM-RSM is represented by an induction machine DTC sensorless driven by an ABB ACS600 bidirectional converter.

The induction machine is coupled by a belt transmission with the PM -RSM test machine.

The belt transmission and the fact that the load induction machine is sensorless driven represents some kind of control system drawbacks. Thus, at low speeds, the test machine is hard to be sensorless controlled even if all inverter nonlinearities and stator resistance variation are compensated.

The ACS 600 introduces electric motors, drive train mechanisms and driven machines to an extended operating range.

The ACS 600 is controlled and programmed by using the Control Panel device (Fig. 6.13). The Panel can be attached directly to the door of the cabinet or it can be mounted, for example, in a control desk [5].

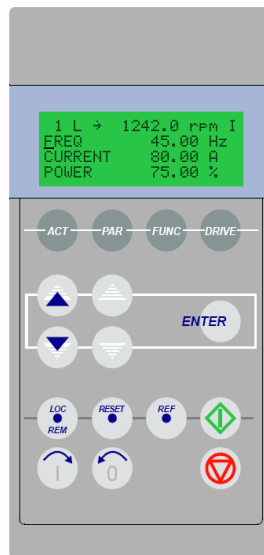


Fig. 6.13. Control Panel Device

6.2.5. Acquisition system

6.2.5.1. Current sensors

The stator phase currents (the third is calculated in the software taking into account that the sum of them is zero) and the DC voltage link were acquired to fulfill the control system requirements.

The 2 current sensors are PK 9508000 IP 66 type in the -300A...+300A. An adequate signal conditioning box is also included between the current sensors and dSpace acquisition board such that at 10A measured current the sensor output will be 10V, required for the control system's A/D channels.

6.2.5.2. Encoder

In order to prove the sensorless position estimation techniques, the IPMSM motor was equipped with an incremental encoder, Telemecanique XCC -1510PR50R, 5000 pulses per revolution (ppr) (see Fig. 6.14).

It provides the real rotor position and speed .



Fig. 6.14. Encoder 3D model

Its output is an usual A QUAD B (A+, A-, B+, B-, INDEX+, INDEX-) which can be directly connected to the control system as it provides encoder interfaces.

6.2.6. dSpace DS1103 platform

The DS1103 platform is identical with the one described in the paragraph 6.1.5.

6.3. Matlab/Simulink Software

The control algorithms for both experimental setups were developed in Simulink environment, compiled automatically using Microtec C compiler for Motorola Power PC and Texas Instruments C compiler and built/downloaded automatically using the dSpace system specialized MLIB/MTRACE mechanism.

The Simulink implementation is shown in Fig.28. The entire algorithm is triggered by a general PWM interrupt at 10 KHz.

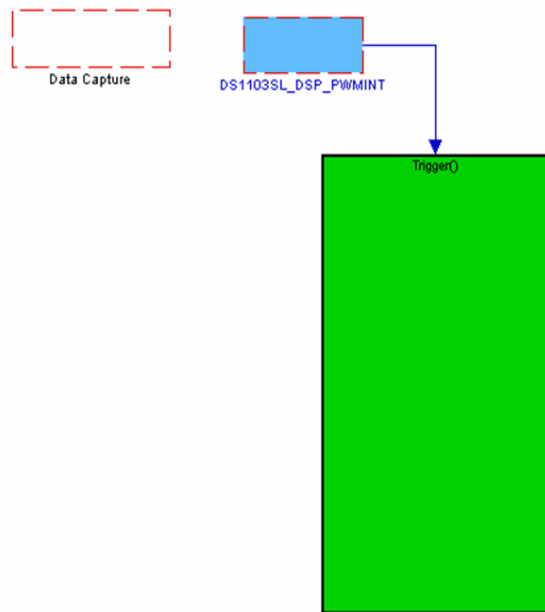


Fig. 6.15. The Simulink software

The Matlab/Simulink software consists in:

- acquisition blocks
- software protection block
- machine control
- estimation algorithms

6.3.1. Acquisition blocks

The stator currents are acquired on the nonmultiplexed A/D channels with 12-bit resolution, 800 ns sampling time.

Then the measured quantities are scaled taking into account the scaling factors of the sensors.

The implemented current acquisition block is illustrated in Fig. 6.16. Also the third current (for the experimental setup 2) is calculated from the other two measured.

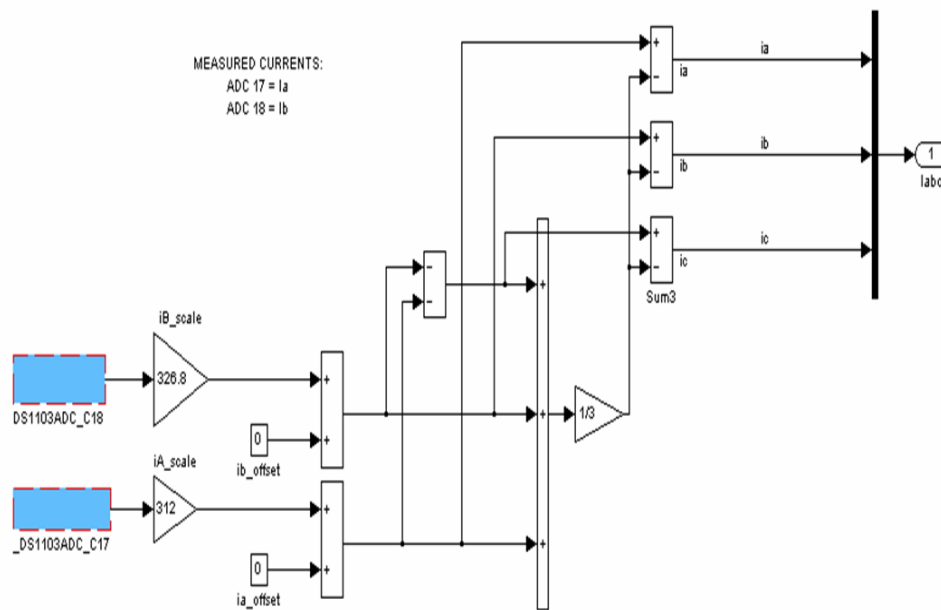


Fig. 6.16 Currents acquisition block

In the encoder interface (shown in Fig. 6.17) the position of the rotor and its speed are computed knowing the encoder resolution (number of the pulses per one revolution) and the system sampling time.

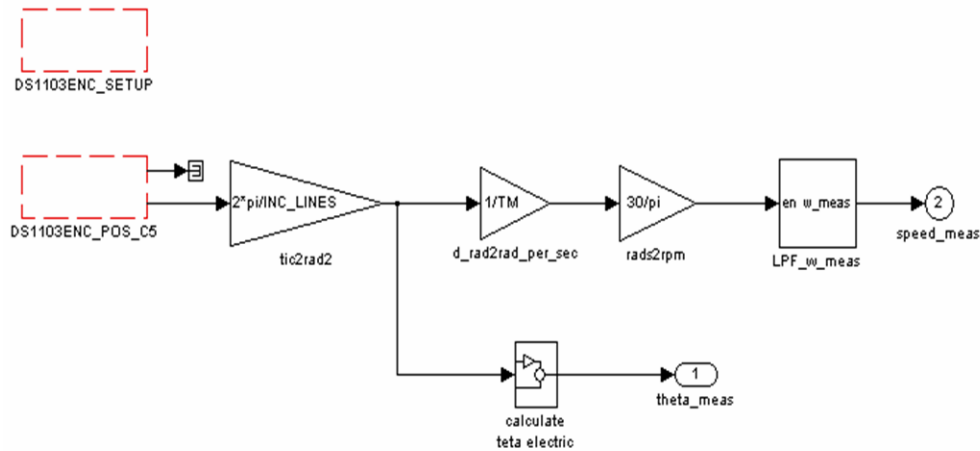


Fig. 6.17 Incremental encoder interface

6.3.2. Software protection block to prevent any damage upon the inverters

Two protections have been implemented: the overcurrent protection and the overspeed protection.

The mask of the protection block is shown in Fig. 6.18.

In order to allow the proper command of the inverter it is necessary that the three control signals (Overcurrent, START and PAUSE) must have the right values.

The block has as inputs the stator currents and the measured speed from the encoder.

The outputs of the protection block are ENABLE and STOP signals for the inverter.

The implementation is done as follows: the measured quantities are compared with the threshold values and the negated output of the comparators passed through an OR gate together with the ENABLE signal. Thus, the output is inhibited by any of the measured values exceeding its threshold value.

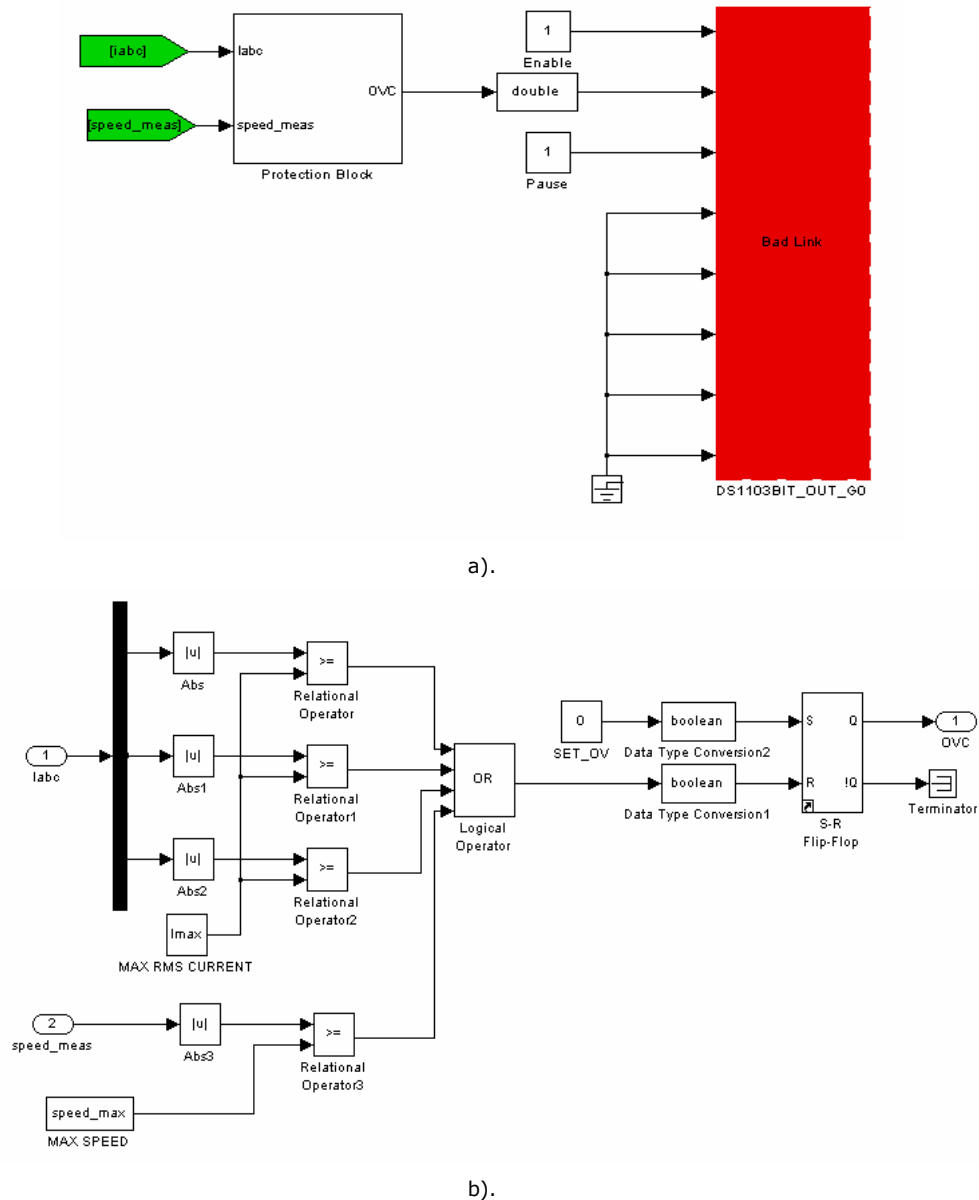


Fig. 6.18. Protection block: a). its outputs; b). the overcurrent and overspeed protection implementation

6.3.3. Machine control and estimation algorithms

The machine is controlled by giving the right PWM command signals for the inverter transistors.

Thus, the `svmtmpl` function automatically provides the duty cycles D_a , D_b and D_c - the t_{on} of the transistor - from the command voltages. Then, these duty cycles are introduced in a dSpace special block (DS1103SL_DSP_PWM) which will provide the PWM command signals for the upside transistors (see the upper side of Fig. 6.19).

The inverter (in our case) is capable to automatically provide the PWM command signals for the downside transistors, taking into account the imposed dead time.

This function is a C S-Function. The inputs are the DC voltage, the components α and β of the reference voltage vector and the measured phase currents for dead-time compensation purposes.

The reference voltage vector is provided by the control block (in which vector control or DTC could be implemented).

In order to realize a sensorless motion control of the interior permanent magnet synchronous motor the rotor position and speed estimation have to be available (as it can be seen in Fig. 6.19).

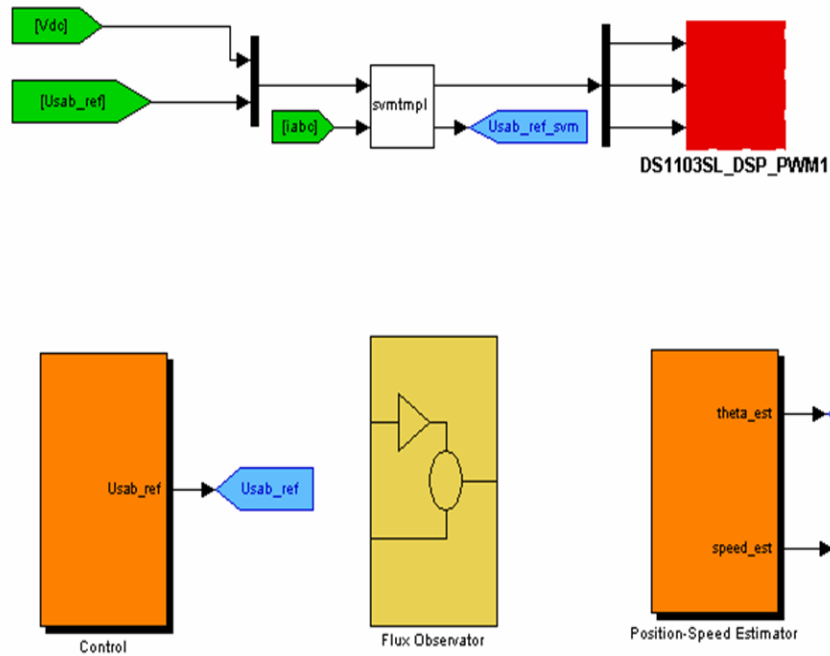


Fig. 6.19 The machine control and estimation algorithms

6.4. Conclusion

The experimental test platform used during the tests of state observers and sensorless controls of an interior permanent magnet synchronous machine system was presented in this chapter.

All the hardware components of the system were presented, discussed and analyzed. The software used for acquisition, inverter protection, control systems (vector control, direct flux control), flux observation and position-speed estimation was also explained.

The way the software developed in Matlab Simulink and the interface Control Desk Developer from the dSpace platform interact was also presented.

References

- [1] *** SIEMENS SIMOVERT Compendium CD ROM, 2000
- [2] *** DS1103 R&D Controller Board Intallation and Configuration Guide, dSPACE GmbH, <http://www.dspace.com>
- [3] *** ControlDesk Experiment Guide, dSPACE GmbH, <http://www.dspace.com>
- [4] <http://www.dspace.com>
- [5] www.abb.com

Chapter 7

Conclusion and contributions

Due to its cost and reduced reliability, a rotor mounted angular position sensor is not desirable. In this situation a sensorless control is needed.

Consequently, the thesis was dedicated to the new sensorless control strategies for synchronous machines and, based on the presented results, the main conclusion can be summarized as follows:

7.1. Sensorless Techniques for PMSMs – State of the Art

- Control techniques, which are being applied to make ac drives a rapidly growing area, have been reviewed, starting with scalar control.
- Speed or position sensorless techniques are of increasing importance. Their features were discussed, splitting techniques into fundamental model-based and signal injection techniques.
- Revising all these sensorless techniques with their advantages and disadvantages, a solution is proposed.

7.2. Active Flux Concept for Unified AC Drives

- A rather novel (or generalization) concept - *active flux* - along the d axis was introduced. It represents the *torque-producing flux*, which renders all salient-pole traveling-field (induction and synchronous) machines into nonsalient-pole machines with $L_q(i_s)$ inductance along the q axis.
- Active-flux orientation control is shown to be applicable to all ac machines by two generic schemes with a sizable common part. For SMs, the rotor position is equal to the active-flux angle.
- Rotor position and speed estimations based on the active-flux observer are shown to be simpler than existing solutions and very similar for all ac machines, as magnetic saliency is no longer a key factor.
- The active-flux concept allows for easy self-commissioning sequences.

- The active-flux concept applies both to vector control and to DTC with active flux and torque-closed loops.
- The active-flux orientation was applied in digital simulations to a high-saliency IPMSM with very promising results — from 1 rpm to 4000 rpm — without signal injection.
- Two stator flux observers were developed and compared. Both are based on the voltage and on the current models, but one is using them in parallel and one in series. The topologies and the results are also illustrated and discussed

7.3. “Active Flux” Sensorless Vector Control of IPMSM

- The stability of the proposed active flux observer is analyzed.
- The compensation methods of all factors which can cause inaccurate active flux estimation are also discussed and some of them proven by digital simulations.
- The current vector control strategy, using the proposed observer and without signal injection, was applied to the IPMSM sensorless drive in a speed range down to 2 rpm and up to 1000 rpm.

7.4. “Active Flux” DTFC-SVM Sensorless Control of IPMSM

- The novel state-observer for flux, rotor position and speed is developed based on the concept of active flux, particularized for motion-sensorless for IPMSM drive using DTFC-SVM. No signal injection is involved.
- The IPMSM drive performs with good results in a wide speed range down to 2 rpm and up to 1400 rpm.
- For making a comparison between theory and practice, digital simulations of the motion-sensorless control system are also presented. Both of them validate the active flux concept for motion sensorless DTFC-SVM for IPMSM drive.

7.5. Wide Speed Range Sensorless Control of PM-RSM via "Active Flux Model"

- Two methods for the motion sensorless control of PM-RSM in wide speed range are presented. The theoretical basis of both proposed control strategies has been described in detail and some analytical forms are also provided for reference.
- Using the proposed control strategy 1 the motor exploits the maximum torque capability in the whole speed range, observing the voltage and current constraints, and good efficiency all over.
- The control strategy 2 is an alternative to the first control, but having the advantage to be more simple and involving less computational off-line effort.
- The conclusion was that both of them perform the same in a wide speed range down to 1 rpm and up to 12000 rpm, thus, up to a speed equal eight times machine base speed.
- The experimental results between 30 rpm and 3000 rpm validate the theoretical background.
- Also, a vector control system was developed and operation below and above rated speed has been studied using it. Then a comparison between vector control system and the control strategy 2 confirmed the effectiveness of the second, especially under loading conditions.

7.6. Original contributions

The main contributions in the thesis, from the author point of view, can be summarized as below:

- Presentation of the state of the art in the sensorless control methods for the synchronous machines with permanent magnets.
- Introduction of the active flux concept for all ac drives by employing a unified state observer.
- Analysis through digital simulations of two active flux observers (one using the current model connected in series with the voltage model and the other using it in parallel).

- Development and simulation in MATLAB/Simulink of a robust control - a vector control with space vector modulation (SVM) for synchronous machines with interior permanent magnets - using the active flux concept and without signal injection.
- Implementation of the sensorless vector control for interior permanent magnets synchronous machines (IPMSM) - using a dSpace DS 1103 system.
- Development and simulation in MATLAB/Simulink of a direct torque and flux control (DTFC) with space vector modulation (SVM) for synchronous machines with interior permanent magnets - also based on the active flux concept and without signal injection.
- Implementation of the sensorless DTFC-SVM for interior permanent magnets synchronous machines (IPMSM) - using a dSpace DS 1103 system.
- Both implemented control systems have results as:
 - Vector control with SVM for IPMSM is shown capable of 1000 rpm to 2 rpm speed range half full loaded in motion-sensorless implementation without signal injection using the active flux for rotor position estimation.
 - DTFC with SVM for IPMSM is shown capable of 1400 rpm to 2 rpm speed range half full loaded in motion-sensorless implementation also, without signal injection and using the active flux for rotor position estimation.
- Introduction and analysis of a compensation method for the magnetic saturation, which is then proven by digital simulation.
- Introduction and analysis of a compensation method for the stator resistance variation, proven also by digital simulation.
- Analysis of the stability of the active flux observer.
- Implementation of a method which permits to identify the magnetic saturation curve for the Pm-RSM.
- Development and simulation in MATLAB/Simulink of a novel torque referencing sensorless strategy (in thesis it is called control strategy 1), which includes a reference torque calculator that is capable to develop maximum available motor torque for an optimal current pair below base speed, but also in flux weakening region.

- Development and simulation in MATLAB/Simulink of a second sensorless control strategy (called control strategy 2) for a wide speed range, which is a simpler alternative to the previous strategy.
- Implementation of the sensorless control strategy 2 for the PM-RSM, using a dSpace DS 1103 system with a Sauer Danfoss 12V, 350A inverter; extensive experimental results down to 30 rpm and up to 3000 rpm, focused on wide speed range sensorless operation for motoring and generating prove the effectiveness of the proposed solution; thus, a constant power speed range up to 8 has been proved with the machine supplied at 12 V.
- Implementation of the sensorless vector control system for the PM-RSM with maintaining the i_q^* at 22 A in order to cancel the q -axis flux; here again, the experimental results down to 30 rpm and up to 3000 rpm confirm the PM-RSM flux weakening operation.
- Realization, based on experimental results at various speeds from very low speed and up to 3000 rpm, of a comparison between the so called control strategy 2 and the vector control system.
- Implementation of the compensation methods of voltage drops on inverter power devices and of inverter dead time; without them the experiments at low speed of 30 rpm and 50 rpm, without motion sensors, could not be obtained.

7.7. Future work

Even through several topics have been addressed in the thesis, there are still a few, which are interesting for future research. Some of those topics are summarized below:

- Testing and analysis the effect of an incorrect measured rotor angle in the current model and presenting an error detection and compensation method.
- Developing an estimation method for the initial angle of the rotor since, when starting a synchronous machine, the initial value of the stator flux linkage must be known.

Further research is still needed to bring the reliable position sensorless speed range near zero speed.

Author's papers related to the Ph. D. thesis

- [1] I. Boldea, M. C. Paicu and G.-D. Andreescu, "Active flux concept for motion-sensorless unified ac drives", IEEE Transactions on Power Electronics, vol. 23, no. 5, pp. 2612–2618, Sept. 2008 ([ISI Journal](#), [IEEE Explore](#), [INSPEC](#), [Compendex](#)).
- [2] I. Boldea, M. C. Paicu, G.-D. Andreescu and F. Blaabjerg, "Active Flux Orientation Vector Sensorless Control of IPMSM", in Proc. OPTIM 2008, Braşov, May 2008, vol. 3, pp. 161-168 ([ISI Proceedings](#), [IEEE Explore](#), [INSPEC](#), [Compendex](#)).
- [3] I. Boldea, M. C. Paicu, G.-D. Andreescu and F. Blaabjerg, "Active Flux DTFC-SVM Sensorless Control of IPMSM", IEEE Transactions on Energy Conversion, vol. 24, no. 2, pp. 314-322, June 2009 ([ISI Journal](#), [IEEE Explore](#), [INSPEC](#), [Compendex](#)).
- [4] M. C. Paicu, L. Tutelea, G.-D. Andreescu, I. Boldea "Active flux sensorless vector control of IPMSM for wide speed range" Journal of Electrical Engineering, JEE, vol. 8, no. 5, Politehnica Publishing House, "Timisoara, 2008.
- [5] M. C. Paicu, L. Tutelea, G.-D. Andreescu, I. Boldea, F. Blaabjerg "Wide speed range sensorless control of PM-RSM via "active flux" model", accepted for presentation to IEEE-ECCE 2009, San Jose, SUA ([ISI](#), [IEEE Explore](#), [INSPEC](#), [Compendex](#)).
- [6] M. C. Paicu, I. Boldea, G.-D. Andreescu "Very low speed performance of active flux based sensorless control: IPMSM vector control versus direct torque and flux control", accepted for publication in IET Electric Power Applications ([ISI Journal](#)).

Author's CV

Mihaela Codruta Paicu

Home Address Slăt. Grigore Haidău, bl.2, sc.1, ap.5
302217 Tîrgu Jiu
Romania
Mobile +40 766 699 556
E-Mail: paicucodruta@yahoo.com

EDUCATION

2005-2009 PhD student at "Politehnica" University of Timișoara,
Romania, Department of Electrical Engineering
2000 Dipl. degree in Electrical Engineering
2000-2005 University " Politehnica " of Timișoara, Timișoara, Romania
1996-2000 National College "Tudor Vladimirescu", Tîrgu Jiu, Romania

PROFESSIONAL EXPERIENCE

3 months in 2007 Guest Researcher at "Institute of Energy technology",
Aalborg University, Denmark
6 months in 2003 Guest Student at "L'Institute National Politechnique de
Grenoble", Grenoble, France

PERSONAL INFORMATION

Born: July 24th 1981

Family: Unmarried